Department of Physics & Astronomy
Curtin Institute of Radio Astronomy
International Centre for Radio Astronomy Research

Regimes of Super-Eddington Accretion and Outflows in Extragalactic X-ray Binaries

Ryan Troy Urquhart

This thesis is presented for the Degree of
Doctor of Philosophy
of
Curtin University

July 2018

To the best of my knowledge and belief this thesis contains no material previously published by any other person except where due acknowledgement has been made. This thesis contains no material which has been accepted for the award of any other degree or diploma in any university.

.....
Ryan Urquhart
July 8, 2018

Kif, old friend, I don't know which disgusts me more: Your cowardice or your stupidity! We'll simply set a new course for that empty region over there. Near that black-ish hole-ish thing.

- Zapp Brannigan

Acknowledgements

First and foremost, I would like to thank my supervisors Roberto Soria, James Miller-Jones, Gemma Anderson, Richard Plotkin and Peter Curran. I am eternally grateful for all the time and effort you have invested in me. You set an incredibly high standard and always pushed me to achieve my best. You have been both friends and mentors, and I couldn't have asked for better role models. Any future success I might see will always be owed to you.

I thank my undergraduate supervisor Steven Tingay for his continued support and encouragement. To my friends at ICRAR, thank you for somehow putting up with me. Special thanks must go to Sam McSweeney for helping me survive my undergraduate degree and providing assistance to this day. And to Pikky Atri, Ronniy Joseph, Steven Tremblay, JT Malarecki, Tom Russell and Brian Crosse, I feel so lucky for the camaraderie I have shared with you all. I would also like to thank the CIRA administration team, Evelyn Clune, Angela Dunleavy and Tina Salisbury, without whom I would have been lost many a time.

I'd also like to thank my friends outside of work, especially Michael Modrzynski and Aaron Mattner. You kept me sane, always providing an escape from my studies. I am truly grateful for your companionship.

To my parents, thank you for your endless love and support. You never gave up on me, no matter how directionless I became, and for that I cannot thank you enough. My greatest desire in life has always been to make you proud.

To Erica, quite simply, thank you for always being there. You provided support when I needed it the most, never asking for anything in return. Thank you for always seeing the best in me, even when I couldn't. Though the future terrifies me, I take comfort in knowing you'll be there to face it with me.

And finally, to Vlad, my partner in crime, I want to thank you for your friendship and your zen-like patience. How you didn't murder me after the fifteenth time I asked you 'is radiatively-driven hyphenated?' or 'should I flag these data?' will remain a mystery to me. I'm not sure how I'm going to cope without you. I've been incredibly lucky to share the last three years with you and I genuinely believe that without you by my side, I would never have made it through. I wish you all the best in the future.

Abstract

Ultraluminous X-ray sources (ULXs) represent stellar-mass binary systems accreting at the highest rates. The ULX population is observationally diverse, with a variety of X-ray spectral properties and variability and outflow characteristics that are attributed to numerous different physical interpretations. In this thesis we analyse multiwavelength observations of a select number of ULXs. While these sources demonstrate a wide range of contrasting observable properties, they are all important examples of super-Eddington accretion. We review how the observational attributes (X-ray spectral and timing properties, outflow characteristics and large-scale optical and radio features of ULXs) are related to the physical properties of our sources, like inclination angle and mass accretion rate.

The generally-accepted view of ULX spectral states is that they are a result of inclination angle rather than being physically distinct. However, here we present work that suggests otherwise. We have discovered the first two eclipsing ULXs (both inferred as being seen almost edge-on), thus providing the first strong constraint on the inclination angle of a ULX. Despite having similar viewing angles and luminosities ($L_{\rm x} \approx 2 \times 10^{39}\,{\rm erg\ s^{-1}}$), the sources have different X-ray properties; the first (M 51 ULX-1) has a soft spectrum and shows signatures of a disk wind, while the second (M 51 ULX-2) has a harder spectrum and no evidence of any strong outflows. Clearly, inclination angle cannot be the sole factor that dictates ULX spectral states.

Additionally, we investigate the X-ray spectral and timing properties of a subclass of ULXs known as ultraluminous supersoft sources (ULSs). The supersoft blackbody spectra synonymous with these objects is thought to be the product of emission from the photosphere of an optically thick disk wind. Consequently, ULSs are often attributed to being ULXs seen at the highest inclination angles, where the disk wind is thickest. However, considering our previous result in which neither eclipsing source is detected in a ULS state, additional physical parameters must be invoked in order to explain ULSs. We suggest that a combination of inclination angle and mass accretion rate is responsible; ULSs represent the high accretion-rate tail of the ULX population, where the resulting outflow is at its most optically dense, and are a physically distinct class.

We also investigate the relation between ULXs and their large-scale properties. A number of ULXs have been observed with coincident optical and radio bubbles. These bubbles are inflated by either the mechanical power of the ULX outflows (either a collimated jet or quasi-spherical winds, or a combination of the two) or from the intense X-ray radiation produced by the inner regions of the accretion flow. We use the radiative power of two optical bubbles around newly discovered ULXs to determine the mechanical power output of these sources. Similar to other ULXs with strong outflows, we find that the mechanical power can dominate over the radiative power. An estimation of the mechanical power is required to quantify the total (radiative plus mechanical) power output and thus recognise different accretion regimes across the ULX population.

Finally, we discuss how the observational properties of ULXs, including X-ray luminosity, spectral hardness, optical depth, presence of bubbles, lobes or hotspots, and jet power, are physically related. We suggest that a combination of changes to the mass accretion rate, inclination angle, type of accretor, magnetic field strength and presence of outflows can be used to describe the wide variety of ULX observational features, and conclude by outlining how this might be tested with future instruments.

Abbreviations and acronyms

2MASS	Two Micron All-Sky Survey
ACIS	Advanced CCD Imaging Spectrometer
ACS	Advanced Camera for Surveys
ADAF	Advection-dominated accretion flow
AGN	Active galactic nucleus
ARF	Ancillary response file
ATCA	Australia Telescope Compact Array
ATOA	Australian Telescope Online Archive
BH	Black hole
CABB	Compact Array Broadband Backend
CASA	Common Astronomy Software Application
CCD	Charge-coupled device
CIAO	Chandra Interactive Analysis of Observations
EPIC	European Photon Imaging Camera
eROSITA	extended ROentgen Survey with an Imaging Telescope Array
EW	Equivalent width
EXTraS	Exploring the X-ray Transient and variable Sky
FOCAS	Faint Object Camera and Spectrograph
FORS	FOcal Reducer and low dispersion Spectrograph
FWHM	Full width at half maximum
GRB	Gamma-ray burst
HEASARC	High Energy Astrophysics Science Archive Research Center
HETGS	High Energy Transmission Grating Spectrometer
HMXB	High-mass X-ray binary
HRC	High Resolution Camera
HRI	High Resolution Imager
HST	Hubble Space Telescope
HWZI	Half-width at zero intensity
ICRF	International Celestial Reference Frame
IMBH	Intermediate-mass black hole
IR	Infrared
IRAF	Image Reduction and Analysis Facility
ISCO	Innermost stable circular orbit

ISM	Interstellar medium
KS	Kolmogorov-Smirnov
LBT	Large Binocular Telescope
LMXB	Low-mass X-ray binary
mag	Magnitude
MJD	Modified Julian Date
MODS	Multi-Object Double Spectrograph
ngVLA	Next Generation Very Large Array
NRAO	National Radio Astronomy Observatory
NS	Neutron star
PA	Position angle
PIMMS	Portable, Interactive Multi-Mission Simulator
PSF	Point-spread function
PSPC	Position-Sensitive Proportional Counter
RFI	Radio frequency interference
RGS	Reflection Grating Spectrometer
RMF	Redistribution matrix file
RSG	Red super-giant
ROSAT	Röntgensatellit
SAS	Science Analysis Software
SFR	Star formation rate
SKA	Square Kilometre Array
SMBH	Super-massive black hole
SN	Supernova
SNR	Supernova remnant
SSS	Supersoft source
TDE	Tidal disruption event
UFO	Ultra-fast outflows
ULX	Ultraluminous X-ray source
ULS	Ultraluminous supersoft source
UV	Ultraviolet
VLA	Very Large Array
VLT	Very Large Telescope
WD	White dwarf
WFC	Wide Field Channel
XMM-Newton	X-ray Multi-Mirror Mission
XRB	X-ray binary
XSPEC	X-ray spectral-fitting program

Contents

List of Tables

List of Figures

Chapter 1

Introduction

Ultraluminous X-ray sources (ULXs) are some of the most energetic stellar objects in the known Universe. They are classified by their unusually high luminosities, which exceed the theoretical limit for stellar-mass objects. The true nature of ULXs is still heavily debated; are they massive objects whose intense luminosity comes from their size or are they smaller objects whose luminosity is a result of a rapid influx of material? In fact, there appears to be different scenarios for a whole spectrum of ULX masses, ranging from low-mass neutron stars to the massive, and long-sought intermediate-mass black holes. Whatever the case, ULXs provide a unique opportunity to study important fundamental physical processes associated with accretion onto compact objects.

1.1 Compact objects

This thesis is the study of how the accretion onto compact objects, neutron stars and stellar-mass black holes, manifests itself observationally at the highest rates. These compact objects are the end points of stellar evolution in massive stars ($\gtrsim 8$ $M_\odot$). Neutron stars are the compacted cores of collapsed stars that have since exhausted their source of nuclear fuel and are now supported by neutron degeneracy pressure. They are extremely dense objects, with a mass of around 1.4 $M_\odot$ compressed into a radius of only 10 km. Neutron stars as massive as $2.3 - 2.4$ $M_\odot$ have been discovered (Linares et al., 2018; van Kerkwijk et al., 2011), although more massive objects would further collapse and result in the formation of a black hole.

Black holes are astrophysical objects whose gravitational pull is so strong that not even light can escape. An entire spectrum of black holes is theorised to exist ranging from stellar mass black holes ($\lesssim 100$ $M_\odot$), the evolutionary end points of the most massive ($\gtrsim 22$ $M_\odot$) stars (Fryer and Kalogera, 2001), to super-massive black holes (SMBHs; $\gtrsim 10^6$ $M_\odot$), found at the centres of most galaxies

(Kippenhahn and Weigert, 1990). While electromagnetic emission from a black hole cannot be detected, emission from the hot gas accreting into the black hole, prior to it crossing the event horizon, can be detected.

Accretion is the power source behind some of the most energetic, and violent, astrophysical objects. We see its effects from explosive and short-lived stellar objects such as gamma-ray bursts (GRBs) up to galactic nuclei, accreting over billions of years. We also witness accretion occurring at different rates; from almost insignificant rates in quiescent sources, such as Sgr A*, up to incredibly rapid accretion rates that were originally thought to be unphysical. Accretion rates play a crucial role in the classification of binary systems, which are studied throughout this thesis.

1.2 Accretion

Accretion is a fundamental process throughout the Universe. It is the most efficient way of extracting energy from matter, able to extract $\sim 15\%$[1] of the rest mass energy for a typical stellar-mass black hole or neutron star. For comparison, nuclear fusion of hydrogen to helium only has an efficiency of 0.7%. The energy released through accretion is the result of gravitational potential energy being converted to radiation. The energy released, E, via this process can be quantified using the equation

$$E \approx \frac{GMm}{r}, \tag{1.1}$$

(Frank et al., 2002) where G is the gravitational constant, m is the mass of a test particle and M and r are the mass and radius of the compact object, or "accretor", respectively. For objects such as white dwarfs and neutron stars, r is the radius of the surface of the star ($r_{\rm WD} \sim 1 \times 10^4\,{\rm km}$ and $r_{\rm NS} \sim 10\,{\rm km}$). However, for black holes, with no surface, r is the radius of the inner boundary of the accretion disk, beyond which matter plunges towards the event horizon in free fall. As an order of magnitude estimate, this radius is proportional to the gravitational radius of the black hole $r_{\rm BH} = \frac{2GM}{c^2} \approx 3\frac{M}{M_\odot}\,{\rm km}$, where c is the speed of light.

The simplest form of accretion that can be considered is spherically symmetric accretion. Better known as Bondi-Hoyle-Lyttleton accretion (Hoyle and Lyttleton, 1941; Bondi, 1952), this process involves an accretor drawing material from its surrounding medium. Examples of Bondi-Hoyle-Lyttleton accretion include

[1] The efficiency can increase up to 42% (Frank et al., 2002) for a maximally spinning black hole.

an isolated star drawing matter from a surrounding gas cloud, an intermediate-mass black hole (IMBH) accreting from the interstellar medium (ISM) or a faint nuclear SMBH, especially in an early-type galaxy, where the hot gas inflow is too tenuous to form an accretion disk.

Although an important aspect of accretion, spherically symmetric accretion cannot be applied to binary systems. In binary systems, there are two forms of accretion; wind and Roche lobe overflow. These two distinct forms are dependent upon the donor star. If the donor star is massive[2], then it will generate a strong wind that drives material off the surface of the star. This matter is ejected isotropically, a small fraction of which can be captured gravitationally by the accretor. Because only a small fraction of material is accreted ($\sim$ a few percent of the wind mass), wind accretion tends to be of low efficiency.

Alternatively, accretion may occur via Roche lobe overflow (Figure 1.1). This is generally seen in systems with low-mass companion stars, but can also occur in high-mass systems, although only during short-lived phases. Roche lobe overflow involves the outer layers being stripped off the star. This is either due to an expansion of the star (a result of stellar evolution) or a reduction in the binary separation (due to the release of gravitational waves). Either way, this causes the star to fill what is known as its Roche lobe, the first gravitational equipotential surface enclosing both objects. The material from the surface of the star is then able to freely flow to the accretor through the L1 Lagrange point. This is a far more efficient way to accrete (relative to wind-driven accretion) and is the form of accretion required to power rapidly-accreting sources.

1.2.1 The Eddington luminosity

As the accretion rate ($\dot{M}$) onto a compact object increases, there is a corresponding increase in the energy production, which leads to a rise in the radiation pressure being exerted on the in-falling matter. This restricts the rate at which material can be accreted, hence there is an upper limit on the accretion rate, and therefore on the luminosity of the compact object. This luminosity is known as the Eddington luminosity, $L_{\rm Edd}$, and the accompanying accretion rate is defined as the critical accretion rate, $\dot{M}_{\rm Edd}$.

The Eddington luminosity is defined as the point at which the outward radiation pressure, $F_{\rm rad}$, is equal to the inward force of gravity, $F_{\rm G}$. Thus we calculate $L_{\rm Edd}$ using,

[2]Metallicity also plays a role in the strength of a stellar wind.

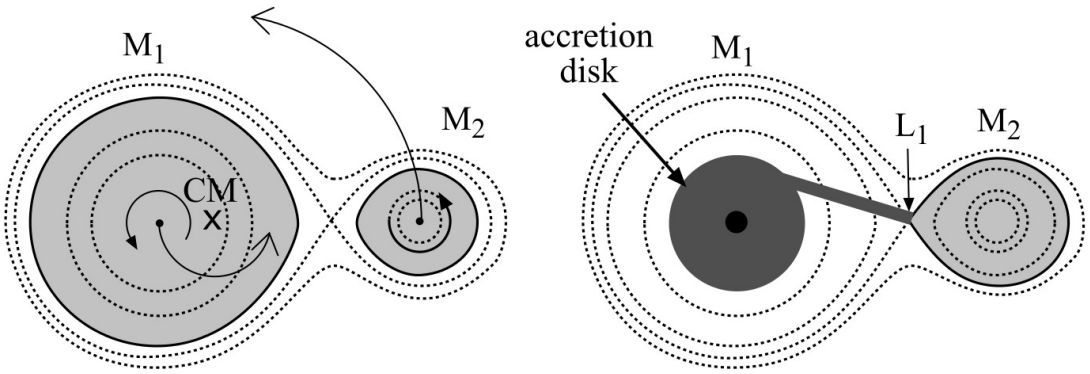

Figure 1.1: Cartoon of Roche lobe overflow from Maoz (2007). The dotted lines indicate surfaces of gravitational equipotential. Left panel: both stars are within their respective Roche lobes and so there is no flow of material. Tidal friction will cause the binary separation to reduce as energy is lost from the system. Right panel: Here M_2 fills its Roche lobe hence material is able to flow through the L_1 Lagrange point and fall into the gravitational potential of the compact object, M_1, and eventually into it.

$$F_{\rm G} = F_{\rm rad}, \tag{1.2}$$

$$\frac{GMm}{r^2} = \frac{L_{\rm Edd}\sigma_{\rm T}}{4\pi c r^2}, \tag{1.3}$$

$$L_{\rm Edd} = \frac{4\pi GMcm_{\rm p}}{\sigma_{\rm T}}, \tag{1.4}$$

which simplifies to,

$$L_{\rm Edd} \approx 1.3 \times 10^{38} \left(\frac{M}{\rm M_\odot}\right) \text{erg s}^{-1}, \tag{1.5}$$

where G is the gravitational constant, $\sigma_{\rm T}$ is the electron scattering cross-section and $m_{\rm p}$ is the mass of a proton. It should be noted that, due to the Coulumbic attraction between electrons and protons, any force on the electrons will cause a drag on the protons. Consequently, the mass of the test particle, m, becomes $(m_{\rm e} + m_{\rm p}) \approx m_{\rm p}$.

The Eddington luminosity is often described as a soft upper limit to the luminosity as there are some rare sources that appear to exceed it. There are a number of factors that can lead to luminosities greater than Eddington. Firstly, the luminosity derived in Equation 1.4 is an approximation and assumes spherical accretion (i.e. Bondi-Hoyle-Lyttleton accretion) of hydrogen. Higher-mass particles would increase the Eddington luminosity; for example, accretion of pure Helium would increase $L_{\rm Edd}$ by a factor of ≈ 2. Non-spherical accretion (such as in accretion disks in binary systems) can lead to geometric funnelling. Here,

radiation can escape via the poles, perpendicular to the disk, where it will no longer impede the infalling matter. An object's luminosity can also be altered by beaming wherein the radiation is Doppler boosted. If the radiation is beamed towards the observer, then the apparent luminosity increases while the intrinsic luminosity remains the same. Finally, a source can simply accrete at super-critical levels. In this case the luminosity is modified by

$$L = L_{\rm Edd}(1 + \ln \dot{m}), \tag{1.6}$$

(Shakura and Sunyaev, 1973; Poutanen et al., 2007) where $\dot{m} = \dot{M}/\dot{M}_{\rm Edd}$ is the accretion rate normalised to the Eddington accretion rate i.e. $\dot{m} = 1$ for sources accreting at the Eddington limit. The disk geometry in itself permits a luminosity slightly above the spherical Eddington limit. This regime will be explored further in Section 1.3.2. A super-Eddington source is likely to incorporate a number of these factors in order to exceed the Eddington limit.

1.2.2 Optical depth

Another important physical concept associated with the inflow and outflow resulting from accretion is optical depth, or optical thickness. Optical thickness is a measure of the likelihood that a photon travelling through a medium will be affected by particles within the medium. This can take the form of scattering or absorption. If the optical depth due to absorption, τ_α, is greater than unity, then a medium is said to be optically thick to absorption (or opaque) and if it is less than unity, then it is optically thin to absorption (or transparent). The same applies to the optical depth due to scattering (τ_σ). The combined effect of both absorption and scattering, known as the effective optical depth, τ^*, (Figure 1.2) is defined as,

$$\tau^* \approx \sqrt{\tau_\alpha(\tau_\alpha + \tau_\sigma)}, \tag{1.7}$$

(Rybicki and Lightman, 1979). Once again, if $\tau* > 1$, then the medium is effectively optically thick (opaque), and if $\tau* < 1$, then the medium is effectively optically thin (translucent – not necessarily transparent). These concepts play an important part in understanding the spectral properties of binary systems.

1.3 Accretion disks

In Section 1.2, we looked at different types of accretion, specifically the contrast between spherically-symmetric accretion and the accretion found in close binary

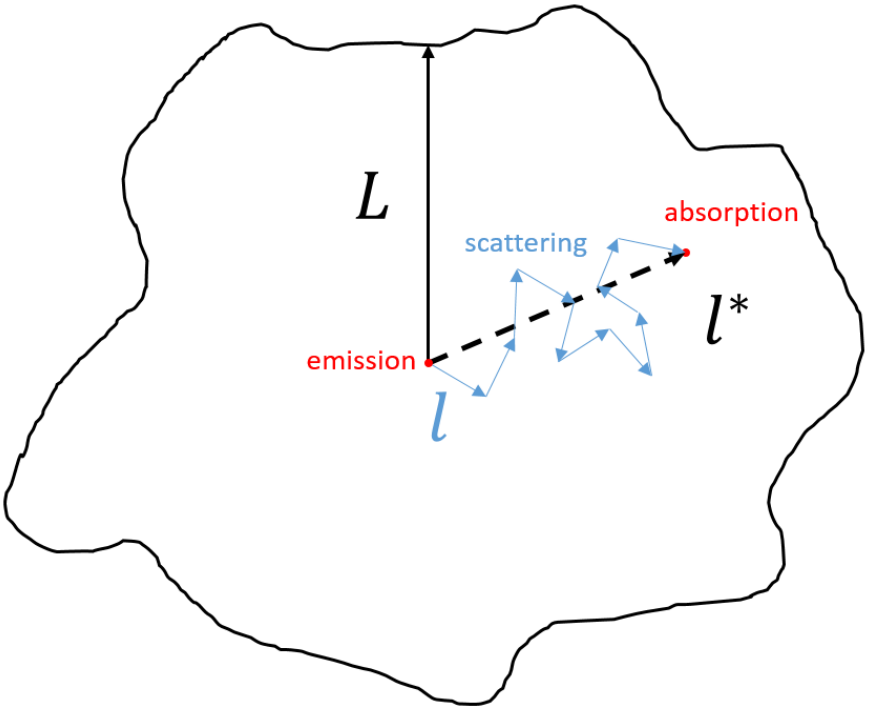

Figure 1.2: Cartoon of an effectively optically thick medium. As the physical size of the medium, L, exceeds the effective mean path, l^*, a photon emitted within the medium will be absorbed before reaching the surface.

systems. The difference arises due to the relative angular velocity between the material being accreted and the compact object. In the case of the binary system, the infalling material must shed angular momentum. In the case of accretion via Roche lobe overflow, the most efficient way to accomplish this is in an accretion disk; the matter stripped from the companion star accumulates in a disk in the orbital plane. In the high-density environment of the disk, matter is able to transfer angular momentum through viscosity. Some fraction of the matter can then fall in towards the accretor, and in doing so, release energy. A by-product of the energy production is a heating of the disk. The thermal disk emits as a blackbody radiator with each subsequent annulus getting hotter the closer it is to the accretor. The resulting spectrum is therefore a superposition of blackbody distributions of increasing temperature, generally peaking in X-rays, depending on the radius of the accretor (large objects tend to have cooler inner disks). The final, and hence hottest, annulus occurs at either (i) the surface of a non-magnetised neutron star; (ii) the radius at which the magnetic field interrupts the disk in a magnetised neutron star; or in the case of a black hole, (iii) the radius of the innermost stable circular orbit, $R_{\rm ISCO}$. For a non-spinning black hole, this

is,

$$R_{\rm ISCO} = 3R_{\rm schw}, \tag{1.8}$$

$$= \frac{6GM}{c^2} = 9\frac{M}{\rm M_\odot}\,{\rm km}, \tag{1.9}$$

where $R_{\rm schw}$ is the Schwarzschild radius[3] (a black hole co-rotating with the accretion disk will have a smaller value of $R_{\rm ISCO}$ while a black hole with a retrograde spin will have a larger value). The observed flux from the disk at frequency f, is,

$$F_f = \frac{4\pi h f^3 \cos i}{c^2 d^2} \int_{R_{\rm ISCO}}^{R_{\rm out}} \frac{R\,dR}{e^{hf/k_{\rm B}T} - 1}, \tag{1.10}$$

(Frank et al., 2002) where h is the Planck constant, $R_{\rm out}$ is the outer radius of the disk, d is the distance to the source, i is the inclination angle of the system, T is the temperature, and $k_{\rm B}$ is the Boltzmann constant.

Different types of accretion disks and accretion flows will be explored in more detail in later sections. For a detailed review of accretion disks, see Abramowicz and Fragile (2013).

1.3.1 Thin disks

In many systems, the infalling material is restricted to the orbital plane, in a geometrically thin accretion disk. For simplicity, the accretion flow is approximated to be a two-dimensional structure – the vertical extent of the disk can generally be ignored. Models that assume this approximation are known as 'thin disk models' and require that $H \ll R$, where H is the scale height of the disk.

The most prevalent thin disk model is the famous steady α-disk structure, known as the 'standard model', from Shakura and Sunyaev (1973). The α parameter is used to relate the kinematic viscosity, ν, to the scale height,

$$\nu = \alpha c_{\rm s} H, \tag{1.11}$$

where $c_{\rm s}$ is the speed of sound of the medium and the only restriction on α is that it be $\lesssim 1$. It is left as a free parameter because the physical process behind the viscosity is not fully understood. With this, we can generate a set of equations using the physical parameters of the disk, such as surface density, Σ, mass density, ρ, pressure, P, central temperature, $T_{\rm c}$, radial drift velocity, $v_{\rm R}$, and opacity, τ. The total set (Equation (1.12)), with eight equations, can be used to solve the

[3]The Schwarzschild radius is the distance from a black hole at which the escape velocity is equal to the speed of light; the event horizon of a non-spinning black hole.

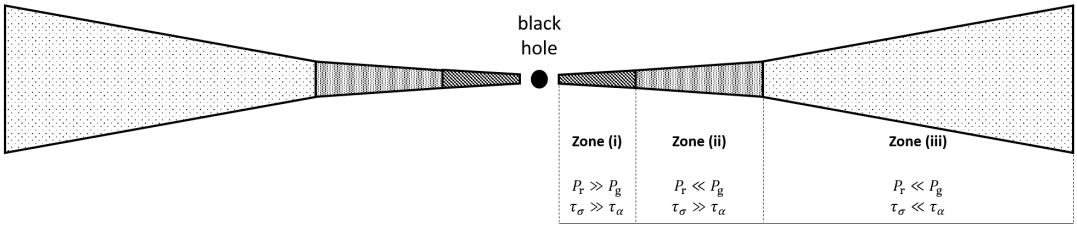

Figure 1.3: Sketch of a cut through a thin accretion disk. The different zones are defined by the changes in the pressure support mechanism and the dominant form of opacity.

eight unknown parameters, ρ,Σ,H,c_s,P,T_c,τ and ν, by relating them to M,R and $\dot{M}$. Finally, we get,

$$\left.\begin{aligned}
\rho &= \tfrac{\Sigma}{H}, \\
H &= c_\mathrm{s}\left(\tfrac{R^3}{GM}\right)^{1/2}, \\
c_\mathrm{s}^2 &= \tfrac{P}{\rho}, \\
P &= \tfrac{\rho k_\mathrm{B} T_\mathrm{c}}{\mu m_\mathrm{p}} + \tfrac{4\sigma T_\mathrm{c}^4}{3c}, \\
\tfrac{4\sigma T_\mathrm{c}^4}{3\tau} &= \tfrac{3GM\dot{M}}{8\pi R^3}\left[1-\left(\tfrac{R_*}{R}\right)^{1/2}\right], \\
\tau &= \Sigma\kappa_\mathrm{R}(\rho, T_\mathrm{c}) = \tau(\Sigma, \rho, T_\mathrm{c}), \\
\nu\Sigma &= \tfrac{\dot{M}}{3\pi}\left[1-\left(\tfrac{R_*}{R}\right)^{1/2}\right], \\
\nu &= \nu(\rho, T_\mathrm{c}, \Sigma, \alpha, ...),
\end{aligned}\right\} \tag{1.12}$$

(Frank et al., 2002), where κ_R is the Rosseland mean opacity and μ is the mean molecular weight.

There are three regions in the disk, outlined in Figure 1.3:

(i) the inner disk, where radiation pressure dominates. Here the disk is primarily supported by electron scattering. $P_\mathrm{r} \gg P_\mathrm{g}$, $\tau_\sigma \gg \tau_\alpha$

(ii) where gas pressure begins to dominate, however, electron scattering still determines opacity. $P_\mathrm{r} \ll P_\mathrm{g}$, $\tau_\sigma \gg \tau_\alpha$

(iii) the outer disk, where scattering is no longer dominant and free-free and bound-free absorption are the main contributors to opacity. This region is also gas pressure dominated. $P_\mathrm{r} \ll P_\mathrm{g}$, $\tau_\sigma \ll \tau_\alpha$

The main drawback to the thin disk approximation is that it fails as $H \to R$. In region (i), the radiation dominated zone and inner part of the accretion disk,

the scale height is,

$$H \approx \frac{3R_{\rm in}\dot{m}}{4\eta}\left[1-\left(\frac{R_{\rm in}}{R}\right)^{1/2}\right], \tag{1.13}$$

(Frank et al., 2002). Assuming a standard accreting black hole efficiency, $\eta = 0.1$, when $\dot{m} > 1$, the inner region of the disk inside $R \sim \dot{m}R_{\rm ISCO}$ can no longer be described by a standard thin disk. This means that for objects approaching Eddington, the thin disk model is not applicable.

1.3.2 Thick disks

The defining characteristic of the standard disk model is that the emission comes from an optically thick, radiatively efficient accretion flow. However, we must also consider radiatively inefficient accretion flows, i.e. instances in which advection becomes significant and modifies the accretion flow. There are two key scenarios in which the disk becomes advectively cooled (as opposed to radiatively cooled like in the standard disk), while remaining both thermally and viscously stable; optically thin gas pressure supported and optically thick radiation pressure supported accretion flows (Abramowicz et al., 1995). The former represents advection-dominated accretion flows (ADAFs), used for very low accretion rates, while the latter is used at very high accretion rates and known as 'slim disks' (Abramowicz et al., 1988). Slim disks are (somewhat confusingly) a subset of thick disks, disk models that describe the quasi-spherical accretion regime (i.e. $H \sim R$) where the standard disk model breaks down. Close to the compact object, the disk becomes puffed up due to the intense radiation pressure, while behaving identically to a standard disk at larger radii (Figure 1.4). In the geometrically thick zone, the accretion flow becomes so dense and optically thick that photons are trapped within the inflowing matter and get dragged down onto the black hole, never reaching the observer[4]. The advection means that not all of the gravitational potential energy is radiated at each disk annulus. This will alter the apparent luminosity and must be accounted for in order to properly quantify the accretion rate based on the observed spectrum. Slim disk models are often used to explain ULXs, matching their observational properties well (Watarai et al., 2001).

Thin disk models introduce a parameter p that governs the scaling relationship between disk radius and temperature. In standard disks, the radial temperature relationship follows $T \propto R^{-3/4}$ (Equations (1.12)), whereas in slim disks it tends

[4]In the case of a neutron star, the energy must eventually be radiated once the material reaches the surface.

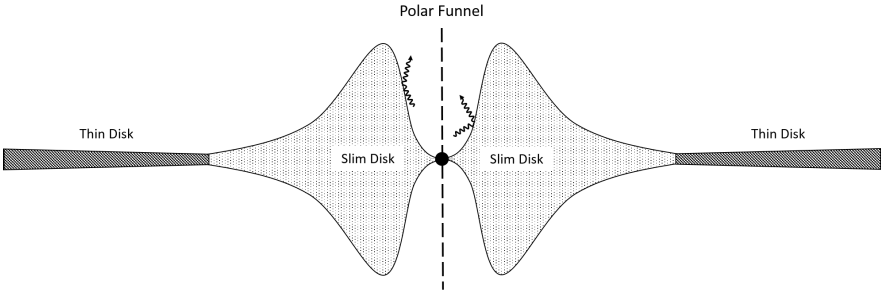

Figure 1.4: Sketch of a cut through a slim disk. At small radii, where $H \sim R$, the disk is radiatively supported. At large radii, the accretion flow takes the form of a standard disk. This model is often used to explain sources at high accretion rates, like ULXs.

to follow $T \propto R^{-1/2}$ (Watarai et al., 2000). With the added free parameter p, the radial dependence on temperature, $T \propto R^{-p}$, disk models can better fit spectra of super-critically accreting sources.

1.4 Outflows

Radiation is not the only form of energy emitted through accretion; the production of mechanical energy may also result from the release of gravitational potential energy. This mechanical energy manifests as outflows, taking two main forms; highly-collimated jet outflows and quasi-spherical, radiation-driven[5] winds. Both factors contribute to the total energy budget of accretion and thus understanding outflows becomes important when trying to quantify the total energy released through accretion, and its efficiency.

1.4.1 Jets

Astrophysical jets are observed to be accelerated from accretion flows around compact objects of all mass scales throughout the Universe. They are made up of a population of relativistic charged particles accelerated from close to the event horizon of an accreting black hole or surface of an accreting neutron star, white dwarf or young stellar object. Jets can be classified as leptonic or baryonic. Leptonic jets primarily consist of highly-relativistic ($\sim 0.99c$) electrons and positrons accelerated by a strong magnetic field generated by either the accretion disk or base of the jet. As the electrons and positrons spiral within the tangled magnetic field, they produce synchrotron radiation which is predominantly detected in the radio band.

[5]Winds can be accelerated by other mechanisms (e.g. magnetically or thermally driven winds). However, strong winds in ULXs are typically radiation-pressure-driven and thus we restrict our focus to these.

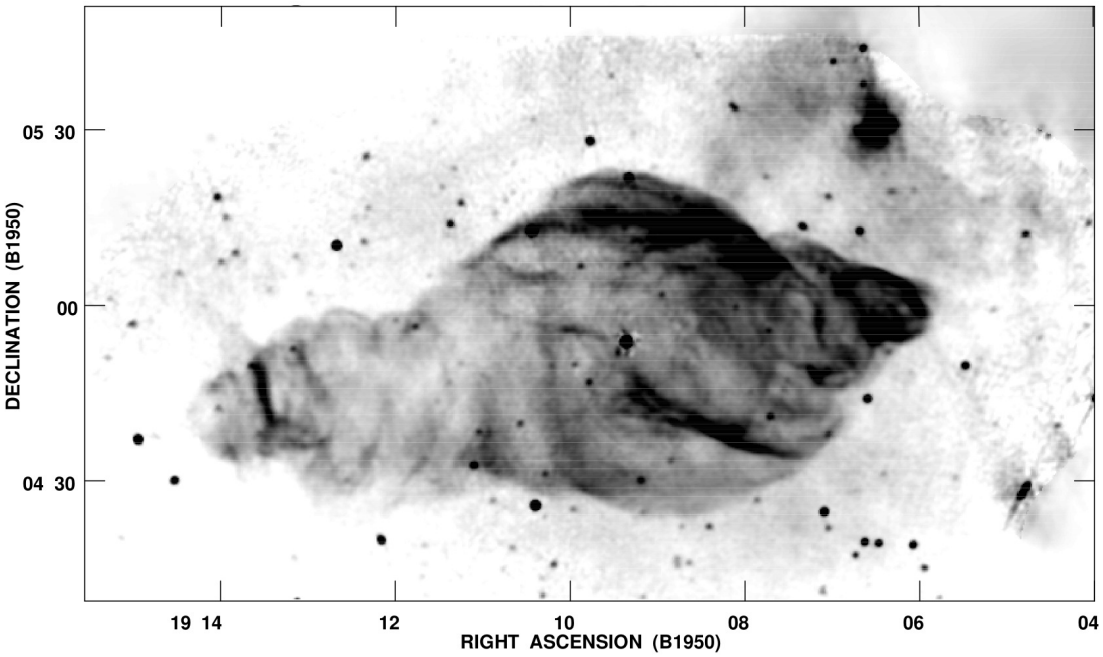

Figure 1.5: VLA radio continuum image of W50 from Dubner et al. (1998). The jets have inflated the eastern and western lobes protruding out from the underlying circular supernova remnant. The total structure has a size of ~ 40 by 100 pc.

Baryonic jets on the other hand comprise much heavier ions, and thus generally only reach speeds of $\sim 0.1c$. They are detected at optical wavelengths using broad Hα emission lines. The prototypical example of a baryonic jet is found in the Galactic source SS 433 (Margon, 1984). Accelerated to $0.26c$, these jets plough into the surrounding medium, inflating the eastern and western lobes of a giant nebula or "bubble", known as W 50 (Figure 1.5). By studying the formation of this bubble, constraints on the mechanical energy of the system, and hence its total energy, can be placed (e.g., Dubner et al., 1998).

1.4.2 Winds

In contrast to jets, winds tend to be less directional and relatively slow-moving outflows. Winds have typical speeds of $\sim 1000\,\mathrm{km\,s^{-1}}$. They are the result of intense radiation pressure from the disk driving inflowing material away from the compact object. Therefore, winds are predominantly found in sources around or above the Eddington limit (although winds are also observed in high-inclination sources in disk-dominated states, e.g. Ponti et al. 2012, and found to be launched in power-law-dominated states but too ionised to detect, e.g. Díaz Trigo et al. 2014), where the radiation pressure begins to overpower the gravitational attraction. The outflowing material moves radially in an equatorial cone-like projection, leaving a polar funnel. However, it is assumed that in some systems, the opening

angle of the polar funnel reaches zero and the source is completely enveloped in a quasi-spherical outflow. For sources with $\dot{m} \sim 1$, the outflows are generally optically thick to scattering (Pounds et al., 2003). For sources with $\dot{m} \gg 1$, the outflows become effectively optically thick.

Like with jets, winds can have a significant impact on the surrounding medium. Identifying how much kinetic energy is imparted into the ISM is important for estimating the mechanical power of the winds.

1.5 X-ray binaries

X-ray binaries (XRBs) are double-star systems in which a compact object (either a neutron star or black hole) accretes matter from a donor star (Frank et al., 2002). They can be broken down into two subclasses dependent on the mass of their donors: high-mass XRBs (HMXBs) with massive companion stars that generally accrete via wind-driven accretion; and low-mass XRBs (LMXBs) with companions less massive than the compact object that accrete through Roche lobe overflow. Galactic XRBs do not (generally[6]) violate the Eddington limit, having peak luminosities $\lesssim 10^{39}\,\mathrm{erg\ s^{-1}}$.

XRBs are comprised of a number of different physical components (top panel in Figure 1.6), each of which have distinct emission signatures (bottom panel in Figure 1.6). The companion star and accretion disk are both thermal radiators resulting in blackbody emission. The companion star emission will peak in the optical band whereas the hotter disk will peak at soft (low energy) X-rays. The corona is a quasi- or non-thermal population of electrons found close to the compact object. It generally has a higher temperature than the disk as it can not cool efficiently because of its low density. It will emit in the hard (high energy) X-ray band with a power-law-like distribution that arises from Compton scattering of softer photons by the energetic electrons of the corona. The final component is the bi-polar jet, which dominates at radio wavelengths. The jet will most likely be emitting via synchrotron radiation and have a reasonably flat spectrum in the radio band, though the synchrotron spectrum can extend to the infra-red, optical and possibly even X-rays, depending on the Lorentz factor of the electron population. Identifying each physical component by its emission properties helps to identify the spectral state of the XRB.

XRBs undergo transient outbursts in which they evolve along a predictable track; they transition through known accretion modes, or 'spectral states', that are a result of a changing accretion rate. The evolving XRB spectra during an

[6]There are a select few Galactic sources that do; e.g. Z-source neutron stars, Cir X-1, SS 433, GRS 1915, V4641 Sgr (Grimm et al., 2002), V404 Cygni (King et al., 2015).

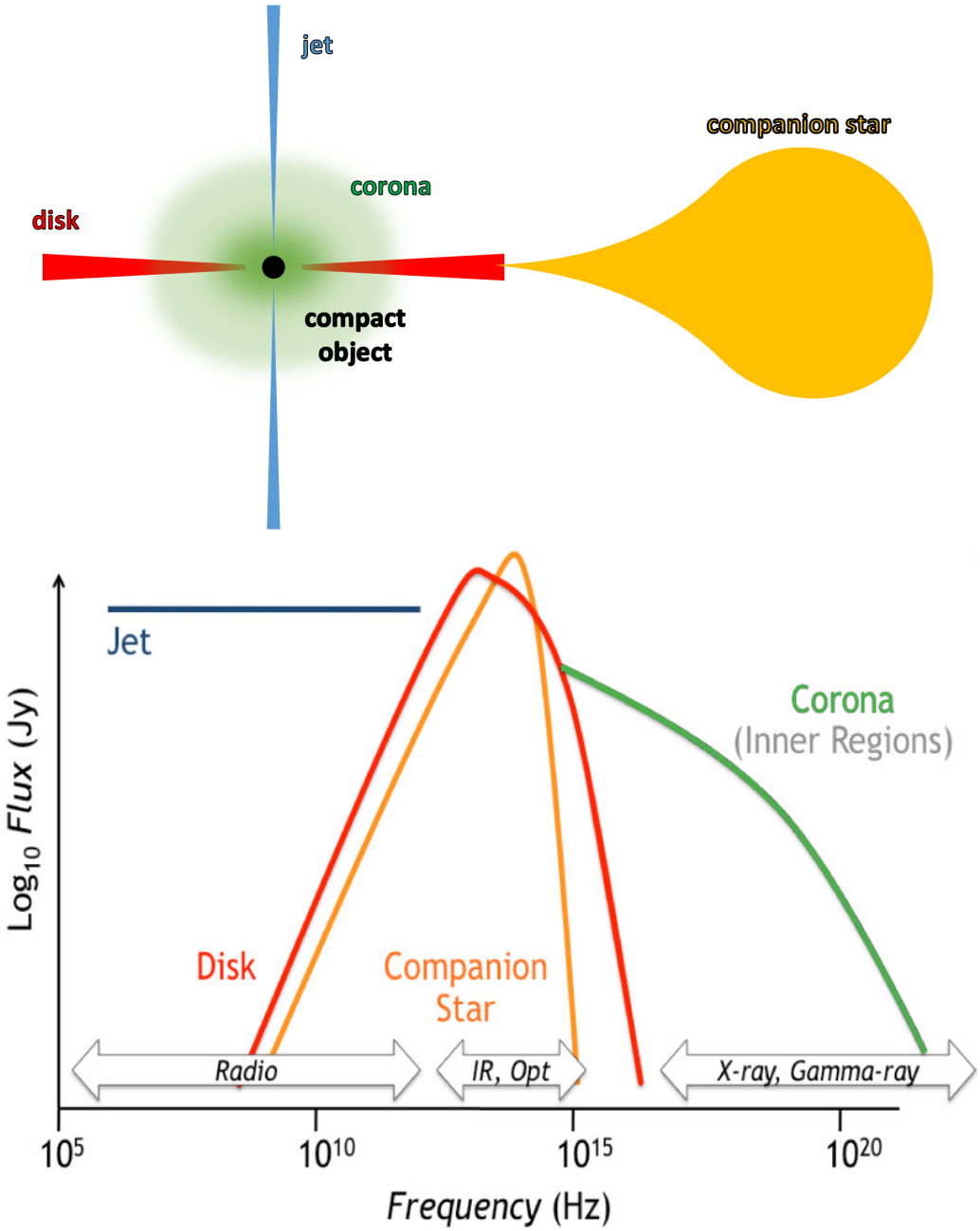

Figure 1.6: Top panel: Cartoon schematic of an XRB accreting via Roche lobe overflow. The system is viewed edge-on. Bottom panel: Canonical spectrum for an XRB (credit P. Curran). The colours for each component match their corresponding physical emission zone from the top panel. Flat-spectrum synchrotron emission from the jet is seen in blue, the soft blackbody curves of the disk and companion star are in red and orange respectively (the companion star spectrum is greatly exaggerated for simplicity, normally being dwarfed by the disk emission) and the hard power-law tail of the corona is in green.

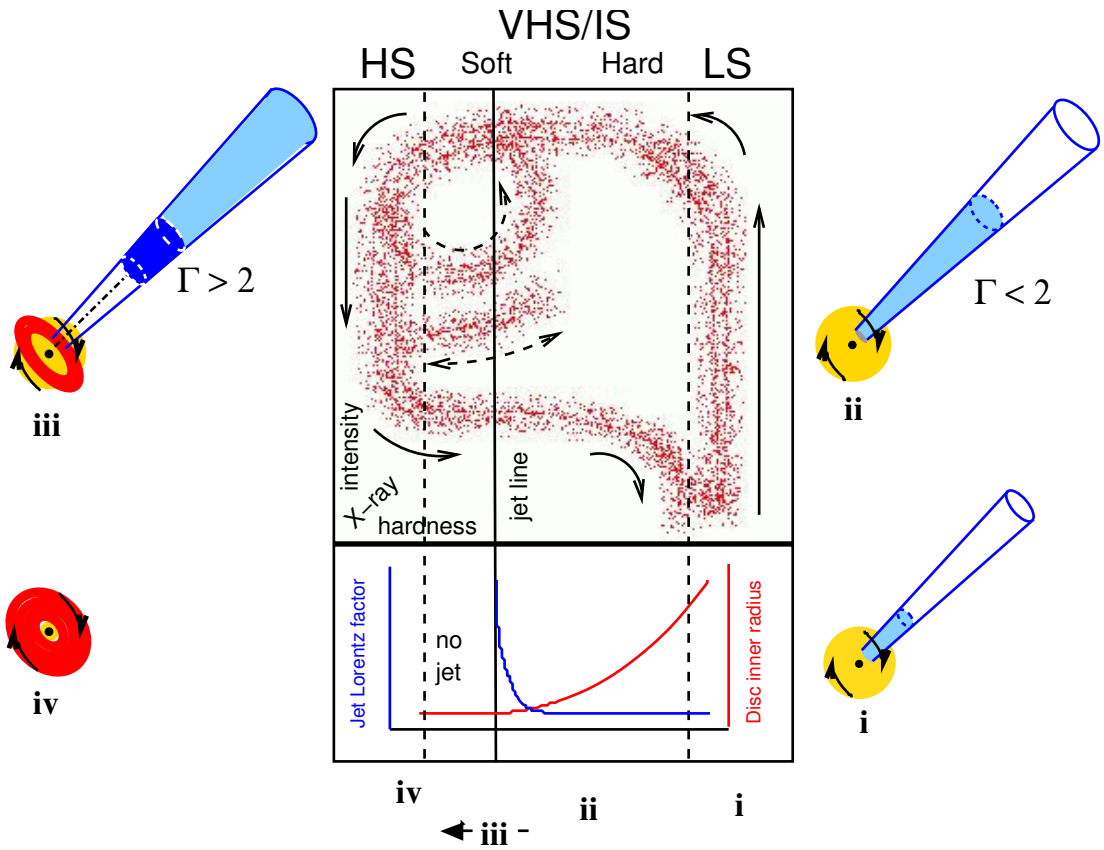

Figure 1.7: Schematic of XRB spectral states from Fender et al. (2004). X-ray hardness (ratio between hard and soft photon count rates) increases to the right, while X-ray luminosity increases upwards. In a typical outburst, the XRB starts in a quiescent state (i), where it is dominated by the corona (yellow), before increasing in luminosity as it transitions into the low/hard state (ii). The truncated accretion disk (red) begins to fill up towards $R_{\rm ISCO}$ (iii-iv), in doing so quenching the jet, and the source reaches the high/soft state. Finally, the source transition back into the low/hard state and quiescence.

outburst can be classified in terms of the type of X-ray emission, specifically the ratio between thermal and non-thermal emission (Belloni, 2010). The thermal contribution arises from the optically thick accretion disk, radiating as a multi-temperature black body. The non-thermal emission is a result of Compton up-scattering of lower energy photons by high energy electrons in the corona or near the base of the jet, or synchrotron emission from the jet (Remillard and McClintock, 2006). A schematic of the standard XRB outburst cycle is depicted in Figure 1.7. Prior to the outburst, the XRB will be in a low-luminosity, or quiescent, state characterised by a luminosity $L_{\rm x} < 10^{33.5}$ erg s^{-1} (Remillard and McClintock, 2006) and in which it spends most of its time. From here, the luminosity begins to increase as the source enters outburst, transitioning into the low/hard state (the LS zone in Figure 1.7). The disk is truncated at larger radii and most ($> 80\%$) of the energy radiated comes from the hard power-law

component. A steady compact jet is also produced in the low/hard state (also in quiescence). However, the jet becomes transient (discrete ejecta replace the steady outflow of the compact jet) as the source moves from the low/hard state to the high/soft state (HS zone in Figure 1.7). The disk is no longer truncated and fills down to $R_{\rm ISCO}$. The majority of the flux now comes from the disk ($> 75\%$; Remillard and McClintock, 2006). The jet is quenched and the system is dominated by thermal emission from the disk. Finally, the outburst ends and the XRB then moves back into the low/hard state (at a lower luminosity) and then decays back down into quiescence. For a complete model, more complex states are also used, like the intermediate state (McClintock and Remillard, 2006) and the very high state (Miyamoto and Kitamoto, 1991; Miyamoto et al., 1993). The very high state is for high-luminosity sources (generally $> 0.1 L_{\rm Edd}$) in which both thermal and power-law components are present. For even more luminous objects, beyond the Eddington limit of most Galactic XRBs, it has been suggested that another state, the ultraluminous state, is needed (Gladstone et al., 2009; Roberts et al., 2010). These objects are discussed in the following section.

1.6 Ultraluminous X-ray sources

ULXs are classified as non-nuclear X-ray sources with peak luminosities greater than 1×10^{39} erg s^{-1}, the Eddington luminosity for a 10 solar mass black hole (Feng and Soria, 2011; Kaaret et al., 2017). As the Eddington limit is proportional to black hole mass, ULXs may contain a missing population of intermediate-mass black holes ($10^2 - 10^4$ M$_\odot$) accreting at sub-Eddington rates. Although most ULXs appear to be persistent sources, some ULX have been observed transitioning from sub-Eddington to super-Eddington luminosities (Gladstone et al., 2009; Middleton et al., 2011b), resulting in the source changing from an XRB to a ULX. Like XRBs, ULX spectra can evolve over time. However, it is still unclear what the relationship is between the thermal and non-thermal components and how the presence/absence of jets modifies the observed spectrum (Sutton et al., 2013b).

Over the last two decades or so, research into ULXs has grown rapidly. This has been achieved through a number of ULX catalogues, allowing for population and spectral studies. Beginning with a ROSAT/HRI (High Resolution Imager) survey of luminous X-ray sources (Colbert and Mushotzky, 1999), astronomers soon began constructing larger catalogues, using instruments/facilities such as *XMM-Newton* (see Foschini et al., 2002) and *Chandra* (see Swartz et al., 2004; Liu and Mirabel, 2005). One of the largest ULX catalogues, created by cross-correlating the 2XMM Serendipitous Survey with the Third Reference Catalogue of Bright Galaxies, found 470 ULXs in 238 galaxies (Walton et al., 2011).

1.6.1 ULX interpretations

There are three interpretations for ULXs: (i) ULXs are stellar-mass black holes ($M < 20\,M_\odot$) or neutron stars (Bachetti et al., 2014) accreting at super-Eddington rates ($\dot{m} > 1$); (ii) ULXs are massive stellar-mass black holes ($20\,M_\odot < M < 100\,M_\odot$) accreting at mildly-Eddington rates ($\dot{m} \sim 1$); and, (iii) ULXs are IMBHs ($10^2\,M_\odot < M < 10^4\,M_\odot$) accreting at sub-Eddington rates ($\dot{m} < 1$) (Feng and Soria, 2011). As outlined in Section 1.2.1, there are several ways to bypass the Eddington limit. Because $L_{\rm Edd} \propto M$, the IMBH scenario does not require super-Eddington accretion. This means that ULXs should been seen in the same accretion states as XRBs, along with having similar spectral properties, just scaled by mass. This, however, is not the case and ULX spectral states are distinct from XRB spectral states, and are explored later. Mild beaming[7] and super-Eddington accretion are able to explain ULXs with luminosities of up to a few $\sim 10^{40}\,{\rm erg\ s^{-1}}$ without invoking IMBHs (Feng and Soria, 2011). A select few extreme ULXs, such as ESO243-49 HLX-1 and M 82 X-1, with peak luminosities of $\approx 10^{42}\,{\rm erg\ s^{-1}}$ (Farrell et al., 2009) and $\approx 10^{41}\,{\rm erg\ s^{-1}}$ (Kaaret et al., 2001; Matsumoto et al., 2001) respectively, are candidate IMBHs.

1.6.2 Distribution of ULXs

ULXs are found in spiral, elliptical and irregular galaxies. However, the most luminous ones are found primarily in spirals and irregulars. More than two thirds of ULXs seen in ellipticals have luminosities less than $2 \times 10^{39}\,{\rm erg\ s^{-1}}$, with no ULX being brighter than $10^{40}\,{\rm erg\ s^{-1}}$ (Swartz et al., 2004). By comparison, one third of ULXs in spirals have luminosities greater than $(4-5) \times 10^{39}\,{\rm erg\ s^{-1}}$, with 10% exceeding $10^{40}\,{\rm erg\ s^{-1}}$ (Swartz et al., 2004; Walton et al., 2011). The luminosity function of ULXs follows a power-law distribution with slope $\alpha \sim -0.8$ to -2.0 and exponential cut-off at a few $10^{40}\,{\rm erg\ s^{-1}}$ (Swartz et al., 2011). A complete sample of ULXs in nearby galaxies (within 14.5 Mpc) conducted by Swartz et al. (2008, 2011) found that, on average, we expect to find approximately two ULXs per $1\,M_\odot{\rm yr}^{-1}$ of star formation. In spiral and irregular galaxies, one ULX is expected per $10^{10}\,M_\odot$ while for elliptical galaxies, one ULX is expected per $10^{11}\,M_\odot$ (Swartz et al., 2008, 2011; Walton et al., 2011). It also appears that low-mass galaxies (down to $\sim 10^{8.5}\,M_\odot$) are more efficient at forming ULXs, per unit mass. This may be due to the increased star formation rate (SFR) per unit mass in lower-mass galaxies.

[7] Strong beaming is ruled out in ULXs. The occupation fraction of ULX bubbles (see Section 1.6.4) argues against any sort of strong beaming.

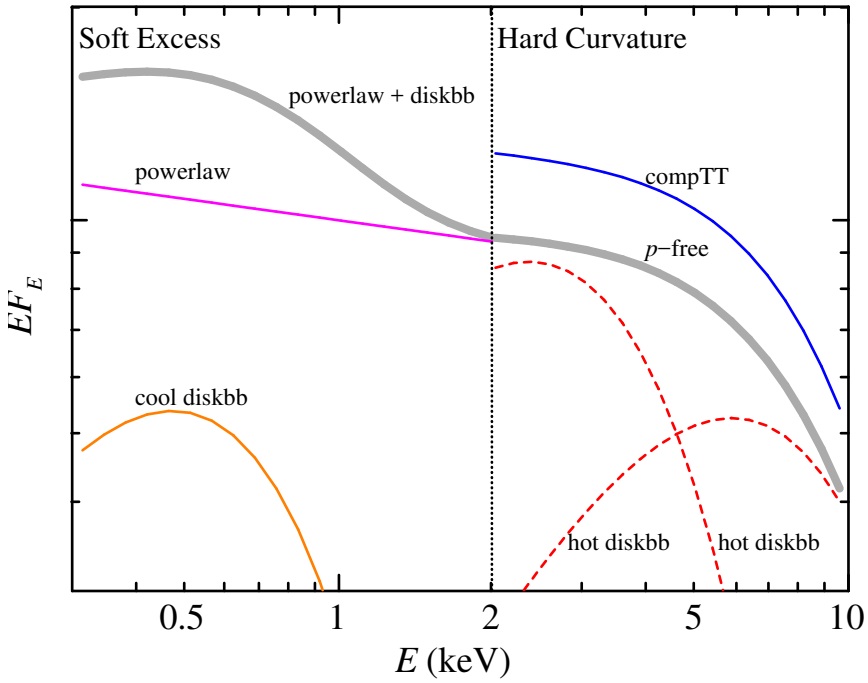

Figure 1.8: Cartoon of general ULX spectrum (grey) from Feng and Soria (2011). The soft excess is modelled by a cool thermal disk (orange) plus a power-law component (magenta). The hard curvature can be fit with either a non-standard disk or by a Comptonised model (blue – offset for clarity). For comparison, a dual disk model (red) would not be able to recreate the spectrum.

1.6.3 Spectral properties and classification

ULXs show a wide variety of spectral properties, whose interpretation remains controversial. The same models used to explain XRB spectral states appear to be inadequate when applied to ULXs (Gladstone et al., 2009). The spectral changes could even be explained through orientation, rather than state (Sutton et al., 2013b). Strong outflows from the inner disk regions can cause quasi-collimation of material leading to geometric beaming out of the plane of the disk (King, 2009). As a result, the observed properties of the thermal and non-thermal components could change depending on whether the system is observed face-on, edge-on or at some intermediate inclination angle. This outflowing material may also be responsible for the variability seen in ULXs, as clumps of matter move out through the wind, evidenced by the fact that face-on systems show little variability (Middleton et al., 2011b).

The typical spectra observed in ULXs have three main components; a soft excess at temperatures $\lesssim 2\,\mathrm{keV}$, a hard power-law tail and a turnover (or steepening) at higher energies ($\sim 5\,\mathrm{keV}$) (see Figure 1.8, Feng and Soria, 2011). These features have been explained with a number of different interpretations. The soft excess is often attributed to a large accretion disk or massive outflow. The disk scenario would be analogous to XRBs, only more luminous and cooler. As the

inner disk temperature ($T_{\rm in}$) and disk luminosity ($L_{\rm disk}$) scale with the mass of the accretor via,

$$M \propto T_{\rm in}^{-2} L_{\rm disk}^{1/2}, \tag{1.14}$$

(Feng and Soria, 2011), a standard ULX, with a luminosity $\sim 10^{39}\,{\rm erg\ s^{-1}}$ and temperature $0.1-0.4\,{\rm keV}$ was initially interpreted as the signature of an accretion disk around a black hole with a mass $\sim 10^3\,{\rm M_\odot}$ (Miller et al., 2003, 2004). Another interpretation is that, instead of a massive accretor, $T_{\rm in}$ is not probing the temperature at $R_{\rm ISCO}$, but instead some much larger (and hence cooler) radius (Roberts, 2007; Soria, 2007). This may arise from the inner disk being obscured or transitioning into a corona or outflow that is optically thick to scattering. Alternatively, it has also been suggested (Poutanen et al., 2007; Soria, 2007) that the soft excess is from strong outflows that develop due to super-critical accretion. The optically thick outflows are generated at the spherisation radius (the radius at which $R = H$) and can downscatter hard emission from the inner regions. The outflow model is in rough agreement with observations by Kajava and Poutanen (2009), who, using a sample of ULXs, found that the luminosity of the soft excess follows a $L_{\rm soft} \propto T^{-3.5}$ trend. Further interpretations have been proposed including non-standard slim disks (i.e. thick disk models) outlined in Section 1.3.2.

The spectral classification of ULXs was expanded upon by Sutton et al. (2013b), who divided ULXs into three spectral classes; broadened disk, hard ultraluminous and soft ultraluminous (Figure 1.9). Using a sample of 20 ULXs, Sutton et al. (2013b) find that the low luminosity ($< 3\times10^{39}\,{\rm erg\ s^{-1}}$) population is dominated by the single component broadened disk ULXs[8] while more luminous sources are almost exclusively double component ULXs in the hard or soft ultraluminous state. They suggest that broadened disk ULXs are likely accreting around the Eddington limit ($\dot{m} \approx 1$) while ultraluminous hard and soft sources represent a super-Eddington population. The increase in accretion rate introduces a strong radiatively-driven wind that forms a polar funnel. The distinction between soft and hard states is a function of viewing angle; objects seen more face-on (down the polar funnel) have harder spectra while soft sources will be those seen more edge-on (through the wind) as the central hard-X-ray-emitting region is then obscured Sutton et al. (2013b).

[8] Broadened disk sources have also been detected at luminosities above $10^{40}\,{\rm erg\ s^{-1}}$, e.g. the ULXs found in NGC 5907 (Sutton et al., 2013a) and NGC 5643 (Pintore et al. 2016).

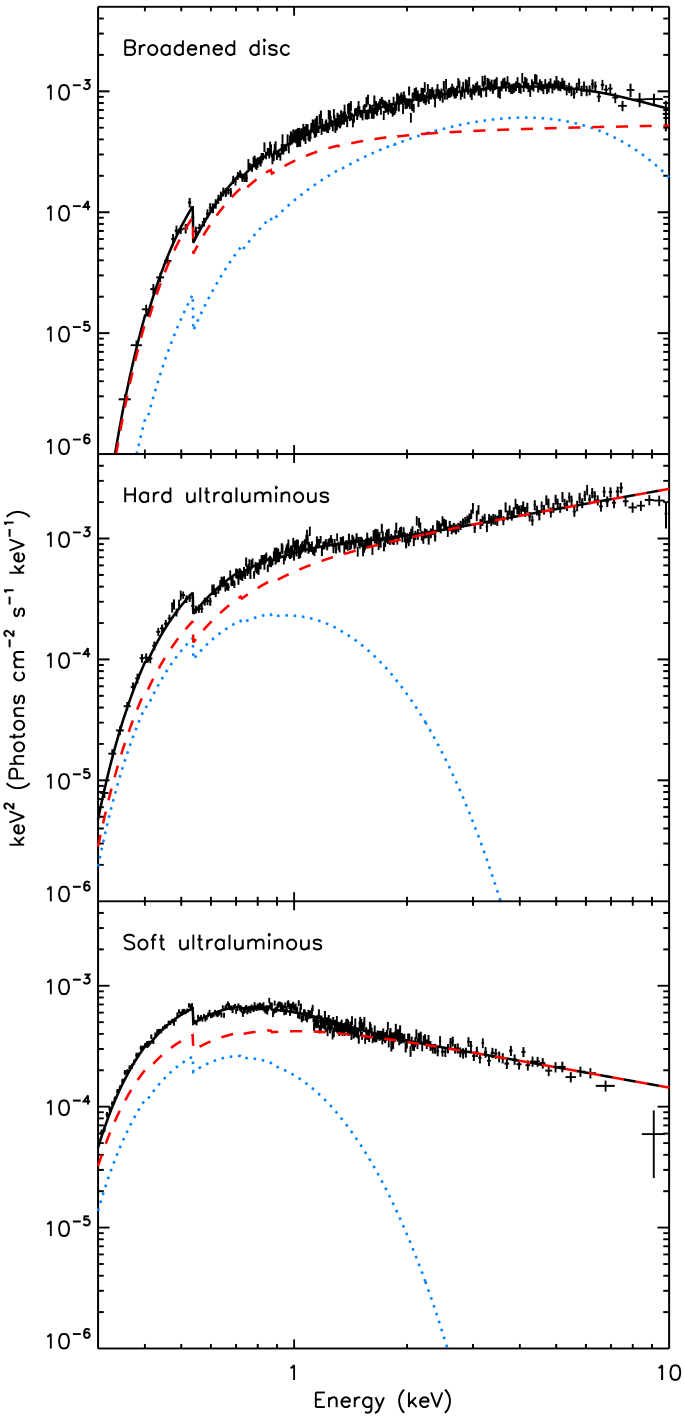

Figure 1.9: ULX spectral classification for broadened disk and hard and soft ultraluminous states from Sutton et al. (2013b). The top panel shows the spectrum for a single-component broadened disk ULX while the middle and bottom panels display the spectra for double-component hard and soft ultraluminous ULXs, respectively.

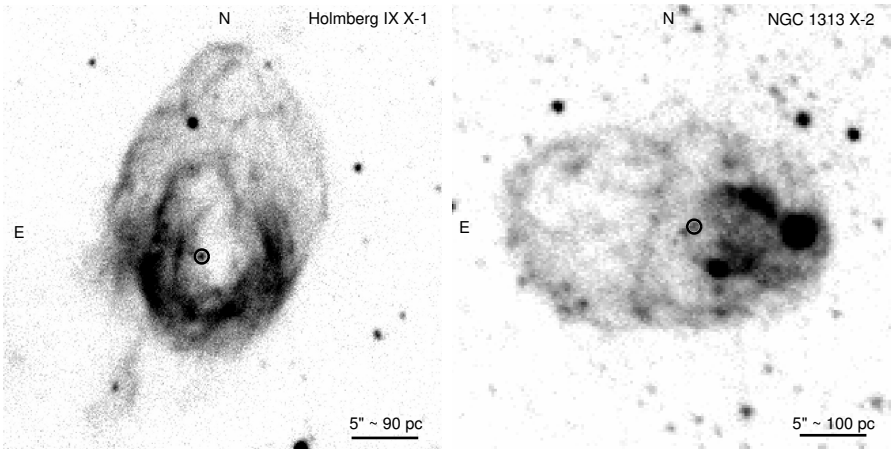

Figure 1.10: Extended Hα emission bubbles around ULXs Holmberg IX X-1 (left; *Subaru*, Faint Object Camera and Spectrograph (FOCAS)) and NGC 1313 X-2 (right; Very Large Telescope (VLT), Focal Reducer and low dispersion Spectrograph 1 (FORS1)) (Feng and Soria, 2011).

1.6.4 ULX outflows and bubbles

ULXs can alter their surrounding medium in two ways. First, because of their extreme luminosities; X-ray photons from the ULX can photo-ionise the surrounding gas. Second, because of their outflows; the strong disk winds and/or jets can plough into the ISM, imparting kinetic energy and ionising the gas via shocks. Thus several ULXs have been observed with coincident giant optical nebulae, known as 'ULX bubbles', that can be $\sim$ 100–400 pc across (Pakull and Mirioni, 2002, 2003). Examples of these ULX bubbles can be seen in Figure 1.10. Importantly, shock-ionised bubbles, those that have primarily been inflated by winds or jets, can be used to measure the average long-term kinetic power output of their host ULXs. Combining this with the radiative power gives the total power output of the compact object, which is required in order to understand the inflow/outflow relation in super-Eddington accretion. Measuring the size of these bubbles could also help constrain the duration over which ULXs are actively accreting.

Some sources also present coincident radio bubbles in addition to their optical nebulae. This emission comes from either optically thin synchrotron radiation produced by a relativistic jet or Bremsstrahlung emission from the hot diffuse gas of the bubble, or even a combination of the two. While the majority of ULXs with shock- or photo-ionised optical bubbles also have coincident radio bright bubbles (e.g. IC 342 X-1 and Ho II X-1; Cseh et al. 2012; Pakull and Mirioni 2002), the bubble around the ULX NGC 1313 X-2 is not detected in the radio band (R. Soria, priv. comm.).

ULX bubbles also have important implications on the beaming fraction of

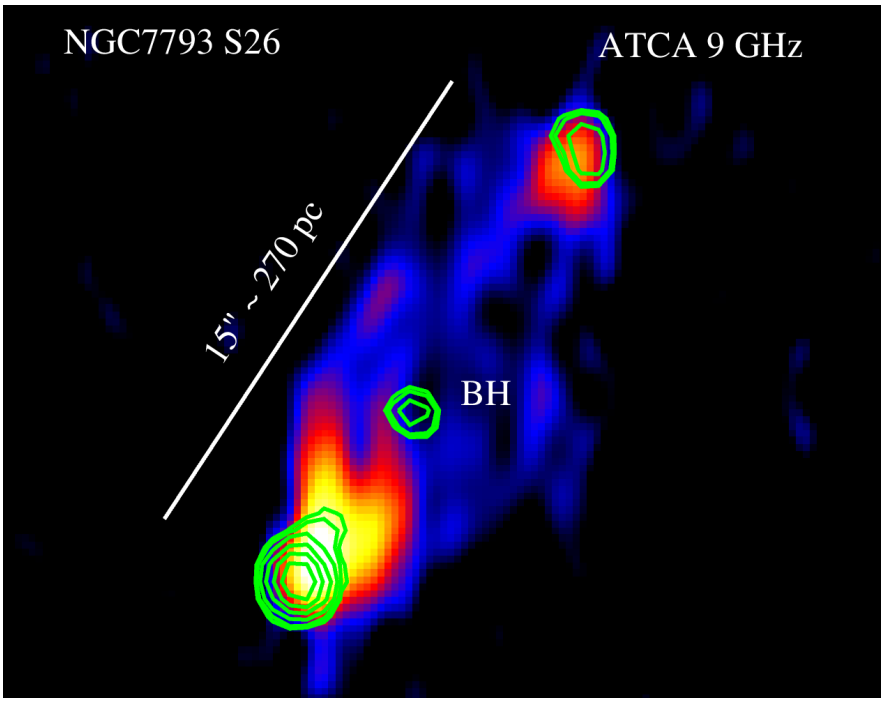

Figure 1.11: Radio image of jet dominated microquasar in NGC 7793, S 26, taken at 9GHz using the Australian Telescope Compact Array (ATCA). The green contours are from $0.3 - 7.0$ keV *Chandra* X-ray data (credit R. Soria).

the central compact object. ULXs may appear more luminous because their X-ray emission is partly collimated along our line of sight. This may happen at super-critical accretion rates, because of the predicted formation of a dense radiatively-driven disk outflow and a lower-density polar funnel, along which more photons can escape (Ohsuga and Mineshige, 2011; Jiang et al., 2014; Sądowski and Narayan, 2015). However, there is indirect evidence that ULXs are not strongly beamed. Studies of photo-ionised and/or shock-ionised plasma bubbles around ULXs (Pakull and Mirioni, 2002; Pakull and Grisé, 2008) provide clues about viewing angles: if fast-accreting black holes or neutron stars appeared as ULXs only for a narrow range of face-on inclinations, we would see many more ionised bubbles without a ULX inside; moreover, the true X-ray luminosity of a beamed source (much lower than the apparent luminosity) would not be enough to explain the strong He II emission observed from some of the photo-ionised ULX bubbles (Pakull et al., 2006). Both the fact that most ULX bubbles do contain a bright, central X-ray source, and the fact that (in photo-ionised bubbles) the apparent X-ray photon flux from the central source is consistent with the He II photon flux from the bubble, suggest that, statistically, ULXs are seen over a broad range of viewing angles.

The ULX bubbles in Figure 1.10 are quasi-spherical and have no direct detection of a relativistic jet. Within the last decade, the first jet-dominated ULX

bubble, similar to the Galactic source SS 433 (see Figure 1.5), was discovered (Figure 1.11). The microquasar S 26 was found in the spiral galaxy NGC 7793 by Pakull et al. (2010). While the jet has an average power of $\sim$ a few 10^{40} erg s^{-1}, the X-ray luminosity of the ULX core is only 6×10^{36} erg s^{-1} (Pakull et al., 2010; Soria et al., 2010). A similar situation is also seen in the super-Eddington microquasar, M 83 MQ1, with $L_X \approx 7 \times 10^{37}$ erg s^{-1} but $P_{\rm jet} \approx 3 \times 10^{40}$ erg s^{-1} (Soria et al., 2014). These objects are usually grouped in the same class as the luminous ULXs with bubbles. This class is generally called "ultrapowerful X-ray sources", and it includes all sources in which the total mechanical plus radiative power exceeds 10^{39} erg s^{-1}. There are two reasons why the X-ray luminosities of these sources may be lower than the average mechanical power: *i*) the jet power is a long-term average while the X-ray luminosity traces the current level of accretion and hence such sources may currently be in a low-luminosity state, or; *ii*) the source may be seen at high inclination and be obscured (Feng and Soria, 2011). Regardless, the total power indicates that these objects are examples of jet formation at super-critical accretion rates. Thus, understanding such sources could offer new insights into the relation between inflows and radiative and mechanical feedback processes.

Of the hundreds of known ULXs (Walton et al., 2011; Liu, 2011; Swartz et al., 2011), only a handful of persistent sources have been seen with collimated jets. Other than S 26 and M 83 MQ1, the ULX Ho II X-1 also shows evidence of jets (Cseh et al., 2014). The average jet power was estimated to be 2.1×10^{39} erg s^{-1} which may have inflated the surrounding radio bubble. Additionally, the bright optically-thin radio nebula associated with NGC 5408 X-1 is interpreted to be a $\approx$ 40 pc (Lang et al., 2007) lobe created by the jet of a super-Eddington microquasar (Soria et al., 2006a). The only other confirmed collimated jet detected in a persistent ULX is the baryonic jet in the M 81 ultraluminous supersoft source (ULS) (Liu et al., 2015). ULSs are thought to be a subset of ULXs, which will be discussed in the following section and Chapter 4. The lack of any evidence for jets in other sources may indicate that collimated jets are rare in ULXs. However, there are likely other factors that contribute to whether or not these jets are detectable, such as ISM density.

1.7 Ultraluminous supersoft sources

Another class of luminous accreting X-ray object, potentially related to ULXs, is the ULS (Figure 1.12). ULSs are defined as compact accreting X-ray sources that have been observed with a bolometric luminosity $\gtrsim 1 \times 10^{39}$ erg s^{-1} at least once and a temperature $\lesssim 100$ eV. They demonstrate strong thermal emission below

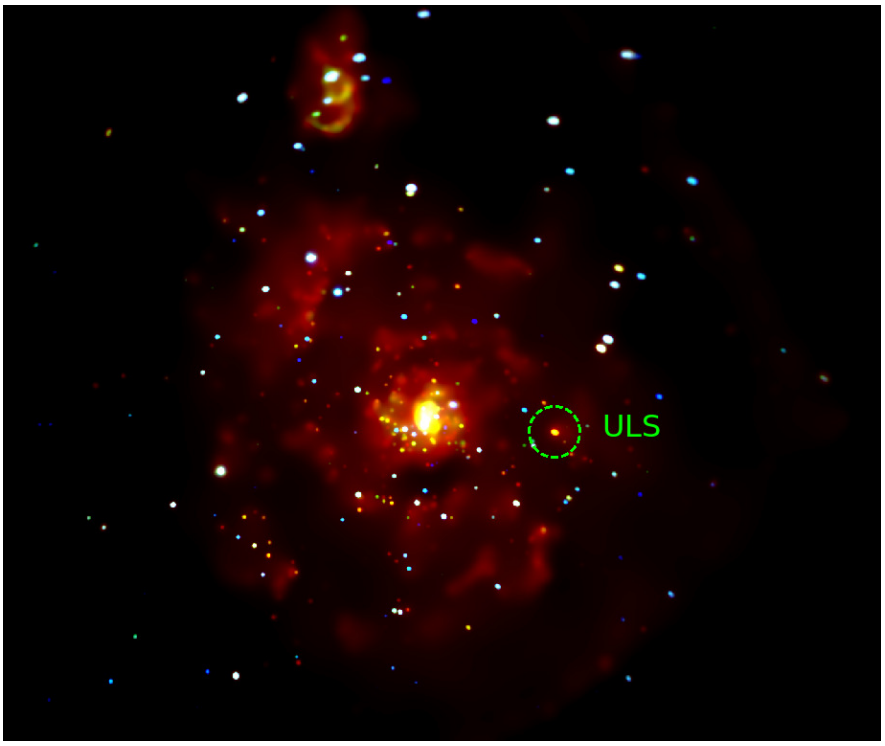

Figure 1.12: False colour *Chandra* image of M 51. Here, red is $0.3-1.0$ keV, green is $1.0-2.0$ keV and blue is $2.0-7.0$ keV. The orange colour of the ULS indicates its relatively cool temperature. Many of the surrounding white or blue objects are likely to be ULXs.

1 keV and little to no flux detected at higher energies (Kong and Di Stefano, 2003). This differs from ULXs, which are generally observed as broadband emitters, luminous across the 1-10 keV range. If fitted with a blackbody model, ULSs have characteristic radii of a few 10^4 km. An X-ray image of the spiral galaxy M 51 containing a ULS can be seen in Figure 1.12.

Originally discovered by *ROSAT* observations of nearby galaxies (Vogler and Pietsch, 1996; Read et al., 1997; Read and Pietsch, 2001; Swartz et al., 2002), these rare sources have been studied in more detail with *Chandra* and *XMM-Newton* over the past 15 years. There are a total of 8 known ULSs to date. These objects have all been observed at various luminosities ($L_{\rm bol} \sim 10^{38} - 10^{40}$ erg s^{-1}) over numerous years indicating that they cannot be explained as classical novae, which have similar spectra and reach comparable luminosities but are not recurrent. The source of the soft thermal emission that defines ULSs has been interpreted in numerous ways: nuclear-surface-burning on white dwarfs; accretion disks around IMBHs in a high/soft state; or simply stellar-mass black holes accreting at super-critical rates. The latter interpretation suggests a common link between ULXs and ULSs.

It has been suggested that ULXs transition into ULSs once they reach extreme accretion rates or when viewed at high inclination angles (Middleton et al., 2015a),

or a combination of the two. At super-critical accretion rates, i.e. accretion rates at which the standard disk model no longer holds, outflows and winds begin to develop as matter is ejected before reaching the compact object. These outflows can obscure the central, hard-photon emitting region of the ULX. If the outflows are strong enough, they may completely envelop this region in an effectively optically thick photosphere. This would explain the soft, thermal emission seen in ULSs along with the complete lack of any hard emission: any hard photons would be emitted internal to the photosphere and thermalised. It is also theorised that ULSs may simply be ULXs viewed edge-on (Middleton et al., 2015a). In this scenario, the soft emission comes from the outer disk and/or clumpy winds. The high inclination angle means that there is no line of sight to the inner regions as it becomes obscured by the disk and outflows. Here, super-critical accretion is still required, although a much lower accretion rate than the photosphere model is needed. The true nature of ULSs is still heavily debated.

1.8 Significance

At present, the accretion flow in super-critical regimes is not fully understood. Studying ULXs provides insight into accretion at these extreme rates. However, the true nature of ULXs is still heavily debated; are they super-Eddington stellar-mass black holes, highly-magnetised super-Eddington neutron stars or, in some cases, even sub-Eddington IMBHs? Placing constraints on the mass of the compact object is obviously the best way to solve this problem. Although this has proven difficult so far, continued discovery of ULXs will no doubt provide systems in which this is possible.

The true nature of ULSs is even more controversial than that of ULXs. The fact that these are rare ($\lesssim$ 10 ULSs known) makes population studies difficult. Determining the similarities between the population of ULSs provides a better understanding of this class of object and how they are related to ULXs. Regardless, both of these types of sources are likely examples of accretion at its highest rates.

The effect inclination angle has on ULXs is believed to play a major role in ULX spectral appearance (Sutton et al., 2013b). It is unclear if the difference between ULXs and ULSs is purely an inclination effect or whether it is due to changes in the accretion rate, or a combination of the two. Placing constraints on the viewing angle would help to uncouple the inclination angle and accretion rate effects. It is also important in distinguishing between the hard, soft and broadband ULX states.

The strong outflows in ULSs are also a cause of debate. The recently discov-

ered baryonic jet in the M 81 ULS (Liu et al., 2015) suggests that jet formation is possible, however, it is unclear how common this is. It was initially believed that extreme outflows resulting from high accretion rates would quench the jet by destroying its collimation. However, recent magnetohydrodynamic simulations have shown that the inner regions of a super-Eddington accretion flow are conducive to jet formation (Ohsuga and Mineshige, 2011). Currently there is insufficient radio data on the remaining ULSs to identify compact jets or jet inflated bubbles. Identifying the presence/absence of jets in ULSs will help to better understand the inflow/outflow coupling at the highest accretion rates.

In a broader context, ULX studies may give insights into active galactic nucleus (AGN) properties. ULXs are analogous examples of AGN working on much shorter (and importantly, humanly observable) timescales and thus provide us with local Universe laboratories to study super-Eddington accretion. For example, studying the radiatively-driven outflows in ULXs will help in understanding AGN feedback and the impact they have on their host galaxies (e.g. Silk and Rees, 1998; Fabian, 2012). Super- and hyper-critical accretion may be important processes when it comes to explaining the presence of SMBHs at high redshifts. Short-lived intermittent periods of extreme accretion rates may account for the growth of early SMBHs that should not have formed via Eddington-limited accretion (Volonteri et al., 2015).

1.9 Thesis structure

This thesis details the study of a select number of newly discovered and already known super-Eddington sources. I use a combination of new and archival multi-wavelength observations to investigate the X-ray spectral and timing properties of the compact accreting source, the optical photometeric and spectroscopic properties of the companion star and extended bubble, respectively, and the spectral and morphological properties of the extended radio emission. With this information, I am better able to probe the radiative and mechanical power outputs of ULXs, studying both the accretion flow and large-scale outflows.

The work conducted during this thesis was undertaken in the hopes of answering the questions:

- What is the relationship between inclination angle and spectral classification in ULXs?

- How do ULSs fit into the scheme of compact accreting sources and how do they relate to ULXs?

- What fraction of power, relative to the radiative luminosity, is released in the outflows of super-critically accreting sources?

I have already given a brief overview of accretion physics and ULXs characteristics in Chapter 1. In Chapter 2, I outline the radiative processes common in ULXs and ULX bubbles, and their multiwavelength observables. Following this, I describe the instrumentation and data analysis tools employed throughout the research project in Chapter 3. Chapters 4-7 present the thesis results. Firstly, Chapter 4 examines X-ray observations of a sample of ULSs to study their spectral properties, evaluating commonly invoked ULS interpretations and their overall relation to the ULX population. Next, I detail the discovery of the first eclipsing ULXs; Chapter 5 presents a comprehensive study of their X-ray timing and spectral features while Chapter 6 outlines their optical and radio counterparts. The final set of results are described in Chapter 7 which examines the X-ray, optical and radio properties of the newly discovered candidate super-Eddington microquasar in NGC 300 in an attempt to determine the true nature of the source and its jet power. Lastly, Chapter 8 summarises the efforts of the thesis, reviewing how all of these super-Eddington sources are linked and the future of ULX research.

Chapter 2

Observational properties of radiative processes

Here I briefly examine some of the important physical mechanisms behind the key radiative processes seen in accreting sources. I also discuss the spectral models commonly used to replicate said processes throughout this research project. This Chapter is divided into sections on optically-thick, optically-thin and relativistic gas. I discussed the distinction between optically-thick and thin media in Section 1.2.2.

Rather than focusing on in-depth derivations of emission processes, which can be found in Rybicki and Lightman (1979) and Longair (2011), I look at why these processes are important to ULXs and the physical motivations behind their interpretations.

2.1 Optically-thick gas

2.1.1 Blackbody radiation

Blackbody radiation is radiation emitted by optically-thick material that is in thermal equilibrium. The spectrum of the emission of a blackbody at temperature T is defined by the Planck function

$$B_\nu(T) = \frac{2h\nu^3}{c^2} \frac{1}{\exp(\frac{h\nu}{k_\mathrm{B}T}) - 1}, \tag{2.1}$$

where h is Planck's constant, ν is the frequency, c is the speed of light and k_B is Boltzmann's constant. An important trait of blackbody spectra is the fact that the frequency at which the spectrum peaks scales linearly with temperature (known as Wien's Displacement Law). This phenomenon is displayed in Figure 2.1. I use blackbody components to model the dominant emission from ULSs,

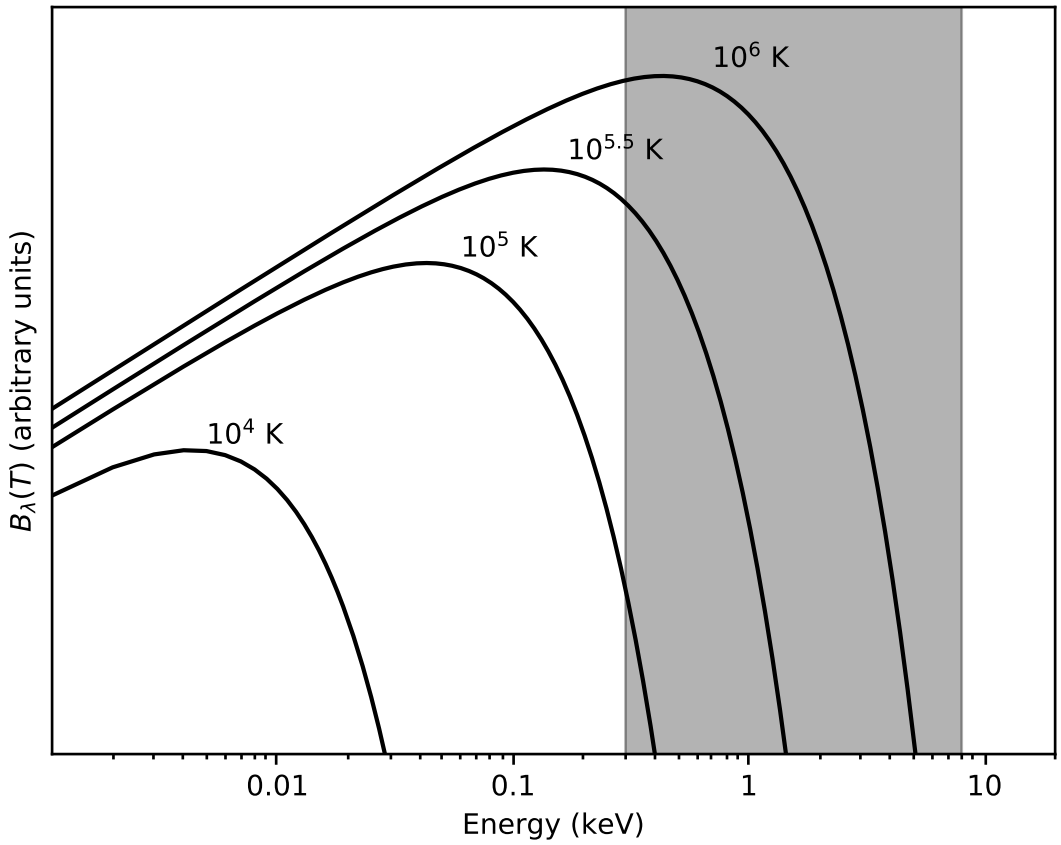

Figure 2.1: Blackbody emission. A sample of curves with peak temperatures ranging from 10,000 K (typical temperature of a supergiant star) to 10^6 K (equivalent to $\sim 100\,\mathrm{eV}$, the typical temperature of the blackbody emission from a ULS). The shaded region indicates the $0.3-8\,\mathrm{keV}$ X-ray band, covered by *Chandra* and *XMM-Newton*.

thought to come from the photosphere of a soft, optically-thick disk wind. This typically has a temperature of the order of 100 eV, equivalent to $\sim 10^6\,\mathrm{K}$, resulting in a peak blackbody frequency that resides within the X-ray band. The binary companion star behaves approximately as a blackbody, and hence I also model it with a blackbody, albeit at a much lower temperature. Typical bright giants and supergiants, common companion stars in ULXs, have temperatures of $\sim 10^4\,\mathrm{K}$. They primarily emit in the optical and ultraviolet (UV) bands, with no emission at X-ray wavelengths. Example blackbody curves for both a ULS and a companion star, and their proximity to the X-ray observing band, are displayed in Figure 2.1.

2.1.2 Thin accretion disks

Radiation is not always restricted to a single temperature. While most accretion disks are comprised of optically-thick, thermally-emitting material, their emission

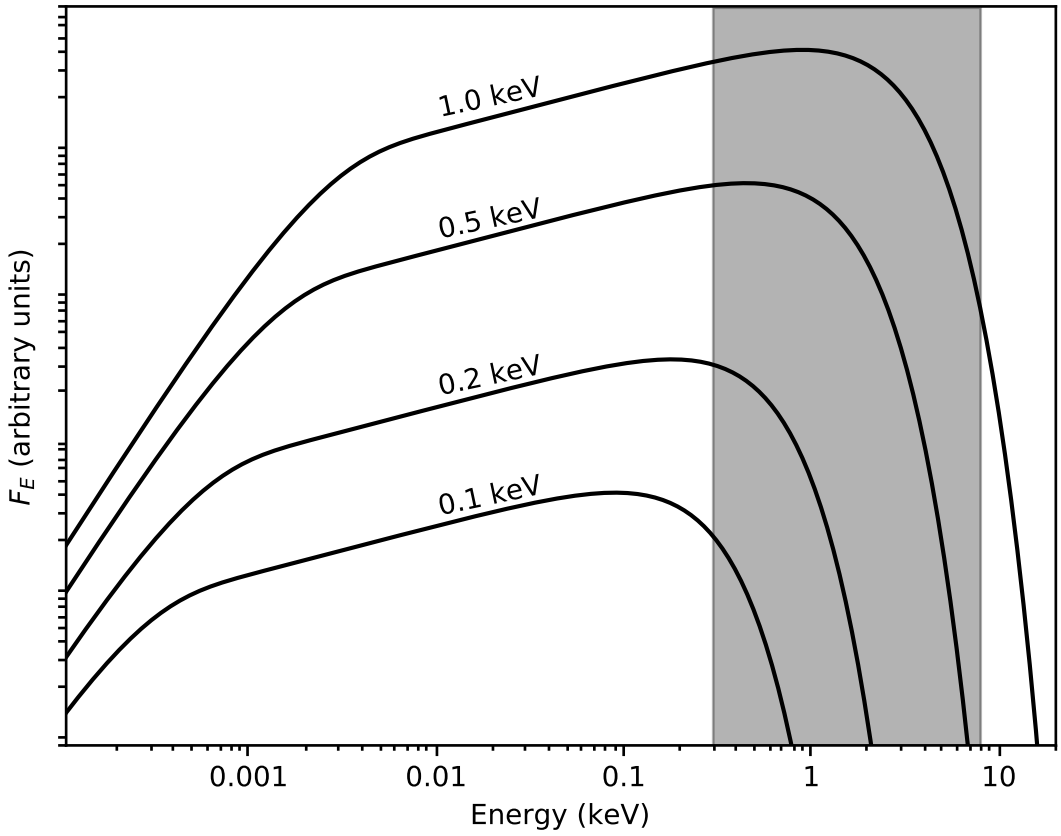

Figure 2.2: Disk blackbody emission. A sample of curves with peak temperatures ranging from $k_{\rm B}T = 0.1$ keV to 1 keV. The shaded region indicates the $0.3-8$ keV X-ray band, covered by *Chandra* and *XMM-Newton*.

cannot be replicated by a simple blackbody model. The characteristic thin-disk spectrum is in fact a multicolour blackbody with a range of temperatures between the temperature of the cool outer-most annulus ($T_{\rm out}$) up to the hot inner-most annulus ($T_{\rm in}$). This gives the spectrum three distinct regions (Figure 2.2); the low-energy downturn that behaves like the Rayleigh-Jeans part of the single-temperature cool blackbody spectrum of the outer disk boundary (scales as $F_E \propto E^2$), the middle flat section that consists of the super-position of many blackbody annuli (scales as $F_E \propto E^{1/3}$), and the high-energy leading edge that behaves like the Wien part of the single-temperature hot blackbody spectrum of the inner disk boundary (scales as $F_E \propto e^{-E}$). The outer disk boundary, beyond which material becomes optically thin and no longer contributes to the continuum spectrum, is defined either by the tidal radius ($\sim 0.7 - 0.9$ times the radius of the compact object Roche lobe; Paczynski 1977) or the point where the disk temperature drops below the hydrogen recombination temperature ($T \sim 6,000\,{\rm K}$). The inner disk boundary is defined by either the surface of the neutron star[1] or $R_{\rm ISCO}$ in the

[1]Or the radius at which the magnetic field pressure truncates the disk in neutron stars with sufficiently high magnetic fields.

case of a black hole. Distinguishing between low-temperature disk models and blackbody models is difficult, as they are identical within the X-ray observing band (c.f. Figures 2.1 and 2.2). This is generally only a problem for modelling the spectra of ULSs, as they are dominated by cool blackbody emission.

It is important to outline the solutions to the full set of steady α-disk structure equations (1.12) for each region highlighted in Section 1.3.1. In region (i)

$$\left.\begin{aligned}
\Sigma &= 4.6\alpha^{-1}\dot{m}_{\rm crit}^{-1}r^{3/2}\left[1-r^{-1/2}\right]^{-1}, \\
H &= 10^{8}M^{-1/2}r^{-3/4}, \\
\rho &= 7.2\times10^{-7}\alpha^{-1}\dot{m}_{\rm crit}^{-2}M^{-1}r^{3/2}\left[1-r^{-1/2}\right]^{-2}, \\
T_{\rm c} &= 2.3\times10^{7}\alpha^{-1/4}\dot{m}_{\rm crit}^{-1/4}r^{-3/4}, \\
\tau &= 8.4\times10^{-5}\alpha^{-17/16}\dot{m}_{\rm crit}^{-2}M^{-1/16}r^{-93/32}\left[1-r^{-1/2}\right]^{-2}, \\
\upsilon_{\rm R} &= 7.7\times10^{10}\alpha\dot{m}_{\rm crit}^{2}r^{-5/2}\left[1-r^{-1/2}\right].
\end{aligned}\right\} \tag{2.2}$$

The dimensionless parameters,

$$m = \frac{M}{\mathrm{M}_{\odot}}, \tag{2.3}$$

$$r = \frac{R}{R_{\rm ISCO}} = \frac{1}{6}\frac{Rc^{2}}{GM}, \tag{2.4}$$

are introduced to simplify the equations. All solutions are in CGS units, with $T_{\rm c}$ in K. Solving Equations (1.12) for region (ii) gives

$$\left.\begin{aligned}
\Sigma &= 1.7\times10^{5}\alpha^{-4/5}\dot{m}_{\rm crit}^{3/5}M^{1/5}r^{-3/5}\left[1-r^{-1/2}\right]^{3/5}, \\
H &= 1.5\times10^{9}\alpha^{1/20}\dot{m}_{\rm crit}^{2/5}M^{-9/20}r^{-51/40}\left[1-r^{-1/2}\right]^{2/5}, \\
\rho &= 7.0\alpha^{-4/10}\dot{m}_{\rm crit}^{2/5}M^{-7/10}r^{-33/20}\left[1-r^{-1/2}\right]^{2/5}, \\
T_{\rm c} &= 3.1\times10^{8}\alpha^{-1/5}\dot{m}_{\rm crit}^{2/5}M^{-1/5}r^{-9/10}\left[1-r^{-1/2}\right]^{2/5}, \\
\tau &= 100\alpha^{-4/5}\dot{m}_{\rm crit}^{9/10}M^{1/5}\left[1-r^{-1/2}\right]^{9/10}, \\
\upsilon_{\rm R} &= 2\times10^{6}\alpha^{4/5}\dot{m}_{\rm crit}^{2/5}M^{-1/5}r^{-2/5}\left[1-r^{-1/2}\right]^{-3/5}.
\end{aligned}\right\} \tag{2.5}$$

Solving Equations (1.12) for region (iii) gives

$$\left.\begin{aligned}
\Sigma &= 5.2\alpha^{-4/5}\dot{m}_{\rm crit}^{7/10}M^{1/4}r^{-3/4}\left[1-r^{-1/2}\right]^{14/20}, \\
H &= 1.7\times10^{8}\alpha^{-1/10}\dot{m}_{\rm crit}^{3/20}M^{-3/8}r^{9/8}\left[1-r^{-1/2}\right]^{3/20}, \\
\rho &= 3.1\times10^{-8}\alpha^{-7/10}\dot{m}_{\rm crit}^{11/20}M^{5/8}r^{-15/8}\left[1-r^{-1/2}\right]^{11/20}, \\
T_{\rm c} &= 1.4\times10^{4}\alpha^{-1/5}\dot{m}_{\rm crit}^{3/10}M^{1/4}r^{-3/4}\left[1-r^{-1/2}\right]^{6/20}, \\
\tau &= 190\alpha^{-4/5}\dot{m}_{\rm crit}^{1/5}\left[1-r^{-1/2}\right]^{1/5}, \\
\nu &= 1.8\times10^{14}\alpha^{4/5}\dot{m}_{\rm crit}^{3/10}M^{-1/4}r^{3/4}\left[1-r^{-1/2}\right]^{6/20}, \\
\upsilon_{\rm R} &= 2.7\times10^{4}\alpha^{4/5}\dot{m}_{\rm crit}^{3/10}M^{-1/4}r^{-1/4}\left[1-r^{-1/2}\right]^{14/20}.
\end{aligned}\right\} \tag{2.6}$$

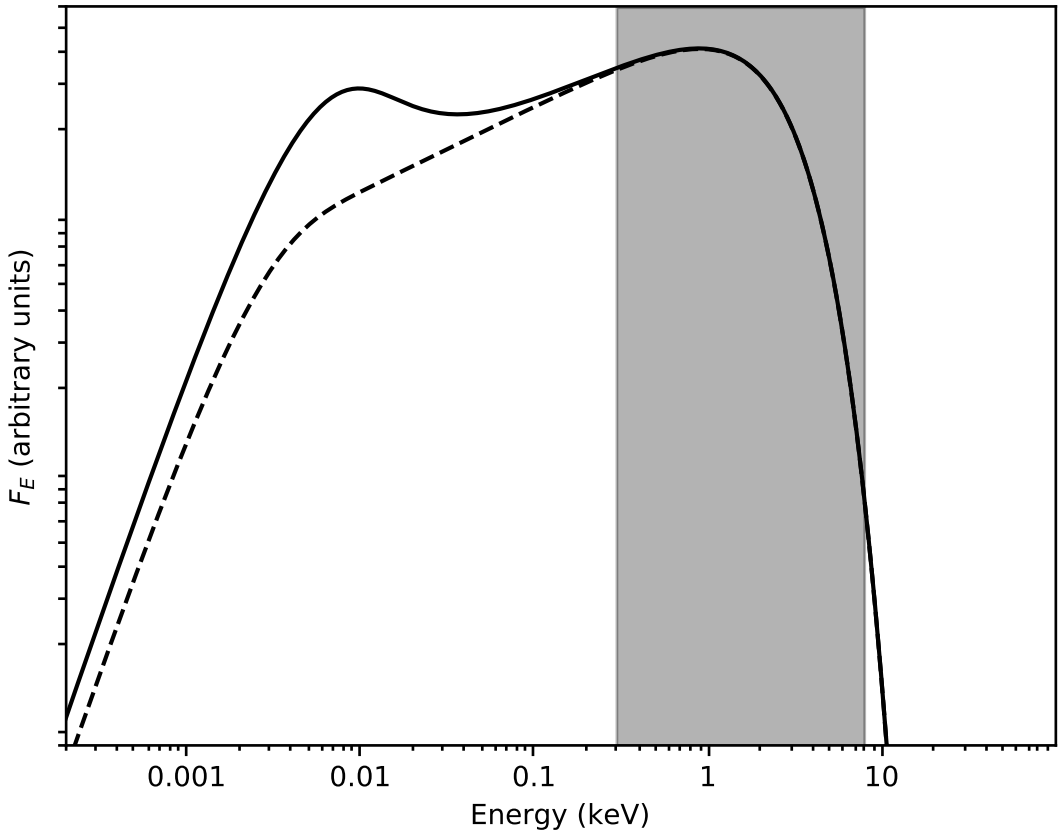

Figure 2.3: The solid curve indicates an irradiated disk model while the dashed line indicates the standard accretion disk model. Both disks have a peak temperature of $k_{\rm B}T = 1$ keV. The important feature in the irradiated disk model is the increased flux at optical and UV wavelengths. The shaded region indicates the $0.3 - 8$ keV X-ray band, covered by *Chandra* and *XMM-Newton*.

The final solution, Equation (2.6), is the standard thin disk solution, also known as the Shakura-Sunyaev disk solution Shakura and Sunyaev (1973). Here, the temperature profile of the standard disk scales with radius according to $T \propto r^{-0.75}$. For advection-dominated disks, this proportionality changes, which I will discuss in the following section.

An important physical process that can modify the emission in accretion disks is irradiation. The outer disk can intercept a few percent of the X-ray emission from the hotter inner region, re-emitting it as thermal emission at longer wavelengths, boosting the disk flux in the UV and optical bands beyond what is expected for a standard blackbody spectrum (Figure 2.3). Optical and UV measurements can help to evaluate the viability of irradiated disk models. However, for ULXs it is difficult to decouple the optical and UV emission contributions from the irradiated disk and the companion star because they share similar physical properties; the outer disk has a typical size of $10^{11} - 10^{12}$ cm and radiates at a few percent of the total X-ray luminosity (i.e. $\sim 10^{38}$ erg s^{-1}), which, coinci-

dentally, is the characteristic radius and luminosity of $15 - 20\,M_\odot$ stars that are often donor stars of ULXs.

2.1.3 Non-standard accretion disks

At super-critical accretion rates, the standard disk model must be modified. One of the consequences is that the observational appearance of ULXs cannot be described in terms of classical (sub-Eddington) states. Instead, ULXs are often modelled with extra emission mechanisms (two-component spectra), usually either high-energy Comptonisation or line emission from hot diffuse gas, both of which I discuss later in this chapter. Additionally, the accretion disk can be modified, similar to the irradiated disk model discussed previously. In non-standard accretion disks, where radiative cooling is no longer dominant, not all gravitational potential energy is radiated at each annulus as the material moves towards the inner disk. The energy either does not have sufficient time to radiate locally and is advected to the innermost radius (or past the event horizon), is used to generate disk winds and thus not emitted as photons, or is carried away by a large-scale electromagnetic field. This modifies the radial temperature profile $T \propto r^{-p}$, where $p = 0.75$ in the standard disk model and $p < 0.75$ for non-standard disks, where advection becomes significant. This has the effect of broadening the disk spectrum as the temperature changes more slowly, which helps to model the broader spectra associated with ULXs. The effect of this is seen in Figure 2.4.

2.2 Optically-thin gas

Different emission mechanisms dominate when dealing with optically-thin gas associated with ULXs. This predominantly includes Comptonised emission and line emission regions, both at X-ray and optical wavelengths.

2.2.1 Compton scattering

Inverse Compton scattering is the process by which low-energy photons gain energy from collisions with high-energy electrons. This boosts the energy of the incident photons at the expense of the kinetic energy of the electrons. The output energy distribution of the Comptonised photons is the convolution of the incident photon distribution and the electron distribution. In the case of ULXs, and other accreting compact objects, the incident, or seed, photons usually come from the thermal accretion disk. For full details of inverse Compton scattering, refer to Rybicki and Lightman (1979).

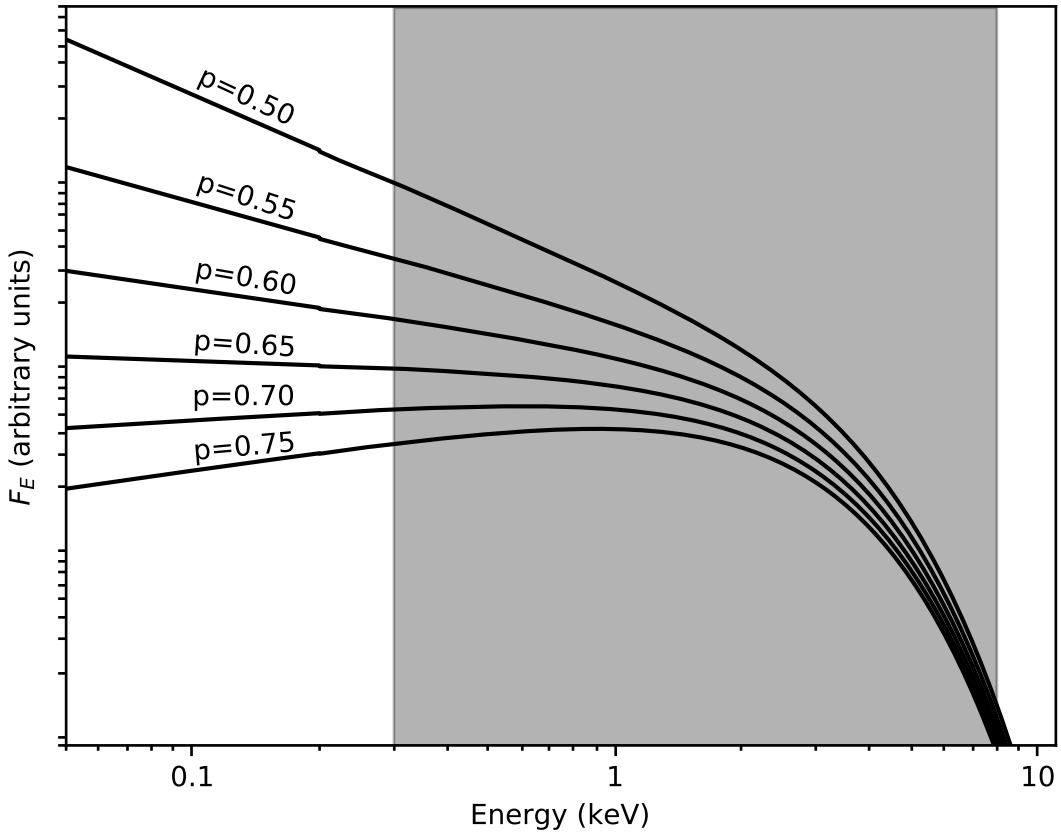

Figure 2.4: Modified disk blackbody emission. In this model, known as a p-free disk model, the accretion disk is dominated by radiation pressure. Most super-Eddington disks have p values of between 0.55 and 0.65. For a value of $p = 0.75$, the standard blackbody disk model is recovered. Each disk has a peak temperature of $k_{\rm B}T = 1\,{\rm keV}$. The shaded region indicates the $0.3 - 8\,{\rm keV}$ X-ray band, covered by *Chandra* and *XMM-Newton*.

The spectrum of a Comptonised blackbody disk is displayed in Figure 2.5. Here the incident photon temperature is fixed to the peak temperature of the blackbody disk, as it is this component that is providing the seed photons. This is a physically motivated two-component model based on the canonical sub-Eddington XRB model; an accretion disk plus corona. However, whereas in XRBs, the coronae are optically-thin and have temperatures of $\sim$ 100 keV, coronae in ULXs are much cooler ($k_{\rm B}T \sim 1 - 2$ keV) and have optical depths $\tau > 6$. These effects are a consequence of dense super-critical accretion flow driving considerable material above the disk plane and strong seed photon flux from a relatively cool ultraluminous accretion disk. Consequently, the hard component in ULXs has a strong curvature with an energy break in the 2-7 keV range, as seen in Figure 2.5.

The photon index of the Compton component in ULXs dictates their spectral classification; soft ultraluminous sources show $\Gamma > 2$ while hard ultraluminous

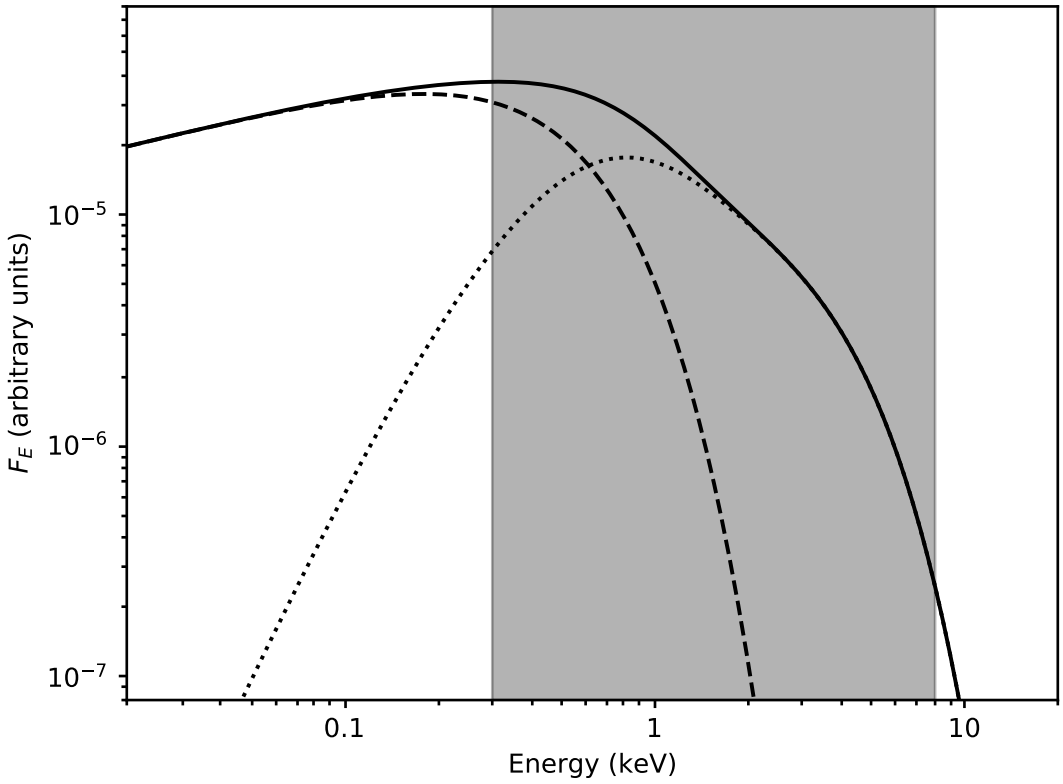

Figure 2.5: Comptonised disk blackbody emission. The solid black line represents the disk emission modified by the presence of a Comptonising component. The underlying disk blackbody component is outlined by the dashed line while the Compton component is shown by the dotted line. This is an example of a physically motivated two-component model often used for ULX spectra. The shaded region indicates the $0.3 - 8$ keV X-ray band, covered by *Chandra* and *XMM-Newton*.

sources show $\Gamma < 2$ (Sutton et al., 2013b). Sources with spectra dominated by the disk are classified as broadened disk sources (Figure 1.9).

2.2.2 Ionised plasma emission

In this section, I detail emission processes that take place in hot gas ($T \sim 10^4 - 10^6$ K). Line-emitting gas can be found at various distances from the accreting source, at a range of temperatures and it can have a number of different origins (e.g. disk winds, shocked gas at the jet/ISM interface).

2.2.2.1 Bremsstrahlung

Bremsstrahlung radiation is emission from the acceleration of a charged particle, usually an electron, in the presence of an electric field from the nucleus of an ion. Also known as free-free radiation, it corresponds to emission from the electron transitioning between unbound states. Because these transitions are not

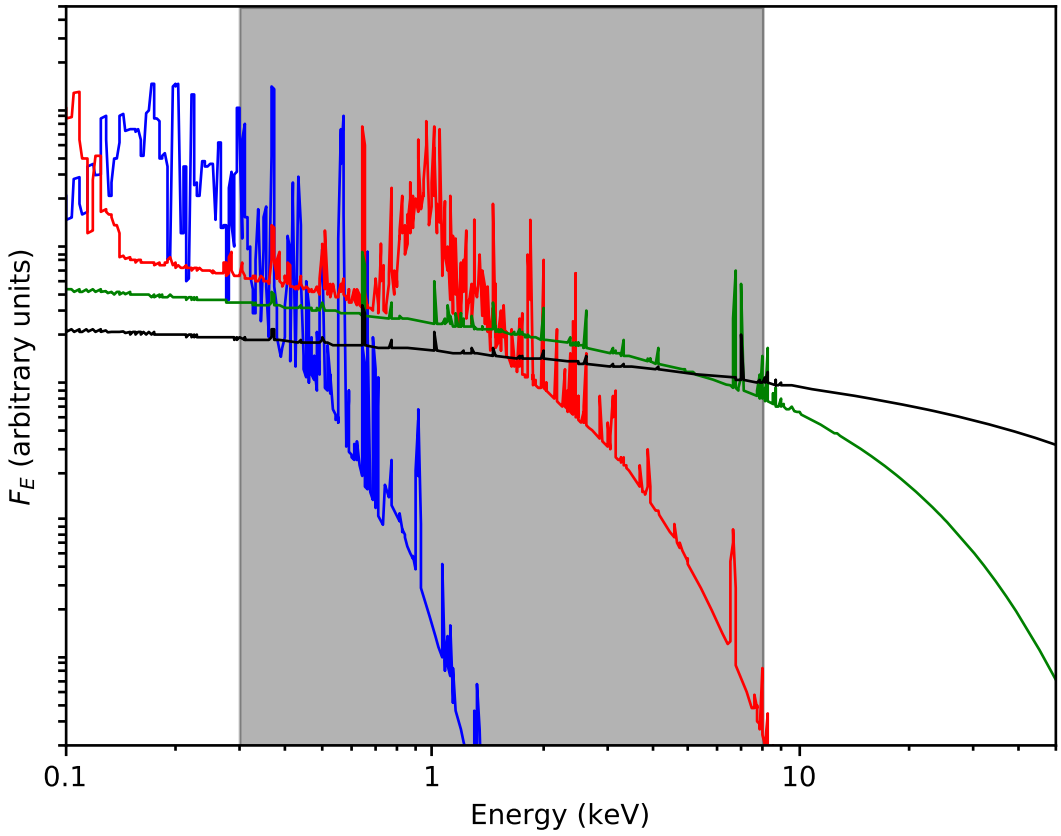

Figure 2.6: The blue model spectrum is a solar-abundance *mekal* model at $k_{\rm B}T = 0.3\,{\rm keV}$; the red spectrum is for $k_{\rm B}T = 1\,{\rm keV}$; the green spectrum is for $k_{\rm B}T = 10\,{\rm keV}$; the black spectrum is for $k_{\rm B}T = 100\,{\rm keV}$. Notice that for T $\gtrsim$ 10 keV, the spectrum increasingly looks like pure Bremsstrahlung emission, as most of the plasma is completely ionised. Temperatures between ~ 0.3–$1\,{\rm keV}$ are typical of outflows around ULXs, but also of shocked gas in the hot spots of microquasars jets and supernova remnants (SNRs). Temperatures $\gtrsim 10\,{\rm keV}$ are typical of hot coronae and accretion columns onto compact objects. The shaded region indicates the $0.3 - 8\,{\rm keV}$ X-ray band, covered by *Chandra* and *XMM-Newton*.

restricted to discrete quantised states, Bremsstrahlung emission is a continuous distribution, outlined by the black curve in Figure 2.6. For a full derivation of the Bremsstrahlung radiation spectrum, refer to Chapter 6 of Longair (2011).

When dealing with ULXs, I primarily come across thermal Bremsstrahlung radiation from the diffuse emission of ionised ULX bubbles. This can manifest at both radio and X-ray wavelengths. The X-ray emission comes from hot gas, usually temperatures of around $10^6 - 10^7$ K, whereas the radio emission will come from cool gas at 10^4 K, similar to what is seen in HII regions. An example of the spectrum of Bremsstrahlung emission in the X-rays can be seen in Figure 2.6. At radio wavelengths, Bremsstrahlung emission tends to be flat spectrum, distinguishing it from the other form of radio emission synonymous with ULXs; steep-spectrum optically-thin synchrotron radiation from relativistic jets (Section

2.3.1).

2.2.2.2 Atomic line emission

Radiative recombination within astrophysical plasmas gives rise to spectral line emission. It is the process in which an electron is captured by an ion, typically in an excited state, radiating away energy lost via photons as the electron cascades down towards the ground state, passing through multiple states as it does so. In the case of Hydrogen-like atoms, the wavelength, λ, of each radiated photon is governed by

$$\frac{1}{\lambda} = Z^2 R_H \left(\frac{1}{n_f^2} - \frac{1}{n_i^2} \right) \tag{2.7}$$

where $R_H = 1.097 \times 10^7\,\mathrm{m}^{-1}$ is the Rydberg constant, Z is the atomic number of the ion and n_i and n_f are the initial and final quantum states respectively.

An important feature of astrophysical plasmas, specifically those associated with diffuse nebulae, is the appearance of what are known as 'forbidden lines'. These are transitions from meta-stable states that do not occur under laboratory conditions, but do arise in the low densities of astrophysical plasmas. This is because they require long-lived electron orbits devoid of any particle collisions. The term *forbidden* is a misnomer; it would be more accurate to claim these transitions as simply *highly improbable*. Forbidden lines are denoted by the use of square brackets (e.g. [O III] as apposed to He II or Hα). The ratio of many of these forbidden lines to the hydrogen recombination lines is fundamental to understanding the physical characteristics of diffuse astrophysical structures, like density, temperature, reddening and metal abundance.

While X-ray Bremsstrahlung emission is associated with hot gas, at cooler temperatures, where the atoms are no longer completely ionised, or at significant metal abundances, the radiation profile transitions into line-dominated emission from collisionally-excited thermal plasma. The underlying continuum remains that of Bremsstrahlung, however, narrow features above the continuum begin to emerge (Figure 2.6). Thermal plasma emission associated with ULXs can come either from hot disk outflows (thus, from a region comparable in size to the binary system, $10^{12} - 10^{13}\,\mathrm{cm}$), or from hot spots and shock-ionised gas where the fast winds or jets interact with the ISM (thus, on a much larger scale, $10^{20}\,\mathrm{cm}$). For the former component, the emission can be identified via X-ray spectral analysis, as a modification of the X-ray continuum spectrum of the accreting source (e.g. Middleton et al. 2015b; Pinto et al. 2016) and is typically modelled using tables of line emissivities at the appropriate temperature and metallicity, provided for example by the *apec* thermal plasma model, or by the *mekal* model (Mewe et al.,

1986, 1985).

In contrast, the spatially-extended thermal plasma emission from the interaction between fast winds or jets and the ISM is associated with ULX bubbles. However, these bubbles can also be ionised via radiation. How the plasma reaches an excited state (i.e. how the gas is ionised) can change the observable characteristics of the emission spectrum. In this research project, I study the spectral line emission of ULX bubbles at UV, optical and infrared (IR) wavelengths. I classify each nebula based on the dominant ionisation mechanism, photo- or shock-ionisation, which has important physical implications on the host ULX. The characteristics of both photo-ionisation and shock-ionisation are outlined below.

2.2.2.2.1 Photo-ionisation Similar to HII regions, ULX bubbles can be ionised by radiation. Whereas the ionising photons in HII regions are UV photons that come from hot, massive stars, ULXs bubbles are ionised by the much hotter X-ray photons from the central accreting source. While a single UV photon with $E > 13.6$ eV can completely ionise a single hydrogen atom, and even helium ($E > 54.4$ eV), a single X-ray photon can ionise multiple hydrogen or helium atoms, along with metals with much higher ionisation energies. The presence (or absence) of high-ionisation lines can help to distinguish between photo-ionised ULX bubbles and HII regions ionised by stellar radiation.

2.2.2.2.2 Shock-ionisation An alternative to photo-ionisation is to inject energy into the ISM via the kinetic output of the radiatively-driven wind or relativistic jet of the ULX. This is known as shock-ionisation. The most noticeable differences between the observed spectra of photo-ionised and shock-ionised gas are the broader line widths seen in shocked gas (indicative of the motion of the gas) and the distinct characteristic line ratios from the much hotter shocked gas.

The winds and/or jets from the ULX create high pressure gas that starts to move out from the central object, against the stationary ISM. This imparts a shock into the ambient gas, heating it and increasing pressure, causing it to expand. As the shockwave propagates outward, energy is transferred into the stationary gas, draining kinetic energy from the expanding medium and causing it to slow. As is well-known in standard bubble theory (e.g. Weaver et al. 1977), this process creates two shock fronts: one that propagates into the stationary ISM (forward shock, also known as the blast wave), and one that propagates into the fast wind (reverse shock). In between the two shock fronts lies the contact discontinuity between shocked ISM and shocked wind. Diagnostic lines can probe the temperatures and densities of the different physical zones of the shock. This

simplified picture was derived for a spherically-symmetric wind, inflating a spherical bubble of shock-ionised gas. Nonetheless, the basic scenario still applies even when the mechanical power is driven by a collimated wind or jet. In that case, the forward shock is usually referred to as the bow shock. Even for a collimated jet, backflow of the swept-up shocked gas usually ensures the formation of a full bubble or cocoon around the accreting compact object (although elongated in the direction of the jet). The total radiative luminosity of the shock-ionised gas can be inferred from the observed flux of particular diagnostic lines (e.g. Balmer lines), with plausible assumptions on the shock velocity (generally $100 - 500\,\mathrm{km\ s^{-1}}$). In turn, the time-averaged kinetic power responsible for the ionisation of the gas is proportional to the total radiative luminosity. Therefore, the line luminosity of ULX bubbles can be used as a proxy for the jet power. Alternatively, the expansion velocity and age of a shock-ionised bubble can be derived from the observed width of the emission lines, which, if the density of the external medium is also known, provides another way to estimate the input kinetic power that is driving the bubble expansion.

With the total luminosity of the bubble, which can be estimated using hydrogen recombination lines, I can determine the mechanical power output that is driving the expansion of the bubble. Thus I can use ULX bubbles as calorimeters for determining the power of the jet.

2.3 Relativistic gas

Finally, I discuss emission from relativistic matter, namely synchrotron emission from a collimated jet. Relativistic jets are a hallmark of compact accreting sources. It is unclear if jets are ubiquitous across the ULX population and whether or not the sources that do show evidence of jets have continuous jets or episodic ejections of relativistic plasma. I discuss this problem in detail in Chapters 6, 7 and 8.

2.3.1 Synchrotron emission

Synchrotron radiation is the emission from relativistic charged particles accelerated in a magnetic field. The emission is channelled into a narrow beam along the direction of the particle. The spectrum of emission for a single electron peaks at a critical frequency, ν_c, scaling as $\nu^{1/3}$ below this and falling off sharply above this. The full spectrum for an astrophysical source is the superposition of each spectrum from the individual relativistic electrons. The resulting spectrum can be broken up into two broad sections; optically-thin or optically-thick synchrotron.

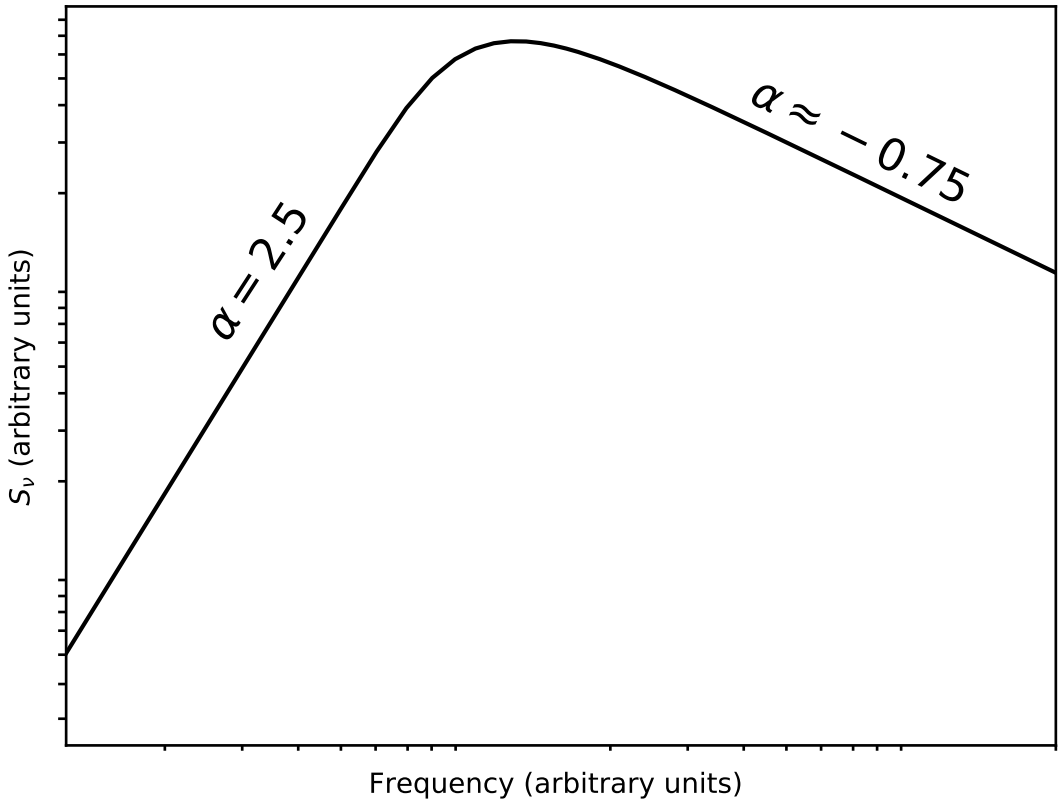

Figure 2.7: Spectrum of synchrotron radiation at radio wavelengths. The peak of the emission corresponds to the frequency at which the source transitions from optically-thick ($S_\nu \propto \nu^{5/2}$) to optically-thin ($S_\nu \propto \nu^{-0.75}$). Synchrotron radio emission from ULXs is exclusively in the optically-thin domain; i.e. it generally has steep spectral indices.

At lower frequencies, where $\tau > 1$, the spectrum scales as $S_\nu \propto \nu^\alpha$ for $\alpha = 5/2$ (Figure 2.7). The optically-thin ($\tau \ll 1$) end is dependent on the power-law distribution of the electrons, $n(E) \propto E^{-\delta}$, where the spectral index of the synchrotron emission, α, in this regime is governed by $\alpha = -(\delta - 1)/2$. For most astrophysical sources emitting optically-thin synchrotron radiation, $\alpha \approx -0.75$.

It is in the optically-thin regime that synchrotron emission from ULXs is observed. Optically-thick synchrotron emission is often seen in jets from Galactic XRBs and indicates the presence of the compact core of a steady jet. While such jets may be present in ULXs, their luminosities would be well below the detection limit of current radio telescopes. Even next-generation radio inteferometers, such as the Square Kilometre Array (SKA), will not be able to detect emission from the compact core of a ULX, expect for the absolute closest sources[2]. Consequently, observations of ULX jets rely on either bright, episodic emission from transient

[2]The IMBH candidate HLX-1 is ignored, whose hard-state radio emission is likely Doppler-boosted (Cseh et al., 2015b), and we only consider stellar-mass sources in which super-Eddington accretion must be taking place.

ejecta (e.g., Ho II X-1; Cseh et al. 2015a) or the detection of radio lobes or hotspots from jet/ISM interactions (e.g., S 26; Soria et al. 2010). Both of these scenarios give rise to optically-thin synchrotron emission. Fortunately, with high enough quality multifrequency radio observation, steep-spectrum synchrotron emission can generally be distinguished from flat-spectrum radio Bremsstrahlung emission, thus confirming if a relativistic jet is present via radio observations.

Chapter 3

Instrumentation and data analysis techniques

We use a combination of astronomical data from across the electromagnetic spectrum to probe different physical characteristics of our sample of ULXs. The instantaneous radiative power of the compact object is derived by measuring the X-ray luminosity and analysing the spectral and timing properties. Relativistic jets and outflows are identified using radio flux density measurements and broad-band spectral analysis. We use spectroscopic measurements and narrow-band imaging of the optical line emission from the shocked gas of ULX bubbles and jet hotspots to measure the kinetic power of these outflows. The velocities of the shock fronts are constrained by measuring the velocity broadening of optical emission lines. The brightness and colours of the point-like optical counterpart, determined using photometric analysis, are measured to constrain the properties of the donor star. Clearly, multiwavelength observations of ULXs are required to fully understand accretion and outflows in the super-Eddington regime. This chapter outlines the basic observational and data reduction techniques implemented throughout the thesis. More specialised techniques are described as they are used in Chapters 4-7.

3.1 X-ray

A key goal of this thesis is to study the X-ray spectral and timing properties of ULXs. X-ray spectral properties of accreting sources give insights into the physical characteristics of the accretion flow and thus are necessary for understanding super-critical accretion. Similarly, X-ray timing analyses probe how the accretion flow varies over time. Consequently, we exploit X-ray observatories that can offer high timing and spectral resolution. In addition, ULXs,

being extragalactic sources, are often embedded in crowded X-ray fields. Similarly, for jetted ULXs, we need to be able to distinguish the central compact object from any potential X-ray hotspots from jet/ISM interactions. To avoid source confusion and contamination, high spatial resolution is therefore critical. Throughout the thesis, we primarily use the current-era X-ray telescopes *Chandra* and *XMM-Newton* due to their complementary characteristics. Both telescopes have similar sensitivities ($4–5\times10^{-15}$ erg cm^{-2} s^{-1} in 10^4 s), energy ranges (0.1–10 keV and 0.15–12 keV, respectively), and are well suited for studying both broadband ULXs and low-energy ULSs. We rely on the *Chandra* Advanced CCD Imaging Spectrometer (ACIS) X-ray imager for its unparalleled spatial resolution ($\sim 0.5''$), out-performing the three European Photon Imaging Cameras (EPIC) of *XMM-Newton* ($\sim 15''$). However, *XMM-Newton* has a superior photon collecting area and timing resolution, hence why we often use the two telescopes in parallel when performing X-ray spectral and timing analyses of ULXs. Finally, we also use regular shallow observations from *Swift* to supplement monitoring campaigns.

Each of these X-ray observatories are placed in orbit to avoid the Earth's atmosphere, which absorbs incoming cosmic X-rays. Current X-ray telescopes, much like optical telescopes, use charge-coupled devices (CCDs) to collect incident photons and digitise the received signal. However, due to their high energies, X-rays can only be focused when they hit a mirror at low grazing angles. Thus, imaging X-ray telescopes use long, cylindrical, nested mirrors. The low fluxes of X-ray sources mean that, unlike optical telescopes, individual photons are counted. Consequently, X-ray data includes information on the arrival time, position and energy of each incident X-ray photon. This section summarises the basic processes involved in X-ray data reduction and calibration. See Arnaud et al. (2011) for more details.

3.1.1 Data reduction and calibration

Raw X-ray data can be downloaded from online, public archives like NASA's High Energy Astrophysics Science Archive Research Center (HEASARC) [1]. The raw data must then be calibrated using software tailored to individual observatories and instruments. This processing involves removing contaminants like background flares, hot pixels and bad rows that degrade signal-to-noise. Another issue facing CCDs that can arise when observing bright sources is known as pileup. This occurs when two (or more) photons strike the detector within a single frame and within only a few pixels of each other. This will be identified as a single event with an energy equal to the total energy of both photons. Consequently,

[1] https://heasarc.gsfc.nasa.gov/

this can cause apparent spectral hardening and a reduced count rate. Pileup can be reduced by observing bright sources off-axis, or through specialised spectral modelling in post-processing. Once these issues have been corrected for, we are able to create the final products, including an image (created by summing over all time and energy bins), a spectrum (energy information taken from a specified region) and a lightcurve (also for a given region but using photon energies and arrival times). Preparation of X-ray images and light curves are relatively straightforward and follow standard data processing techniques. Production of X-ray spectra is more complicated as it requires the deconvolution of the observed spectrum and telescope response function. Thus we detail this process below. For details on imaging and light curve generation, see Chapters 4 and 5.

3.1.2 Spectral modelling

Spectral modelling of X-ray data is important for gaining insight into the physical processes behind the detected emission. In ULXs, and other accreting sources, spectral properties can help in determining physical properties such as the geometry of the accretion flow, inclination angle and type of accretor. The aim of spectral fitting is to identify the model that best represents the data, and thus the underlying emission processes.

In X-ray spectroscopy, the observed spectrum has been convolved with the instrumental response. The relationship between the incident source flux, S_{E}, and the observed counts, C_{N}, is a function of the telescope and detector response such that

$$C_{\mathrm{N}} = T \int R_{\mathrm{N,E}} \cdot A_{\mathrm{E}} \cdot S_{\mathrm{E}} \cdot \mathrm{d}E, \tag{3.1}$$

where T is the observation time and $R_{\mathrm{N,E}}$ and A_{E} represent the effects of the instrument. $R_{\mathrm{N,E}}$ is the energy resolution of the telescope, incorporated into the redistribution matrix file (RMF), while A_{E} is the effective area, incorporated into the ancillary response file (ARF). For more information on the response functions, see Davis (2001). Each mission provides both the RMF and ARF, or software to generate them. Due to the non-unique nature of the solutions, Equation (3.1) cannot simply be inverted to solve for the source spectrum. Instead, forward fitting techniques are used to constrain what physical model most likely represents the data. An initial, physically-motivated, model spectrum is chosen, which is then convolved with the response of the detector and effective area, and compared against the observed counts using a maximum likelihood statistical measure. The model fit parameters are modified until the best value of the statistic is discovered. The model is rejected if the best-fit value is not satisfactory, and the process is repeated with a different model.

Poisson and Gaussian distributions are the most commonly used probability distribution employed for spectral fitting in X-ray astronomy. For a sufficiently large sample size, the Poisson distribution tends to a Gaussian approximation. Thus, for bright sources, with moderate-to-high count rates, a sufficient number of counts ($\gtrsim 15$ counts per bin) may be grouped into spectral bins allowing Gaussian statistics to be used. In the Gaussian regime, χ^2 minimisation is utilised to test the likelihood of spectral models. The fit statistic is defined by

$$\chi^2 = \sum_i \frac{(X_i - M_i)^2}{\sigma_i^2}, \tag{3.2}$$

where X is the observed data, M is the model and σ represents the uncertainties on the data. The best fit is recovered when the fit statistic is equal to the number of degrees of freedom, i.e., $\chi^2/dof \approx 1$. Values greater than unity suggest that the model is a poor fit, while values less than unity indicate that the model is over-fitting the data, suggesting that there are too many fit parameters or the uncertainties are overestimated. In the low-count regime, the Poisson fit statistic, known as the C statistic, is defined by

$$C = 2\sum_i (M_i - X_i \ln M_i), \tag{3.3}$$

(Cash, 1979). Minimising C yields the best statistical fit. For background-subtracted spectra, a modification of Cash statistics known as W statistics must be implemented where the average background is selected from a nearby, source-free region. The forward fitting routines that test spectral models are performed by specialised software packages (e.g., XSPEC; Arnaud 1996). The source data, along with the response files and background files, are ingested into these software packages and best-fit parameters and their errors are produced.

3.2 Radio

As with the X-ray, our choice of radio telescopes is motivated by the observational properties of our targets. As with all compact accreting sources, radio observations are necessary for studying the relativistic jets. However, unlike in Galactic XRBs, the vast distances to ULXs often preclude us from detecting the core emission from these jets. Instead we generally rely on finding less direct evidence for the presence of a jet. This includes, but is not limited to, more extended structures like radio hotspots, lobes and bubbles. It follows that we require radio telescopes with high sensitivities to detect the low flux densities of the diffuse emission. In addition, moderate spatial resolution is needed; high

enough to image the large-scale structures but not so high that structure is resolved out and source flux is missed. Given these criteria, we predominantly use radio interferometers. For sources in the northern hemisphere, we utilise the Very Large Array (VLA) while for southern sources we utilise the Australia Telescope Compact Array (ATCA). Data for these telescopes can be downloaded from the National Radio Astronomy Observatory (NRAO) online data archive[2] and CSIRO's Australian Telescope Online Archive (ATOA)[3], respectively. In this section we outline the basics of radio interferometry, as described in Taylor et al. (1999), Burke and Graham-Smith (1997), and Thompson et al. (2001).

3.2.1 The basics of radio interferometry

Radio interferometry is the combination of electromagnetic signals from cosmic sources received by pairs of antennas. The necessity for radio interferometry arises from the fact that the angular resolution of single radio antennas is limited by the size of the dish that is practical to build. For example, the largest fully steerable single-dish radio telescope, the Green Bank Telescope, has a diameter, $D = 100\,\mathrm{m}$. When observing at 1.4 GHz, it has an angular resolution,

$$\theta \sim \frac{\lambda}{D}, \tag{3.4}$$

of $\sim$ 1 degree. While single-dish radio telescopes still have their place (ideal for pulsar timing and spectral line work), the workhorse of high-resolution radio astronomy imaging is the multi-dish radio interferometer. Here, the value of D in Equation (3.4) now becomes the longest distance between a pair of antennas, known as a baseline. This allows for arcsecond to sub-arcsecond resolution in current generation radio interferometers.

The simplest interferometer is a two-element array. As seen in Figure 3.1, the two antennas receive the signal from an incident plane wave at different times, according to the light travel time. In order to compensate for this, a delay is introduced, equal to the light travel time. With this delay in place, the amplitudes of the voltages from the two antennas are cross-correlated to form the average interferometer response. The ultimate goal is to relate the voltages to the true sky brightness. This can be accomplished by using the combination of both the real and imaginary parts of the interferometer response, known as the visibility. The visibility is a component of the frequency-domain 2-D Fourier transform of the sky brightness. Thus a single interferometer observation probes the Fourier transform of the sky brightness, projected onto a plane perpendicular to the line

[2]https://science.nrao.edu/facilities/vla/archive/index
[3]https://atoa.atnf.csiro.au/

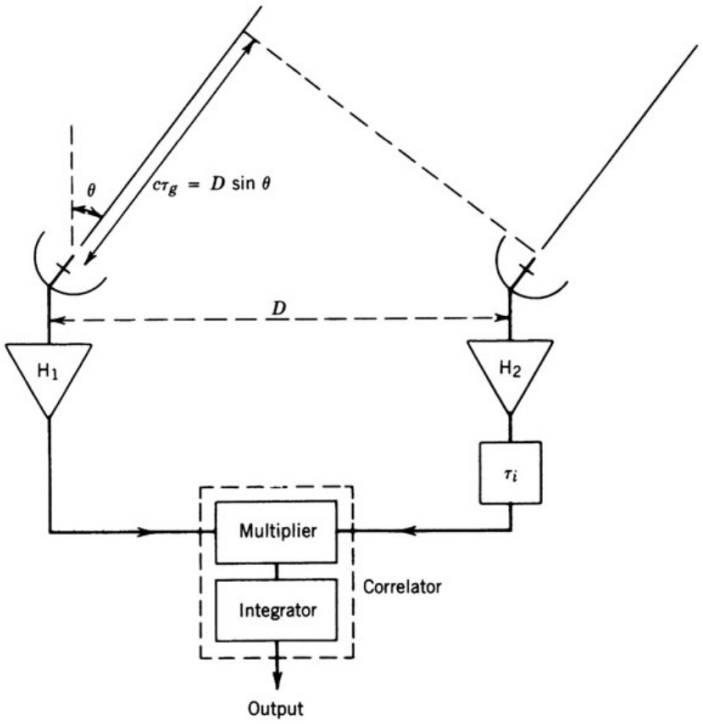

Figure 3.1: Illustration of a two-element Michelson interferometer. The two antennas are separated by a distance D. The geometric time delay, τ_g is introduced to compensate for the light travel time taken for the wavefront to reach the second antenna. Image credit Thompson et al. (2001).

of sight with coordinates corresponding to the projections of the baselines used – what is referred to as the *uv*-plane.

This is what is used to create a radio image (the Fourier inversion of the visibilities). Image fidelity depends on how well the *uv*-plane is sampled. As a single baseline results in two opposing points in the *uv*-plane, increasing the number of independent baselines increases *uv*-plane coverage. This is the motivation behind aperture-synthesis arrays. With N elements, an array will have N(N-1)/2 independent baselines and hence visibilities. With a sufficient number of elements, a simple snapshot image can recover a crude approximation to the sky brightness distribution. Otherwise, the rotation of the Earth can help to augment the visibilities – as the Earth rotates, the projection of each baseline changes, tracing out a continuous arc in the *uv*-plane. This increases the number of Fourier components measured, resulting in better sampling of the *uv*-plane. This is known as Earth rotation synthesis. An important caveat is that Earth rotation synthesis assumes the fluxes of sources in the image are not changing over the duration of the observation. Regardless, incomplete sampling of the *uv*-plane must be accounted for, and will be discussed in Section 3.2.3.

3.2.2 Calibration

As with most telescopes, calibration is required to remove instrumental and atmospheric signatures from the source measurements. For radio interferometry observations, over the course of any observation, flux, bandpass (the frequency response across the observing band), phase and polarisation calibration sources may be observed. The choice of a flux and bandpass calibrator is motivated by the need for a source that is stable with time, has a well-known flux and is unresolved (or has a well-defined source model) at the observing frequency. The flux and bandpass calibrators are generally observed once at the beginning or end of the observations. They are required to characterise what instrument response corresponds to what flux density on the sky. While the phase calibrator does not need to have a stable flux, it must be constant in position and unresolved (or has a good model). The phase calibrator must be observed frequently over the course of the observation for interpolation of the antenna complex gains and on timescales shorter than variation timescales of the atmosphere. Consequently, the ideal phase calibrator should be close to the source on the plane of the sky to ensure that the atmospheric conditions are similar, and to minimise telescope slew times, maximising time on source. Polarisation measurements are not part of this thesis and thus we will not discuss polarisation calibrators.

During the calibration process, for each calibration and target source, corrupted data must be excised. The compromised data may be a result of poor weather, instrumental failures or terrestrial radio frequency interference (RFI). It is important to remove these contaminants as they degrade the signal-to-noise and cause calibration issues. Specially-designed software, such as the MIRIAD (Sault et al., 1995) and Common Astronomy Software Application (CASA; McMullin et al., 2007) packages, can be used to automatically or manually identify and remove (flag) these bad data.

3.2.3 Synthesis imaging and deconvolution

The final stages of radio data reduction centre around imaging. Once the data have been calibrated, the visibilities are inverse Fourier transformed to re-create the sky brightness. However, as the *uv*-plane is not completely sampled, the resulting image is patchy, as information is missing. This 'dirty image', so-called as its point-spread function (PSF), the Fourier transform of the *uv*-plane sampling function, is known as the 'dirty beam', can be corrected for because the *uv*-plane distribution is known. We need to deconvolve the dirty beam from the true sky brightness distribution. This is accomplished using a process developed by Högbom (1974), called CLEAN. If a bright point source dominates the field, then

it is removed by subtracting a dirty beam at the same position multiplied by the peak amplitude of the source and what is known as the "loop break" (often ~ 0.1). This process is repeated until the source peak drops below a specified threshold (usually $\approx 3-5$ times the noise level). This not only removes the source, but also the strong sidelobes (ring-like structures in the image) associated with the source. Dimmer sources, that were obscured by the sidelobes, may now appear. If more sources do appear, the process is repeated until all sources have been removed from the image. Finally, the removed sources are returned, however, they are replicated by idealised PSFs without any of the sidelobes associated with the dirty beam. This is known as the clean beam. A adaptation of this algorithm, known as "multi-scale" CLEAN (Cornwell, 2008), is used for extended sources, where successive peaks are removed from the image, once again using the dirty beam. However, rather than subtracting off the PSF of a delta function (which can produce imaging errors when used for extended sources), the PSF of an elliptical Gaussian of finite size is used.

The final image, reconstructed with the clean beam, is ready for scientific purposes. While additional reduction steps, such as self-calibration, are often used, this thesis did not rely on such techniques as our targets were too faint and thus will not be covered.

3.3 Optical

Finally, we review the data reduction techniques of our optical studies. Once again, we used telescopes best suited to study the optical counterparts of ULXs. In the optical band, we study both point-like and extended emission. To perform the photometric and imaging science required for this work, we used large telescopes with high spatial resolution and sensitivity. ULXs reside in external galaxies with crowded stellar fields and have relatively faint ($\gtrsim$ 23 mag) companion stars. Consequently, we rely on the high spatial resolution and sensitivity of the space-based *Hubble Space Telescope (HST)* to conduct photometry and imaging. Spectroscopic work on the extended bubbles surrounding ULXs is performed with ground-based facilities like the Very Large Telescope (VLT) and the Large Binocular Telescope (LBT). These observatories have the spectral resolution required to identify the motion of the ionised gas, providing key physical information about the outflows of the host ULX. In this section we outline the basics of optical CCD data reduction techniques for producing imaging, photometric and spectroscopic data, as detailed in Howell (2006).

3.3.1 Data reduction

As with data at other wavelengths, optical data can be downloaded from public archives (e.g., the ESO Science Archive Facility[4] or Hubble Legacy Archive[5]). These raw data contain both source information and instrumental signatures that must be removed. Several calibration frames must be created and applied to the raw source frames before any science can be done.

Firstly, bias frames are created to estimate the underlying noise levels of each data frame. They indicate the base charge level that is always present on the CCD and thus must be subtracted from the data frame. Bias frames are obtained from zero-second exposures with the shutter closed so that no light reaches the detector. For a true statistical representation of the bias, multiple bias frames are taken and the average is used for calibration.

Similar to bias frames, dark frames are taken with the shutter closed but for a non-zero exposure, generally of similar length as the source frame. Dark frames estimate the dark current; the thermal noise of the CCD. They are also used to identify "hot" or bad pixels. To reduce the effects of dark currents, current telescopes with CCD detectors cool instruments to the point where the need for dark frames can generally be ignored.

Finally, flat field frames correct for sensitivity variations across the CCD. They require the detector to be uniformly illuminated, either by observing the inside of the dome (domeflats) or a blank patch of sky (skyflats). Once again, multiple flat field exposures should be taken and averaged before being used for calibration.

The bias/dark frames are additive effects and are thus first subtracted from the source frame. Next, to correct for the sensitivity variations, which are multiplicative effects, the bias-subtracted source frame is divided by the averaged flat field exposure. The final result is a science frame that is free of instrumental signatures and is ready for photometric or spectroscopic analyses.

3.3.2 Photometry

Photometry is the process of measuring the flux of an astronomical source, a logarithmic scale where source intensity is given in units of magnitudes (mag). In its most simplest case, photometry is relative; the magnitude of a standard star, m_2, defines the magnitude of the target star, m_1, according to

$$m_1 - m_2 = -2.5 \log \frac{F_1}{F_2}, \tag{3.5}$$

[4]http://archive.eso.org/cms.html
[5]https://hla.stsci.edu/

where F_1 and F_2 are the fluxes of the target and standard stars, respectively. In order to determine absolute photometric measurements, we must first account for instrumental effects. This is accomplished using what are known as photometric zero points, ZP; a magnitude equivalent to a hypothetical source that produces one photon/electron/count per second. The zero points for each instrument/filter are provided by the telescope[6]. We normalise for the instrument response using

$$m_{app} = -2.5 \log F - ZP, \tag{3.6}$$

where m_{app} is the apparent magnitude of the source. The source flux is measured by defining a (typically) circular region and extracting the number of counts within that region. The source region is determined either from a pre-defined aperture (known as aperture photometry) or through taking the average of several PSFs of nearby, bright, unsaturated and isolated reference stars (known as PSF photometry). The brightness of dimmer stars (where the signal-to-noise is lower) or stars in crowded fields (where source confusion is an issue) can be measured more accurately with PSF photometry, however, it is a more laborious procedure. Regardless of which approach is used, a background flux must also be determined. This is usually calculated using an annulus around the target source with area a few times larger. The background-subtracted flux is then applied to Equation (3.6) to find the apparent magnitude. This tells us how bright the source appears for an observer on Earth (albeit for an observer at the top of the atmosphere).

The next step is to determine the absolute magnitude, m_{abs}, or intrinsic brightness of the source. This is calculated by correcting for distance effects using

$$m_{app} - m_{abs} = 5 \log \frac{d}{10}, \tag{3.7}$$

where d is the distance to the source in parsecs. Finally, the absolute magnitude can be de-reddened to correct for any line-of-sight or local extinction due to intervening gas and dust. This gives the true intrinsic intensity of the source.

3.3.3 Spectroscopy

Spectroscopy is the study of dispersed light used to identify fine spectral details in the emitted energy distribution of a source. High spectral resolution is required to distinguish narrow atomic transition features (emission and absorption lines) from the continuum and hence determine physical characteristics of the source. Most modern optical spectrographs use gratings to split the incoming

[6] e.g., the *HST* zero points are found at http://www.stsci.edu/hst/acs/analysis/zeropoints/old_page/localZeropoints

radiation into wavelength bins of the order 0.1–10 Å with bandwidths of order 1000–2000 Å. The telescope focuses the incident light onto a narrow entrance slit. Some spectrographs, like instruments on the LBT (which is used in this thesis), have double spectrographs, which use a beam splitter to divide the light onto a red and blue slit. The angle of the spectrograph slit is important as it can introduce dispersion effects due to the atmosphere. Differential refraction is the change in the angle of refraction of an incident photon due to the atmosphere. If the slit is not placed parallel to the direction of the dispersion, flux can fall outside of the slit and hence is lost. The degree to which the light is dispersed will also depend on the wavelength. Aligning the slit with the angle of the dispersion or using a device that compensates for atmospheric dispersion (known as an Atmospheric Dispersion Corrector) will solve this issue.

Like with imaging and photometry, bias and flat field calibration is required for CCD spectroscopy data reduction, though additional steps are also needed. Following bias and flat field corrections, for spectroscopy of a point-source, the next step is to extract the spectrum and collapse it down to a 1-D image in terms of pixel position. This source spectrum is then calibrated against spectra of hollow cathode lamps taken during the observations. These cathode lamp spectra have emission lines with known wavelengths and thus are used to scale the source spectrum, converting it from pixel space to wavelength space, known as 'determining the wavelength solution'. The source spectrum is next corrected for atmospheric extinction. Finally, using spectra of standard stars, also taken during the observation, the pixel count values of the source spectrum are scaled to absolute flux values. The resulting final spectrum is ready for analysis.

For extended sources, such as ULX bubbles that are resolved, long-slit spectroscopy is used. While there is no fundamental difference in the data reduction techniques, additional measures must be taken as some of the source emission will fall outside of the slit. While emission line ratios will not be affected, the absolute flux will be underestimated. One method to correct for this, which I employ in the thesis (Chapter 6), is to supplement the spectroscopic data with narrow-band imaging data. This will provide the true flux of the source, to which the spectrum can be scaled. The addition of narrow-band imaging will also provide spatial information that the slit will miss.

3.4 Astrometry corrections

This thesis exploits data from numerous telescopes across the electromagnetic spectrum. The differing positional accuracies of these telescopes results in the need for astrometric corrections. Slight shifts can even be introduced between

observations by the same telescope. Because many of the instruments used have sub-arcsecond precision, and the fact that ULXs reside in external galaxies with crowded fields, images must be aligned in order to identify counterparts at multiple wavelengths.

The most accurate astrometric frame, the International Celestial Reference Frame (ICRF), was created using VLBI position measurements of 212 compact radio galaxies and has an angular precision of 250 μas (Johnston and de Vegt, 1999)[7]. Ideally, images from all other bands would be aligned to the ICRF. However, this is not always possible as there may not be sufficient suitable point-like X-ray/radio or optical/radio associations within a given field of view. The next best option is to align all images to the *Gaia* DR2 astrometric frames, which are accurate to better than ≈ 0.7 mas (Lindegren et al., 2018), or the Two Micron All-Sky Survey (2MASS) astrometric frames, with an angular precision of 0.3 arcseconds (Skrutskie et al., 2006). Once again, a lack of suitable associations may make this unviable in some cases (e.g., when dealing with small fields of view). For some purposes, like identifying the companion stars of ULXs, relative astrometry will suffice. If enough common point-like source can be identified in both bands, then the images can be aligned, though their absolute astrometry will remain uncertain. Finally, if no, or too few, multi-band associations are available, we rely on the absolute *Chandra*/ACIS-S or ACIS-I astrometry, which is within $\approx 0''.70$ and $\approx 0''.75$, respectively, for 90% of observations.

[7] The updated version, ICRF2, which uses the positions of 295 quasars, has an angular precision of 40 μas (Fey et al., 2015)

Chapter 4

Ultraluminous supersoft sources

This chapter is adapted from:

R. Urquhart and R. Soria. 2016. "Optically thick outflows in ultraluminous supersoft sources", *Monthly Notices of the Royal Astronomical Society*, Volume 456, Issue 2, p.1859-1880, DOI:10.1093/mnras/stv2293

For this chapter, my supervisor R. Soria performed X-ray spectral fitting for the Chandra observations of M 101 ULX-1. I conducted all remaining work under the guidance of my supervisory panel.

In this chapter we reanalyse a large sample of *Chandra* and *XMM-Newton* observations of seven previously-known ULSs in nearby galaxies. We discuss some of their X-ray colour, spectral and timing properties in an attempt to determine whether they form a single physical class of sources, and identify their nature. We compare the physical properties of this population of sources with those of broad-band ULXs and accreting white dwarfs. Finally, we propose a model based on mass accretion rate and viewing angle that relates ULSs to ULXs, and draw attention to select sources that appear to transition between the two classes.

As previously stated, the interpretation of ULSs is still heavily debated. The soft, thermal emission of ULSs is often interpreted as the signature of a large, cool accretion disk around a much more massive black hole. This would suggest that ULSs are IMBHs in a standard high/soft state (Kong et al., 2004). If the fitted radius comes from the innermost stable circular orbit of an accretion disk, the mass of the central object is $\sim 10^3$–$10^4\,M_\odot$. One problem with the IMBH interpretation is that such massive accretors are not expected to be in their high/soft state at the luminosities inferred for ULSs. For example, an IMBH with a mass of $10^3\,M_\odot$ has an Eddington luminosity, from Equation (1.5), of

$L_{\rm Edd} \approx 1.3 \times 10^{41}\,{\rm erg\ s^{-1}}$. This means that a standard ULS, with a luminosity of $\sim 10^{39}\,{\rm erg\ s^{-1}}$, would be accreting at $\lesssim 1\%$ of its Eddington limit. Standard black hole binaries transition into the high/soft state at $\gtrsim 2\%$ Eddington (Maccarone, 2003; Kalemci et al., 2013). Therefore, an IMBH would likely not be in the high/soft state and hence would not produce the soft spectrum observed in ULSs.

Another problem with the IMBH interpretation has recently arisen due to the discovery of a baryonic jet in the ULS system in M 81 (Liu et al., 2015). Jets in Galactic black hole binaries occur in the low/hard state (compact; a steady continuous jet) or at the transition from the low/hard state into the high/soft state (transient; a jet made up of discrete ejecta) (Fender et al., 2004). We do not expect to see a jet in the purely soft state that an IMBH would need to be in to satisfy the physical characteristics of ULSs.

Another interpretation proposed is that ULSs may be the extreme end of the 'classical' supersoft source (SSS) class, first discovered in the Large Magellanic Cloud (Long et al., 1981). Classical SSSs are likely powered by surface-nuclear-burning on white dwarf accretors (van den Heuvel et al., 1992). A problem with this interpretation is that ULSs exceed the Eddington limit ($\approx 2 \times 10^{38}\,{\rm erg\ s^{-1}}$) of a $1.35\,{\rm M_\odot}$ white dwarf by up to two orders of magnitude. Another possible problem is the discrepancy between typical white dwarf radii and the larger characteristic blackbody radii fitted to ULS spectra. This may be alleviated if the white dwarf produces an expanding photosphere or optically thick outflow. Ultimately though, it appears unlikely that most ULSs could be powered by white dwarfs.

In the end, the hyper-critically accreting stellar-mass black hole scenario is found to be the most likely interpretation of ULSs. If this interpretation is correct, and ULSs are indeed a subclass of ULXs, then it may also explain an intriguing property of the ULX population. The ULX luminosity distribution shows an exponential cut-off at X-ray luminosities $\gtrsim 2 \times 10^{40}\,{\rm erg\ s^{-1}}$ (Swartz et al., 2011; Mineo et al., 2012). This can be explained either as an effect of the upper limit to the mass of stellar black holes (likely maximum mass $\approx 80\,{\rm M_\odot}$: Belczynski et al., 2010), and/or a scarcity of donor stars able to supply such high accretion rates ($\dot{M} \gtrsim 3 \times 10^{-6}\,{\rm M_\odot\,yr^{-1}}$) and short duration of those phases. However, it may also be a result of dense winds and the appearance of a photosphere at the highest accretion rates. Above a threshold accretion rate corresponding (for an unobscured ULX) to $L_{\rm X} \approx 2 \times 10^{40}$ erg s^{-1}, more and more sources appear shrouded in the thick outflow. That obviously decreases their X-ray luminosity dramatically, removing them from the high-end of the luminosity function. It also slightly decreases their bolometric luminosity, because a significant fraction of the initial radiative power output is used to launch the outflow. As a very preliminary

investigation of this issue, the number of "missing" ULXs above $\approx 5 \times 10^{40}$ erg s^{-1} (number of ULXs expected for an unbroken power-law luminosity function minus those observed in reality) for example in the Swartz et al. (2011) study is consistent with the number of ULSs found in the same sample of galaxies.

In this chapter, we present the X-ray spectral and timing properties of seven ULSs. We evaluate the different ULS interpretations based on the observational properties of our sample and discuss how ULSs likely fit into the overall population of compact accreting sources.

4.1 Target Selection

4.1.1 Definition of ULS

To provide a more quantitative definition of ULSs for our study, we introduce a classification similar (but not identical) to the one adopted by Di Stefano and Kong (2003). We define three X-ray energy bands: 0.3–1.1 keV (S), 1.1–2.5 keV (M) and 2.5–7 keV (H). We measure the net count rates in the three bands and in the total 0.3–7 keV band (T). We consider "supersoft" all those sources that have a hardness ratio $(M - S)/T \lesssim -0.8$, and "ultraluminous" supersoft sources those that have reached an extrapolated bolometric luminosity of the thermal component $L_{bol}^{bb} \gtrsim 10^{39}$ erg s^{-1} in at least one observation, during which time they also had $(M - S)/T \lesssim -0.8$.

We only consider sources observed with *Chandra* and *XMM-Newton*, because they cover a similar energy range and provide roughly similar hardness ratios. We stress that the hardness ratio condition is a purely empirical criterion for a practical target selection. There are small differences between the colours determined from *Chandra* and *XMM-Newton*, as well as between *Chandra* observations taken in different years, because of the sensitivity degradation at soft energies. Also, extrapolating the blackbody spectrum to the UV gives only a crude estimate of the true bolometric luminosity. At the same time, the characteristic appearance of those sources (their soft thermal spectrum) makes them sufficiently distinct from ordinary XRBs and ULXs, regardless of small changes in the choice of empirical definition, and suggests that they do belong to a physically different class or accretion state. One of the objectives of this chapter is to quantify the common properties of such sources, so that we can then move from a purely empirical to a more physical identification.

We illustrate our selection criterion in Figure 4.1, for three different values of absorbing column density ($n_H = 3 \times 10^{20}$ cm^{-2}, $n_H = 10^{21}$ cm^{-2} and $n_H = 3 \times 10^{21}$ cm^{-2}) broadly representative of the range empirically found in our sample (Sec-

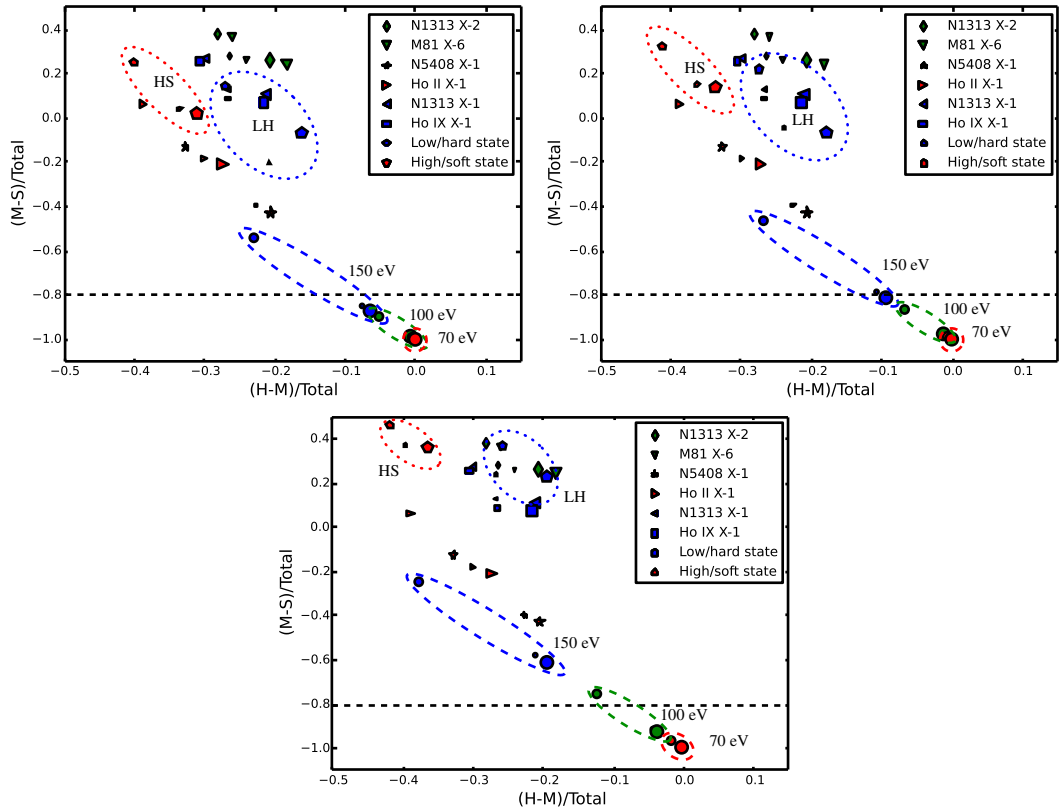

Figure 4.1: Top left panel: X-ray colours expected for five different spectral models, when observed through a column density $n_{\rm H} = 3 \times 10^{20}$ cm^{-2}, by three different detectors: ACIS-S in 2001 (smallest-size symbols), ACIS-S in 2014 (medium-size symbols) and EPIC-pn in 2014 (largest-size symbols). The models are: LH = low/hard state = power-law with $\Gamma = 1.7$ (blue pentagons); HS=high/soft state = disk-blackbody with $kT_{\rm in} = 1$ keV (red pentagons); and pure blackbodies at 70 eV, 100 eV and 150 eV (red, green and blue circles, respectively). Finally, we overplotted the colours expected through the same three detectors for six ULX spectral models, from Sutton et al. (2013b). The dashed and or dotted regions are simply visual aids to help locating the different models. The dashed horizontal line is an empirical colour threshold for thermal sources at $kT_{\rm bb} \lesssim 100$ eV. Top right panel: as in the top left panel, but for $n_{\rm H} = 10^{21}$ cm^{-2}. Bottom panel: as in the top panels, but for $n_{\rm H} = 3 \times 10^{21}$ cm^{-2}.

tion 4.3.1). For each value of $n_{\rm H}$ we plotted the "observable" X-ray colours of two simple spectral models representative of accreting black holes (Remillard and McClintock, 2006): a power-law spectrum with photon index $\Gamma = 1.7$ (low/hard state), and a disk-blackbody with peak temperature $kT_{\rm in} = 1$ keV (high/soft state). By "observable", we mean the colours that such model spectra would have if they had been observed by *Chandra*/ACIS-S in 2001, or by *Chandra*/ACIS-S in 2014, or by *XMM-Newton*/EPIC-pn (the colour evolution of this detector over the years is negligible). Then, in each of the three panels, we added the observable colours of three pure blackbody models which may be more representative of ULSs: one at $kT_{\rm bb} = 70$ eV, one at $kT_{\rm bb} = 100$ eV, and one at $kT_{\rm bb} = 150$ eV. The empirical hardness criterion $(\mathrm{M}-\mathrm{S})/\mathrm{T} < -0.8$ clearly separates 70 eV and 100 eV blackbody sources from the low/hard state and high/soft state colours, for all three values of $n_{\rm H}$; for $n_{\rm H} \lesssim 10^{21}$ cm^{-2}, 150 eV blackbody emitters also satisfy $(\mathrm{M}-\mathrm{S})/\mathrm{T} < -0.8$ at least for early *Chandra* observations (no longer today). Finally, in all three plots we added the observable colours of six real ULX spectra, modelled by Sutton et al. (2013b): two in the broadened-disk regime (*XMM-Newton* observations ObsID 0405090101 of NGC 1313 X-2 and ObsID 0200980101 of M 81 X-6), two in the soft-ultraluminous regime (ObsID 0200470101 of Holmberg II X-1 and ObsID 0653380301 of NGC 5408 X-1) and two in the hard-ultraluminous regime (ObsID 0200980101 of Holmberg IX X-1 and ObsID 0405090101 of NGC 1313 X-1). Each of those six ULXs has only one value of $n_{\rm H}$ (the actual value determined from that particular observation, fitted by Sutton et al. 2013b) but is plotted three times, to represent the "equivalent" colours such a source would have in *Chandra*/ACIS-S 2001, *Chandra*/ACIS-S 2014, and *XMM-Newton*/EPIC-pn. The message to take home from Figure 4.1 is that the observed colours of standard ULXs are somewhat intermediate between those expected for black holes in the low/hard and high/soft states, but are clearly well above the threshold defined by $(\mathrm{M}-\mathrm{S})/\mathrm{T} \approx -0.8$; conversely, sources observed below that threshold are clearly not in the low/hard or high/soft state, do not overlap with standard ULXs, and are likely to be blackbody emitters at $kT_{\rm bb} \lesssim 100$ eV. It can be also noted from Figure 4.1 that some soft thermal sources observed with *Chandra*/ACIS-S today (as opposed to a decade ago) would not appear supersoft, based on their X-ray colours alone. The reason is of course the loss of sensitivity of the detector at low energies, which means that the tail of the blackbody emission in the 1.1–2.5 keV band now represents a larger *relative* fraction of the total detected count rate (which has decreased by a factor of 3). Finally, we do not plot the expected colours for $n_{\rm H} > 3 \times 10^{21}$ cm^{-2} because at such column densities it becomes increasingly difficult to identify supersoft sources, so it is no longer relevant to our selection criterion.

In any classification based purely on X-ray hardness and colours (as discussed in Di Stefano and Kong 2003), the supersoft group of sources is likely to contain a mix of different physical objects, in particular nuclear-burning white dwarfs as well as fading supernova remnants. Indeed, a deep X-ray study of the spiral galaxy M 83 has shown (Long et al., 2014) two types of supersoft spectra, one dominated by optically thick thermal emission and the other by an optically thin thermal plasma. However, for this work we are considering only sources that have reached $L_{\rm bol}^{\rm bb} \gtrsim 10^{39}$ erg s^{-1}, which screens out thermal supernova remnants (typically fainter than about 10^{37} erg s^{-1}). We used the extrapolated bolometric luminosity as a selection criterion, rather than the X-ray luminosity, because most of the emission falls below the sensitivity band of *Chandra* and *XMM-Newton*.

4.1.2 Definition of our target sample

We analysed a sample of sources that were unequivocally identified in the literature as very luminous and unusually soft, and we checked whether such sources satisfied our selection criterion defined in Section 4.1.1. We also examined the sample of ULXs from the catalogues of Swartz et al. (2011) and Swartz et al. (2004), looking for any other unrecognised ULS candidates. We limited our search to sources that had enough counts for at least a rough spectral fitting ($\gtrsim$50 net counts, using Cash statistics) in at least one epoch, in order to have a meaningful estimate of temperature and bolometric luminosity. For this pilot study, we did not intend to define a statistically complete sample or analyse every single archival X-ray observation of each target source; however, our sample is large enough that we can draw general conclusions on the nature of ULSs as a possibly distinct population.

We selected the following seven targets, summarised below with the traditional nomenclature more often found in the literature (see also Table 4.1.2):

(i) CXOAnt J120151.6-185231.9. Located in the Antennae Galaxies, it has been observed by *Chandra* multiple times. In 2002 it had a best-fit blackbody temperature of $\approx$ 90 eV; the observed 0.1–2 keV luminosity increased from $\approx 2 \times 10^{38}$ erg s^{-1} in December 1999 to $\approx 1 \times 10^{39}$ erg s^{-1} in May 2002 (Fabbiano et al., 2003). Corrected for absorption, the bright state equates to an intrinsic blackbody-fitted bolometric luminosity of $\approx 2 \times 10^{40}$ erg s^{-1} (Fabbiano et al., 2003, scaled to the different distance adopted in this chapter).

(ii) NGC 4631 X1. The source was first detected in *ROSAT/PSPC* observations taken from 1991 December 15 to 1992 January 4 (Vogler and Pietsch, 1996). Carpano et al. (2007) observed it in 2002 June using *XMM-Newton* and

found a best-fitting blackbody temperature $\approx 67\,\mathrm{eV}$ and bolometric luminosity of $\approx 3.2 \times 10^{40}\,\mathrm{erg\ s^{-1}}$. The source also appeared to have an ≈4 hour modulation (Carpano et al., 2007). Soria and Ghosh (2009) re-examined the same *XMM-Newton* data and found that when an absorption edge ($kT_{\mathrm{edge}} \approx 1.0\,\mathrm{keV}$) was added to the model, the fit significantly improved, with a blackbody temperature of $\approx 90\,\mathrm{eV}$ and intrinsic bolometric luminosity of $\approx 4 \times 10^{39}\,\mathrm{erg\ s^{-1}}$.

(iii) NGC 247 ULX. Observed in 2009 with *XMM-Newton*, NGC 247 ULX has a dominant thermal component with temperature of $\approx 100\,\mathrm{eV}$ along with a harder component, modelled as a power-law tail by Jin et al. (2011). Based on its X-ray spectral appearance, it has been interpreted as a candidate IMBH with a suggested black hole mass of $\approx 600\,\mathrm{M_\odot}$ (Tao et al., 2012a).

(iv) NGC 300 SSS1. Originally found in a *ROSAT* observation from 1992 (Read and Pietsch, 2001), this source exhibits bright and dim states. For example, it was not seen by *ROSAT* in later observations but was seen by *XMM-Newton* in a bright state in 2000 December and became an order of magnitude dimmer in another *XMM-Newton* observation only 6 days later . During its bright state, it appeared to have a temperature of $\approx 60\,\mathrm{eV}$ and a bolometric luminosity of a few times $10^{39}\,\mathrm{erg\ s^{-1}}$.

(v) M 81 N1. One of the best known ULSs, M 81 N1 was observed by *ROSAT* several times in the 1990s, by *Chandra* in a long observation in 2000 May (Swartz et al., 2002) and again in a series of shorter *Chandra* observations over 2005–2008 (Liu and Di Stefano, 2008; Liu, 2008). In the 2000 May observation it was fitted with a blackbody model and had a temperature of $\approx 70\,\mathrm{eV}$ and bolometric luminosity of $\approx 2.5 \times 10^{39}\,\mathrm{erg\ s^{-1}}$. The source shows significant flux variability within individual observations as well as between observations (Swartz et al., 2002).

(vi) M 101 ULX-1. Observed more than 20 times by *Chandra* between 2000 and 2005, it has short- and long-term flux and spectral variability, with fitted blackbody temperatures ranging between ≈ 50–150 eV (Kong et al., 2004; Mukai et al., 2005; Kong and Di Stefano, 2005). The interpretation of this source has been actively debated in recent years. A Wolf-Rayet companion was identified from *HST* observations by Liu (2009). A claimed period of 8.2 days led to the suggestion that this ULS is powered by a stellar-mass black hole (Liu et al., 2013).

(vii) CXOM51 J132943.3+471135. Located in M 51, this is source 12 in the catalogue of Di Stefano and Kong (2003), and source 9 in that of Terashima and Wilson (2004). Observed in two *Chandra* observations, the source is best-fit with a blackbody model with temperatures ranging from $\approx 80 - 120\,\mathrm{eV}$. It appears to drop in flux by 50% between the two observations, becoming slightly harder in

the process (Di Stefano and Kong, 2003).

As is the case with any purely empirical selection criterion, there may be a few other supersoft sources that just missed out on our ULS selection (reaching a maximum $L_{\rm bol}^{\rm bb}$ just below 10^{39} erg s^{-1}) but are still more luminous than expected for a nuclear-burning white dwarf. We found two of them:

(i) NGC 300 SSS2. It was not seen by *ROSAT* in the 1990s or *XMM-Newton* in 2000–2001, but was discovered in 2005 with *XMM-Newton* (Carpano et al., 2006). We processed and analysed both *XMM-Newton* observations from 2005 (ObsID 0305860401 and 0305860301), and fitted the source spectrum with blackbody models. We found a blackbody temperature of ≈ 50 eV and a bolometric luminosity of $\approx 7 \times 10^{38}$ erg s^{-1} in the first observation and $\approx 6 \times 10^{38}$ erg s^{-1} in the second one, taken six months later.

(ii) r2-12. An SSS in M31 that has reached a bolometric luminosity up to $\approx 8 \times 10^{38}$erg s^{-1} (Trudolyubov and Priedhorsky, 2008; Orio et al., 2010; Chiosi et al., 2014). It was first observed with *Einstein* (Trinchieri and Fabbiano, 1991) and later with *Chandra* (Kong et al., 2002) and *XMM-Newton* (Pietsch et al., 2005).

Although we shall not present a detailed study of those two sources in this chapter, we have included them in some of our plots to highlight their intermediate physical properties between ULSs and classical SSSs. We used our own spectral analysis to obtain temperatures, radii and luminosities of NGC 300 SSS2, and we used the fit results of Trudolyubov and Priedhorsky (2008) for r2-12.

Table 4.1: List of *Chandra* and *XMM-Newton* observations used in our sample study of seven ULSs. Numbered epochs (column 1) designate observations for which we fitted a spectrum; in a few cases, numbers are repeated because a single spectrum was fitted to a stack of observations in the same state. Non-numbered epochs designate observations with too few counts for spectral analysis but still used for our X-ray colour-colour plot.

Epoch No.	Galaxy	Distance (Mpc)	Source RA	Source Dec	Telescope	Obs ID	Exp Time (ks)	Date
1	NGC 4038/39	22.3 ± 2.8^a	12:01:51.62	-18:52:31.87	*Chandra*	315	72.24	1999-12-01
2						3040	69.04	2001-12-29
3						3041	72.91	2002-11-22
4						3042	67.28	2002-05-31
5						3043	67.10	2002-04-18
6						3044	36.50	2002-07-10
7						3718	34.72	2002-07-13
8	NGC 4631	7.4 ± 0.2^b	12:42:15.96	+32:32:49.4	*XMM-Newton*	0110900201	53.76	2002-06-28
9	NGC 247	3.4 ± 0.1^c	00:47:03.90	-20:47:43.8	*Chandra*	12437	4.99	2011-02-01
10						17547	5.01	2014-11-12
11	NGC 300	1.9 ± 0.1^d	00:55:10.7	-37:38:55.0	*XMM-Newton*	0112800201	34.05	2000-12-26
12						0112800101	43.80	2001-01-01
13					*Chandra*	9883	10.07	2008-07-08
14	M 81	3.6 ± 0.2^e	09:55:42.15	69:03:36.2	*Chandra*	390	2.38	2000-03-21

Table 4.1: *continued*

Epoch No.	Galaxy	Distance (Mpc)	Source RA	Source Dec	Telescope	Obs ID	Exp Time (ks)	Date
15						735	50.02	2000-05-07
16						5938	11.81	2005-06-03
						5936	11.41	2005-05-28
						5937	12.01	2005-06-01
17						5939	11.81	2005-06-06
18						5940	11.97	2005-06-09
19						5941	11.81	2005-06-11
20						5942	11.95	2005-06-15
21						5943	12.01	2005-06-18
22						5944	11.81	2005-06-21
23						5945	11.58	2005-06-24
24						5946	12.02	2005-06-26
25						5947	10.70	2005-06-29
26						5948	12.03	2005-07-03
27						5949	12.02	2005-07-06
28						9805	5.11	2007-12-21
29						9122	9.91	2008-02-01
30	M 101	6.4 ± 0.5^{f}	14:03:32.37	+54:21:02.75	*Chandra*	934	98.38	2000-03-26

Table 4.1: *continued*

Epoch No.	Galaxy	Distance (Mpc)	Source RA	Source Dec	Telescope	Obs ID	Exp Time (ks)	Date
31						2065	9.63	2000-10-29
32						5337	9.94	2004-07-05
32						5338	28.57	2004-07-06
32						5339	14.32	2004-07-07
32						5340	54.42	2004-07-08
32						4734	35.48	2004-07-11
33						6170	47.95	2004-12-22
33						6175	40.66	2004-12-24
34						6169	29.38	2004-12-30
35						4737	21.81	2005-01-01
						4731	56.24	2004-01-19
						5297	21.69	2004-01-29
						5300	52.09	2004-03-07
						5309	70.77	2004-03-14
						4732	69.79	2004-03-19
						6114	66.20	2004-09-05
						6115	35.76	2004-09-08
						4735	28.78	2004-09-12

Table 4.1: *continued*

Epoch No.	Galaxy	Distance (Mpc)	Source RA	Source Dec	Telescope	Obs ID	Exp Time (ks)	Date
						4736	77.35	2004-11-01
36					*XMM-Newton*	0212480201	32.41	2005-01-08
37	M 51	8.0 ± 0.6^{g}	13:29:43.30	+47:11:34.7	*Chandra*	354	14.86	2000-03-21
38						1622	26.81	2001-06-23
39						3932	47.97	2003-08-07
40						13813	179.20	2012-09-09
41						13812	157.46	2012-09-12
42						15496	40.97	2012-09-19
43						13814	189.85	2012-09-20
44						13815	67.18	2012-09-23
						13816	73.10	2012-09-26
						15553	37.57	2012-10-10

Notes: [a] Schweizer et al. (2008); [b] Radburn-Smith et al. (2011); [c] Gieren et al. (2009); [d] Rizzi et al. (2006); [e] Gerke et al. (2011); [f] Shappee and Stanek (2011); [g] Bose and Kumar (2014)

4.2 Data Analysis

We selected a representative sample of *Chandra* and *XMM-Newton* observations of the seven known ULSs (Table 4.1.2). We considered only observations in which the sources had enough counts for a meaningful colour ($\gtrsim$20 net counts) or at least a rough spectral analysis ($\gtrsim$50 net counts). We do not analyse and discuss in this chapter the observations in which the same sources were not detected or were just at the detection limit, the fraction of time in which each source was detectable over the course of all its observations or the reason for this on/off behaviour.

For the *Chandra* observations, we downloaded the data from the public archives and re-processed them with standard tasks in the Chandra Interactive Analysis of Observations (CIAO) Version 4.7 data analysis system (Fruscione et al., 2006). We filtered out exposure intervals with high particle background. We defined circular source extraction regions with 2" radii. We extracted the local background from suitably selected nearby regions at least three times as large as the source region. We used the CIAO task *specextract* to extract a spectrum (with its associated background, response and ancillary response files) from each observation. Spectra with $\gtrsim$200 counts were grouped to a minimum of 15 counts per bin so that χ^2 statistics could be used. Spectra with fewer counts were left unbinned and fitted with W statistics. We used *dmextract* to build background-subtracted light curves.

We downloaded the *XMM-Newton* data from NASA's HEASARC archive. We processed the EPIC observation data files with the Science Analysis System (SAS) version 14.0.0 (`xmmsas_20141104_1833`). As with the *Chandra* data, we filtered out exposure intervals with high particle backgrounds. We defined circular source extraction regions with 20" radii whenever possible, and rectangular regions (of approximately equivalent area) on a couple of occasions when the source was located near a chip gap. We extracted the background from nearby regions at least three times as large, not including any other bright sources or chip gaps, and located at similar distances from readout nodes. We selected single and double events (pattern 0–4 for the pn camera and pattern 0–12 for MOS1 and MOS2 cameras), with the standard flagging criteria `#XMMEA_EP` and `#XMMEA_EM` for pn and MOS, respectively, and `FLAG=0`. After building response and ancillary response files with the SAS tasks *rmfgen* and *arfgen*, we used *epicspeccombine* to create average EPIC spectra and response files for each source. Finally, we grouped the spectra to a minimum of 20 counts per bin, so that we could use Gaussian statistics. We built background-subtracted light curves using the SAS tasks *evselect* and *epiclccorr*.

We used XSPEC version 12.8.2 for spectral fitting (Arnaud, 1996). For timing analysis, we used standard FTOOLS tasks (Blackburn, 1995), such as *lcurve*, *powspec*, *efsearch* and *statistics*.

4.3 Main Results

4.3.1 X-ray spectral properties

For each source, and each observing epoch with at least ≈50 net counts, we fitted the background-subtracted spectrum, starting with one-component models: *phabs*phabs*bbody* and *phabs*phabs*diskbb*. The first photoelectric absorption component was fixed at the line-of-sight value for the relevant host galaxy; the second component was left free. From this initial level of fitting, two things are apparent: that a single thermal component is already the best fit for most epochs, and, to first order, a satisfactory fit for all epochs; and that for all epochs, blackbody and disk-blackbody models are statistically equivalent. The first statement is another way of saying that ULSs (by definition) are not dominated by a broad-band tail above 1 keV, unlike standard ULXs. The second statement is not surprising, considering that the peak temperature of the thermal component is ≈100 eV and the detectors are only sensitive to energies $\gtrsim$300 eV, in the Wien tail. A similar situation occurs when fitting the low-energy soft excess in ULXs. The only difference between the two models is in the definition of blackbody temperature $kT_{\rm bb}$ compared with the colour temperature of the disk $kT_{\rm in}$. For the same thermal spectrum, $kT_{\rm in}$ is always systematically higher than $kT_{\rm bb}$ by ≈20%.

In a few cases, our spectral fitting showed significant residuals in addition to the dominant soft thermal component, particularly around 0.7–2 keV (sometimes with a distinctive residual feature at ≈1 keV). It was necessary to add one or more spectral components to account for the harder emission. At this stage we make no specific assumptions on the physical nature of this harder component. The nature of the fit residuals suggests that the harder component could be optically-thin thermal plasma emission, which we modelled with *mekal*[1] in XSPEC. Spectral residuals in addition to the smooth continuum have been seen in some two-component ULXs (for example, NGC 5408 X-1 and NGC 6946 X-1) and were also successfully modelled with thermal plasma emission (Roberts and Colbert, 2003; Stobbart et al., 2006; Strohmayer et al., 2007; Middleton et al., 2014), with luminosities ∼ a few 10^{38} erg s^{-1}. However, an alternative interpretation was provided by Middleton et al. (2014), who showed that similar residuals

[1]Even at our best signal-to-noise level, there were no statistically significant differences between *mekal* and *apec* models.

are also consistent with broadened, blue-shifted absorption in the line of sight of a fast, partially ionised, optically-thin outflow. Our ULS spectra have a substantially lower signal-to-noise ratio than the spectra of NGC 5408 X-1 and NGC 6946 X-1 discussed by Middleton et al. (2014), making a test between those two alternative interpretations more difficult. For this chapter, we limit our spectral analysis to the thermal-plasma emission model.

In summary, when significant residuals were detected above the blackbody/disk-blackbody base model, we tried improving the fit with two methods: by adding one or two thermal plasma components at fixed solar abundance, with characteristic temperatures ≈0.6–0.9 keV; and by testing for the presence of an absorption edge at $kT_{\rm edge} \approx 1$ keV. We found significant (and variable) thermal-plasma contributions in the spectra of the M 101 ULS, in several epochs: they are discussed in more details in Section 4.3.2; see also (Soria and Kong, 2016). Thermal plasma emission is also seen in some of the epochs for the ULSs in NGC 247, the Antennae Galaxies and M 51. Adding an absorption edge provides significant improvements to some of the spectra with the high signal-to-noise in four out of seven sources: those in the Antennae, NGC 247, M 101 and NGC 4631. In some sources (most notably those in NGC 247 and M 101), the spectrum is best fitted with a blackbody (or disk-blackbody) plus thermal-plasma emission in some epochs, and blackbody (or disk-blackbody) plus an absorption edge in other epochs (Section 4.3.2).

We stress that the main objective of this chapter is to determine the properties of the dominant optically-thick thermal component and attempt a physical interpretation; nonetheless, careful treatment of additional first-order components (absorption edges, harder emission above 1 keV, and line residuals consistent with thermal-plasma) is necessary to make sure that the characteristic temperature and radius of the dominant blackbody component is not over- or under-estimated. After finding successful fits for all epochs (with or without additional components), we summarised the physical parameters of the blackbody components in Table 4.2; when a disk-blackbody replaces the blackbody component in the same spectra, we obtain the physical parameters listed in Table 4.3; the additional thermal-plasma and edge features and their significances are listed in Table 4.4.

The bolometric blackbody luminosity is defined as $L^{\rm bb}_{\rm bol} \equiv 4\pi r^2_{\rm bb}\sigma T^4_{\rm bb}$, independent of the viewing angle θ. It is obtained directly from one of the XSPEC *bbody* fit parameters, namely the normalisation constant, because $L^{\rm bb}_{\rm bol} = \sqrt{N_{\rm bb}}\, d_{\rm 10kpc}\, 10^{39}$ erg s^{-1}. The adopted galaxy distances are quoted in Table 4.1.2. The bolometric disk luminosity is defined as $L^{\rm diskbb}_{\rm bol} \equiv 4\pi r^2_{\rm in}\sigma T^4_{\rm in}$, where $r_{\rm in} = \sqrt{N_{\rm diskbb}}\, d_{\rm 10kpc}/\sqrt{\cos\theta}$ km and $N_{\rm diskbb}$ is the normalisation constant in XSPEC. Physically, the fit pa-

rameter $r_{\rm in}$ is related to the true inner-disk radius $R_{\rm in} = 1.19 r_{\rm in}$ (Kubota et al., 1998). We cannot obtain $L_{\rm bol}^{\rm diskbb}$ directly from our XSPEC *diskbb* fit parameters, because of its intrinsic dependence on $\cos\theta$; we can only obtain $L_{\rm bol}^{\rm diskbb} \times \cos\theta$, and $r_{\rm in}\sqrt{\cos\theta}$. As a double check on our bolometric disk-blackbody luminosities, we re-derived them with an alternative method: we defined a dummy response from 0.01 to 10 keV (*dummyrsp* in XSPEC), calculated the model flux $f_{\rm bol}^{\rm diskbb}$ over that (essentially bolometric) energy range, and converted it to a luminosity with the relation $L_{\rm bol}^{\rm diskbb} = 2\pi\,(d^2/\cos\theta)\,f_{\rm bol}^{\rm diskbb}$, suitable for accretion disks. The two methods give the same result, as expected. For plotting purposes, and for consistency with the luminosities given in a comparison sample of ULXs from the literature, we assumed $\cos\theta = 1/2$ throughout this chapter. With this conventional choice of viewing angle, disk luminosities are simply obtained as $4\pi d^2$ times the observed fluxes, like for a spherically symmetric emitter[2]. $L_{\rm bol}^{\rm diskbb}$ for a generic angle θ is simply obtained from the values listed in Table 4.3, divided by $2\cos\theta$.

Table 4.2: Characteristic radii, temperatures and bolometric luminosities of the *bbody* component in each ULS observation with enough counts for spectral fitting. The row number identifies the source and the epoch, from the observation list in Table 4.1.2. ObsID 934 of the M 101 ULS was split into three sub-intervals based on count rate (Section 4.3.2). Errors are 90% confidence limits for single parameters.

Row	$n_{\rm H}$ (10^{22} cm^{-2})	$r_{\rm bb}$ (10^3 km)	$kT_{\rm bb}$ (eV)	$L_{\rm bol}^{\rm bb}$ (10^{39} erg s^{-1})
1	$0.07^{+0.20}_{-0.07}$	$7.4^{+68.6}_{-3.4}$	100^{+35}_{-31}	$0.7^{+8.0}_{-0.4}$
2	$0.13^{+0.17}_{-0.12}$	$12.3^{+70.0}_{-5.4}$	107^{+24}_{-20}	$2.6^{+14.0}_{-0.9}$
3	$0.12^{+0.32}_{-0.12}$	$17.9^{+1315}_{-8.8}$	82^{+34}_{-24}	$1.9^{+72.2}_{-1.6}$
4	$0.36^{+0.31}_{-0.17}$	$15.4^{+75.0}_{-7.1}$	119^{+33}_{-22}	$6.1^{+22.3}_{-4.3}$
5	$0.06^{+0.17}_{-0.06}$	$7.5^{+53.9}_{-3.0}$	118^{+26}_{-27}	$1.4^{+6.3}_{-0.7}$
6	$0.21^{+0.43}_{-0.18}$	$23.0^{+127.1}_{-11.1}$	98^{+30}_{-31}	$6.3^{+75.9}_{-5.1}$
7	$0.22^{+0.29}_{-0.17}$	$38.2^{+162.2}_{-18.5}$	87^{+25}_{-20}	$10.7^{+63.2}_{-9.0}$
8	$0.18^{+0.20}_{-0.13}$	$6.6^{+59.8}_{-3.0}$	127^{+50}_{-32}	$1.5^{+7.3}_{-0.9}$
9	$0.22^{+0.26}_{-0.17}$	$10.0^{+198.3}_{-4.7}$	119^{+47}_{-33}	$2.6^{+26.4}_{-1.9}$

[2]This is often an implicit assumption in many studies of X-ray binaries and ULXs in the literature, in which the luminosities of all emission components are defined as $L \equiv 4\pi d^2 f$. The alternative choice of $\theta = 0$ is also sometimes adopted in the literature; however, this is not suitable for our sample of sources because they are more likely to be high-inclination objects, as discussed in Section 4.4.3.

Table 4.2: *continued*

Row	$n_{\rm H}$ ($10^{22}\,{\rm cm}^{-2}$)	$r_{\rm bb}$ ($10^3\,{\rm km}$)	$kT_{\rm bb}$ (eV)	$L_{\rm bol}^{\rm bb}$ ($10^{39}\,{\rm erg\ s}^{-1}$)
10	$0.22^{+0.26}_{-0.17}$	$6.8^{+45.6}_{-3.1}$	132^{+53}_{-41}	$1.3^{+8.2}_{-0.4}$
11	$0.05^{+0.06}_{-0.05}$	$11.2^{+17.8}_{-5.6}$	68^{+9}_{-8}	$0.3^{+0.6}_{-0.2}$
12	$0.07^{+0.05}_{-0.04}$	$14.8^{+17.4}_{-7.4}$	59^{+5}_{-5}	$0.3^{+0.5}_{-0.2}$
13	$0.11^{+0.16}_{-0.11}$	$87.5^{+389.9}_{-42.8}$	43^{+12}_{-10}	$3.4^{+14.0}_{-3.2}$
14	$0.03^{+0.12}_{-0.03}$	$2.1^{+3.2}_{-0.7}$	168^{+30}_{-34}	$0.5^{+0.7}_{-0.1}$
15	$0.05^{+0.02}_{-0.02}$	$22.3^{+5.3}_{-3.6}$	78^{+3}_{-3}	$2.3^{+0.7}_{-0.5}$
16	$0.16^{+0.13}_{-0.09}$	$52.2^{+133.5}_{-26.3}$	70^{+7}_{-7}	$8.3^{+25.4}_{-5.5}$
17	$0.01^{+0.09}_{-0.01}$	$15.4^{+33.1}_{-3.3}$	79^{+6}_{-10}	$1.2^{+2.6}_{-0.3}$
18	< 0.15	$2.4^{+11.8}_{-0.6}$	109^{+13}_{-21}	$0.1^{+0.4}_{-0.03}$
19	< 0.04	$8.3^{+1.9}_{-1.4}$	97^{+6}_{-7}	$0.8^{+0.5}_{-0.1}$
20	$0.08^{+0.10}_{-0.08}$	$28.6^{+77.6}_{-14.4}$	73^{+12}_{-9}	$3.0^{+8.1}_{-2.0}$
21	$0.03^{+0.07}_{-0.03}$	$13.1^{+15.7}_{-3.4}$	91^{+8}_{-9}	$1.5^{+1.9}_{-0.5}$
22	$0.34^{+0.28}_{-0.21}$	$38.9^{+660.0}_{-19.6}$	84^{+22}_{-16}	$9.5^{+130.3}_{-8.2}$
23	$0.11^{+0.09}_{-0.07}$	$41.6^{+72.8}_{-20.9}$	69^{+8}_{-7}	$5.1^{+10.2}_{-3.2}$
24	$0.05^{+0.11}_{-0.05}$	$23.0^{+95.9}_{-11.5}$	73^{+16}_{-12}	$1.9^{+6.7}_{-1.2}$
25	< 0.14	$29.6^{+183.6}_{-14.9}$	49^{+13}_{-12}	$0.7^{+2.4}_{-0.4}$
26	< 0.06	$12.7^{+24.2}_{-4.1}$	66^{+9}_{-9}	$0.4^{+0.7}_{-0.2}$
27	$0.02^{+0.26}_{-0.02}$	$8.7^{+48.1}_{-4.4}$	71^{+16}_{-19}	$0.2^{+0.7}_{-0.1}$
29	< 0.07	$14.3^{+51.2}_{-7.2}$	69^{+14}_{-13}	$0.6^{+1.6}_{-0.3}$
29	$0.13^{+0.31}_{-0.13}$	$19.9^{+115.2}_{-10.0}$	71^{+23}_{-18}	$1.3^{+8.6}_{-1.1}$
30-high	$0.04^{+0.01}_{-0.01}$	$10.2^{+0.4}_{-0.3}$	135^{+3}_{-4}	$4.6^{+0.2}_{-0.3}$
30-med	$0.04^{+0.01}_{-0.01}$	$10.5^{+0.3}_{-0.3}$	119^{+2}_{-2}	$2.9^{+0.2}_{-0.2}$
30-low	$0.04^{+0.01}_{-0.01}$	$18.4^{+0.9}_{-1.0}$	90^{+2}_{-2}	$2.9^{+0.2}_{-0.2}$
31	$0.08^{+0.07}_{-0.05}$	$29.0^{+32.7}_{-14.4}$	77^{+11}_{-10}	$3.6^{+6.8}_{-2.0}$
32	$0.10^{+0.04}_{-0.04}$	$47.0^{+32.6}_{-17.0}$	69^{+7}_{-7}	$6.6^{+5.9}_{-2.9}$
33	$0.20^{+0.13}_{-0.12}$	> 54	< 49	> 2.1
34	$0.12^{+0.06}_{-0.05}$	$43.5^{+29.3}_{-17.2}$	75^{+6}_{-6}	$7.7^{+8.6}_{-3.8}$
35	$0.13^{+0.03}_{-0.03}$	$22.5^{+10.3}_{-4.7}$	100^{+13}_{-10}	$6.6^{+1.2}_{-1.0}$

Table 4.2: *continued*

Row	$n_{\rm H}$ ($10^{22}\,{\rm cm}^{-2}$)	$r_{\rm bb}$ ($10^3\,{\rm km}$)	$kT_{\rm bb}$ (eV)	$L_{\rm bol}^{\rm bb}$ ($10^{39}\,{\rm erg\ s}^{-1}$)
36	$0.13^{+0.05}_{-0.04}$	$101.5^{+82.7}_{-43.1}$	56^{+5}_{-5}	$12.8^{+17.9}_{-6.9}$
37	$0.01^{+0.04}_{-0.01}$	$6.0^{+9.0}_{-1.3}$	114^{+11}_{-16}	$0.8^{+1.0}_{-0.2}$
38	< 0.07	$3.5^{+4.8}_{-0.8}$	135^{+17}_{-20}	$0.5^{+0.5}_{-0.1}$
39	$0.003^{+0.084}_{-0.003}$	$5.6^{+10.0}_{-1.0}$	122^{+12}_{-23}	$0.9^{+1.2}_{-0.1}$
40	< 0.04	$7.8^{+13.1}_{-1.7}$	98^{+10}_{-10}	$0.7^{+1.1}_{-0.1}$
41	$0.03^{+0.15}_{-0.03}$	$10.4^{+30.1}_{-3.1}$	92^{+12}_{-8}	$1.1^{+3.1}_{-0.4}$
42	< 0.20	$6.2^{+56.3}_{-1.2}$	115^{+8}_{-25}	$0.9^{+5.3}_{-0.2}$
43	$0.12^{+0.09}_{-0.02}$	$25.1^{+41.3}_{-9.5}$	84^{+8}_{-7}	$4.5^{+9.3}_{-2.5}$
44	< 0.21	$7.5^{+16.3}_{-1.9}$	105^{+16}_{-18}	$0.9^{+1.6}_{-0.1}$

Table 4.3: Characteristic inner-disk radii, peak colour temperatures and bolometric luminosities of the *diskbb* component in each ULS observation with enough counts for spectral fitting. Row numbers are defined as in Table 4.2. An angle $\theta = 60°$ was adopted in the expressions for $r_{\rm in}$ and $L_{\rm bol}^{\rm diskbb}$. Errors are 90% confidence limits for single parameters.

Row	$n_{\rm H}$ ($10^{22}\,{\rm cm}^{-2}$)	$r_{\rm in}$ ($10^3\,{\rm km}$)	$kT_{\rm in}$ (eV)	$L_{\rm bol}^{\rm diskbb}$ ($10^{39}\,{\rm erg\ s}^{-1}$)
1	$0.09^{+0.19}_{-0.09}$	$7.9^{+20.4}_{-3.9}$	120^{+62}_{-41}	$1.7^{+18.9}_{-1.3}$
2	$0.14^{+0.16}_{-0.11}$	$16.3^{+169.5}_{-7.4}$	123^{+31}_{-26}	$8.9^{+52.6}_{-6.5}$
3	$0.09^{+0.29}_{-0.09}$	$22.9^{+374.3}_{-11.5}$	95^{+49}_{-30}	$5.5^{+28.5}_{-4.8}$
4	$0.23^{+0.36}_{-0.15}$	$13.4^{+101.6}_{-6.3}$	153^{+53}_{-36}	$12.8^{+56.9}_{-9.1}$
5	$0.10^{+0.16}_{-0.10}$	$8.6^{+84.4}_{-4.0}$	140^{+49}_{-36}	$3.6^{+19.6}_{-2.6}$
6	$0.29^{+0.43}_{-0.21}$	$43.5^{+848.7}_{-21.3}$	106^{+42}_{-35}	$30.9^{+2475.8}_{-27.4}$
7	$0.26^{+0.29}_{-0.18}$	$58.7^{+*}_{-29.1}$	97^{+33}_{-24}	$38.6^{+836.4}_{-33.3}$
8	$0.22^{+0.19}_{-0.14}$	$6.8^{+81.7}_{-3.3}$	157^{+116}_{-45}	$3.2^{+19.2}_{-2.5}$
9	$0.29^{+0.24}_{-0.17}$	$14.5^{+335.8}_{-6.9}$	134^{+61}_{-38}	$8.7^{+99.6}_{-6.8}$
10	$0.29^{+0.24}_{-0.17}$	$9.3^{+248.9}_{-4.4}$	151^{+42}_{-49}	$5.8^{+67.0}_{-4.0}$
11	$0.06^{+0.06}_{-0.06}$	$14.5^{+28.4}_{-7.3}$	77^{+11}_{-9}	$1.0^{+1.7}_{-0.6}$
12	$0.08^{+0.05}_{-0.04}$	$21.2^{+29.7}_{-10.7}$	66^{+7}_{-6}	$1.1^{+1.6}_{-0.6}$

Table 4.3: *continued*

Row	$n_{\rm H}$ ($10^{22}\,{\rm cm}^{-2}$)	$r_{\rm in}$ ($10^3\,{\rm km}$)	$kT_{\rm in}$ (eV)	$L_{\rm bol}^{\rm diskbb}$ ($10^{39}\,{\rm erg\ s}^{-1}$)
13	$0.12^{+0.16}_{-0.12}$	153^{+999}_{-76}	47^{+16}_{-11}	$14.1^{+624}_{-13.4}$
14	$0.10^{+0.13}_{-0.09}$	$2.9^{+9.9}_{-1.0}$	203^{+70}_{-50}	$1.1^{+2.5}_{-0.6}$
15	$0.08^{+0.02}_{-0.2}$	$29.0^{+7.4}_{-5.1}$	89^{+3}_{-3}	$6.8^{+2.0}_{-1.5}$
16	$0.20^{+0.13}_{-0.10}$	$89.0^{+278.3}_{-35.3}$	76^{+8}_{-8}	$35.6^{+122.1}_{-24.3}$
17	$0.03^{+0.09}_{-0.03}$	$19.9^{+50.2}_{-7.0}$	91^{+12}_{-13}	$3.5^{+8.2}_{-1.7}$
18	$0.03^{+0.17}_{-0.03}$	$2.7^{+28.3}_{-1.0}$	129^{+16}_{-28}	$0.3^{+1.5}_{-0.1}$
19	< 0.05	$6.7^{+2.0}_{-1.3}$	124^{+10}_{-9}	$1.4^{+0.2}_{-0.2}$
20	$0.09^{+0.10}_{-0.08}$	$35.9^{+108.7}_{-15.3}$	84^{+16}_{-12}	$8.3^{+23.0}_{-5.7}$
21	$0.07^{+0.07}_{-0.06}$	$17.0^{+24.6}_{-6.0}$	104^{+13}_{-11}	$4.4^{+6.3}_{-2.3}$
22	$0.40^{+0.28}_{-0.21}$	$66.2^{+*}_{-32.0}$	92^{+27}_{-19}	$40.5^{+669}_{-36.1}$
23	$0.13^{+0.08}_{-0.07}$	$57.8^{+111.2}_{-27.4}$	78^{+10}_{-9}	$16.2^{+32.9}_{-10.3}$
24	$0.07^{+0.10}_{-0.07}$	$25.6^{+135.1}_{-11.4}$	86^{+26}_{-17}	$4.6^{+17.4}_{-3.3}$
25	< 0.01	$36.7^{+309.2}_{-16.8}$	56^{+18}_{-14}	$1.7^{+7.8}_{-1.2}$
26	< 0.06	$13.8^{+34.4}_{-4.9}$	77^{+13}_{-12}	$0.9^{+1.7}_{-0.4}$
27	$0.05^{+0.26}_{-0.05}$	$6.8^{+10.7}_{-2.6}$	88^{+20}_{-15}	$0.4^{+0.3}_{-0.2}$
28	< 0.08	$13.4^{+70.5}_{-5.2}$	85^{+19}_{-19}	$1.2^{+3.5}_{-0.5}$
29	$0.17^{+0.17}_{-0.17}$	$30.1^{+*}_{-17.1}$	80^{+35}_{-21}	$4.6^{+194}_{-4.2}$
30-high	$0.06^{+0.01}_{-0.01}$	$8.3^{+0.4}_{-0.4}$	174^{+6}_{-7}	$8.2^{+0.4}_{-0.4}$
30-med	$0.06^{+0.01}_{-0.01}$	$6.1^{+0.3}_{-0.3}$	178^{+2}_{-2}	$4.8^{+0.4}_{-0.4}$
30-low	$0.06^{+0.01}_{-0.01}$	$18.4^{+1.6}_{-1.1}$	109^{+2}_{-2}	$6.2^{+0.8}_{-0.8}$
31	$0.10^{+0.06}_{-0.06}$	$33.9^{+48.5}_{-17.4}$	90^{+14}_{-13}	$9.8^{+21.2}_{-5.6}$
32	$0.11^{+0.04}_{-0.04}$	$39.7^{+30.4}_{-16.5}$	81^{+9}_{-6}	$17.0^{+14.2}_{-8.0}$
33	$0.22^{+0.13}_{-0.12}$	> 88	< 54	> 8.0
34	$0.15^{+0.06}_{-0.06}$	$66.0^{+48.5}_{-17.4}$	84^{+8}_{-6}	$27.8^{+32.4}_{-15.0}$
35	$0.11^{+0.03}_{-0.03}$	$12.2^{+21.1}_{-4.9}$	147^{+6}_{-6}	$8.8^{+15.8}_{-2.2}$
36	$0.14^{+0.05}_{-0.04}$	$146.7^{+146.4}_{-63.1}$	62^{+5}_{-5}	$41.0^{+70.8}_{--21}$
37	$0.05^{+0.08}_{-0.05}$	$6.8^{+12.9}_{-2.6}$	135^{+25}_{-21}	$2.0^{+2.8}_{-1.0}$

Table 4.3: *continued*

Row	$n_{\rm H}$ (10^{22} cm^{-2})	$r_{\rm in}$ (10^3 km)	$kT_{\rm in}$ (eV)	$L_{\rm bol}^{\rm diskbb}$ (10^{39} erg s^{-1})
38	$0.004^{+0.093}_{-0.004}$	$2.1^{+7.9}_{-0.6}$	194^{+32}_{-49}	$0.8^{+0.1}_{-0.1}$
39	$0.04^{+0.03}_{-0.04}$	$6.1^{+12.4}_{-2.2}$	145^{+27}_{-27}	$2.1^{+2.3}_{-0.9}$
40	$0.001^{+0.084}_{-0.001}$	$5.8^{+23.7}_{-1.7}$	128^{+24}_{-29}	$1.3^{+2.5}_{-0.4}$
41	$0.04^{+0.01}_{-0.04}$	$11.2^{+40.2}_{-4.1}$	111^{+18}_{-17}	$2.4^{+4.7}_{-1.1}$
42	$0.06^{+0.26}_{-0.06}$	$8.9^{+214.4}_{-3.3}$	129^{+23}_{-35}	$2.9^{+36.7}_{-1.6}$
43	$0.13^{+0.17}_{-0.08}$	$23.9^{+54.4}_{-8.0}$	104^{+11}_{-9}	$8.7^{+8.5}_{-1.5}$
44	< 0.09	$6.5^{+18.0}_{-2.0}$	131^{+25}_{-22}	$1.6^{+1.4}_{-0.3}$

The first, most obvious result of our spectral modelling is that there is no $L \propto T^4$ trend in any of the sources (when observed multiple times) or in the sample as a whole (Figure 4.2, and Tables 4.2 and 4.3). This is equivalent to saying that the radius of the emitting region is not constant between sources or for the same source at various epochs. A constant inner-disk radius $R_{\rm in} \approx 1.19 r_{\rm in} \approx R_{\rm ISCO}$ (radius of the innermost stable circular orbit) is usually taken as the defining property of the high/soft state in luminous black holes at accretion rates $\gtrsim$ a few percent of the Eddington limit (Kubota et al., 2002; Remillard and McClintock, 2006). The IMBH scenario was based on the interpretation of the thermal component as disk emission in the high/soft state; however, we see that the thermal component in ULSs does not behave like a standard disk in the canonical high/soft state. Instead, temperature variations at approximately constant bolometric luminosity are often found in systems with expanding photospheres, such as some novae and classical SSSs, which have been observed to oscillate between an X-ray bright (interpreted as a hotter, smaller photosphere) and a UV-bright (cooler, larger photosphere) state (van den Heuvel et al., 1992; Pakull et al., 1993).

Another important result of our fits is that there is an anticorrelation between fitted radii and temperatures (Figure 4.3, and Tables 4.2 and 4.3). For example, using blackbody models, we find that for the ULS in M 101 $r_{\rm bb} \propto T_{\rm bb}^{-1.88\pm0.87}$ (Spearman rank $r = -0.82$ ignoring errors and $r = -0.87 \pm 0.10$ when considering errors using a Monte Carlo perturbation error analysis outlined in Curran, 2014). For the whole sample of ULSs $r_{\rm bb} \propto T_{\rm bb}^{-2.16\pm0.46}$ (Spearman rank $r = -0.73$ ignoring errors and $r = -0.46 \pm 0.09$ with errors). This is again consistent with the behaviour of a moving photosphere.

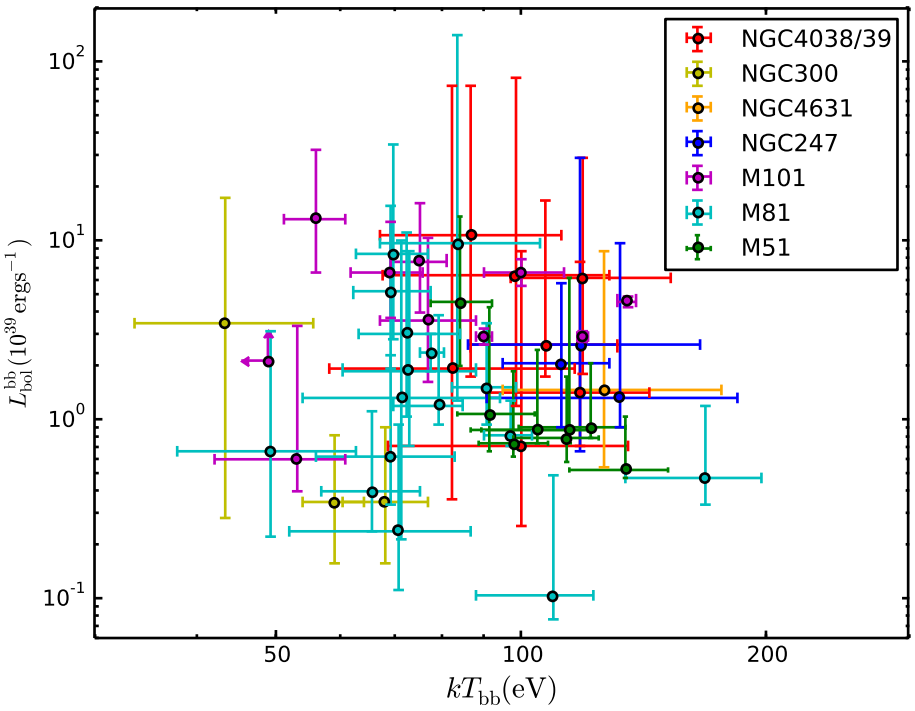

Figure 4.2: Bolometric luminosity inferred from single-temperature blackbody fits, for each observation, plotted against the corresponding best-fitting blackbody temperature. No significant correlation exists between the two quantities, either for individual sources or for the population as a whole.

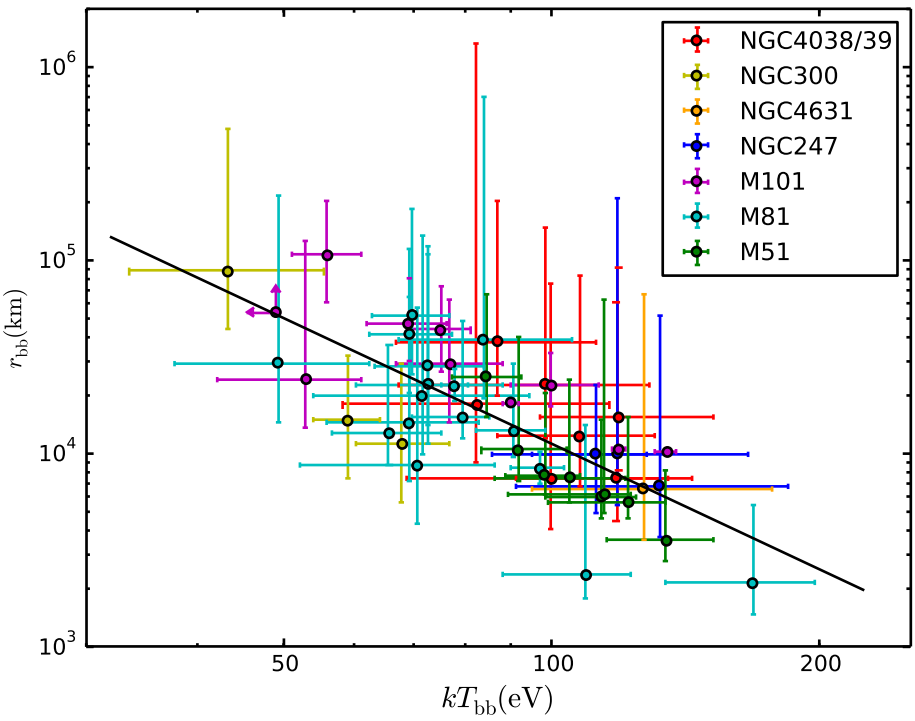

Figure 4.3: Best-fitting blackbody radius, plotted against the best-fitting blackbody temperature, for each observation with spectral information. The best-fitting inverse correlation $r_{\rm bb} \propto T_{\rm bb}^{-2.16\pm0.46}$ is overplotted.

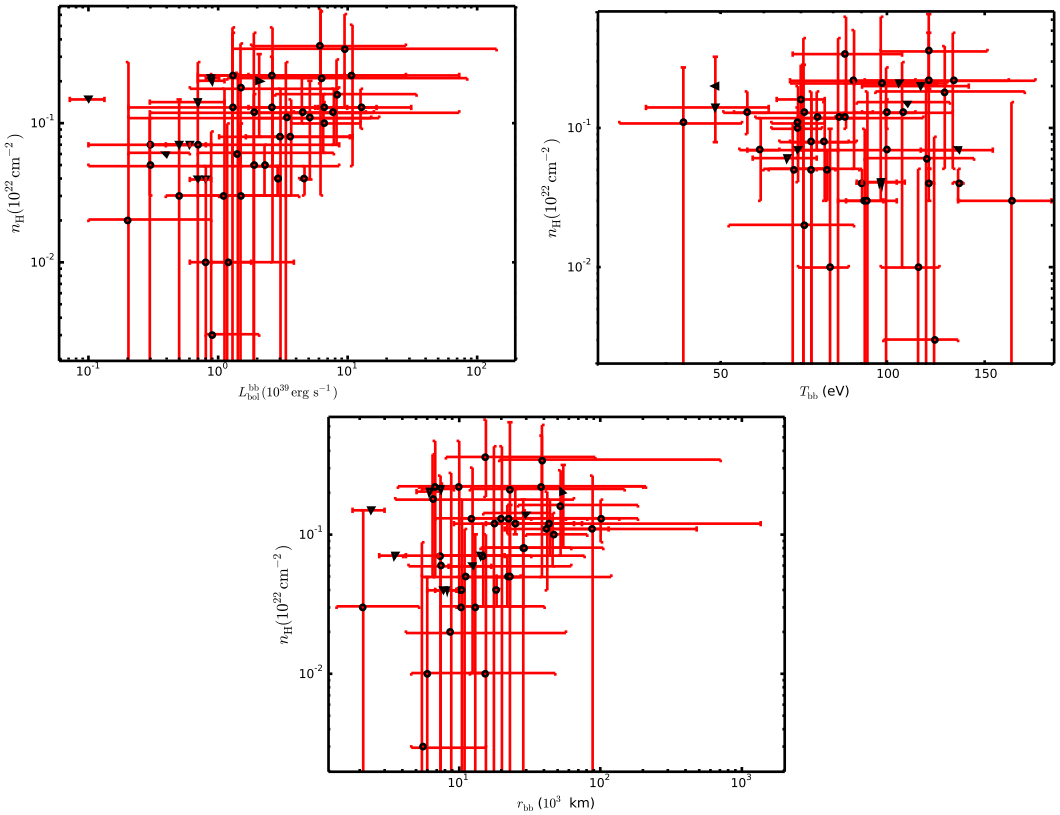

Figure 4.4: Top left panel: best-fitting column density $n_{\rm H}$ plotted against the extrapolated blackbody bolometric luminosity. Top right panel: $n_{\rm H}$ plotted against the best-fitting blackbody temperature. Bottom panel: $n_{\rm H}$ plotted against the best-fitting blackbody radii. In all panels, triangles indicate values that are only upper or lower limits in one of the parameters.

For completeness, we also plot the best-fitting values of the absorbing column density $n_{\rm H}$ versus the bolometric luminosity, the temperature and the radius (Figure 4.4). There is always, inevitably, a degree of degeneracy between column density and the other fit parameters for supersoft thermal components. We do not find any systematic trend between $n_{\rm H}$ and blackbody temperature, which supports our claim that the fitted spread in temperatures is a real effect. Some of the observations with low $n_{\rm H}$ also have low fitted radii, but this needs not be a fitting degeneracy: it is physically plausible that $n_{\rm H}$ increases when our line of sight goes through a thicker, larger outflow. In particular, for ObsID 934 of the M 101 ULS, it was shown by Soria and Kong (2016) that the strong intra-observation evolution (in the sense of smaller radii for hotter temperatures) is recovered both when the column density is locked between all three sub-intervals, and when it is left free; therefore at least in that case it is not due to a fitting degeneracy.

Two classes of physical sources show soft thermal emission at temperatures $\sim$0.1 keV, comparable with those fitted to ULSs. The first class is that of classical

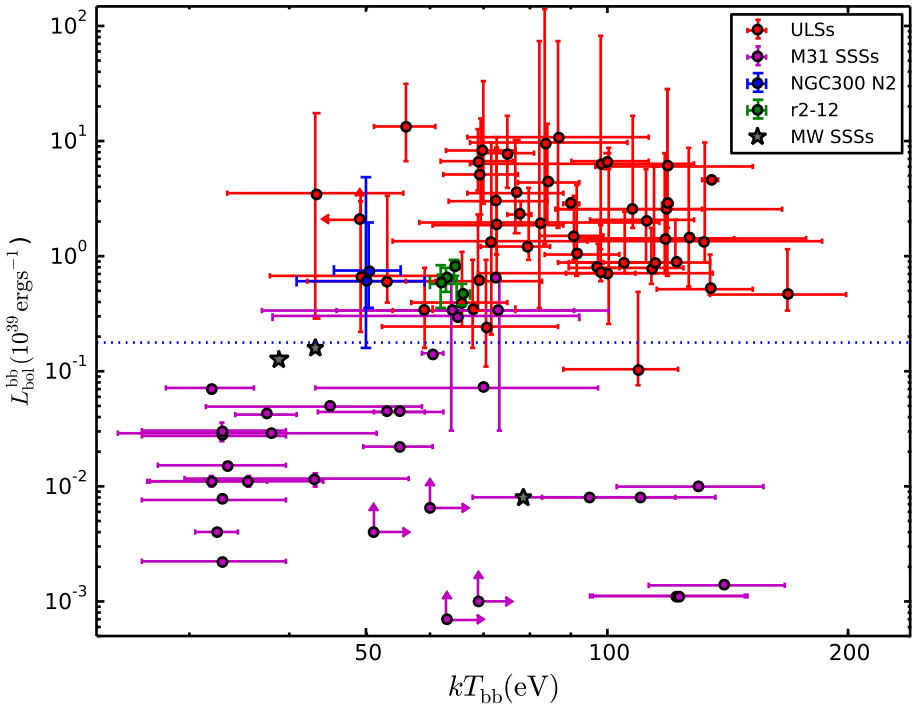

Figure 4.5: Red datapoints: bolometric luminosity versus blackbody temperature distribution of the seven ULSs in our sample at various epochs (values from Table 4.2). Magenta datapoints: same, for a sample of classical SSSs in M 31, from Orio et al. (2010); stars mark representative locations of the three best-known SSSs in the Local Group (Cal83, Cal87 and RXJ0513.9−6951), from Ness et al. (2013). Green and blue datapoints are the luminosities and temperatures of the (variable) supersoft sources r2-12 in M 31 (data from Trudolyubov and Priedhorsky, 2008) and NGC 300 SSS2 (from our own spectral analysis) respectively; both sources are brighter than classical SSSs but narrowly missed out on our threshold 10^{39} erg s^{-1} luminosity for the definition of ULSs. The dashed line shows the Eddington luminosity of a 1.4 $M_\odot$ accretor, which should provide an approximate upper limit to the luminosity of classical SSSs if powered by nuclear-burning white dwarfs.

SSSs. For our comparison, we used a sample of SSSs in M31 with well-constrained distance and spectral parameters (Orio et al., 2010), and we added the three best-studied SSSs in the Local Group (Cal87, Cal83 and RXJ0513.9−6951), with fit parameters from Ness et al. (2013). We find (Figures 4.5 and 4.6) that ULSs and classical SSSs represent two separate populations. Although their temperature range largely overlaps, ULSs have larger radii, and bolometric blackbody luminosities at least an order of magnitude higher. While there is uncertainty in the extrapolation of a blackbody spectrum from soft X-rays to (unobserved) UV, the difference in luminosity between the two populations is a robust result, and applies also to the directly observed luminosity above 0.3 keV. Only ULSs reach luminosities one order of magnitude above the Eddington limit of a nuclear-burning white dwarf. As we mentioned in Section 4.1.2, a couple of sources (r2-12 in M 31

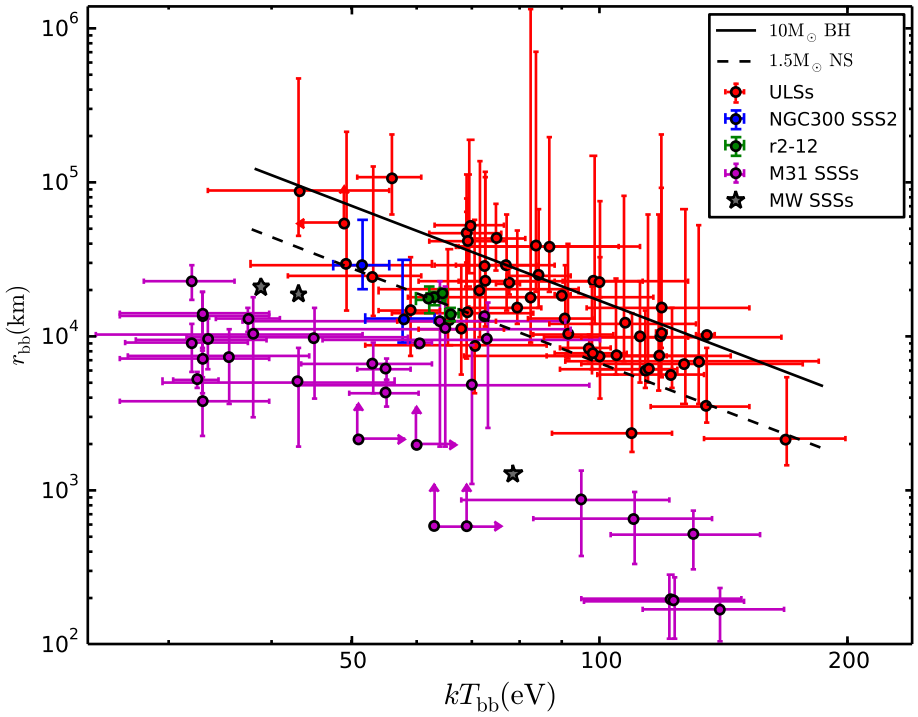

Figure 4.6: Red datapoints: fitted inner-disk radius versus blackbody temperature for our sample of ULSs. Magenta datapoints: same, for the classical SSSs in M 31 (Orio et al., 2010). Green and blue datapoints are the luminosities and radii of r2-12 in M 31 and NGC 300 SSS2 respectively. Stars are representative values for Cal83, Cal87 and RXJ0513.9−6951. Solid line: radii and temperatures predicted by the super-Eddington outflow model described in Soria and Kong (2016), for a 10-$M_\odot$ black hole. Dashed line: same, for a 1.5-$M_\odot$ neutron star.

and SSS2 in NGC 300) seem to have intermediate properties, and it is not clear whether they should be classified as ULSs or as extremely bright classical SSSs. In summary, apart from those two ambiguous cases, the luminosity distribution of ULSs and SSSs is consistent with the scenario that the former group contains accreting black holes or neutron star and the latter group nuclear-burning white dwarfs.

The second class of accreting sources with a cool thermal component is that of ULXs with a soft excess. The physical origin of the soft excesses in ULXs is still disputed. Currently, perhaps the most popular interpretation is that the soft excess is emitted from a super-critical disk wind, launched from near the spherisation radius (King and Pounds, 2003; Poutanen et al., 2007; Sutton et al., 2013b; Middleton et al., 2015a). An alternative scenario (Miller et al., 2013) is that it comes from the disk—either from a full standard disk around an IMBH or from the outer part of the disk around a super-Eddington stellar-mass black hole. In addition to the thermal component, ULXs have a (dominant) harder component, with a downturn at energies $\gtrsim$5 keV. The origin of the hard compo-

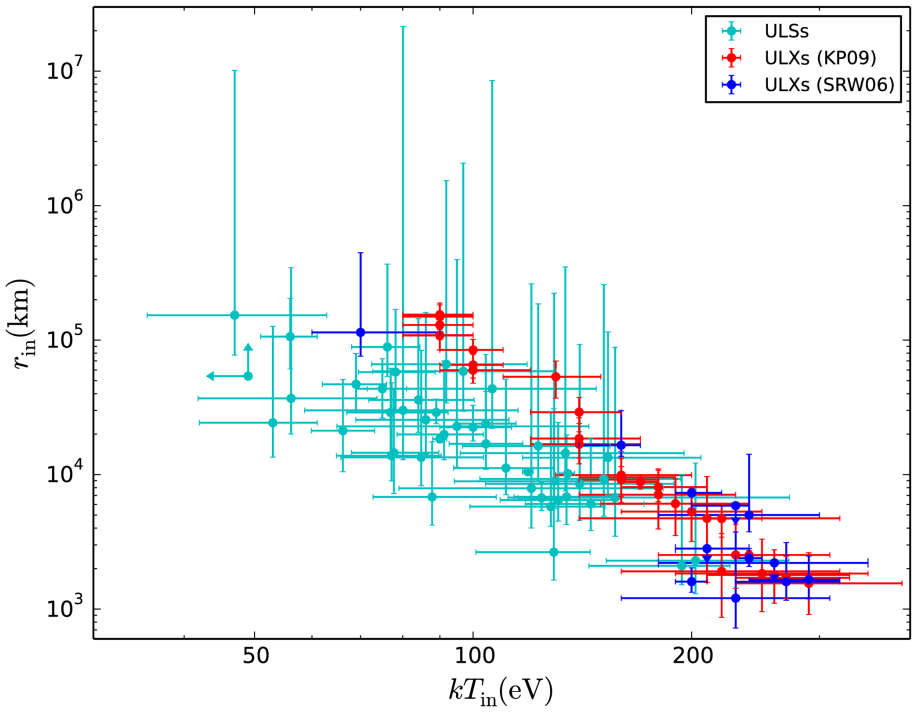

Figure 4.7: Light blue datapoints: best-fitting disk-blackbody radius versus best-fitting peak colour temperature, for each ULS observation with spectral information. Red datapoints: disk-blackbody radius versus peak temperature for the soft thermal component in a sample of ULX spectra fitted by Kajava and Poutanen (2009). Blue datapoints: disk-blackbody radius versus peak temperature for the soft thermal component in a sample of ULXs studied by Stobbart et al. (2006). This diagram suggests a physical connection between the soft thermal component of ULSs and ULXs—although, in the latter case, a dominant harder component is also present.

nent (absent or very faint in ULSs) is also disputed, but is likely to be associated with the hot inner region of the inflow—either a non-standard disk or a warm corona (Roberts, 2007; Miller et al., 2014; Middleton et al., 2015a). Regardless of the true physical origin of the two components, ULX spectra have traditionally been fitted with a disk-blackbody model plus a Comptonised component. For our comparison of ULX and ULS properties, we used two samples of well-studied ULXs in nearby galaxies, from Stobbart et al. (2006) and Kajava and Poutanen (2009). This is by no means a statistically complete sample; however, it is representative of the general appearance of ULXs with a broad-band component and a soft thermal component. We compared the disk-blackbody temperatures and radii of our sample of ULSs (Table 4.3) with the disk-blackbody temperatures and radii of those ULXs from the published literature[3]. We find (Figure 4.7 and Figure 4.8) that thermal components in ULXs lie at the high-temperature

[3]Similar results are expected if we compare single-temperature blackbody rather than disk-blackbody fit parameters in ULS and ULX spectra; we leave this exercise to further work.

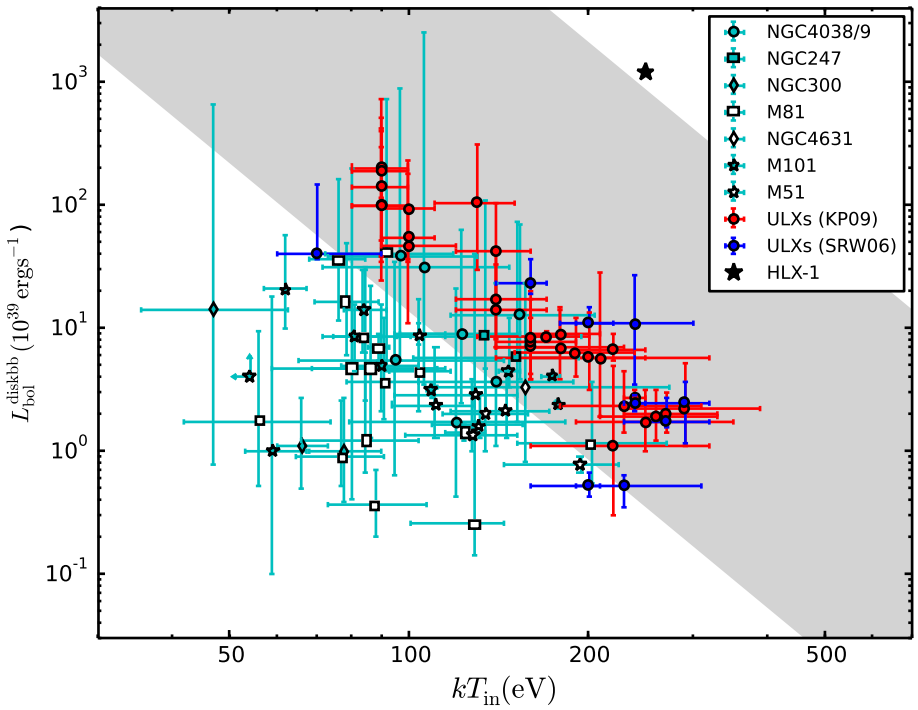

Figure 4.8: Bolometric disk-blackbody luminosity versus peak colour temperatures for ULSs and ULXs, showing no sign of the $L \propto T^4$ standard disk relation. (See Soria (2007) and Kajava and Poutanen (2009), for a discussion of the lack of such correlation in ULXs.) The grey shaded area represents the range of temperatures and luminosities in which the spectrum of an accreting black hole is expected to be in the canonical high/soft state, dominated by a thermal disk component (i.e., for $0.02 \lesssim \dot{m} \lesssim 1$): almost all ULSs fall outside this region, effectively ruling out an IMBH interpretation. The star near the top of the diagram represents the characteristic luminosity and peak temperature of the IMBH candidate HLX-1 (Farrell et al., 2009) at the peak of its recurrent outbursts.

end of the ULS population. There is a degree of overlapping in temperature and luminosity for sources with a thermal component at $kT_{\rm in} \approx 0.10$–0.15 keV. Above those temperatures, we find almost exclusively ULXs with the additional, dominant harder component; below those temperatures, most sources are ULSs without hard tails. The lack of ULXs with a dominant hard tail and a thermal component cooler than ≈100 eV may be partly due to the fact that it is more difficult to identify a statistically significant soft excess at such low temperatures if the spectrum is dominated by the broad-band component. However, the lack of a population of soft sources with no hard tail and a thermal component hotter than ≈150 eV must be due instead to a real threshold in the physical structure of the inflow/outflow.

4.3.2 Transition ULSs in M 101 and NGC 247

In some epochs, the two ULSs in M 101 and NGC 247 overlap with the spectral parameters typical of the ULX population. In both sources, a harder component appears in epochs when their blackbody temperature is highest (Soria and Kong, 2016), approaching 150 eV (corresponding to the brightest X-ray state for both sources, although not necessarily the most luminous in bolometric terms). Both ULSs show an interesting and somewhat similar spectral change at those high count rates.

For M 101, we fitted two sub-intervals (at "high" and "medium" count rate) of the long *Chandra* observation from 2000 March 26 (ObsID 934); those time intervals were empirically defined by Mukai et al. (2003), and were later analysed and discussed also by Kong and Di Stefano (2005) and Soria and Kong (2016). The fitted blackbody temperature in the medium count-rate interval is $kT_{\rm bb} \approx 120$ eV, and there is a highly significant (Table 4.4) thermal-plasma component at $kT_1 \approx 0.6$ keV (red datapoints and residuals in Figure 4.9). The thermal-plasma emission contributes $\approx$ 10% of the unabsorbed luminosity in the 0.3–10 keV band, that is $\approx 3 \times 10^{38}$ erg s^{-1}, compared with a total (blackbody plus *mekal* components) 0.3–10 keV emitted luminosity of $\approx 2.5 \times 10^{39}$ erg s^{-1} in that time interval. Above 1 keV, the spectrum is significantly modified by an absorption edge at $E \approx 1.05 \pm 0.05$ keV, with optical depth $\tau \approx 2$ (Table 4.4).

In the high count-rate interval, the temperature of the optically thick thermal component increases to $kT_{\rm bb} \approx 135$ eV; the thermal-plasma component at $kT_1 \approx 0.6$ keV is still detected and another one is required at $kT_1 \approx 1.0$ keV, suggesting a spread of temperatures in the thermal plasma. No edge is present in the spectrum this time; instead, an additional, harder emission component (Table 4.4) provides significant flux in the 1–5 keV band (blue datapoints and residuals in Figure 4.9). This hard tail can be equally well fitted with an additional *mekal* or bremsstrahlung component at $kT \gtrsim 2$ keV, or with inverse-Compton emission (e.g., *comptt*). In fact, if we had no other knowledge of this source from other epochs, the inverse-Compton model would have been the default choice, and this accreting source would have been classified as a standard broad-band ULX with a strong blackbody soft excess at $kT_{\rm bb} \approx 0.14$ keV (or a disk temperature $kT_{\rm in} \approx 0.18$ keV). The 0.3–10 keV luminosity emitted in the three *mekal* components (or in the two *mekal* plus Comptonised component) is $\approx 7 \times 10^{38}$ erg s^{-1} during the high count-rate interval. The total emitted luminosity (blackbody plus all other components) in the same band is $\approx 4 \times 10^{39}$ erg s^{-1} during the same interval.

Another epoch when the M 101 ULS spectrum displays a significant harder

Table 4.4: Best-fitting parameters and F-test significance of additional spectral features (absorption edges or line emission) at all epochs in which they significantly improve the fit. Errors are 90% confidence limits for single parameters.

Galaxy & Obs ID	Thermal Plasma			Edge		
	kT (keV)	Normalisation	Significance	E (keV)	$\tau_{\max}$	Significance
Antennae-3042				$1.04^{+0.03}_{-0.04}$	$3.68^{+3.06}_{-2.41}$	$> 99.9\%$
NGC 4631-0110900201				$0.94^{+0.03}_{-0.02}$	$4.18^{+4.30}_{-1.82}$	$> 99.999\%$
NGC 247-12437				$0.95^{+0.03}_{-0.02}$	$4.45^{+2.98}_{-1.93}$	$> 99.999\%$
NGC 247-17547	$1.50^{+*}_{-0.50}$	$9.8^{+7.8}_{-6.9}\times10^{-5}$	$> 95\%$			
M 51-1622				$0.98^{+0.12}_{-0.08}$	$1.6^{+*}_{-1.0}$	$> 95\%$
M 51-3932	$0.61^{+0.11}_{-0.12}$	$6.6^{+5.3}_{-3.1}\times10^{-6}$	$> 99\%$			
M 51-13813	$0.60^{+0.11}_{-0.14}$	$4.9^{+1.8}_{-1.4}\times10^{-6}$	$> 99.99\%$			
M 51-13812	$0.56^{+0.06}_{-0.06}$	$5.2^{+2.3}_{-1.6}\times10^{-6}$	$> 99.99\%$			
	$5.1^{+*}_{-3.2}$	$1.5^{+1.1}_{-1.0}\times10^{-6}$	$> 95\%$			
M 51- 13814	$0.64^{+0.08}_{-0.04}$	$1.6^{+0.4}_{-0.3}\times10^{-5}$	$> 99.99\%$	$1.02^{+0.05}_{-0.05}$	$0.52^{+0.30}_{-0.24}$	$> 99.9\%$
M 51- 13815	$0.67^{+0.10}_{-0.08}$	$6.9^{+3.4}_{-2.9}\times10^{-6}$	$> 95\%$	$1.30^{+0.06}_{-0.04}$	$5.3^{+*}_{-3.9}$	$> 99\%$
M 101-934-high	$0.61^{+0.06}_{-0.06}$	$1.7^{+1.0}_{-1.1}\times10^{-5}$	$> 99.9\%$			
	$0.98^{+0.16}_{-0.17}$	$3.9^{+1.4}_{-1.4}\times10^{-5}$	$> 95\%$			
	$2.5^{+*}_{-1.2}$	$1.9^{+1.9}_{-1.6}\times10^{-5}$	$> 95\%$[1]			
M 101-934-med	$0.61^{+0.06}_{-0.06}$	$2.6^{+0.5}_{-0.4}\times10^{-5}$	$> 99\%$	$1.07^{+0.03}_{-0.03}$	$2.1^{+1.3}_{-0.8}$	$> 99.9\%$
M 101-row 32	$0.59^{+0.21}_{-0.26}$	$2.9^{+4.6}_{-1.5}\times10^{-6}$	$> 99\%$	$0.93^{+0.05}_{-0.04}$	$2.1^{+1.6}_{-0.9}$	$> 99\%$
M 101-4737	$0.70^{+0.17}_{-0.13}$	$3.1^{+1.5}_{-1.5}\times10^{-5}$	$> 95\%$			
	$1.30^{+0.20}_{-0.20}$	$4.3^{+1.7}_{-1.6}\times10^{-5}$	$> 99\%$			

[1] This thermal plasma component is statistically equivalent to a *bremsstrahlung* or *comptt* component.

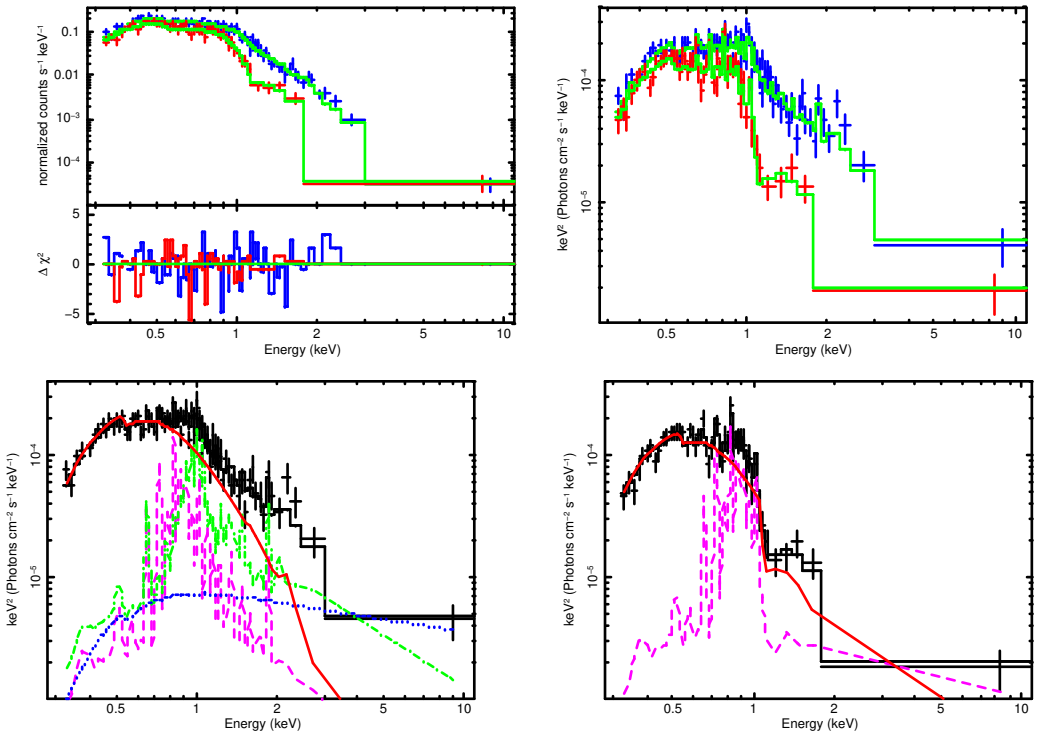

Figure 4.9: Top left panel: *Chandra*/ACIS-S spectral data, model fits and χ^2 residuals for the M 101 ULS during the high count-rate (blue datapoints) and medium count-rate (red datapoints) time intervals of ObsID 934 (2000 March 26). The intervals were originally defined by Mukai et al. (2003) and were also used by Kong and Di Stefano (2005) and by Soria and Kong (2016). Both spectra were grouped to > 15 counts per bin before χ^2 fitting. Top right panel: unfolded spectra of the M 101 ULS during the high and medium count-rate intervals of ObsID 934 (blue and red datapoints, respectively), corresponding to the spectral fits shown in the top left panel. Bottom left panel: detailed view of the model components required to fit the high count-rate interval: a blackbody component at $T_{\rm bb} \approx 135$ eV (solid red curve), and three *mekal* components with $T_1 \approx 0.6$ keV (dashed magenta curve), $T_2 \approx 1.0$ keV (dot-dashed green curve) and $T_3 \approx 2.5$ keV (dotted blue curve). Bottom right panel: model components required to fit the medium count-rate interval: a blackbody component at $T_{\rm bb} \approx 119$ eV (solid red curve), a single *mekal* component with $T \approx 0.6$ keV (dashed magenta curve), and an absorption edge at $E \approx 1.05$ keV with optical depth $\tau \approx 2$. The harder, high count-rate interval has spectral properties more in-line with those of the ULX population, suggesting that sources are able to transition between ULS and ULX spectral classes.

component is 2005 January 1 (ObsID 4737), as shown in Soria and Kong (2016). The hard excess above the blackbody component is again well fitted with *mekal* components, providing once again an emitted luminosity $\approx 7 \times 10^{38}$ erg s^{-1} in the 0.3–10 keV band out of a total in the same band of $\approx 4 \times 10^{39}$ erg s^{-1}.

For the ULS in NGC 247, we compared the *Chandra* spectra from 2011 February 1 (ObsID 12437) and from 2014 November 12 (ObsID 17547). In the first epoch (red datapoints and ratios in Figure 4.10), the fitted blackbody temperature is $kT_{\rm bb} \approx 120$ eV. Adding thermal-plasma components here does not improve the fit, although this may be due to the low signal-to-noise ratio and few counts available (we had to use the Cash statistics for spectral fitting). An absorption edge is detected at $E = 0.95 \pm 0.02$ keV, with optical depth $\tau \approx 4$. In the 2014 spectrum (blue datapoints and ratios in Figure 4.10), the fitted blackbody temperature has increased to $kT_{\rm bb} \approx 140$ eV. The absorption feature has disappeared, and a hard tail is now significantly detected above the blackbody spectrum, up to ≈2 keV. The hard component can be equally well modelled as thermal-plasma emission at $kT \approx 1.5$ keV, or as an inverse-Compton component with a high-energy cut-off at ≈2 keV. Based on this epoch alone, this source could also be classified as a standard ULX with soft excess. The unabsorbed 0.3–10 keV luminosity of the harder component is $\approx 2 \times 10^{38}$ erg s^{-1}, out of a total emitted luminosity in the same band of $\approx 1.5 \times 10^{39}$ erg s^{-1}.

Among the observations listed in Table 4.1.2 for all seven ULSs, only a few have enough counts to allow multi-component fitting. However, the presence of harder spectral components in several observations (in addition to those already discussed for M 101 and NGC 247) may be indirectly inferred from model-independent X-ray colour-colour plots. Using the energy bands defined in Section 4.1.1, we expect that supersoft sources with a pure blackbody spectrum at $kT_{\rm bb} \lesssim 100$ eV should cluster around (H−M)/T≈ 0, (M−S)/T ≈ −1. Instead, we find (compare Figure 4.11 with Figure 4.1) that the distribution of all the observations suggests a possible small scatter towards slightly harder colours (a type of colours characteristic of what were called "quasi-soft sources", Di Stefano and Kong, 2003, 2004). Such colours are consistent with the presence of either a thermal-plasma emission or a soft inverse-Compton or power-law tail in many epochs. The appearance of this hard component suggests that ULSs can transition into ULXs.

4.3.3 Preliminary study of short-term variability

Although the focus of this chapter is on the spectral properties of the ULS population, we also briefly examined the intra-observation variability of the indi-

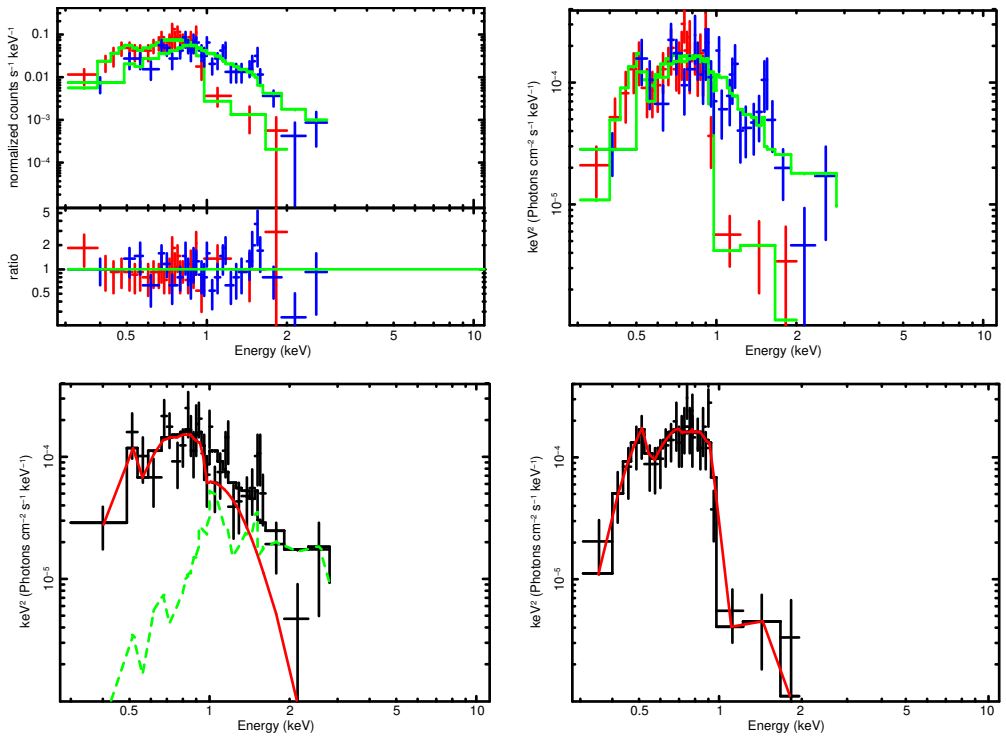

Figure 4.10: Top left panel: *Chandra*/ACIS-S spectral data, model fits and data/model ratios for the NGC 247 ULS during two different observations: blue datapoints are for ObsID 17547 (2014 November 12), red datapoints for ObsID 12437 (2011 February 1). As for the M 101 ULS (see Figure 4.9), both spectra are dominated by blackbody emission (see Table 4.2 for the fit parameters), but during ObsID 17547 there is additional harder emission, while during ObsID 12437 there is an absorption edge. Model ratios rather than residuals were plotted because both spectra were fitted (unbinned) with the Cash statistics and were later rebinned for plotting purposes only. Top right panel: unfolded spectra of the NGC 247 ULS during ObsID 17547 (blue datapoints) and ObsID 12437 (red datapoints), corresponding to the fits shown in the top left panel. Bottom left panel: detailed view of the model components required to fit ObsID 17547: a blackbody component at $T_{\rm bb} \approx 130$ eV, and a *mekal* component with $T_1 \approx 1.3$ keV. Bottom right panel: model components required to fit ObsID 12437: a blackbody component at $T_{\rm bb} \approx 120$ eV, and an absorption edge at $E \approx 0.95$ keV with optical depth $\tau \approx 4$.

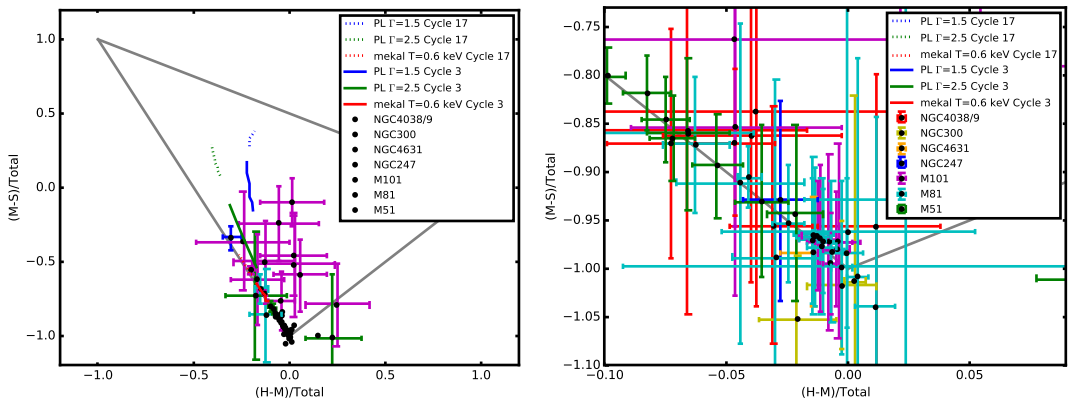

Figure 4.11: Left panel: X-ray colour-colour plot of all ULS observations considered in our study (Table 4.1.2). Error bars are plotted only for datapoints not clustered around $(0.0, -1.0)$; error bars for the clustered datapoints are shown in the zoomed-in right panel. The colours are defined based on the background-subtracted count rates in the following bands: S = 0.3–1.1 keV; M = 1.1–2.5 keV; H = 2.5–7.0 keV. Purely supersoft thermal spectra would cluster exactly at $(0.0, -1.0)$. As an indicative comparison, we plot the expected colours of sources with different spectral models. Red solid line: colours of a thermal-plasma spectrum with $kT = 0.5$ keV, and absorbing column density ranging from 2×10^{20} cm^{-2} to 2×10^{21} cm^{-2}, if observed with *Chandra*/ACIS-S during Cycle 3. Red dotted line: same as above but for *Chandra*/ACIS-S observations during Cycle 17. Green solid line: colours of a power-law spectrum with photon index $\Gamma = 2.5$, and absorbing column density ranging from 2×10^{20} cm^{-2} to 2×10^{21} cm^{-2}, if observed with *Chandra*/ACIS-S during Cycle 3. Green dotted line: same as above but for *Chandra*/ACIS-S observations during Cycle 17. Blue solid line: as above, for a photon index $\Gamma = 1.5$ during *Chandra* Cycle 3. Blue dotted line: as above, for *Chandra* Cycle 17. Right panel: X-ray colour-colour plot with error bars, zoomed in around $(0.0, -1.0)$ for clarity. These plots show that in most of the epochs, the observed colours are consistent with a pure supersoft thermal spectrum (essentially consistent with the predicted regions plotted in Figure 4.1 for temperatures of 70–150 eV), but in a few cases there is a hint of additional harder components.

vidual sources. The main objectives are to search for possible eclipses and to test whether there is a difference between the variability of the harder and softer photons. Finding eclipses in a ULS would confirm that it is viewed at high inclination, and would provide other useful constraints on the size of the system and the type of donor star, hence it would also help us understand the ULS class as a whole. Finding different variability behaviour at lower and higher energies would confirm the presence of two separate emission components, strengthening the link with the behaviour of standard ULXs (Middleton et al., 2011a; Sutton et al., 2013b).

Possible detection of an eclipse was claimed for M 81 N1 in the *Chandra* ObsID 390 (Swartz et al., 2002). At the beginning of that observation, the observed count rate and flux were at the highest recorded value for this source, ≈0.2 counts s^{-1}, but dropped to a value consistent with zero in ≈ 200 s. That drop happened simultaneously in a softer (0.3–0.7 keV) and harder (0.7–1.5 keV) subband (Figure 4.12, top panel). Possibilities such as a sudden change in accretion rate, or in the size of the photosphere, were examined in Swartz et al. (2002), but the most likely explanation was considered to be an eclipse by the companion star. Therefore, we searched for evidence of similar sudden flux changes in other epochs. We examined all 20 *Chandra* observations, and found that sharp drops of the count rate to effectively zero for a few hundred or a few 1000 s occur several times, with different durations, no regular pattern, and sometimes interspersed with small flarings. We also found no relation between the hardness of the source (ratio between the count rates at 0.7–1.5 keV and 0.3–0.7 keV) during an observation and the likelihood of flux dips. In short, those dips appear as random fluctuations, as far as we can ascertain. We show (Figure 4.12, top panel) the original Swartz et al. (2002) claim of an eclipse, together with a similar episode during ObsID 5940 (Figure 4.12, middle panel), and, conversely, a sudden increase of the count rate in ObsID 5944 (Figure 4.12, bottom panel) after an initial part of the observation consistent with no observed flux. Dips in the count rate from an average baseline value to zero often occur over timescales as short as ≈100 s. The morphology of these dips (and a few other dips of shorter duration during some of the other epochs) suggests that we are not seeing an eclipse from the donor star. Instead, we argue that we are looking at occultations from cold, optically thick "clouds" (or equivalent structures) located near or above the outer disk. In the super-Eddington outflow interpretation of ULSs, we do indeed expect the emitting region to be surrounded by denser, cooler clouds, possibly falling onto the outer disk in a "failed wind" scenario. Another possibility is that the obscuring material is associated with the accretion stream from the donor star, or where such stream impacts the outer disk. In the case of M 81 N1, assuming that it is a stellar-mass

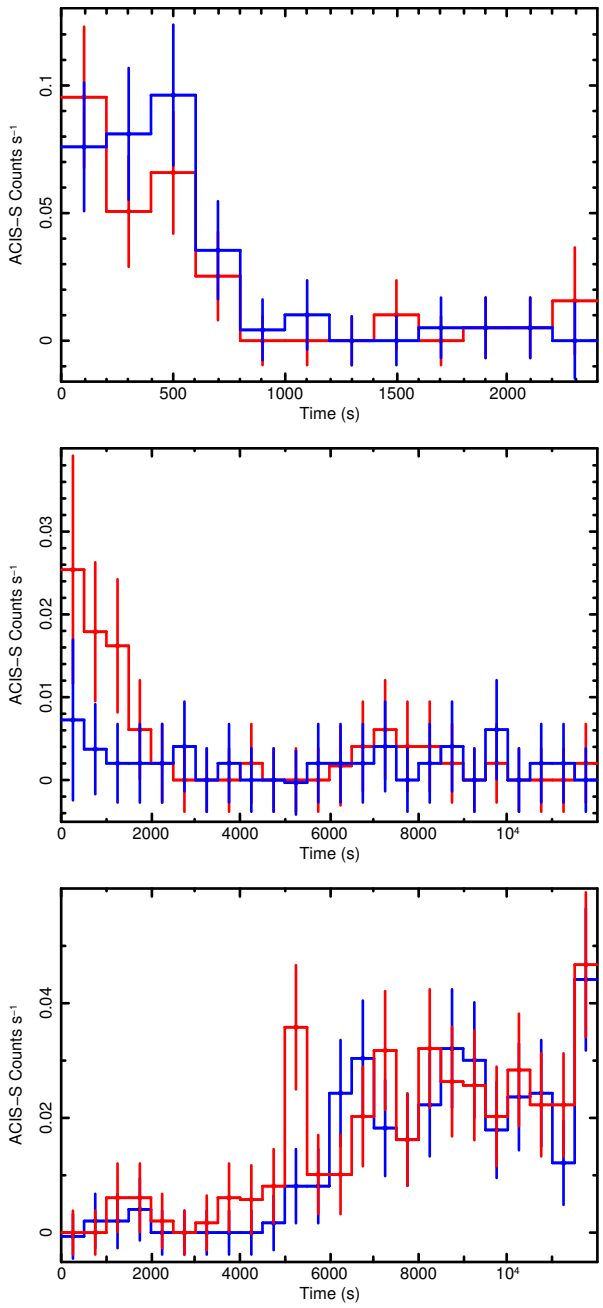

Figure 4.12: Top panel: *Chandra*/ACIS-S background-subtracted lightcurve of M 81 N1 during ObsID 390. Red datapoints = 0.3–0.7 keV band; blue datapoints = 0.7–1.5 keV band. The data have been binned to 200-s intervals. Middle panel: as above, for ObsID 5940 and 500-s bins. Bottom panel: as above, for ObsID 5944 and 500-s bins. Error bars in all plots have been calculated using Poisson statistics (Gehrels, 1986). The strong short-term variability may be due to eclipses or occulations from cold, optically thick clouds. (See Table 4.1.2 for details of the observing epochs.)

X-ray binary, with typical outer radius of the accretion disk $\sim 10^{11}$–10^{12} cm, we can easily verify that obscuring clouds or clumps in virial motion or Keplerian rotation, located at the outer edge of the disk, would be able to occult the emitting region (size $r_{\rm bb} \approx$ a few 10^9 cm) in a time $t \sim 2r_{\rm bb}/v_{\rm K} \lesssim 100$ s.

We found analogous energy-independent dips in the *Chandra* lightcurves of the M 51 ULS, at some epochs. The two most striking examples are shown in Figure 4.13. In the top panel, we show the full-band lightcurve from ObsID 13814. We examined other point-like sources and background regions in the same field to verify that the dip that occurred at observation time $\approx 1.5 \times 10^5$ s is real, and not a glitch or detector artifact. The full duration of the dip is $\approx$8000 s. We also show (Figure 4.13, middle panel) a zoomed-in view of the same dip in the 0.3–0.7 keV and 0.7–1.5 keV bands. Only 3 days later (ObsID 13815), in the subsequent *Chandra* observation of M 51, the ULS appeared at a very low flux level at the start of the observation (Figure 4.13, bottom panel) and then jumped up to an average flux an order of magnitude higher in less than an hour; the initial low-flux interval lasted for at least 18 ks. Clearly, we cannot explain both dips as due to an eclipse by the donor star, because of their different duration. On the other hand, it is also unlikely (especially for the dip in ObsID 13814) that such sharp, energy-independent flux suppressions and recoveries are due to state transitions in the emitting region of the flow. Thus, occulting material in the outer disk or outer part of the black hole Roche lobe passing in front of the emitting region seems to be the most likely explanation, especially if ULSs are seen at high inclination angles.

Somewhat similar dips were previously seen in a ULX in NGC 55 (Stobbart et al., 2004) and were also interpreted as orbiting clumps of obscuring material passing in front of our line of sight. In that case, the relative depth of the flux dips increased at higher energies (Stobbart et al., 2004); instead, in the M 81 and M 51 ULSs, the dips appear energy-independent. However, the energy bands over which we detected the dips in those two ULSs are only 0.3–0.7 keV and 0.7–1.5 keV, because of a lack of higher-energy photons. Another ULX that showed non-periodic dipping behaviour, found from *Swift* monitoring, is NGC 5408 X-1 (Grisé et al., 2013); incidentally, both ULXs in NGC 55 and NGC 5408 are in the soft-ultraluminous regime (Sutton et al., 2013b), which is relevant for what we shall discuss in Section 4.4.3. A possible comparison can also be made with the transitions between Compton-thin and Compton-thick spectra in some AGN, most notably NGC 1365, which have been interpreted (Risaliti et al., 2005, 2007) as occultations by rotating clouds or similar circumnuclear absorbers.

A discussion of the complex high intra-observation variability of the ULS in M 101 is presented in Soria and Kong (2016); here we shall only mention a couple

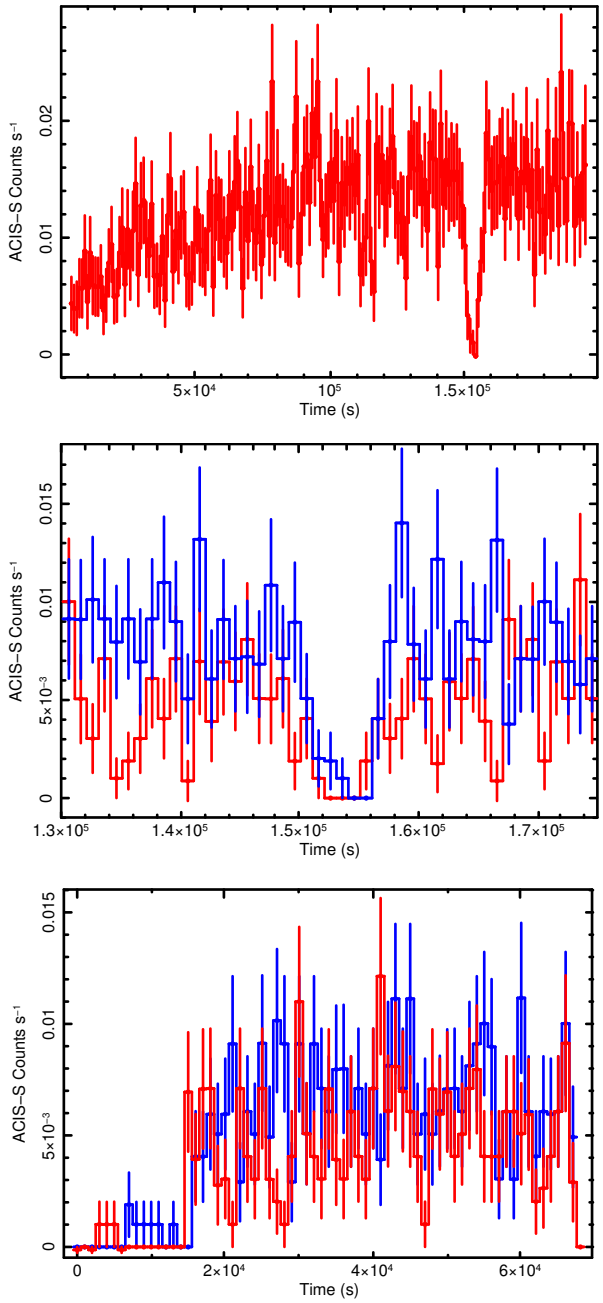

Figure 4.13: Top panel: *Chandra*/ACIS-S background-subtracted lightcurve of the M 51 ULS during ObsID 13814, in the 0.3–1.5 keV band (1000-s bins). Middle panel: zoomed-in view of the time around the dip, during ObsID 13814 (1000-s bins). Red datapoints = 0.3–0.7 keV band; blue datapoints = 0.7–1.5 keV band. Bottom panel: *Chandra*/ACIS-S 0.3–1.5 keV lightcurve of the M 51 ULS during ObsID 13815 (1000-s bins). Red datapoints = 0.3–0.7 keV band; blue datapoints = 0.7–1.5 keV band.

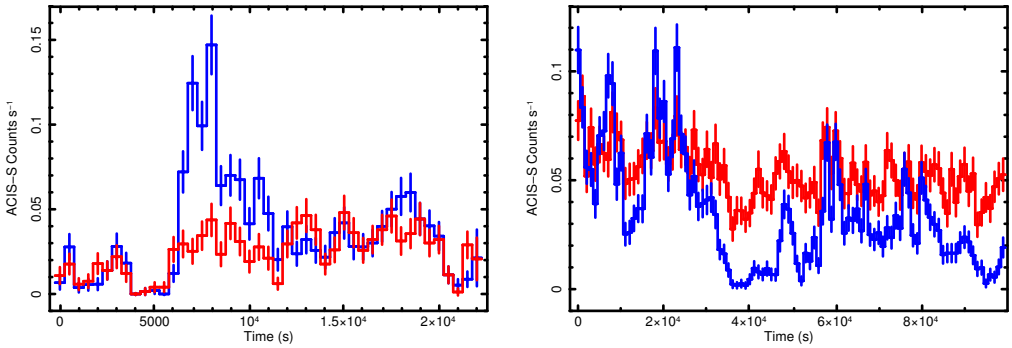

Figure 4.14: Left panel: *Chandra*/ACIS-S background-subtracted lightcurve of the M 101 ULS during ObsID 4737 (500-s bins). Red datapoints = 0.3–0.7 keV band; blue datapoints = 0.7–1.5 keV band. Right panel: *Chandra*/ACIS-S background-subtracted lightcurve of the M 101 ULS during ObsID 934 (1000-s bins). Red datapoints = 0.3–0.7 keV band; blue datapoints = 0.7–1.5 keV band.

of issues more directly relevant to the questions addressed in this chapter. We did not find conclusive evidence of sharp energy-independent dips at any epoch, although there are possible hints of similar behaviour, for example the interval between 4000 and 6000 s into *Chandra* ObsID 4737 (Figure 4.14, left panel). Instead, M 101 ULS is notable for the short-term variability and irregular flaring of the emission, especially in the harder energy band (0.7–1.5 keV). The different behaviour of the soft-band and hard-band lightcurves (Figure 4.14, both panels) is consistent with the presence of two emission components, which is what we have already shown from spectral analysis (Section 4.3.2). For a more quantitative estimate, we calculated the root-mean-square (rms) fractional variability (Edelson et al., 2002; Markowitz et al., 2003; Vaughan et al., 2003; Gierliński and Zdziarski, 2005; Middleton et al., 2011a) in the two individual observations with the highest signal-to-noise ratio: ObsID 934 and ObsID 4737. The lightcurves from both observations were binned to 10-s intervals. The results are summarised in Table 4.5 (see also Soria and Kong, 2016). The huge fractional variability is another strong argument against IMBH models and more generally against the standard disk emission. Accretion disks in a high/soft state have low ($<$ a few %) variability (Belloni, 2010). The increase in rms variability at higher energies is similar to what is found in ULXs in the soft-ultraluminous state (Sutton et al., 2013b; Middleton et al., 2011a, 2015a).

Although the lightcurves in the 0.3–0.7 and 0.7–1.5 keV bands for the M 101 ULS appear different and probably dominated by two distinct emission components, such components cannot be independent of each other. As we discussed in Section 4.3.2 (see also Soria and Kong, 2016), the harder component appears only when the soft thermal component is warmer (blackbody temperature $\gtrsim$100 eV) and its emitting area smaller (blackbody radius $\lesssim$20,000 km). In the framework

Table 4.5: rms fractional variability in different energy bands, for the two observations of the M 101 ULS with higher signal-to-noise ratio.

Parameter	ObsID 934	ObsID 4737
Band (Hz)	10^{-5}–0.05	5×10^{-5}–0.05
rms (0.3–0.7 keV)	$< 36\%$	$(58 \pm 12)\%$
rms (0.7–1.5 keV)	$(70 \pm 4)\%$	$(89 \pm 6)\%$
rms (1.5–7.0 keV)	$(100 \pm 24)\%$	$(162 \pm 17)\%$

of the optically thick wind model, the harder component becomes visible when the outflow photosphere shrinks. Another caveat is that the variability of the observed count rate in the softer band is not necessarily a good proxy for the variability of the thermal component. We know that its radius and temperature vary in anticorrelation within a single observation (as is the case in ObsID 934) and between epochs, with smaller changes in the emitted flux (the larger emitting area somewhat compensating for the lower temperature). The observed changes in the 0.3–0.7 keV count rate mostly track the shift of the blackbody peak between soft X-rays and far-UV (in and out of the detector's sensitivity) rather than changes in the intrinsic bolometric luminosity of the thermal component; conversely, the dramatic flaring of the lightcurve above 0.7 keV probably tracks real flux changes in the harder component.

Finally, we examined the remaining four ULSs of our sample, looking for further examples of interesting short-term variability in the 0.3–0.7 and 0.7–1.5 keV bands, at least at epochs with better signal-to-noise ratio (Figure 4.15). We already showed that NGC 247 ULS has two emission components during *Chandra* ObsID 17547: its lightcurve shows the harder component decline and disappear over the 5000-s duration of that observation. Independent short-term variability is seen in both the 0.3–0.7 and 0.7–1.5 keV bands for the Antennae ULS, but the low signal-to-noise ratio prevents more quantitative analysis. Only emission in the 0.3–0.7 keV band was detected in the NGC 300 ULS, the softest of all the sources in our sample. The *XMM-Newton* observation of the NGC 4631 ULS provides another possibly different type of variability, with a characteristic timescale of ≈15 ks independently seen both in the softer and harder band. This quasi-periodic variability was discovered by Carpano et al. (2007) and interpreted as the binary period of the system; alternatively, Soria and Ghosh (2009) suggested it might also be explained as a pulsation period of a B-type donor star. Considering that the periodicity is based only on two dips during an ≈40-ks good-time-interval of a single observation, we cannot rule out a non-periodic flaring behaviour, similar

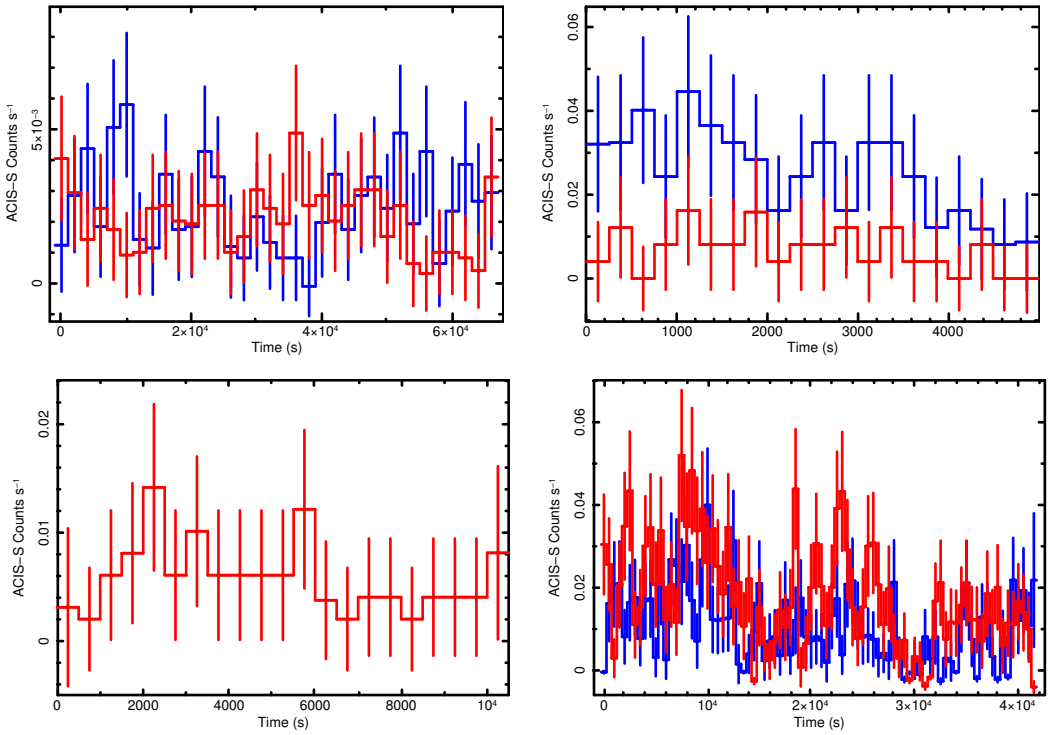

Figure 4.15: Top left panel: *Chandra*/ACIS-S background-subtracted lightcurve of the Antennae ULS during ObsID 3042 (2000-s bins). Top right panel: *Chandra*/ACIS-S background-subtracted lightcurve of the NGC 247 ULS during ObsID 17547 (250-s bins); see Figure 4.10 for a spectrum of that same observation. Bottom left panel: *Chandra*/ACIS-S background-subtracted lightcurve of the NGC 300 ULS during ObsID 9883 (500-s bins); only soft (0.3–0.7 keV) emission was detected. Bottom right panel: *XMM-Newton*/EPIC-pn background-subtracted lightcurve of the NGC 4631 ULS during ObsID 0110900201 (500-s bins). In all panels, red datapoints = 0.3–0.7 keV band; blue datapoints = 0.7–1.5 keV band. Error bars were calculated using Gehrels statistics.

to flaring behaviour of other ULSs.

4.4 Physical interpretation

4.4.1 Alternative models for ULSs

Our results show that ULSs share common properties and deserve to be identified as a distinct sub-class of accreting sources. Their characteristic blackbody temperatures are ≈50–140 eV, their fitted radii span a range ≈5,000–100,000 km, and their extrapolated bolometric luminosities are ≈ a few times 10^{39} erg s^{-1}. We have presented a sample of observations large enough to show a significant anticorrelation between temperature and luminosity, but no trend between bolometric luminosities and temperatures. Based on the population properties presented in Section 4.3, we can now address some of the unsolved problems.

The most exotic and intriguing scenario proposed for ULSs is that we are seeing the optically thick, geometrically thin disk of an accreting IMBH in the high/soft state, by analogy with the thermal state of stellar-mass black holes. This implies that the fitted disk-blackbody radius corresponds to the inner radius of the accretion disk and should be a good approximation for the innermost stable circular orbit. Assuming non-spinning Schwarzschild black holes, the characteristic range of radii observed in our sample translates to a black hole mass range $\approx$500–10,000 $M_\odot$. However, there are several problems with this interpretation. Firstly, we see the fitted radius change from epoch to epoch for the same source, indicating that it cannot be fixed at $r_{\rm ISCO}$. This point is reinforced by the fact that none of the sources follow the $L \propto T^4$ trend that is expected of accretion disks in the high/soft state (e.g., Remillard and McClintock, 2006), nor the flatter $L \propto T^2$ trend observed when the accretion rate approaches the Eddington limit (Kubota and Makishima, 2004). Instead, we observe no significant trend in luminosity associated with changes in radius and temperature (Figures 4.2 and 4.3).

Secondly, the high/soft state scenario is not self-consistent, in the sense that the inferred luminosities and temperatures are too low for the fitted radii. This can be better illustrated in the following way. The characteristic relation between peak colour temperature and dimensionless accretion rate (in Eddington units) for a standard disk is

$$kT_{\rm in} \approx 230\,(\dot{m}/M_4)^{1/4}\ {\rm eV} \tag{4.1}$$

(Shakura and Sunyaev, 1973; Kubota et al., 1998; Soria, 2007; Done et al., 2012), where M_4 is the black hole mass in units of $10^4 M_\odot$. For a black hole to be in the canonical high/soft state, the accretion rate must be (on average) $\dot{m} \gtrsim 0.02$ (Maccarone, 2003); we can also take $\dot{m} \lesssim 1$ as a safe upper limit above which stellar-mass black holes are in the very high state or ultraluminous state, with an additional power-law component or broad-band inverse-Compton emission, and will appear non-thermal (Remillard and McClintock, 2006; Gladstone et al., 2009). Taken together, those relations imply that for each fitted colour temperature, we can determine the range of black hole masses for which the accretor is in the thermal-dominant state:

$$M_{\rm min,4} \equiv 0.02 \left(\frac{230\ {\rm eV}}{kT_{\rm in}}\right)^4 \lesssim M_4 \lesssim \left(\frac{230\ {\rm eV}}{kT_{\rm in}}\right)^4 \equiv M_{\rm max,4} \tag{4.2}$$

From this mass range, we can then determine the corresponding luminosity range of the thermal-dominant state at a given temperature, because $L \approx \dot{m}\, L_{\rm Edd}$ in

that state. Thus:

$$L_{\rm min} \equiv 0.02 L_{\rm Edd}(M_{\rm min}) \lesssim L \lesssim L_{\rm Edd}(M_{\rm max}) \equiv L_{\rm max}, \tag{4.3}$$

that is

$$5.2 \times 10^{38} \left(\frac{230 \text{ eV}}{kT_{\rm in}}\right)^4 \lesssim \frac{L}{\text{erg s}^{-1}} \lesssim 1.3 \times 10^{42} \left(\frac{230 \text{ eV}}{kT_{\rm in}}\right)^4. \tag{4.4}$$

The luminosity range of Equation (4.4) is plotted as a grey shaded area in Figure 4.8. For example, for $kT_{\rm in} = 100$ eV, the high/soft state condition $\dot{m} \gtrsim 0.02$ requires a black hole mass $M \gtrsim 5600 M_\odot$ and a bolometric disk luminosity $L \gtrsim 1.5 \times 10^{40}$ erg s^{-1}. The extrapolated disk luminosity of all the ULSs in our sample at almost all epochs falls below the shaded area; therefore, if they were IMBHs, their accretion rates would be too low to be in the high/soft state. The M 101 ULS is the only source in our sample for which a direct mass estimate has been attempted, based on the optical spectra and time variability properties. Liu et al. (2013) argued that they have determined strong constraints to its dynamical mass, suggesting that it is a stellar-mass black hole or neutron star. Some of the results of that study are still partly disputed (Soria and Kong, 2016), but the evidence in favour of a stellar-mass accretor appears to be stacking up, as it is also for standard ULXs (Motch et al., 2014).

The second possible physical interpretation for ULSs is that they are the high-luminosity tail of the classical SSS population, which is thought to be powered by surface-nuclear-burning white dwarfs (van den Heuvel et al., 1992; Greiner, 1996; Kahabka and van den Heuvel, 1997; Greiner and Di Stefano, 2002; Starrfield et al., 2009). ULSs and SSSs largely overlap in their temperature range; however, ULSs are on average an order of magnitude more luminous than the upper luminosity threshold of SSSs (Figure 4.5), with very few detections in the gap between the two populations. In itself, this does not prove that classical SSSs and ULSs are distinct physical systems, because ULSs have been specially selected over a large volume of space based on their extreme luminosity. (A study of the luminosity distribution of SSSs and ULSs in an identical, complete sample of galaxies is beyond the scope of this work.) Models of soft, thermal X-ray emission from the expanding atmosphere of a white dwarf have been successfully used to reproduce nova outburst behaviour (e.g., Ness, 2010; van Rossum, 2012; Ness et al., 2013). The anticorrelation between temperatures and radii observed in ULSs (Figure 4.6) is at least qualitatively in agreement with this scenario, corresponding to the transition between optically bright and X-ray bright phases of SSSs (Southwell et al., 1996; McGowan et al., 2005; Rajoelimanana et al., 2013).

The fast variability (typical of clumpy ejecta), the occasional dips possibly caused by cold absorbers transiting in front of the emitting source, and the detection of additional thermal-plasma components may also be consistent with an optically thick outflow, which cools as it expands, launched from the white dwarf surface. What is more problematic is that ULSs are persistently seen at luminosities an order of magnitude higher than the Eddington limit of the most massive white dwarfs. It is hard to explain how quasi-steady nuclear burning can be sustained at such luminosities for decades, instead of triggering runaway processes leading to nova-like outbursts on timescales of a few tens of days (e.g., as observed in MAXIJ0158−744: Li et al., 2012; Morii et al., 2013).

The third possible interpretation for ULSs is that they are powered by either black holes or neutron stars accreting at highly super-critical rates. In this scenario, massive radiatively-driven outflows are launched from the disk; if the accretion rate is high enough and our viewing angle sufficiently high, such outflows may be optically thick and create a large photosphere that shrouds the source of X-ray photons near the compact object (King and Pounds, 2003; Poutanen et al., 2007; King, 2010; Shen et al., 2015). The expansion and contraction of the wind photosphere accounts for the anticorrelated changes in the observed radius and luminosity, similarly to the expanding and contracting white dwarf atmosphere in the thermonuclear burning scenario. Density inhomogeneities in the outflow can explain the highly variable nature of ULSs and the coexistence of optically-thin and optically-thick thermal emission components at some epochs, and absorption edges at other epochs. Clumpy, optically thick outflows are indeed predicted by MHD simulations of super-critically accreting black holes (Jiang et al., 2014; Takeuchi et al., 2013, 2014). It was shown (Soria and Kong, 2016) that with plausible assumptions on the super-Eddington luminosity and launching radius of the outflow (near the spherisation radius), the observed temperatures and blackbody radii of ULSs suggest a highly super-Eddington $\dot{m} \sim$ a few 100 (Figure 4.6), which for a 10-$M_\odot$ black hole corresponds to $\dot{M} \approx 10^{-4} M_\odot$ yr^{-1}. This is certainly extreme but similar to the accretion rate inferred for example in SS 433 (Fabrika, 2004). Mass transfer rates $> 10^{-4} M_\odot$ yr^{-1} from a donor star onto a black hole or neutron star, on a thermal timescale, were shown to be viable (Wiktorowicz et al., 2015) at various stages of stellar evolution, most notably when intermediate-mass stars pass through the Hertzsprung gap.

We suggest that the accretion rate and viewing angle determine the average temperature, radius and luminosity over a viscous timescale, while the clumpiness of the outflow causes the observed short-term variability and possible occultation episodes, on timescales of a few 100 to a few 1000 s. The simple model proposed by Shen et al. (2015) and Soria and Kong (2016) is based on a spherically symmetric

approximation of the outflow. In reality (as already noted in Poutanen et al., 2007), the viewing angle is also important, because the outflow is expected to be denser closer to the disk plane, and may have an open funnel along the polar axis. Therefore, a super-Eddington accreting black hole may appear as a ULS (in which the source of hard photons is completely masked by the wind photosphere) when seen at high inclination angles *and* extremely high accretion rates (effectively optically thick outflow); or as a ULX in the soft-ultraluminous regime (in which there is a soft inverse-Compton tail) when seen at slightly lower inclination angles and/or accretion rates (outflow only optically thick to scattering); or as a ULX in the hard-ultraluminous regime (in which there is a harder, more extended inverse-Compton tail) when seen at low inclination angles (looking into the polar funnel). See Figure 4.16 for a cartoon description of this spherically-symmetric scenario.

4.4.2 ULS accretors: neutron stars or black holes?

For a large enough accretion rate, neutron star accretors should be just as viable as black hole accretors in powering ULSs. If the magnetic field of the neutron star is too strong, it will impede the accretion flow and truncate the accretion disk at the magnetospheric radius. However, at near- or super-Eddington accretion rates, the pressure of the inflow can push the magnetospheric radius down to $r_{\rm ISCO}$ or just outside the neutron star surface. The magnetospheric radius is defined as

$$r_{\rm M} = 5.1 \times 10^8 \dot{M}_{16}^{-2/7} m_1^{-1/7} \mu_{30}^{4/7} \,{\rm cm}, \tag{4.5}$$

(Frank et al., 2002) where $\dot{M}_{16}$ is the accretion rate in $10^{16}\,{\rm g\,s^{-1}}$, m_1 is the neutron star mass in $\rm M_\odot$, μ_{30} is the magnetic moment $\mu = Br^3$ in units of $10^{30}\,{\rm G\,cm^3}$. For a 1.4-$M_\odot$ neutron star, $r_{\rm ISCO} \approx 1.2 \times 10^6$ cm $\approx r_{\rm NS}$. Hence, the magnetospheric radius is pushed down to $r_{\rm ISCO}$ for $\dot{M} \gtrsim 4.4 \times 10^{19} B_9^2$ g s^{-1} $\approx 7 \times 10^{-7} B_9^2 M_\odot$ yr^{-1} (with B_9 the magnetic field in units of 10^9 G). Such values of the accretion rates are plausible not only for Hertzsprung-gap stars but even for massive donors evolving on their nuclear timescale. For comparison, the Eddington accretion rate for a neutron star is $\approx 10^{18}$ g s^{-1}. Moreover, if a super-Eddington disk outflow develops and forms a large, optically thick photosphere at $\dot{M} \sim$ a few $10^{-5} M_\odot$ yr^{-1}, the details of what happens near the inner edge of the accretion disk or at the surface of the neutron star become irrelevant, and a neutron star would look very similar to a black hole, scaled to their respective Eddington luminosities. Since extremely super-critical accretion is expected to happen both in neutron star and black hole systems (Wiktorowicz et al., 2015), we suggest that some ULSs may contain neutron stars, as is also the case for some ULXs

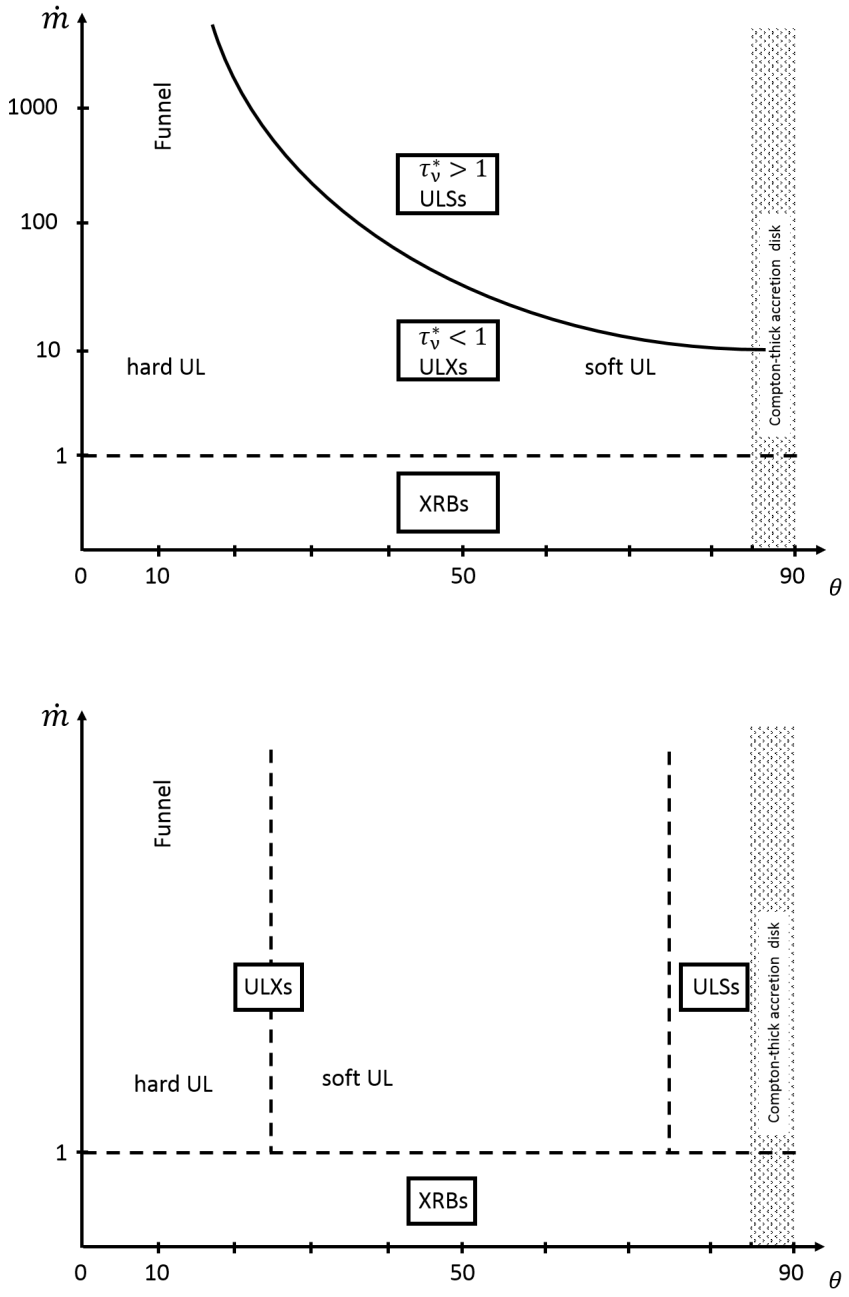

Figure 4.16: Top panel: cartoon sketch of our proposed classification of ULXs and ULSs, function both of the accretion rate $\dot{m}$ and of the viewing angle θ. For super-critical accretors, at most lines-of-sight (except for the polar funnel), there will be an accretion rate threshold at which the outflow becomes dense enough to be effectively optically thick to the X-ray emission from the inner accretion disk. However, this threshold will be reached at lower values of $\dot{m}$ for sources seen at higher inclination angles, because the wind is thicker at higher θ. Bottom panel: an alternative classification in which the difference between ULXs and ULSs depends only on θ. This is not our preferred scenario, because it ignores the fact that the optical thickness of the outflow increases with $\dot{m}$ (Poutanen et al., 2007), and the opening angle of the funnel decreases with $\dot{m}$ (e.g., King, 2009).

(Bachetti et al., 2014). When the fitted blackbody radii and temperatures of the 7+2 supersoft sources in our sample are compared with the predictions of the optically thick outflow model of Soria and Kong (2016), we see (Figure 4.6) that there is an observational spread between the expected location of 10-$M_{\odot}$ black holes and 1.4-$M_{\odot}$ neutron stars. Systems such as r2-12 and NGC 300 SSS2 are indeed consistent with super-Eddington accreting neutron stars.

4.4.3 Link between ULXs and ULSs

The X-ray spectra of most ULXs can be described as a slightly curved broad-band component with an additional, soft thermal component (sometimes known as soft excess) at $kT \approx 0.15$–0.30 keV (Feng and Soria, 2011, for a review). The origin of both components is still unclear. In a super-Eddington accretion scenario (King and Pounds, 2003; Poutanen et al., 2007; Middleton et al., 2015a), the soft emission comes from the wind, near or just outside the spherisation radius. Smeared line-like residuals are sometimes seen at energies $\sim$0.7–2 keV particularly for soft-ultraluminous ULXs; those features are consistent either with thermal plasma emission from a collisionally ionised wind, or with absorption of the smooth broad-band continuum in a partially ionised region of the outflow (Middleton et al., 2014). The broad-band component becomes steeper, and truncated at lower energies (typically, $E \approx 5$ keV) for sources seen at higher inclination angles, which are probably seen through a thicker disk wind (soft ultraluminous regime: Sutton et al., 2013b). This interpretation is consistent with theoretical models of super-Eddington accretion flows (e.g., Kawashima et al., 2012). Conversely, ULXs seen at low inclination angles (i.e., looking down the polar funnel) have a harder spectrum, caused by higher-energy photons emitted in the innermost part of the inflow.

By contrast, ULSs are dominated by the thermal component, at even lower temperatures than ULXs; in most observations, that is in fact the only component significantly detected. At some epochs, a non-dominant harder emission in the 1–5 keV band is also detected (Section 4.3.2). This harder component is consistent with multi-temperature thermal-plasma emission; however, given the relatively low signal-to-noise ratio, we are unable to rule out the alternative interpretation of a soft Comptonised component with superposed absorption lines from partially ionised plasma. In the former case, the harder component may be due to emission from shock-heated gas just outside the outflow photosphere; in the latter case, we may be seeing occasional glimpses of the hard emission from the innermost part of the inflow, down-scattered and partly absorbed through the outflow. The presence of absorption edges at ≈ 1 keV in some sources at some epochs (most

notably, the M101 ULS in the *Chandra* ObsID 934, the NGC 247 ULS in the *Chandra* ObsID 12437, and the NGC 4631 ULS in the *XMM-Newton* observation) is another indication of absorption through a clumpy, variable wind.

The intense short-term variability seen in many ULSs (Table 4.5, and Figures 4.12–4.15) provides a further observational test of the relation between ULSs and ULXs. Low variability is seen from (sub-Eddington) standard disks in the high/soft state (Belloni, 2010). Instead, high variability is seen in ULXs in the soft-ultraluminous regime (Sutton et al., 2013b), in which the fractional variability appears to increase at higher energy bands (Middleton et al., 2011a; Sutton et al., 2013b). For ULXs, this finding was interpreted as evidence that most of the variability is associated with the high-energy tail rather than the soft thermal emission; Sutton et al. (2013b) argued that the variability is due to clumpy material at the edge of the super-Eddington outflow intermittently occulting our direct view of the hot central regions of the inflow. For the brightest ULS in our sample, the one in M 101, we also find that when a harder component is present, its emission is more variable and distinct from than that of the soft component (Figure 4.14), which is consistent with the ULX interpretation. However, we stress again that with the data at hand, we cannot yet determine whether the harder ULS component is optically-thin thermal plasma emission in the outflow, or a glimpse of direct hard emission from the innermost part of the inflow, down-scattered and absorbed through the outflow.

The soft thermal component is itself variable from observation to observation and sometimes within individual observations. We showed (Section 4.3.1) that there is a correlation between lower blackbody temperatures and higher blackbody radii. For example, the fitted temperature of the thermal component in the M 101 ULS went from < 50 eV (90% confidence limit) on 2004 December 22–24, up to 75 ± 6 eV on 2004 December 30, then 100 ± 10 eV on 2005 January 1, and down to 56 ± 5 eV on 2005 January 8 (Table 4.2). At the same epochs, the fitted radius changed from $> 54,000$ km (90% confidence limit) to $43,500^{+29,300}_{-17,200}$ km, to $22,500^{+10,300}_{-4,700}$ km, and back up to $100,000^{+80,000}_{-40,000}$ km. This behaviour suggests that the soft emission comes from the moving photosphere of a variable outflow rather than a fixed-sized structure like an accretion disk, consistent with the interpretation for ULXs. We speculate that we are seeing day-to-day stochastic variability in the density and kinetic energy of the outflow, analogous to the stochastic variability in X-ray luminosity seen in bright X-ray binaries.

Based on the empirical properties summarised above, we propose that ULSs are the most extreme form of the soft-ultraluminous regime, in which the hard photons from the innermost regions are completely (or almost completely) masked and reprocessed by the optically-thick outflow. Like soft-ultraluminous ULXs,

ULSs are likely to be seen at higher inclination angles. We propose that the key qualitative and quantitative difference between soft-ultraluminous ULXs and ULSs is that in the former, the outflow is optically thick to scattering but still effectively optically thin; in ULSs, it is effectively optically thick. In quantitative terms, we can express this condition as follows. Let us assume that the wind (with density ρ) is launched from radius R and observed from infinity; let us define an absorption opacity κ_ν^a and a scattering opacity κ_s. For ULSs we have:

$$\tau_\nu^*(R) = \int_R^\infty \rho\sqrt{\kappa_\nu^a\left(\kappa_\nu^a+\kappa_\mathrm{s}\right)}\,\mathrm{d}r \approx \int_R^\infty \rho\sqrt{\kappa_\nu^a\kappa_\mathrm{s}}\,\mathrm{d}r > 1$$

$$\tau_\mathrm{s}(R) = \int_R^\infty \rho\,\kappa_\mathrm{s}\,\mathrm{d}r > 1, \tag{4.6}$$

while for ULXs it is:

$$\tau_\nu^*(R) = \int_R^\infty \rho\sqrt{\kappa_\nu^a\left(\kappa_\nu^a+\kappa_\mathrm{s}\right)}\,\mathrm{d}r \approx \int_R^\infty \rho\sqrt{\kappa_\nu^a\kappa_\mathrm{s}}\,\mathrm{d}r < 1$$

$$\tau_\mathrm{s}(R) = \int_R^\infty \rho\,\kappa_\mathrm{s}\,\mathrm{d}r > 1. \tag{4.7}$$

We suggest that this is the main reason why ULXs still have a dominant broad-band tail (rolling over at $E \gtrsim 5$ keV) even in the soft ultraluminous state, consisting of hard photons down-scattered multiple times but not absorbed by the outflow. Instead, ULSs lose their tail and are dominated by soft thermal photons emitted near the photosphere. In order for the outflow to be effectively optically thick, at a given viewing angle, the mass outflow rate (likely to be proportional to the mass accretion rate at the outer edge of the disk) must exceed a characteristic threshold, which in a spherical approximation can be estimated as $\dot{m} \gtrsim$ a few 100 (Soria and Kong, 2016; Shen et al., 2015). Soft-ultraluminous ULXs are more likely to be in a regime with $10 \lesssim \dot{m} \lesssim 100$. These numbers are purely indicative, and depend on our viewing angle: we do not expect the wind to be optically thick along near-face-on lines-of-sight regardless of accretion rate, while more moderate accretion rates may be enough to produce an optically thick outflow if the source is viewed almost edge on. For the same reason, the fitted photospheric radius will appear larger when a system is seen more edge-on. Then, epoch-to-epoch variability in ULSs may occur because of changes in the accretion rate (and consequently in the outflow density), or because of changes in our viewing angle, due to disk precession.

If our scenario is correct and ULSs have a highly super-critical mass accretion rate, we might wonder why their extrapolated bolometric luminosities (Table 4.2) are only $\sim$ a few 10^{39} erg s^{-1}, barely reaching 10^{40} erg s^{-1} in the most luminous

epochs. This is a few times lower than the most luminous ULXs found in the same volume of space. This can be justified as follows. Firstly, given the logarithmic dependence of emitted luminosity on $\dot{m}$, with (in the outflow-dominated case) $L \sim L_{\rm Edd}\,(1 + 0.6 \ln \dot{m})$ (Shakura and Sunyaev, 1973; Poutanen et al., 2007), the supposedly higher accretion rate of ULSs does not make a large difference: for example, for $\dot{m} = 30$, $L \approx 3L_{\rm Edd}$, while for $\dot{m} = 300$, $L \approx 4.4L_{\rm Edd}$. Secondly, in the model of Soria and Kong (2016), the main parameter that determines whether or not the outflow is effectively optically thick along a given line of sight (and therefore whether the source will appear as a ULS or a ULX along that line of sight) is the dimensionless mass accretion rate $\dot{m}$ (normalised by black hole mass), not the absolute accretion rate $\dot{M}$. The absolute value of $\dot{M}$ available for accretion is limited by the evolutionary stage of the donor star, but for a fixed $\dot{M}$, smaller black holes (and neutron stars) will have a higher value of $\dot{m}$ and therefore a higher chance to be seen as ULSs than more massive black holes. For example, a 50-$M_\odot$ black hole with $\dot{M} \approx 2 \times 10^{21}$ g s^{-1} will have $\dot{m} \approx 30$ (probably not high enough to make the outflow effectively optically thick) and an intrinsic luminosity $L \approx 2 \times 10^{40}$ erg s^{-1} (typical of the brightest ULXs). Instead, a 10-$M_\odot$ black hole with $\dot{M} \approx 4 \times 10^{21}$ g s^{-1} will have $\dot{m} \approx 300$ and an intrinsic luminosity $L \approx 6 \times 10^{39}$ erg s^{-1} (typical of ULSs). Thirdly, if the outflow is denser and effectively optically thick as we suggest it is in ULSs, a larger fraction of radiative power is absorbed and converted to thermal and kinetic energy of the outflow: the photospheric luminosity may be only $\sim$ 20–50 per cent of the intrinsic radiative power (Lipunova, 1999; Poutanen et al., 2007). Finally, the higher apparent luminosity of hard-ultraluminous ULXs is boosted by geometric collimation along the polar funnel, while the apparent luminosity of ULSs is more likely to be reduced, if they are seen at high inclination angles.

Another corollary of our proposed scenario is that ULSs may become similar to soft-ultraluminous ULXs when their photospheric radius seen along our line of sight decreases (corresponding to a decrease in $\dot{m}$ and in the total mass in the outflow or to a change in viewing angle), thus revealing the underlying inverse-Compton scattering region and/or inner disk region, sources of the harder emission component. This is consistent with our observed temperature distribution of the thermal component in ULSs (Figure 4.7): sources with $kT_{\rm bb} \lesssim 150$ eV are mostly ULSs, while sources with $kT_{\rm bb} \gtrsim 150$ eV generally contain a harder component and are classified as standard ULXs. For temperatures $\approx$ 100–150 eV we expect a degree of overlapping between the two classes, as for the same accretion rate and outflow structure, a system can appear as a ULX if seen more face-on, or as a ULS if seen more edge-on. The observed appearance of harder emission components in some ULSs (particularly those in M 101 and NGC 247) only when

their blackbody temperature reached ≈130 eV and their radius shrank below ≈20,000 km may be additional evidence in favour of our proposed connection.

4.5 Conclusions

Individually identified ULSs in nearby galaxies have often been considered odd sources, difficult to place in the X-ray binary and ULX classification schemes. Here we have re-examined *Chandra* and *XMM-Newton* data for a sample of seven previously identified ULSs, showing that they share common properties: a thermal spectrum with a characteristic range of temperatures, luminosities, sizes, and an anticorrelation between radius and temperature, consistent with $r_{\rm bb} \sim T_{\rm bb}^{-2}$. Thus, they may represent a new sub-type or state of accreting systems.

We discussed the main alternative interpretations of ULSs presented in the literature, and showed that the IMBH scenario is strongly disfavoured for several reasons: rapid changes in the fitted radius of the thermal component; inconsistency of temperatures and luminosities with the standard disk parameters; strong short-term flux variability. Steady nuclear burning on the surface of a white dwarf (with a possibly inflated or outflowing atmosphere) is usually invoked for classical SSSs at luminosities $\lesssim 10^{38}$ erg s^{-1}, but there are no convincing models able to explain steady sustained luminosities $\sim$ 10–50$L_{\rm Edd}$ (for a white dwarf) over decades without the triggering of nova-like outbursts. Instead, we argued that optically-thick outflows from super-critically accreting black holes (and possibly also neutron stars) are the most likely explanation for this class. In particular, a clumpy optically-thick wind with an expanding or contracting photosphere (function of the mass density in the outflow and therefore also related to the accretion rate) seems a natural explanation for the anti-correlation between observed temperatures and radii, and for the strong short-term variability.

We showed that in some ULSs, a harder emission component is detected alongside the dominant thermal component at some epochs, resulting in a spectrum that sometimes resembles those of typical ULXs; more specifically, those in the soft-ultraluminous regime (Sutton et al., 2013b), which are probably seen through a dense wind at high inclination. The appearance of a harder component in ULSs happens preferentially at epochs when the fitted blackbody radius of the thermal component is smallest ($r_{\rm bb} \lesssim 20,000$ km) and the fitted blackbody temperature is highest ($T_{\rm bb} \gtrsim 100$ eV), consistent with a reduced size of the photosphere and therefore a more direct view of the inner regions. Based on this finding, and on the analogies between the thermal component in ULXs and ULSs, we proposed that ULSs are simply the regime of the ULX population seen through the densest outflow: a state in which any direct, harder emission from the inner disk and the

inverse-Compton region has been completely masked and thermalised by the optically thick wind. In our scenario, the difference between ULSs and ULXs in the soft-ultraluminous regime is that the outflow is effectively optically thick in ULSs (leading to complete absorption and thermal reprocessing of the harder photons from the inner region) and only optically thick to scattering in ULXs, sources in which a harder tail is still carrying most of the flux. This may be due to a higher viewing angle and/or a higher accretion and outflow rate in ULSs. As previously discovered in soft-ultraluminous ULXs (Sutton et al., 2013b; Middleton et al., 2015a), we found at least for one ULS in our sample (M 101 ULS, the only one with sufficiently high signal-to-noise ratio for this kind of analysis) that the harder component has a higher fractional variability than the softer component.

The nature of the harder component remains unclear, given the relatively low signal-to-noise ratio of even the brightest sources, and the fact that only CCD-resolution spectra are available for ULSs. Such a low spectral resolution, compounded by the degradation in the soft response of *Chandra*/ACIS-S, makes it almost impossible to identify individual emission or absorption features in the soft and medium energy bands. However, even at this low resolution, we confirmed that several ULSs have strong absorption edges at $E \approx 1$ keV (as noted by Kong et al., 2004), which appear and disappear at different epochs. Their physical interpretation remains unclear, and is beyond the scope of this work, but it is another piece of evidence in favour of massive, optically thick outflows in those sources. As for the excess emission above the dominant thermal component, particularly in the 0.7–1.5 keV band, we showed that it is consistent with thermal plasma emission, but we cannot rule out more complex interpretations, such as an inverse-Compton component with superposed absorption features caused by absorption in a partially ionised outflow, as suggested by Middleton et al. (2014) for analogous spectral features in some ULXs.

Using a spherically symmetric approximation and standard assumptions about the launching radius of the wind, we estimated that $\dot{m} \sim$ a few 100 is required to make the outflow effectively optically thick (although, this value is likely to be an overestimate for more edge-on systems). Thus, if our interpretation is correct, ULSs are some of the best case studies of super-critical accretion and super-Eddington outflows in the local Universe. Their extrapolated bolometric luminosities are between a few 10^{39} erg s^{-1} and $\approx 1 \times 10^{40}$ erg s^{-1}, a few times lower than for the most luminous ULXs. We explained (Section 4.4.3) why this is not in contradiction with our suggestion that ULSs have extremely high $\dot{m}$. This is partly because a substantial fraction of the initial radiative power is converted to mechanical and thermal energy of the optically-thick outflow; partly because ULSs may have higher $\dot{m}$ but lower black hole mass and lower intrinsic

luminosity than the most luminous ULXs; and partly because at least some of the (apparently) most luminous ULXs may benefit from geometric collimation of the emission along the polar direction.

Another consequence of our proposed scenario is that when the photosphere expands beyond ≈100,000 km, and the blackbody temperature decreases below ≈50 eV (either because of real physical changes in the two quantities, or because of a change in our line of sight), a ULS should become undetectable in the X-ray band, its thermal emission having shifted to the far UV. ULSs that were detected as bright sources in some observations are sometimes not detected in others. M 101 ULS provides a typical example, with a detected *Chandra*/ACIS-S 0.3–2 keV count rate ≈0.1 ct s^{-1} in the brightest observation, but $< 5 \times 10^{-4}$ ct s^{-1} in 14 of the 25 *Chandra* observations examined in Soria and Kong (2016). The NGC 300 ULS is another good example: detected in a bright state in one *Chandra* and two *XMM-Newton* observations (listed in Table 4.1.2 and analysed in this chapter), it was not detected in another three *Chandra* and three *XMM-Newton* observations. By analogy with the behaviour of transient X-ray binaries, we could interpret those non detections (or extremely faint detections) as the off (or low) state of ULSs. However, this would be hard to reconcile with our classification, because it is very contrived to imagine that an accreting black hole can only switch between extremely super-Eddington ($\dot{m} > 100$) and low sub-Eddington ($\dot{m} < 0.01$) accretion rates, without ever being seen in other canonical accretion states (e.g., hard intermediate state, high/soft state, broadened-disk ULX state). Our scenario implies that a ULS non-detection at a certain epoch is not due to a real drop in luminosity, and is caused instead by one of the following three reasons: (a) its photosphere has physically expanded to the point that the source is now in an ultraluminous UV regime (perhaps similar to the "ultraluminous UV source" in NGC 6946 discussed by Kaaret et al. 2010); or (b) our view of the source is completely occulted by cold absorbing material (as is briefly the case during the dips observed at some epochs for the M 81 and the M 51 sources); or (c) our line-of-sight has changed (become more edge-on) due to systemic precession.

4.6 Summary

In this chapter, we analysed *Chandra* and *XMM-Newton* data of seven known ULSs to identify how these sources fit into the general scheme of accreting compact objects. The key results from this work are:

- ULSs show little variation in their radiative energy outputs over a wide range of temperatures and emitting areas.

- The anticorrelation between the emitting area and temperature in ULSs ($r_{\rm bb} \sim T_{\rm bb}^{-2}$) is expected for an expanding/contracting photosphere.
- We reject the interpretation that ULSs represent the emission from cool accretion disks around IMBHs or nuclear-burning on the surface of accreting white dwarfs.
- For the outflow to have a photosphere that is effectively optically thick ($\tau^* > 1$), the outflow rates, and hence accretion rates, should be $\dot{m} > 100$. This is our proposed model for ULSs; they represent ULXs at the highest accretion rates.

Chapter 5

Eclipsing ultraluminous X-ray sources

This chapter is adapted from:

R. Urquhart and R. Soria. 2016. "Two eclipsing ultraluminous X-ray sources in M 51", *The Astrophysical Journal*, Volume 831, Issue 1, article id. 56, 23 pp., DOI:10.3847/0004-637X/831/1/56

I conducted all work for this chapter under the guidance of my supervisory panel.

In Chapter 4, we explored the possibility that ULSs are ULXs at the highest accretion rates and/or seen at high inclination angles. If this is the case, then ULSs should be preferentially seen at high inclination angles and, consequently, there should be a higher fraction of sources in the ULS state that demonstrate eclipses. In fact, in the most extreme case, ULSs could simply be ULXs seen at the highest inclination angles, rather than being physically distinct sources. In this chapter, we outline the serendipitous discovery of the first eclipsing ULXs. We detail the identification of two ULXs within the galaxy M 51 (Figure 5.1) that demonstrate sharp transitions in their lightcurves indicative of occultations by their respective companion stars. We use this property to help constrain physical characteristics of the binaries such as inclination, period, and mass function. Finally, we discuss the implication that ULX spectral properties are not inherently linked to inclination angle, as previously suggested in the literature.

X-ray spectroscopic studies have previously been used to qualitatively constrain ULX viewing angles: it was suggested (Sutton et al., 2013b) that ULXs seen at lower inclination (down the polar funnel) have harder X-ray spectra while

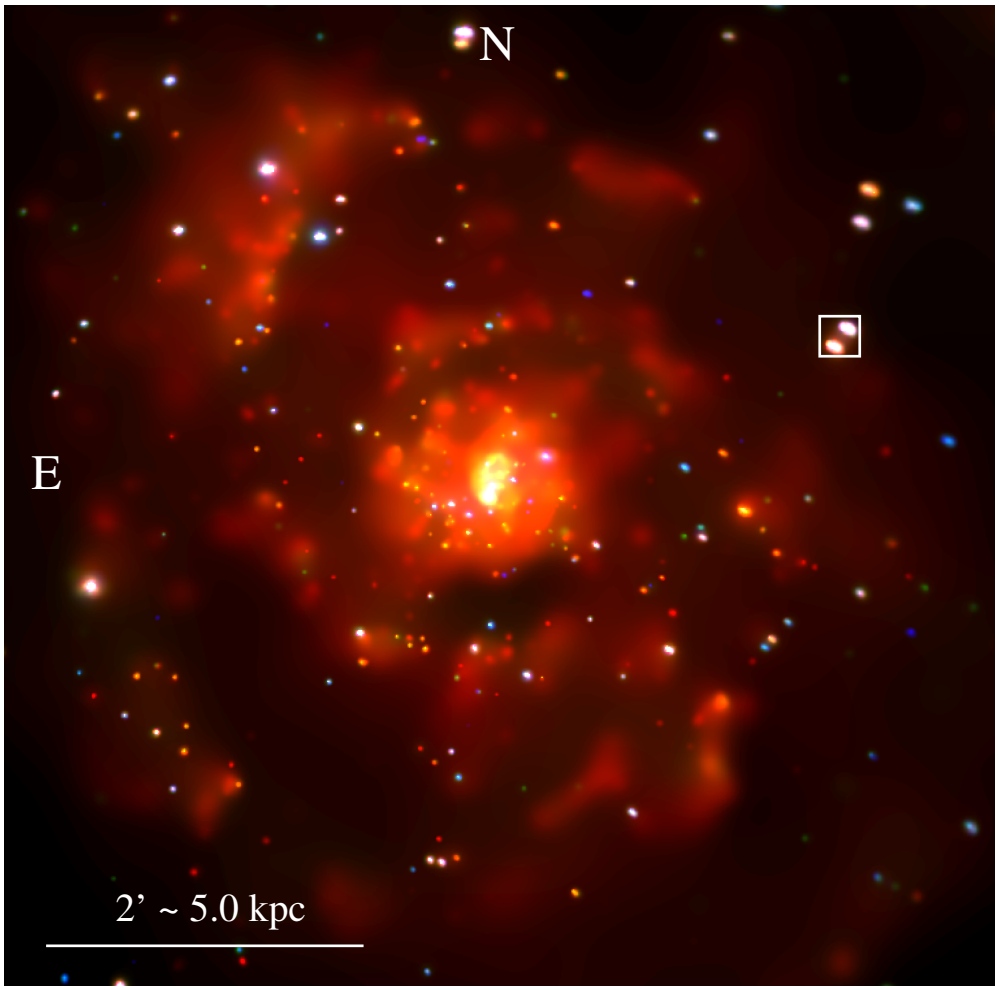

Figure 5.1: *Chandra*/ACIS X-ray colour image. Red = 0.3–1 keV, green = 1–2 keV, and blue = 2–7 keV. Inside the 15″ × 15″ box, ULX-1 is the lower source (slightly redder and hence softer colour) while ULX-2 is the upper source (harder colour).

those seen at higher inclination (through the disk wind) have softer spectra with a lower-energy downturn, due to a higher degree of Compton scattering in the wind. This interpretation is consistent with the presence of absorption and emission features (interpreted as signatures of the outflow) in the X-ray spectra of ULXs with softer spectra (Middleton et al., 2014, 2015b). It is also in agreement with a higher degree of short-term variability (interpreted as the imprint of a clumpy wind) in sources with softer spectra (Middleton et al., 2015a). However, in this chapter we will challenge this interpretation.

Apart from those indirect or statistical arguments, until recently there was no bright extragalactic stellar-mass black hole for which the viewing angle could be directly pinned down. We have now discovered two such sources, both located in the same spiral arm of the spiral galaxy M 51; in fact, surprisingly, they appear

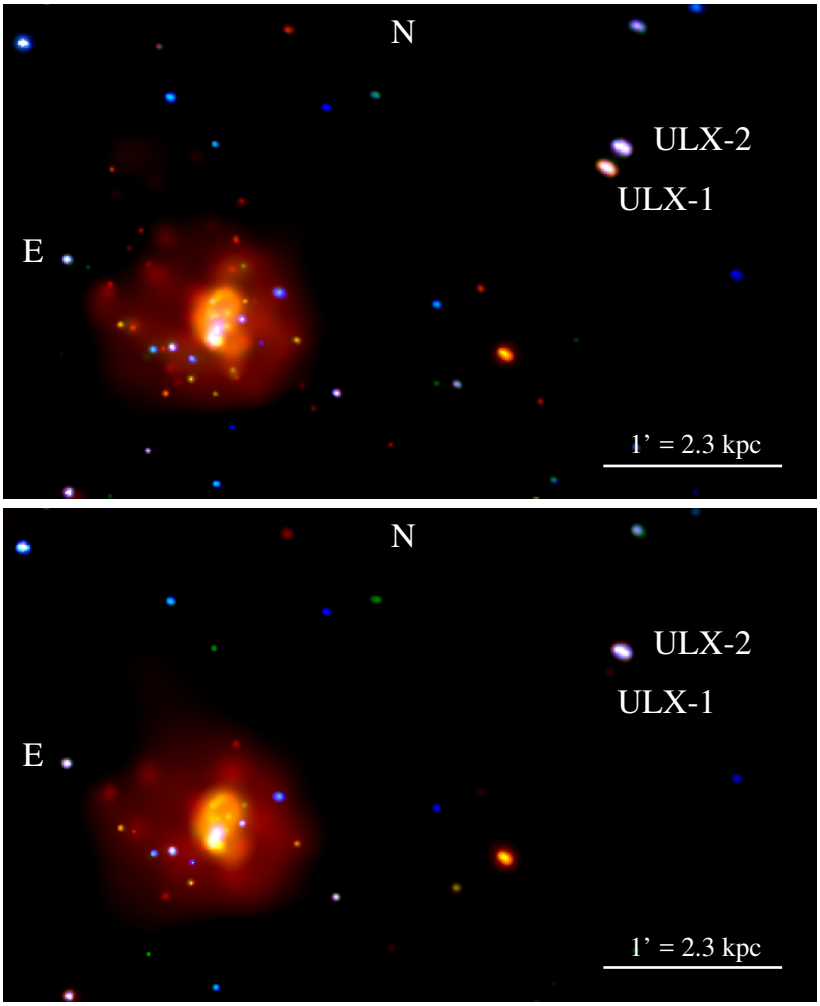

Figure 5.2: Top panel: *Chandra*/ACIS-S adaptively smoothed 190-ks image of M 51 during ObsID 13814, showing the location of ULX-1 and ULX-2 with respect to the nuclear region on the left side of the images. Red represents the 0.3–1 keV band, green the 1–2 keV band, and blue the 2–7 keV band. Bottom panel: as in the top panel, but only for the portion of ObsID 13814 during which ULX-1 is in eclipse (70 ks).

projected on the sky within only ≈ 350 pc of each other (see Figure 5.2). Both sources have X-ray luminosities $\gtrsim 10^{39}$ erg s^{-1}, and crucially, they both show sharp X-ray drops and rebrightenings, which we interpret as eclipses by their donor stars, occulting the inner region of the disk. The presence of eclipses places a lower limit on the inclination angle ($i \gtrsim 75°$) as we must be viewing the X-ray sources near edge-on. In this chapter, we present the eclipse discovery and the main X-ray timing and spectral properties of the two sources. We will also briefly discuss more general implications and opportunities for our modelling of these systems provided by the detection of eclipses. In Chapter 6, we will present a study of the newly-discovered optical and radio evidence of jets and winds of those same two ULXs.

5.1 Targets of our study

M 51, also known as the Whirlpool Galaxy, is an interacting face-on spiral at a distance of 8.0 ± 0.6 Mpc (Bose and Kumar, 2014). The two eclipsing sources discussed in this chapter are those catalogued as CXOM51 J132940.0+471237 (henceforth, ULX-1) and CXOM51 J132939.5+471244 (henceforth, ULX-2) in Terashima and Wilson (2004). We re-estimated their positions using all the *Chandra* data available to-date, and obtained RA (J2000) = $13^{\rm h}29^{\rm m}39\overset{\rm s}{.}94$, Dec. (J2000) = $+47°12'36\overset{''}{.}6$ for ULX-1, and RA (J2000) = $13^{\rm h}29^{\rm m}39\overset{\rm s}{.}44$, Dec. (J2000) = $+47°12'43\overset{''}{.}3$ for ULX-2. Both positions are subject to the standard uncertainty in the absolute astrometry of *Chandra* pointings, $\approx 0\overset{''}{.}7$ at the 90% confidence level[1]. A more precise determination of their positions is left to our follow-up study of their optical and radio counterparts (Chapter 6).

ULX-1 and ULX-2 were first discovered as a single unresolved source by the *Einstein Observatory* (Palumbo et al., 1985). This was followed up with observations with *ROSAT* (source C in Ehle et al. 1995; source R7 in Marston et al. 1995). The higher spatial resolution of *Chandra*/ACIS finally led to the two sources being resolved (source 6 and source 5 in Terashima and Wilson, 2004). ULX-1 was found to be a relatively soft source, with very few counts above 2 keV. ULX-2 was found to be variable, decreasing in luminosity by a factor of ≈ 2.5 between observations (Terashima and Wilson, 2004). Further spectral studies of the two sources, based on a 2003 *XMM-Newton* observation, were carried out by Dewangan et al. (2005). With a much larger database of *Chandra* and *XMM-Newton* observations available since then, we have now studied the two sources in more detail, and found more intriguing properties.

5.2 Data Analysis

M 51 was observed by *Chandra*/ACIS-S fourteen times between 2000 and 2012: two of those observations were too short ($\leq$2 ks) to be useful, and another two did not include our sources in the field of view; the other 10 observations are listed in Table 5.1. (See Kuntz et al. 2016 for a full catalog and discussion of all the *Chandra* sources in M 51.) We downloaded the *Chandra* data from the public archives and re-processed them using standard tasks within the CIAO Version 4.7 software package (Fruscione et al., 2006). Any intervals with high particle backgrounds were filtered out. We extracted spectra and lightcurves for ULX-1 and ULX-2 using circular regions of $\approx 4''$ radii and local background regions three times as large as the source regions. For each observation, background-subtracted

[1] See http://cxc.harvard.edu/cal/ASPECT/celmon/

Table 5.1: Log of the *Chandra* and *XMM-Newton* observations used in this study.

Observatory	ObsID	Exp Time (ks)	Date
Chandra	354	14.9	2000-03-21
	1622	26.8	2001-06-23
	3932	48.0	2003-08-07
	13813	179.2	2012-09-09
	13812	157.5	2012-09-12
	15496	41.0	2012-09-19
	13814	189.9	2012-09-20
	13815	67.2	2012-09-23
	13816	73.1	2012-09-26
	15553	37.6	2012-10-10
XMM-Newton	0112840201	20.9	2003-01-15
	0212480801	49.2	2005-07-01
	0212480901	closed	2005-07-01
	0303420101	54.1	2006-05-20
	0303420301	closed	2006-05-20
	0303420201	36.8	2006-05-24
	0303420401	closed	2006-05-24
	0677980701	13.3	2011-06-07
	0677980801	13.3[a]	2011-06-11

[a]Due to background flaring, only ≈2.5 ks of epoch 0677980801 can be used.

light curves were created with the CIAO task *dmextract*. Spectra were extracted with *specextract*, and were then grouped to a minimum of 15 counts per bin, for χ^2 fitting.

M 51 was also observed by *XMM-Newton* nine times between 2003 and 2011, although no data were recorded on three occasions due to strong background flaring (Table 5.1). We downloaded the *XMM-Newton* data from NASA's HEASARC archive. We used the EPIC observations and re-processed them using standard tasks in the SAS version 14.0.0 software package; we filtered out high particle background exposure intervals. Due to the lower spatial resolution of *XMM-Newton*/EPIC (relative to *Chandra*), the ULXs are not fully resolved, although the elongated appearance of the EPIC source is consistent with the two separate *Chandra* sources (as discussed in Section 5.3.1). For each observation we extracted a single background-subtracted lightcurve and spectrum for both sources combined, using a circular extraction region of 20″ radius, and a local background

Table 5.2: ULX-1 eclipse times and net count rates for the *Chandra* observations. Square brackets signify that the eclipse continues beyond the start/end of the observation for some time.

ObsID	In Eclipse (ks)	Out of Eclipse (ks)	MJD Observation	MJD Eclipse	Count Rate in Eclipse (10^{-3} ct s^{-1})	Count Rate out of Eclipse (10^{-3} ct s^{-1})
354	0	15	51715.34–51715.51			18.1 ± 1.1
1622	25	2	52083.78–52084.09	52083.81–[52084.09]	1.2 ± 0.2	10.7 ± 1.9
3932	0	48	52858.61–52859.16			12.0 ± 0.5
13813	40	139	56179.74–56181.82	[56179.74]–56180.20	0.4 ± 0.1	14.7 ± 0.3
13812	0	157	56182.77–56184.59			12.2 ± 0.3
15496	0	41	56189.39–56189.86			14.8 ± 0.6
13814	70	120	56190.31–56192.50	56191.64–[56192.50]	0.3 ± 0.1	15.6 ± 0.4
13815	0	67	56193.34–56194.12			14.0 ± 0.5
13816	0	73	56196.22–56197.06			12.0 ± 0.4
15553	0	38	56210.03–56210.47			10.2 ± 0.5

Table 5.3: ULX-2 eclipse times and net count rates for the *Chandra* observations. Square brackets signify that the eclipse continues beyond the start/end of the observation for some time.

ObsID	In Eclipse (ks)	Out of Eclipse (ks)	MJD Observation	MJD eclipse (10^{-3} ct s^{-1})	Count Rate in Eclipse (10^{-3} ct s^{-1})	Count Rate out of Eclipse
354	0	15	51715.34–51715.51			18.0 ± 1.1
1622	0	27	52083.78–52084.09			7.6 ± 0.5
3932	0	48	52858.61–52859.16			9.9 ± 0.5
13813	48	131	56179.74–56181.82	[56179.74]–56180.30	0.6 ± 0.1	10.5 ± 0.3
13812	0	157	56182.77–56184.59			10.7 ± 0.3
15496	0	41	56189.39–56189.86			13.7 ± 0.6
13814	0	190	56190.31–56192.50			11.5 ± 0.2
13815	0	67	56193.34–56194.12			3.3 ± 0.2
13816	0	73	56196.22–56197.06			14.6 ± 0.5
15553	0	38	56210.03–56210.47			7.9 ± 0.5

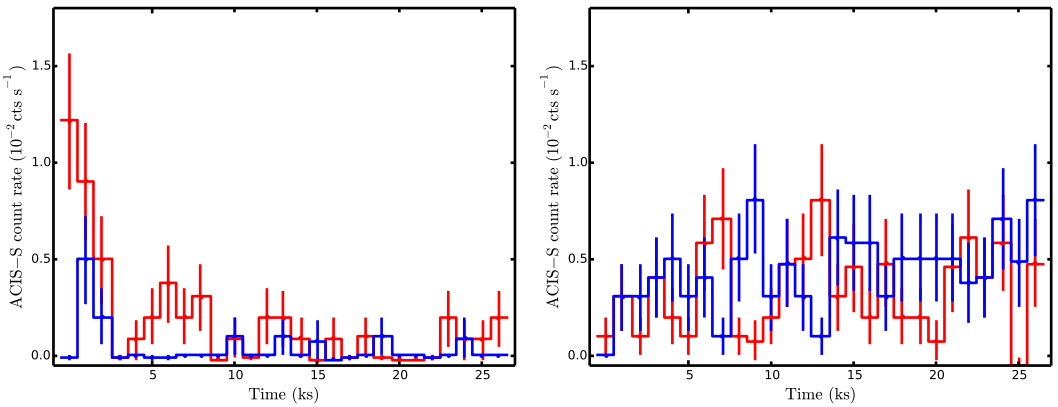

Figure 5.3: Left panel: *Chandra*/ACIS-S background-subtracted lightcurve of ULX-1 from observation 1622, split into a soft band (0.3–1.2 keV: red datapoints) and a hard band (1.2–7.0 keV; blue datapoints). It shows a sharp drop in flux about 2 ks into the observation. The data are binned into 1000-s intervals. Right panel: as in the left panel, for ULX-2 in the same observation.

region that is at least three times larger, does not fall onto any chip gap and is of similar distance to the readout nodes as the source region. Standard flagging criteria `#XMMEA_EP` and `#XMMEA_EM` were used for pn and MOS respectively, along with `FLAG=0`. We also selected patterns 0–4 for pn and 0–12 for MOS. For our timing study, we extracted lightcurves with the SAS tasks *evselect* and *epiclccorr*. For our spectral study, we extracted individual pn, MOS1 and MOS2 spectra with standard *xmmselect* tasks; whenever possible, we combined the pn, MOS1 and MOS2 spectra of each observation with *epicspeccombine*, to create a weighted-average EPIC spectrum. In some observations, the pn data were not usable because the source falls onto a chip gap; in those cases, we used only the MOS1 and MOS2 data in *epicspeccombine*. Finally, we grouped the spectra to a minimum of 20 counts per bin so that we could use Gaussian statistics.

For both *Chandra* and *XMM-Newton* data, spectral fitting was performed with XSPEC version 12.8.2 (Arnaud, 1996). Timing analysis was conducted with standard FTOOLS tasks (Blackburn, 1995), such as *lcurve*, *efsearch* and *statistics*. Imaging analysis was done with HEASARC's DS9 visualisation package, and adaptive image smoothing with CIAO's *csmooth* routine.

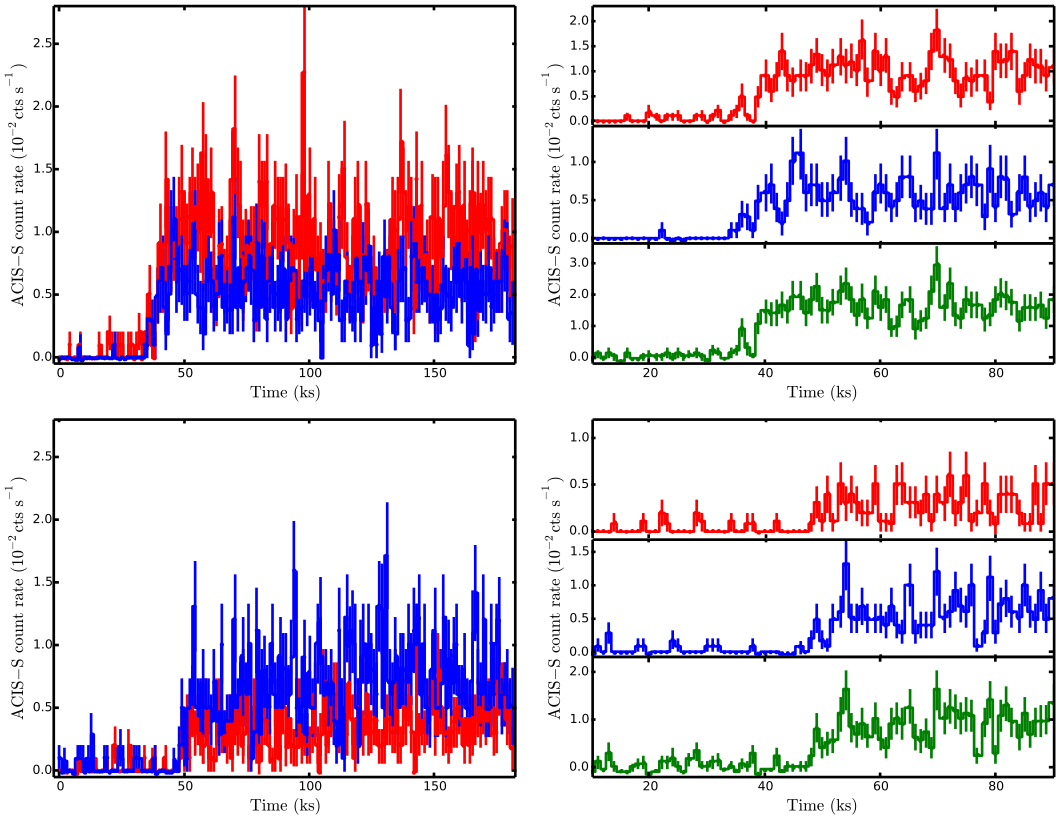

Figure 5.4: Top left panel: *Chandra*/ACIS-S background-subtracted lightcurves of ULX-1 during ObsID 13813 (red for the 0.3–1.2 keV band, blue for the 1.2–7.0 keV band), showing the end of an eclipse about 40 ks into the observation. The data are binned into 1000-s intervals. Top right panel: soft (red curve, 0.3–1.2 keV), hard (blue curve, 1.2–7.0 keV) and total (green curve, 0.3–7.0 keV) *Chandra*/ACIS-S background-subtracted lightcurves of ULX-1 during ObsID 13813, zoomed in around the time of eclipse egress. The data are binned into 1000-s intervals. Bottom left panel: as in the top left panel, for ULX-2 during the same *Chandra* observation showing the end of an eclipse about 50 ks into the observation. Bottom right panel: as in the top right panel, for ULX-2 during ObsID 13813, zoomed-in around the time of eclipse egress.

5.3 Results

5.3.1 Eclipses

5.3.1.1 ULX-1 eclipses and dips in the *Chandra* data

From our inspection of the *Chandra* lightcurves, we have discovered 3 epochs (ObsIDs 1622, 13813 and 13814) in which the flux of ULX-1 is strongly reduced for at least part of the observation (Table 5.2 and Figures 5.3, 5.4, 5.5). The transition between the long-term-average flux level and the lower level occurs too quickly ($\Delta t \sim 10^3$ s) to be explained by a state transition in the inflow, or a change in the mass accretion rate. Our identification of the low state in ObsID 1622 as a

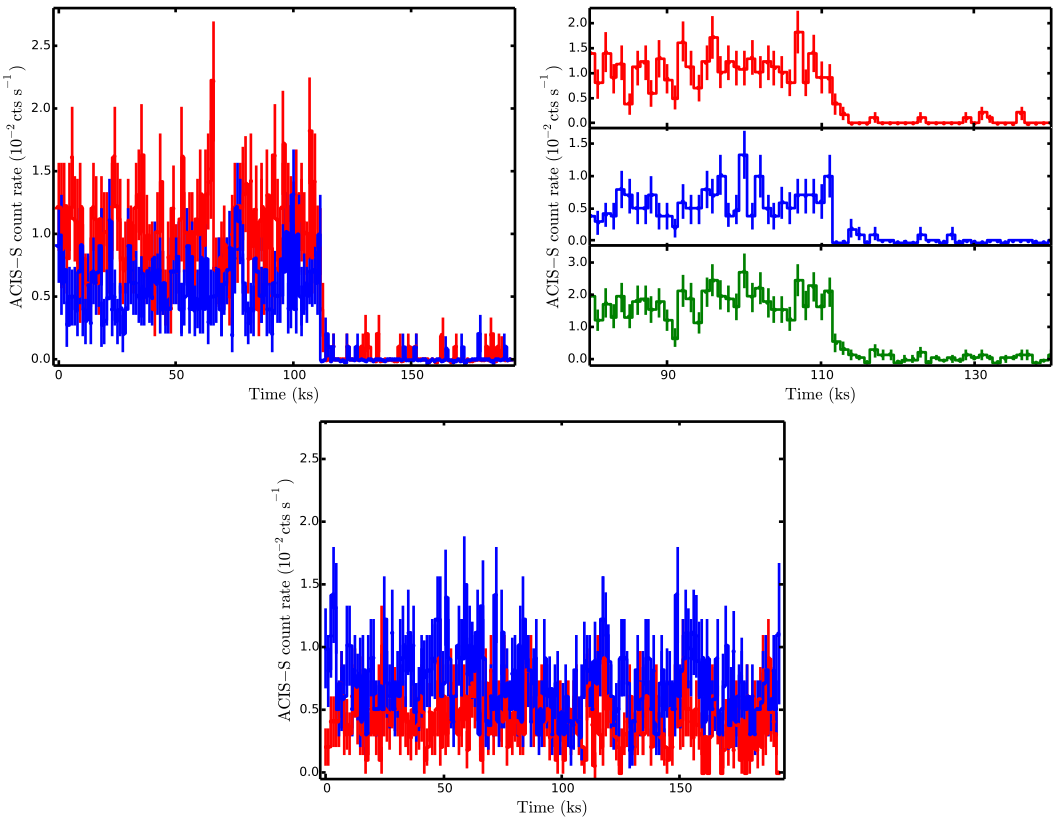

Figure 5.5: Top left panel: *Chandra*/ACIS-S background-subtracted lightcurves of ULX-1 during ObsID 13814 (red for the 0.3–1.2 keV band, blue for the 1.2–7.0 keV band), showing the beginning of an eclipse about 110 ks into the observation. The data are binned into 1000-s intervals. Top right panel: soft (red curve, 0.3–1.2 keV), hard (blue curve, 1.2–7.0 keV) and total (green curve, 0.3–7.0 keV) *Chandra*/ACIS-S background-subtracted lightcurves of ULX-1 during ObsID 13814, zoomed in around the time of eclipse ingress. The data are binned into 1000-s intervals. Bottom panel: as in the top panel, for ULX-2 during the same *Chandra* observation.

true stellar eclipse rather than a dip may be debatable, given that the flux drop happens right at the start of the observation; however, the presence of eclipses is very clear in ObsIDs 13813 (2012 September 9) and 13814 (2012 September 20), which show a low-to-high and a high-to-low transition, respectively. We also checked that ULX-1 is not at the edge of the chip, there are no instrumental glitches, and no other source in the field has a count-rate step change at the same time. We conclude that the simplest and most logical explanation is an eclipse of the X-ray emitting region by the donor star. The flux during the eclipse is not exactly zero: by stacking the time intervals during eclipses, we can find a faint but statistically significant residual emission, softer than the emission outside eclipses. We will discuss the spectrum of the residual emission in Section 5.3.4.

The way ULX-1 enters the eclipse in ObsID 13814 (Figure 5.5) is also interesting. The transition to eclipse in the soft band (0.3–1.2 keV) appears less

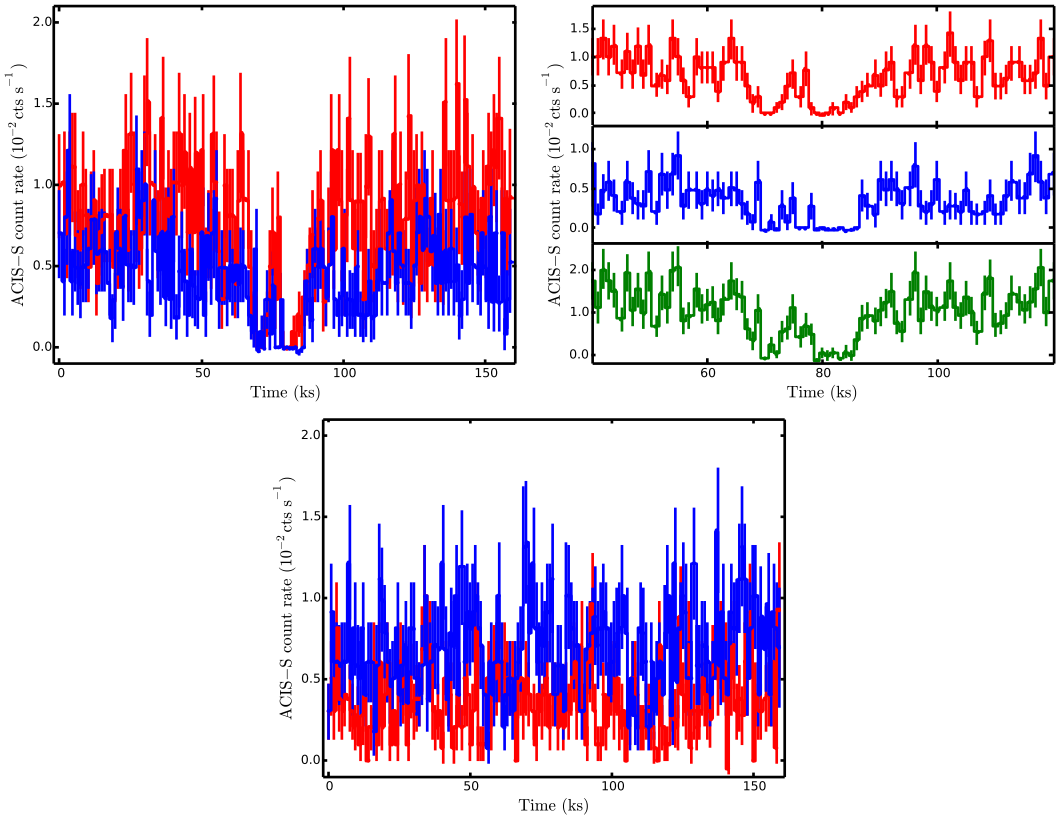

Figure 5.6: Top left panel: as in Figure 5.5, for the *Chandra*/ACIS-S observation 13812 of ULX-1, showing a dip around 70–90 ks into the observation. All data in this panel and in those below are binned to 1000 s. Top right panel: zoomed-in view of the dip in the soft band (red datapoints), hard band (blue datapoints) and total band (green datapoints). Bottom panel: as in Figure 5.5, for observation 13812 of ULX-2.

sharp than the transition in the hard band (1.2–7.0 keV): the soft-band count rate drops to effectively zero in ≈4 ks, while the same transition happens in $\lesssim$1 ks for the hard band. This can be explained if the softer X-ray photons come from a more extended region that takes longer to be completely occulted than the effectively point-like central region responsible for the harder X-ray photons (Bonnet-Bidaud et al., 2001); for example, the softer emission may have contributions from the outer, cooler parts of an outflow. However, we cannot rule out that the discrepancy is simply due to small-number statistics.

Finally, we find a deep dip in the *Chandra* light curve of ULX-1 during ObsID 13812 (Figure 5.6). The count rate drops to zero and then recovers to the pre-dip level, just like during an eclipse. However, the short duration (≈20 ks) and double-dipping substructure of this phase suggest that this occultation is not due to the companion star; we suggest that it is more likely the result of lumps or other inhomogeneities in the thick outer rim of the disk, or is caused by the accretion stream overshooting the point of impact in the outer disk and covering our view

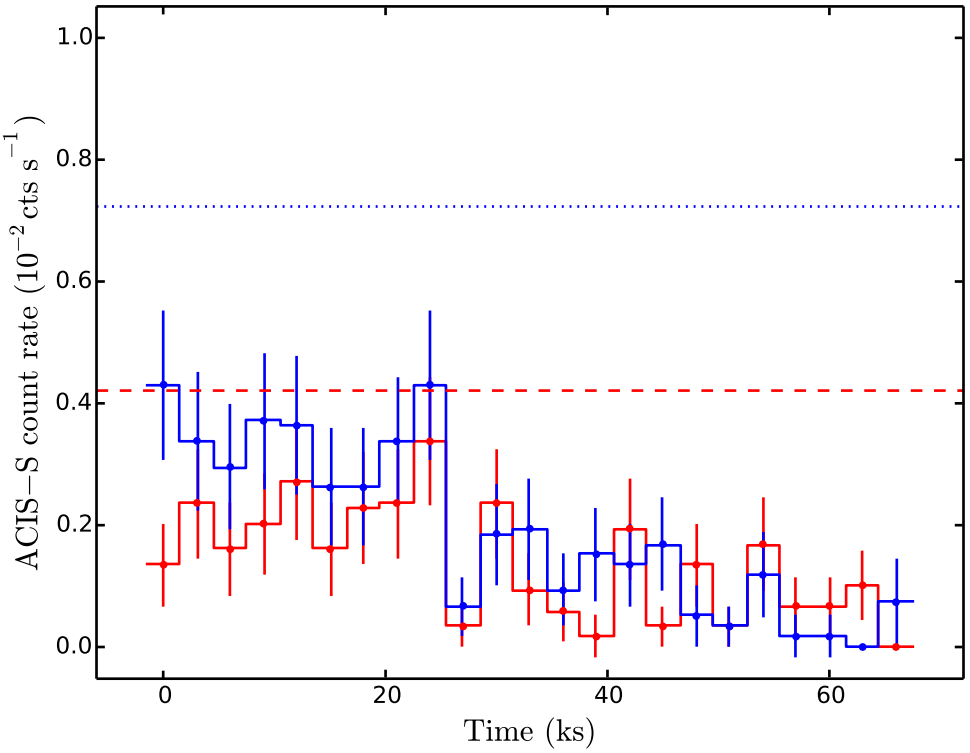

Figure 5.7: *Chandra*/ACIS-S background-subtracted lightcurves for ULX-2 during observation 13815; red datapoints are for the 0.3–1.2 keV band, blue datapoints for the 1.2–7.0 keV band. Data are binned to 300 s. As a comparison, the dashed and dotted lines represent the average count rates for the soft and hard band, respectively, during the previous *Chandra* observation, ObsID 13814, taken 3 days earlier.

of the inner regions (Frank et al., 1987; Armitage and Livio, 1996). Analogous X-ray dips are seen in several Galactic X-ray binaries (e.g., White and Swank, 1982; Bonnet-Bidaud et al., 2001; Homan et al., 2003; Díaz Trigo et al., 2006) and are interpreted as evidence of a high viewing angle. Assuming that the occultation is produced by a geometrically thick structure in Keplerian rotation, we can estimate the angular extent of this feature by scaling the duration of the dipping phase to the binary period of ULX-1. If the period is ≈6 d (see Section 5.3.2), the occulting structure spans $\Delta\phi \approx 14°$; for a ≈13 d period, $\Delta\phi \approx 6°$.

5.3.1.2 ULX-2 eclipse in the *Chandra* data

In the same set of *Chandra* observations, we also discovered one eclipse in ULX-2, in observation 13813 (Figure 5.4, bottom panels). The abrupt nature of the transition from low to high count rates and the long duration of the low phase once again suggests that we are looking at an occultation by the companion star. Remarkably, the egress from the eclipse of ULX-2 happens only ≈8ks later than the egress from the ULX-1 eclipse, at MJD 56180.30 and 56180.20, respec-

tively (cf. bottom and top panels of Figure 5.4). The small but significant time difference guarantees that the two count-rate jumps seen in the two ULXs are not instrumental anomalies but real physical events. Moreover, we did extensive checks on other bright X-ray sources in the same ACIS-S3 chip, and found that none of them shows similar jumps around that time; this also rules out instrumental problems. We also examined the lightcurves of ULX-2 in all other *Chandra* observations, including those where eclipses or dips were found in the lightcurve of ULX-1 (left panel of Figure 5.3 and bottom panels of Figures 5.5, and 5.6). We found no other unambiguous eclipses or deep dips.

ULX-2 does show significant intra-observational variability in ObsID 13815. Throughout the 67-ks observation, the source displays a much lower count rate than its average out-of-eclipse count rate, in both the soft and the hard band (Table 5.3 and Figure 5.7). The count rate further decreases during that *Chandra* epoch, until it becomes consistent with a non-detection at the end of the observation. The decrease is slow enough (compared with the eclipse in ObsID 13813, Figure 5.4) to rule out a stellar occultation. We do not have enough evidence or enough counts to test whether this flux decrease is due to intrinsic variability of ULX-2, or to an increased absorption by colder material in the outer disk. As usual, we checked the behaviour of ULX-1 and other bright sources in ObsID 13815 to ascertain that the lower count rate seen from ULX-2 is not an instrumental problem.

5.3.1.3 ULX-2 eclipse in the *XMM-Newton* data

We then searched for possible eclipses of either ULX-1 or ULX-2 during the *XMM-Newton* observations. Due to the poorer spatial resolution of EPIC relative to ACIS-S, ULX-1 and ULX-2 are not completely resolved by *XMM-Newton*; however, the point spread function in the combined EPIC MOS1+MOS2 images is clearly peanut-shaped, consistent with the positions and relative intensities of the two *Chandra* sources, and the upper source (ULX-2) has significantly harder colours (Figure 5.8, top panel). Firstly, we extracted and examined background-subtracted EPIC lightcurves for the combined emission of the two unresolved sources, for each *XMM-Newton* observation. Because the two sources have comparable count rates (Tables 2 and 3), an eclipse in either source would cause the observed count rate to drop by a factor of $\approx$2. This is the scenario we find in observation 0303420101: there is an apparent increase in the observed EPIC-MOS count rate by a factor of $\approx$2, some 22 ks from the start of the observation, which we tentatively interpret as the egress from an eclipse (Figure 5.9, top panel), superposed on short-term intrinsic variability. Unfortunately we cannot use EPIC-pn data for this crucial epoch, because the source falls onto a

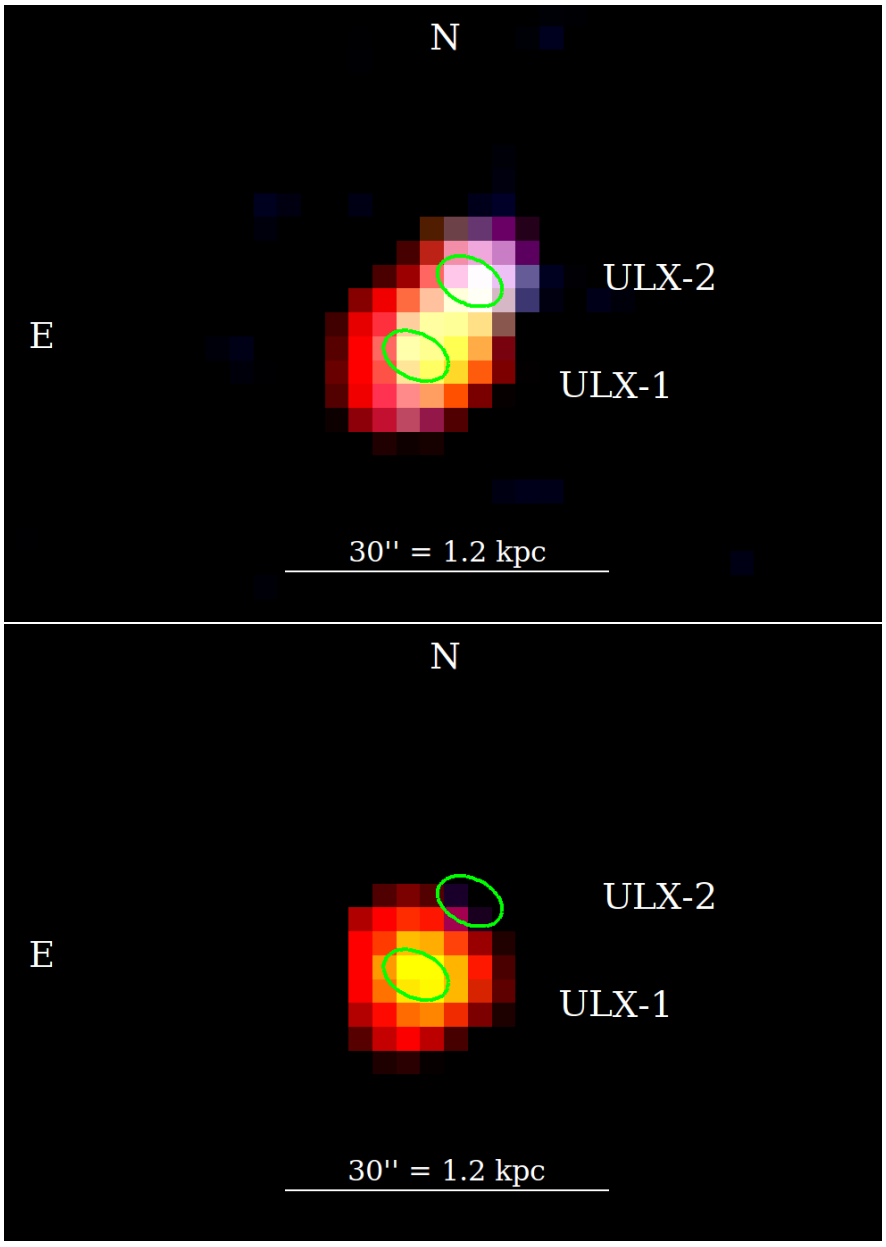

Figure 5.8: Top panel: stacked *XMM-Newton* MOS1+MOS2 image for non-eclipse interval of observation 0303420101. Red represents photons in the 0.3–1 keV band, green is for 1–2 keV and blue is for 2–7 keV. The green ellipses indicate the locations of ULX-1 and ULX-2 as determined from the *Chandra*/ACIS-S images; their point spread functions appear elongated because the ULXs were observed a few arcmin away from the ACIS-S3 aimpoint. The two sources are not clearly resolved by *XMM-Newton*, but the colour difference between the two ends of the peanut-shaped EPIC-MOS source is consistent with the colour and spectral differences seen by *Chandra*. Bottom panel: as in the top panel, but for the ULX-2 eclipse interval of observation 0303420101.

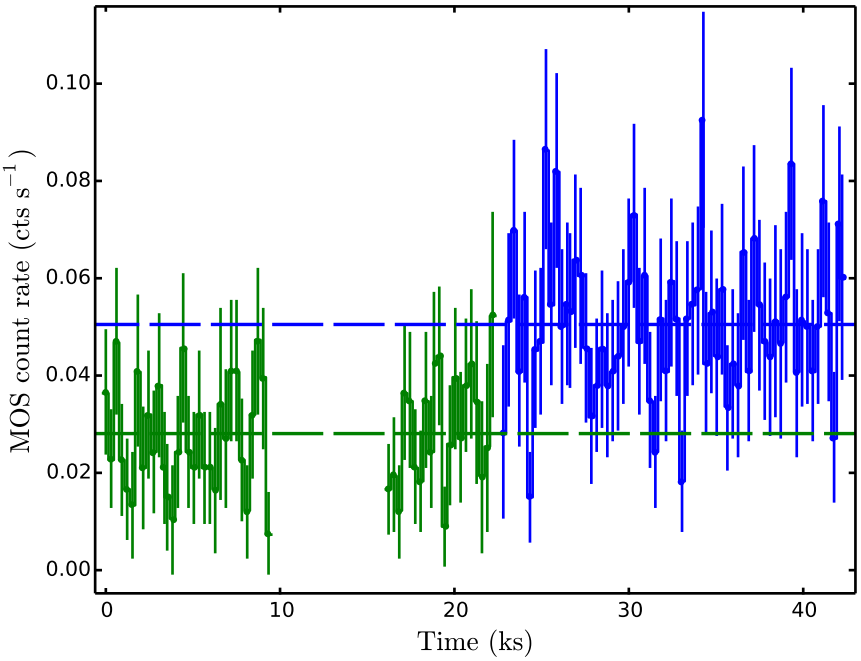

Figure 5.9: Background-subtracted *XMM-Newton*/EPIC MOS1+MOS2 lightcurve for the unresolved ULX source in observation 0303420101. Time intervals affected by background flaring have been removed. The lightcurve was extracted in the 0.2–8 keV band and the datapoints have been binned to 300 s for display purposes. The lightcurve is broken into two sections: the first ≈22 ks (green datapoints) have a lower count rate and correspond to an eclipse of ULX-2; in the remaining ≈20 ks, both ULXs are out of eclipse (blue datapoints). Dotted lines indicate the average count rates for the two sub-intervals.

chip gap. To quantify the step change in the count rate between the first and second part of the observation (green and blue datapoints in Figure 5.9), we performed a Kolmogorov-Smirnov (KS) test on the two distributions of datapoints, to determine whether they are drawn from different populations. We find a KS statistic of 0.65 and p-value of 3.8×10^{-11}, suggesting that the two sections of the lightcurve are indeed statistically different. The average MOS1+MOS2 net count rate in the "eclipse" part of the lightcurve is $\approx 0.026 \pm 0.003$ ct s^{-1} (90% confidence limit), while in the "non-eclipse" part it is $\approx 0.046 \pm 0.003$ ct s^{-1}. Having ascertained from the X-ray lightcurve that ObsID 0303420101 probably includes an eclipse, we extracted MOS1+MOS2 images from the low-rate and high-rate sections of that observation, and confirmed (Figure 5.8) that in the low-rate interval, the emission from ULX-2 is missing.

We extracted and inspected the lightcurves of every other *XMM-Newton* observation. No eclipses of ULX-1 and no further eclipses of ULX-2 were detected; however, several of those observations are much shorter than the typical *Chandra* observations, and the background count rate is much higher in the EPIC cameras. Thus, ruling out the presence of an eclipse as opposed to intrinsic variability is

no easy task in some of the *XMM-Newton* observations.

5.3.2 Constraints on the binary period of ULX-1

We noted (Table 5.2 and Section 5.3.1.1) that for ULX-1, two fractions of eclipses are seen ≈12 days apart, in ObsID 13813 and ObsID 13814. The egress from the eclipse in ObsID 13813 occurs at MJD 56180.21; the ingress into the eclipse in ObsID 13814 occurs at MJD 56191.64. This enables us to place some constraints on binary period, which must be,

$$P \approx \frac{(11.43 + \text{eclipse duration})}{n} \text{ days}, \tag{5.1}$$

with $n \geq 1$. To refine this constraint, we take into account that the minimum duration of an eclipse is ≈90 ks (≈1.0 days), as observed in ObsID 13814. We also know that the maximum duration of an eclipse is ≈150 ks (≈1.7 days) as this is the time between the start of the eclipse in ObsID 13814 and the start of the next observation, ObsID 13815, which has no eclipse. Assuming the shortest possible duration of the eclipse implies a binary period of ≈12.5/n days. If we use the maximum eclipse time, ≈1.7 days, the binary period is ≈13.1/n days.

We tested a range of eclipse durations and binary periods, to determine which combination of parameters is consistent with the observed sequence of eclipses/non-eclipses in our *Chandra* observations. Based solely on the minimum duration of an uninterrupted non-eclipse phase (≈160 ks) and the minimum duration of the eclipse (≈90 ks), the minimum acceptable binary period, from Equations (5.1), is P ≈230 ks ≈2.7 d (that is, $n = 4$). However, if the binary period were ≈3 days, the eclipse found during ObsID 13813 implies that another eclipse should be detected in ObsID 13812. The start of ObsID 13812 is only 2.56 days after the end of the eclipse in ObsID 13813. We do not find an eclipse in ObsID 13812, and this rules out a period of ≈3 days. Moreover, an eclipse time $\gtrsim$90 ks over a period of about 3 days would imply that ULX-1 should be in eclipse $\gtrsim$30% of the time. A Roche-lobe filling donor star can eclipse a point-like X-ray source for such a long fraction of the orbit only for mass ratios $q \equiv M_2/M_1 \gtrsim$ a few 100 (Figure 2 in Chanan et al., 1976), which is impossible for any combination of compact objects and normal donor stars. Next, we consider the possibility that $n = 3$ in Equation (5.1), which corresponds to a period range between ≈4.08 and ≈4.38 days. In this case, too, we would have seen at least part and more likely all of an eclipse in ObsID 13812, which is not the case: this rules out the $n = 3$ case, too. Therefore, the only two acceptable options for the binary period are $n = 2$ ($P \sim$ 6–6.5 days) or $n = 1$ ($P \sim$ 12–13 days).

We summarise the acceptable region of the period versus eclipse duration

parameter space in Figure 5.10. We iterated over all possible eclipse durations (1.04–1.70 days, in iteration steps of 0.01 days) and for values of $n = 1, 2, 3, 4$, and compared the predicted occurrences of eclipses with what is detected in the seven *Chandra* observations between 2012 September 9 to 2012 October 10. Along the line corresponding to each value of n, some periods are consistent with the *Chandra* data (red intervals), others are ruled out (black intervals). In addition, for Roche-lobe-filling donors, eclipse durations $> 20\%$ of the binary period (dark shaded area in Figure 5.10) require a mass ratio $q \gtrsim 8$ at an inclination angle of 90°, or $q \gtrsim 10$ at an inclination of 80° (Chanan et al., 1976). This is highly implausible if the accretor is a black hole, but it is acceptable for a neutron star accreting from an OB star. On the assumption that ULX-1 has a black hole primary, the mass-ratio constraint further restricts the viable $n = 2$ case to the narrow range $P = 6.23$–6.35 days, with an eclipse duration range of 1.04–1.26 days. If we allow for a neutron star primary, the period can be as long as 6.55 days, corresponding to an eclipse fraction of 26%. Finally, for the $n = 1$ case, the predicted fractional time in eclipse goes from ≈8% ($P = 12.48$ d, eclipse duration ≈1.0 d) to ≈13% ($P = 13.14$ d, eclipse duration ≈1.7 d), with mass ratios $q \sim 0.3$–1, more typical of a black hole primary in orbit with an OB star.

Based on the previous analysis, we compared the predicted eclipse fractions with the total fraction of time ULX-1 was observed in eclipse. Over all *Chandra* epochs, the system is seen in eclipse for a total of ≈135 ks out of ≈835 ks, equating to a total eclipsing fraction of ≈ 16%. No eclipses of ULX-1 are significantly detected in 177 ks of *XMM-Newton*/EPIC observations; therefore, the combined eclipse fraction observed by *Chandra* plus *XMM-Newton* becomes ≈13.3%. This is slightly lower than the minimum predicted time in eclipse in the case of $n = 2$ (fractional eclipse duration $\gtrsim 16.7\%$: Figure 5.10). Conversely, for the case of $n = 1$, the observed time in eclipse is slightly larger than expected (between ≈8% and ≈13%). We do not regard such discrepancies as particularly significant, because of the limited and uneven sampling of the system; we may have been slightly lucky or slightly unlucky in catching ULX-1 during its eclipses.

We also note that dips in the X-ray flux can sometime provide phasing information in binary systems, if they are caused by bulging, denser material located where the accretion stream splashes onto the disk. For example, regular dips at phases ∼0.6–0.7 are sometimes seen in low-mass X-ray binaries (e.g., EXO 0748-676; Lubow, 1989; Homan et al., 2003), and other Roche-lobe overflow systems. We have already mentioned (Section 5.3.1.1) that ULX-1 shows a dip in ObsID 13812. A second possible dip can also be seen in the full lightcurve (Figure 5.11) at the start of the final observation, ObsID 13816. Although only detected in a single 1000-s bin (the first 1000 s of the observation), this drop in flux appears

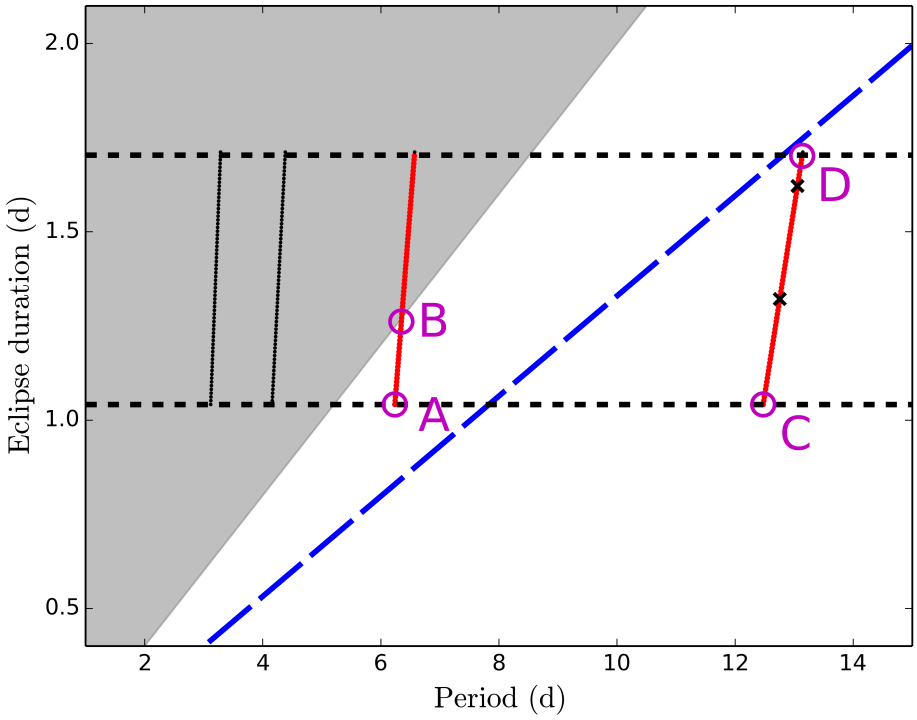

Figure 5.10: Test of potential binary periods for ULX-1, based on the spacing between observed eclipses in the *Chandra* series of observations. We know that $P \approx$(11.43 + eclipse duration)$/n$ days, with $n \geq 1$ and the eclipse duration is between 1.0 days and 1.7 days (horizontal dashed black lines). Each line segment represents a choice of n (from left to right: $n = 4, 3, 2, 1$), and is plotted between the minimum (1.04 days) and maximum (1.70 days) permitted value of the eclipse duration. On each segment, black intervals indicate a combination of period and eclipse duration that is not consistent with the sequence of *Chandra* observations; instead, red intervals do fit the observed data. The dashed blue line is the region of the parameter space where the eclipse duration is 13.3% of the period, which is the observed eclipsing fraction from all *Chandra* and *XMM-Newton* observations. The grey shaded region marks the region of the parameter space where the eclipse duration is greater than 20% of the period, which we consider less likely for empirical reasons (too far from the observed value). For each value of the ratio between eclipse duration and binary period, there is a unique value of the mass ratio $q(\theta)$ (see Section 5.4.3 for details). For $\theta = 90°$, points A, B, C, D correspond to $q = 3.6, 9.7, 0.25, 1.2$, respectively; the two points marked with crosses correspond to $q(90°) = 0.5$ and 1.0. Acceptable solutions in the shaded region require mass ratios $q(\theta) \geq q(90°) \gtrsim 10$ (Section 5.3.2); such high values are ruled out in the case of a black hole accretor, but are still possible if ULX-1 is powered by a neutron star.

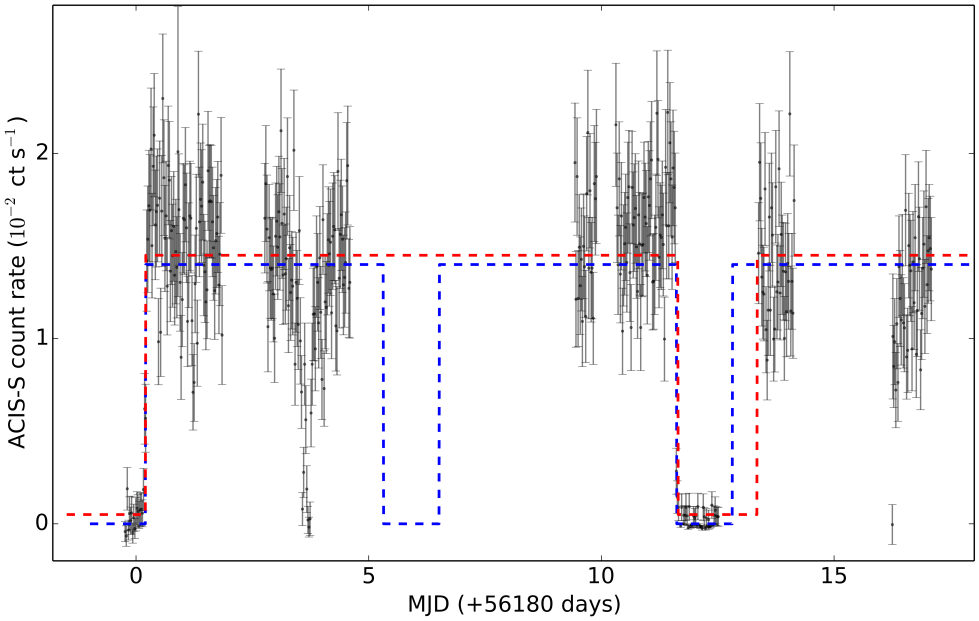

Figure 5.11: *Chandra*/ACIS-S background subtracted lightcurve for ULX-1 for all epochs in September 2012 (in chronological order: ObsIDs 13813, 13812, 15496, 13814, 13815, 13816). We overlaid two schematic lightcurves corresponding to two alternative periods consistent with the observations: a 6.3-day period with a 1.3-day eclipse (dashed blue line), and a 13.1-day period with a 1.7-day eclipse (dashed red line, slightly shifted upwards for clarity). In addition to the two eclipses, two shorter dips are also seen. The second dip appears only in the first data point from the final epoch, but is at approximately the same orbital phase as the first dip with respect to their preceding eclipses. The first 2 datapoints of the final epoch are plotted as 1000-s bins (to highlight the short dip), while all other datapoints are binned to 2000 s.

to be intrinsic to ULX-1, as other nearby sources do not show this feature and there are no instrumental problems in those first 1000 s. Intriguingly, both dips appear to be at the same phase with respect to the preceding eclipses (i.e., ≈3.5 days after the eclipse), which strengthens our confidence that the second dip is also real. For a binary period ≈6 days, the dips would be at phase ≈0.6; for the alternative period range ≈12.5–13 days, the dips would be at phase ≈0.25–0.30.

Finally, two eclipses were found for ULX-2. Unfortunately, the large time interval between the two eclipses seen by *Chandra* in 2012 September and by *XMM-Newton* in 2006 May precludes any attempt to constrain the binary period. All we can say is that the total fraction of time spent in eclipse by ULX-2 in our ≈ 1Ms *Chandra* plus *XMM-Newton* dataset is ≈7%. Since the minimum eclipse duration is 48 ks (≈0.55 d), we expect the binary period to be ∼10 d.

5.3.3 Hardness ratios in and out of eclipses

Residual emission is detected at the position of ULX-1 during eclipses (Table 5.2). This is particularly evident in ObsID 1622, with a residual eclipse count rate ≈10% of the average out-of-eclipse count rate. It is also marginally significant in ObsIDs 13813 and 13814. The reason why the residual emission appears less significant in ObsID 13813 and 13814 than in ObsID 1622 is likely because of the decreasing sensitivity of ACIS-S in the soft band between 2001 and 2012 (Plucinsky et al., 2004). We stacked the eclipse intervals from all three ULX-1 eclipses and display the resulting 135-ks ACIS-S X-ray-colour image in Figure 5.12 (top panel). The residual emission of ULX-1 is centred at the same coordinates as the out-of-eclipse emission, and is unresolved, but appears softer (most photons below 1 keV). We also show (Figure 5.12, bottom panel) the 48-ks ACIS-S image corresponding to the only *Chandra* eclipse of ULX-2; the signal-to-noise ratio is lower, but there is significant residual emission for ULX-2 in eclipse, as well.

To quantify the colours and the colour differences in and out of eclipse, we determined the hardness ratio between the net count rates in the 1.2–7 keV band and in the 0.3–1.2 keV band (i.e., the same bands used in our lightcurve plots). It appears (particularly in ObsID 13813) that ULX-1 is softer in eclipse than out of eclipse (Figure 5.13 and Table 5.4).The difference becomes more significant when we compare the hardness ratio of the stacked eclipse data (Table 5.4) with that of the stacked out-of-eclipse ones. For ULX-2, we cannot identify significant colour differences in and out of eclipse, because of the short duration of the only detected *Chandra* eclipse. Our hardness ratio study also clearly shows (Table 5.4 and Figure 5.13) that ULX-1 is always softer than ULX-2, both in and out of eclipse.

Another difference between the two ULXs is their degree of hardness ratio variability from epoch to epoch in the *Chandra* series. For ULX-1, all the 2012 observations are consistent with the same hardness ratio (Table 5.4). The source appears softer in ObsIDs 354, 1622 and 3932; however, this is misleading because such observations were taken in Cycle 1, Cycle 2 and Cycle 4, respectively, when ACIS-S was more sensitive to soft photons (Plucinsky et al., 2004). A rough way to account for this effect is to assume simple power-law models and use the *Chandra* X-Ray Center online installation of the Portable, Interactive Multi-Mission Simulator (PIMMS; Version 4.8) to convert the observed count rates into "equivalent" count rates that would have been observed in Cycle 13 (year 2012) when all the other observations took place. A more accurate conversion from observed count rates to Cycle 13-equivalent count rates requires proper spectral modelling in the various epochs. The corrected count rates listed in Table 5.4 and

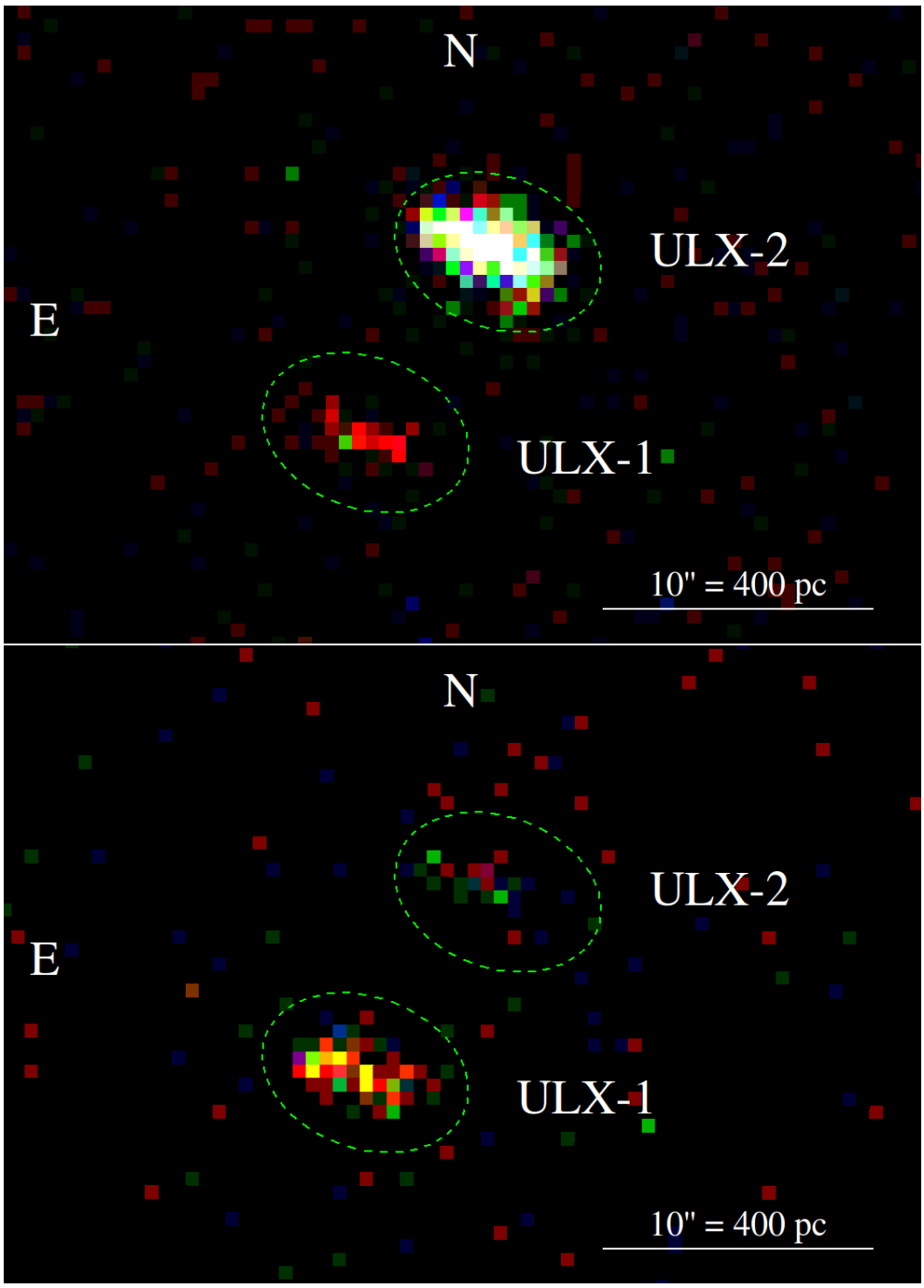

Figure 5.12: Top panel: stacked *Chandra*/ACIS-S image during the ULX-1 eclipse intervals from ObsIDs 1622, 13813 and 13814. Colours are red for 0.3–1 keV, green for 1–2 keV, blue for 2–7 keV. The dashed green ellipses represent the *Chandra* extraction regions for ULX-1 and ULX-2. Bottom panel: same as the top panel, for the ULX-2 eclipse interval during *Chandra* ObsID 13813. Coincidentally, ULX-1 is also in eclipse for the majority of this interval.

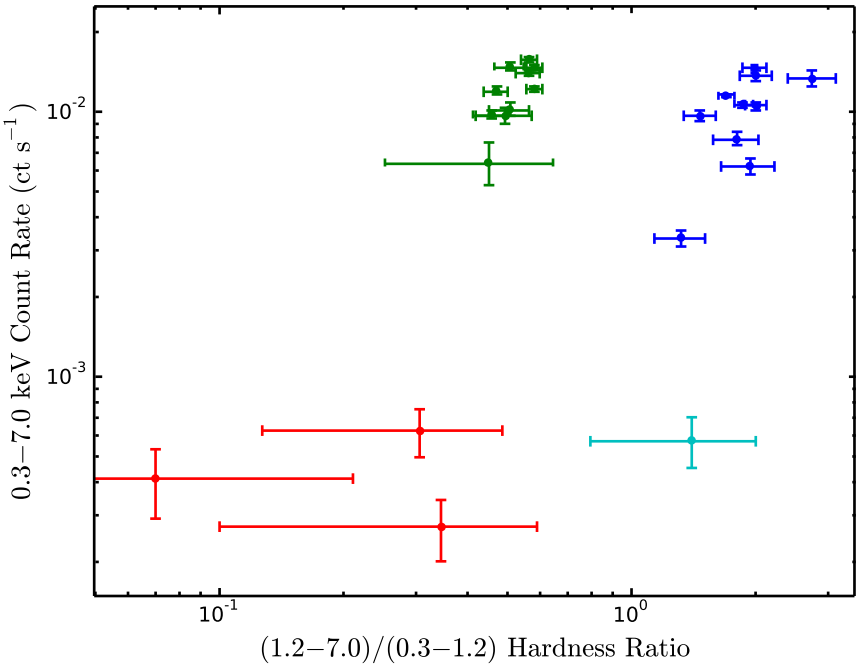

Figure 5.13: (1.2–7.0)/(0.3–1.2) hardness ratio versus 0.3–7.0 keV count rate for ULX-1 and ULX-2 in eclipse and non-eclipse intervals during the *Chandra* observations. Red datapoints correspond to ULX-1 in eclipse, green datapoints to ULX-1 out of eclipse, the single cyan datapoint to ULX-2 in eclipse and blue datapoints to ULX-2 out of eclipse. Colours have been corrected for the change in sensitivity of the ACIS-S detector over the years (Section 5.3.3, Table 5.4)

plotted in Figure 5.13, for both ULX-1 and ULX-2, were obtained with the latter method, after we carried out the spectral analysis discussed in Section 5.3.4, the best-fitting spectral models were convolved with response and auxiliary response functions of the detector at different epochs, to determine the predicted count rates. Inspection of the corrected count rates confirms that the hardness of ULX-1 is approximately constant, whereas that of ULX-2 is intrinsically variable from epoch to epoch.

Based on the observed hardness of the residual eclipse emission of ULX-1, we most plausibly interpret it as thermal plasma emission, for the purpose of converting count rates into fluxes and luminosities. Assuming a temperature ∼0.5 keV, and using again the online PIMMS tool, we estimate a residual ULX-1 luminosity $L_{\rm X} \sim 10^{37}$ erg s^{-1} in the 0.3–8 keV band. Again, this is only a simple, preliminary estimate. We will present a more accurate estimate of the residual emission based on spectral fitting, and we will discuss its physical origin, after we carry out a full spectral modelling of ULX-1 (Section 5.3.4.1). We do not have any constraints on plausible models for the residual eclipse emission of ULX-2; however, a selection of thermal plasma and power-law models also give typical luminosities $L_{\rm X} \sim 10^{37}$ erg s^{-1}. What is clear is that it is harder than the residual

Table 5.4: Hardness ratios of ULX-1 and ULX-2 for eclipsing and non-eclipsing intervals of the *Chandra* observations. Values in brackets are rescaled to their *Chandra* Cycle 13-equivalents.

Epoch	ULX-1 hardness ratios		ULX-2 hardness ratios	
	Non-eclipsing	Eclipsing	Non-eclipsing	Eclipsing
354	0.27 ± 0.04		1.71 ± 0.23	
	$[0.49 \pm 0.07]$		$[2.75 \pm 0.36]$	
1622	0.28 ± 0.12	0.17 ± 0.10	1.31 ± 0.19	
	$[0.40 \pm 0.17]$	$[0.31 \pm 0.18]$	$[1.90 \pm 0.27]$	
3932	0.33 ± 0.03		1.11 ± 0.10	
	$[0.42 \pm 0.04]$		$[1.43 \pm 0.13]$	
13812	0.58 ± 0.03		1.87 ± 0.10	
13813	0.58 ± 0.03	$0.07^{+0.14}_{-0.07}$	2.01 ± 0.11	1.4 ± 0.6
13814	0.56 ± 0.03	0.35 ± 0.25	1.69 ± 0.08	
13815	0.56 ± 0.04		1.32 ± 0.18	
13816	0.47 ± 0.03		1.99 ± 0.13	
15496	0.51 ± 0.04		2.00 ± 0.18	
15553	0.51 ± 0.06		1.80 ± 0.22	
stacked	0.55 ± 0.01	0.21 ± 0.09	1.78 ± 0.04	1.4 ± 0.6
	$[0.56 \pm 0.01]$	$[0.23 \pm 0.10]$	$[1.86 \pm 0.06]$	$[1.4 \pm 0.6]$

emission of ULX-1.

5.3.4 Spectral properties

The presence of eclipses implies that both system are viewed at high inclination. Therefore, these two ULXs, although not exceptionally luminous, can help us investigate the relationship between the spectral appearance of ULXs and their viewing angles. During out-of-eclipse intervals, both ULXs have sufficiently high count rates for multi-component spectral fitting. Here, we present the results of spectral fitting to the three longest *Chandra* observations: ObsIDs 13812 (158 ks), 13813 (179 ks) and 13814 (190 ks), taken between 2012 September 9–20. For each source, we fitted the three spectra simultaneously, keeping the intrinsic absorption column density and the parameters of any possible thermal plasma components locked between them but leaving all other model parameters free. The reason for this choice is that we are assuming for simplicity that cold absorption and thermal

Table 5.5: Goodness-of-fit χ^2_ν values from fits for several alternative models simultaneously fitted to the spectra of ULX-1 and ULX-2 in *Chandra* epochs 13812, 13813 and 13814. Each model was multiplied by both a fixed line-of-sight and a free intrinsic *TBabs* component. mk_1 and mk_2 are two *mekal* components.

Model	χ^2_ν	
	ULX-1	ULX-2
powerlaw	1.94 (478.4/246)	0.99 (259.3/261)
diskbb	1.61 (395.8/246)	1.01 (264.3/261)
diskir	1.25 (297.2/237)	0.96 (241.8/252)
diskpbb	1.53 (371.1/243)	0.93 (238.9/258)
cutoffpl	1.23 (298.5/243)	0.93 (239.5/258)
diskbb+powerlaw	1.39 (334.6/240)	0.96 (245.6/255)
diskbb+cutoffpl	1.11 (264.1/237)	0.93 (234.8/252)
diskbb+comptt	1.17 (278.2/237)	0.93 (234.1/252)
bb+comptt	1.17 (278.0/237)	0.93 (234.1/252)
diskbb+powerlaw+mk_1*+*mk_2	1.02 (241.6/236)	0.95 (239.5/251)
diskbb+comptt+mk_1*+*mk_2	1.01 (234.4/233)	0.93 (230.2/248)
bb+comptt+mk_1*+*mk_2	1.01 (236.3/233)	0.94 (233.0/248)
diskir+mk_1*+*mk_2	1.01 (235.6/233)	0.96 (237.2/248)
diskpbb+mk_1*+*mk_2	1.00 (238.3/239)	0.92 (234.3/254)

plasma emission vary on timescales longer than a few days, while the emission from the inner disk and corona may change rapidly. In addition, we assumed a line-of-sight absorption column $n_{\rm H,0} = 2 \times 10^{20}$ cm^{-2} (Dickey and Lockman, 1990; Kalberla et al., 2005).

5.3.4.1 Spectral models for ULX-1

The first obvious result of our modelling (Table 5.5) is that the spectrum of ULX-1 is intrinsically curved, and not well fitted by a simple power-law ($\chi^2_\nu \approx 1.9$) regardless of the value of $n_{\rm H,int}$. Therefore, we tried several other models, roughly belonging to two typical classes: disk-dominated models, in which the disk is responsible for most of the emission above 1 keV and for the high-energy spectral curvature; and Comptonisation-dominated models, in which the disk (or other thermal component) provides the seed photon emission below 1 keV, and a cut-off power-law or Comptonisation component provides the bulk of the emission above 1 keV. Much of the debate in the literature about the spectral classification of

ULXs reduces to the choice between these two interpretations (e.g., Gladstone et al., 2009; Feng and Soria, 2011; Sutton et al., 2013b). Finally, we tested whether the addition of a thermal plasma emission component improves the fit: the justification for this component is that some ULXs (especially those seen at high viewing angles) may show emission features in the ∼1 keV region (Middleton et al., 2014, 2015b).

We started by fitting single-component disk models: *TBabs* × *TBabs* × *diskbb* for a standard disk (Mitsuda et al., 1984; Makishima et al., 1986), and *TBabs* × *TBabs* × *diskpbb* for a slim disk (Kubota et al., 2005). They fare relatively better ($\chi^2_\nu \approx 1.6$ and $\chi^2_\nu \approx 1.5$, respectively) than a power-law model, but they are still not good fits. They also require a surprisingly low peak colour temperature, $kT_{\rm in} \approx 0.6$–0.7 keV; this is inconsistent with the disk temperatures expected near or just above the Eddington limit (≈ 1.0–1.3 keV: e.g., Kubota and Makishima, 2004; Remillard and McClintock, 2006), and would require a heavy stellar-mass black hole (as we shall discuss later).

Next, we tried adding a power-law component to the disk model: *TBabs* × *TBabs* × (*diskbb* + *powerlaw*). This is probably the most commonly used model in the literature for the classification of accretion states in stellar mass black holes (despite the interpretation problems caused by the unphysically high contribution of the power-law component at low energies). The quality of the fit improves slightly ($\chi^2_\nu \approx 1.4$) but there are still significant systematic residuals. One source of fit residuals is the high-energy downturn. By using instead a *TBabs* × *TBabs* × (*diskbb* + *cutoffpl*) model, we obtain a substantially better fit ($\chi^2_\nu \approx 1.1$), with an F-test statistical significance ≈ $(1 - 10^{-12})$. The presence of a high-energy downturn is of course one of the main spectral features of ULXs (Stobbart et al., 2006), compared with stellar-mass black holes in sub-Eddington states. However, in this case the best-fitting cut-off energy $E \approx 1$ keV, much lower than the typical ∼5 keV high-energy cutoff seen in other ULXs (Gladstone et al., 2009); this is quantitative evidence that the spectrum of ULX-1 is extremely soft compared with average ULX spectra. Fitting a cutoff power-law alone (without the disk component) gives a $\chi^2_\nu \approx 1.2$; from this, we verify that an additional soft thermal component is significant to $> 99.99\%$. There is still a third source of fit residuals, at energies around 1 keV, which we will discuss later in this section.

The successful models discussed so far are phenomenological approximations of physical models; therefore, we fitted several alternative Comptonisation models that produce a soft excess and a high-energy downturn: *TBabs* × *TBabs* × (*diskbb* + *comptt*) (Titarchuk, 1994), *TBabs* × *TBabs* × (*bb* + *comptt*), and *TBabs* × *TBabs* × *diskir* (Gierliński et al., 2009). They provide moderately good fits, with $\chi^2_\nu \approx 1.2$ (Table 5.5). In this class of Comptonisation models, the disk component

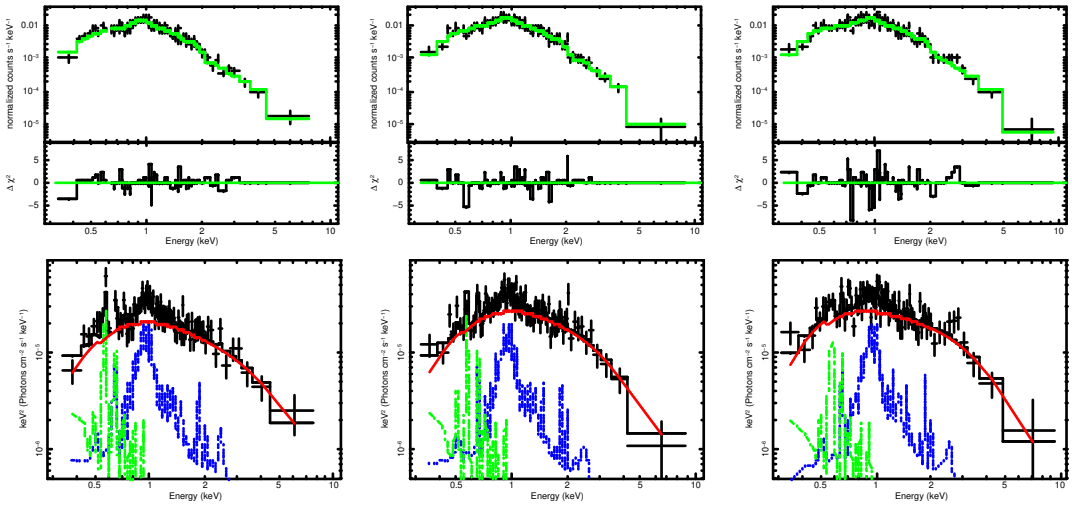

Figure 5.14: Upper panels: *Chandra*/ACIS-S spectra of ULX-1 in ObsIDs 13812, 13813 and 13814, with model fits and χ^2 residuals. The model is *TBabs* × *TBabs* × (*mekal* + *mekal* + *diskbb* + *comptt*); see Table 5.6 for the best-fitting parameters. Lower panels: unfolded spectra with model components. The dot-dashed green line represents the cooler *mekal* component, the dotted blue line represents the hotter *mekal* component and the solid red curve is the *comptt* component. The seed *diskbb* component does not appear in the plots because the direct contribution from the disk is negligible.

is used as the source of seed photons, and the electron temperature sets the location of the high-energy cutoff. For ULX-1, typical seed photon temperatures are $kT_0 \lesssim 0.3$ keV, and the range of electron temperatures in the Comptonising region is $kT_e \approx 0.8$–1.2 keV, with optical depths ≈ 7–9. The electron temperature of the Comptonisation region is substantially cooler than in most other two-component ULXs (where $kT_e \sim 1.5$–3 keV: Gladstone et al. 2009). This is the physical reason why ULX-1 appears as one of the softest sources in its class, with an unfolded $E\,F_E$ spectrum peaking at ≈1 keV (c.f. the ULX classification of Sutton et al., 2013b). The optically-thick thermal continuum component used as seed to the Comptonisation models can be equally well modelled with a disk-blackbody or a simple blackbody, given its low temperature at the lowest edge of the ACIS-S sensitivity. Its direct flux contribution to the observed spectrum is small, although difficult to constrain precisely, because of the low number of counts at very soft energies. Individual fits to the three longest observations with a *diskir* model suggest a direct disk contribution an order of magnitude lower than the Comptonised component.

The main reason why none of the smooth continuum models described above are really good fits is the presence of strong residuals (F-test level of significance >99.99%) below and around 1 keV. A single-temperature *mekal* component is not sufficient to eliminate the residuals. Instead, two *mekal* components with temperatures $kT_1 \approx 0.2$ keV and $T_2 \approx 0.9$ keV significantly improve the fits

(Figure 5.14), providing $\chi^2_\nu \approx 1.01$ for the Comptonisation models and $\chi^2_\nu \approx 1.00$ for the disk models. In the latter case, the temperature profile index is $p \lesssim 0.6$ ("broadened disk"), favouring the slim disk over the standard disk model.

The presence of soft X-ray residuals and the strong continuum curvature are robust and independent of the choice of cold absorption model. We also tried combinations of neutral and ionised absorbers (*tbabs* × *varabs*), but they do not reproduce the strong residual feature at energies ≈0.8–1.0 keV. Lower-energy residuals at ≈0.5–0.6 keV are relatively less constrained because of the degraded sensitivity of ACIS-S at low energies, rather than because of intrinsic absorption. For all our Comptonisation-type and disk-type models, the intrinsic cold absorption $n_{\rm H}$ is $\lesssim$ a few 10^{20} cm^{-2} and in most cases, consistent with 0 within the 90% confidence level.

Disk models with additional thermal plasma emission produce equally good χ^2 values as Comptonisation models with thermal plasma emission (Table 5.5). Therefore, it is worth examining in more detail whether disk models are physically self-consistent, and what their physical interpretation could be. Let us start with a standard disk, to account for the possibility that ULX-1 is a rather massive black hole accreting at sub-Eddington rates. We may be tempted to discard this possibility straight away, because the best-fitting temperature profile index $p \lesssim 0.6$ (rather than $p = 0.75$) is generally considered the hallmark of a disk at the Eddington accretion rate, not of a standard disk; however, it was recently shown that broadened disks with $p \approx 0.6$ may also occur in the sub-Eddington regime with accretion rates an order of magnitude lower (Sutton et al., 2016). Therefore, we will consider that case here. In standard accretion disk models, with the inner disk fixed at the innermost stable circular orbit, there are two approximate relations between the observable quantities $T_{\rm in}$ and L, and the non-directly-observable physical properties $\dot{m}$ (Eddington-scaled mass accretion rate) and M (black hole mass):

$$L \approx 1.3 \times 10^{39}\, \dot{m} M_{10} \ \ {\rm erg\ s^{-1}} \tag{5.2}$$

$$kT_{\rm in} \approx 1.3\, (\dot{m}/M_{10})^{1/4} \ \ {\rm keV} \tag{5.3}$$

(Shakura and Sunyaev, 1973), where M_{10} is the black hole mass in units of 10 $M_\odot$. Equation (5.2) is simply the luminosity as a fraction of Eddington, in the radiatively efficient regime; Equation (5.3) follows from the relation $L \approx 4\pi r_{\rm in}^2 \sigma T_{\rm in}^4$. For ULX-1, the best-fitting peak temperature is $kT_{\rm in} \approx (0.7 \pm 0.1)$ keV, and the luminosity $L \approx 2 \times 10^{39}$ erg s^{-1} (as we shall discuss later). From Equations (5.2) and (5.3), this would correspond to a black hole mass $M \approx 40$–$50\ M_\odot$ at accretion rates $\dot{m} \approx 0.3$–0.4. Even if we allow for the possibility of

Table 5.6: Best-fitting parameters for the spectra of ULX-1 in ObsIDs 13812, 13813 and 13814, modelled with *TBabs* × *TBabs* × (*mekal* + *mekal* + *diskbb* + *comptt*). The first *TBabs* component (in square brackets) is fixed to the line-of-sight value for all epochs, while the intrinsic absorption is left free. The *mekal* components are locked across the three epochs, fitted simultaneously. Errors indicate the 90 per cent confidence interval for each parameter of interest. Fluxes are the observed values; luminosities are corrected for absorption and assume an inclination angle $\theta = 80°$. Goodness-of-fit $\chi^2_\nu = 1.01(234.4/233)$.

Component	Parameter	Epoch 13812	13813	13814
TBabs	$n_{\rm H,0}$ (10^{22}cm^{-2})		[0.02]	
TBabs	$n_{\rm H,int}$ (10^{22}cm^{-2})	< 0.02	< 0.02	< 0.02
mekal	kT_1 (keV)		$0.17^{+0.05}_{-0.04}$	
	N_1[a]		$4.1^{+2.1}_{-1.9}\times10^{-6}$	
mekal	kT_2 (keV)		$0.87^{+0.09}_{-0.08}$	
	N_2[a]		$4.6^{+1.0}_{-0.9}\times10^{-6}$	
diskbb	$kT_{\rm in}$ (keV)	$0.32^{+0.23}_{-0.08}$	$0.19^{+0.02}_{-0.03}$	$0.18^{+0.02}_{-0.01}$
	K[b]	< 0.6	< 0.5	< 2.5
comptt	kT_0 (keV)[c]	$0.32^{+0.23}_{-0.05}$	$0.19^{+0.02}_{-0.03}$	$0.18^{+0.02}_{-0.01}$
	$kT_{\rm e}$ (keV)	$1.1^{+*}_{-0.3}$	$0.9^{+2.0}_{-0.2}$	$0.9^{+0.9}_{-0.2}$
	τ	$7.6^{+0.4}_{-0.4}$	$7.4^{+0.4}_{-0.4}$	$8.3^{+0.5}_{-0.4}$
	$N_{\rm c}$	$1.4^{+0.3}_{-0.3}\times10^{-5}$	$8.0^{+0.5}_{-0.6}\times10^{-5}$	$7.0^{+0.7}_{-0.8}\times10^{-5}$
	$f_{0.3-8.0}$ (10^{-14} erg cm^{-2} s^{-1})	$7.32^{+0.19}_{-0.41}$	$8.59^{+0.27}_{-0.39}$	$9.26^{+0.39}_{-0.35}$
	$L_{0.3-8.0}$ (10^{39} erg s^{-1})	$1.5^{+0.3}_{-0.3}$	$1.8^{+0.3}_{-0.3}$	$2.0^{+0.4}_{-0.4}$
	$L_{\rm bol}$ (10^{39} erg s^{-1})	$2.1^{+0.4}_{-0.4}$	$2.2^{+0.5}_{-0.5}$	$2.6^{+0.5}_{-0.5}$

[a]The *mekal* normalisations (N_1 and N_2) are in units of $10^{-14}/(4\pi d^2)\int n_e\, n_{\rm H}\, {\rm d}V$.
[b]The *diskbb* normalisation is in units of $(r_{\rm in}/{\rm km})^2 \cos\theta\, (d/10\,{\rm kpc})^{-2}$, where $r_{\rm in}$ is the apparent inner-disk radius.
[c]The seed photon temperature for the Comptonising medium, kT_0, is locked to peak colour temperature of the disk, $kT_{\rm in}$.

$p < 0.6$ in a sub-Eddington disk, the presence of strong line residuals in the soft X-ray band is another, stronger piece of evidence against the standard disk model; it is instead indicative of Eddington accretion and associated outflows (Middleton et al., 2015b; Pinto et al., 2016). For these reasons, we dis-favour the sub-Eddington standard disk model for ULX-1.

Next, we test the self-consistency of the slim disk model. In the super-Eddington regime, the disk luminosity is modified as

$$L \approx 1.3 \times 10^{39}\,(1 + 0.6 \ln \dot{m})\, M_{10} \ \ {\rm erg\ s^{-1}} \tag{5.4}$$

(Shakura and Sunyaev, 1973; Poutanen et al., 2007). A slim disk is no longer truncated exactly at the innermost stable circular orbit: the fitted inner disk

Table 5.7: As in Table 5.6, for a *TBabs* × *TBabs* × (*mekal* + *mekal* + *diskir*) model. Goodness-of-fit $\chi^2_\nu = 1.01(235.6/233)$.

Component	Parameter	Epoch 13812	13813	13814
TBabs	$n_{\rm H,0}$ (10^{22}cm^{-2})		[0.02]	
TBabs	$n_{\rm H,int}$ (10^{22}cm^{-2})	< 0.06	< 0.08	< 0.12
mekal	kT_1 (keV)		$0.17^{+0.05}_{-0.03}$	
	N_1		$3.8^{+3.9}_{-1.4}\times10^{-6}$	
mekal	kT_2 (keV)		$0.87^{+0.08}_{-0.10}$	
	N_2		$4.5^{+1.1}_{-0.8}\times10^{-6}$	
diskir	$kT_{\rm in}$ (keV)	$0.13^{+0.40}_{-0.05}$	$0.13^{+0.09}_{-0.01}$	$0.11^{+0.21}_{-0.01}$
	Γ	$2.85^{+0.16}_{-*}$	$2.49^{+0.18}_{-0.15}$	$2.43^{+0.13}_{-0.13}$
	$kT_{\rm e}$ (keV)	$1.2^{+0.5}_{-0.5}$	$0.71^{+0.11}_{-0.17}$	$0.87^{+0.17}_{-0.12}$
	$\rm L_c/L_d$	$7.2^{+*}_{-0.4}$	> 9.5	> 4.4
	$f_{\rm in}$	[0.1]	[0.1]	[0.1]
	$r_{\rm irr}$	[1.2]	[1.2]	[1.2]
	$f_{\rm out}$	$[1 \times 10^{-3}]$	$[1 \times 10^{-3}]$	$[1 \times 10^{-3}]$
	$\log(r_{\rm out})$	[4]	[4]	[4]
	K[a]	$1.05^{+0.05}_{-0.06}$	$1.23^{+0.06}_{-0.05}$	$3.03^{+0.15}_{-0.16}$
	$f_{0.3-8.0}$ (10^{-14} erg cm^{-2} s^{-1})	$7.13^{+0.28}_{-0.29}$	$8.46^{+0.28}_{-0.36}$	$9.05^{+0.18}_{-0.60}$
	$L_{0.3-8.0}$ (10^{39} erg s^{-1})	$1.5^{+0.3}_{-0.3}$	$1.8^{+0.3}_{-0.4}$	$2.0^{+0.3}_{-0.3}$
	$L_{\rm bol}$ (10^{39} erg s^{-1})	$2.0^{+0.5}_{-0.5}$	$2.3^{+0.5}_{-0.6}$	$2.6^{+0.5}_{-0.6}$

[a]Disk normalisation in units of $(r_{\rm in}/{\rm km})^2 \cos\theta\,(d/10\,{\rm kpc})^{-2}$.

radius can be approximated by the empirical scaling $r_{\rm in}(\dot{m}) \approx r_{\rm in}(\dot{m}=1)\,[T_{\rm in}(\dot{m}=1)/T_{\rm in}(\dot{m})]$ (Watarai et al., 2000). As a result, the disk luminosity becomes $L \propto M_{10}^{3/2} T_{\rm in}^2$. Substituting L from Equation (5.4), and matching the normalisation to that of the sub-Eddington case (Equation (5.3)), we obtain:

$$kT_{\rm in} \approx 1.3\,(1 + 0.6 \ln \dot{m})^{1/2}\, M_{10}^{-1/4} \ \ {\rm keV}. \tag{5.5}$$

A proper treatment of the observed properties of a slim disk requires additional parameters such as the viewing angle and the black hole spin (Vierdayanti et al., 2008; Sądowski, 2009; Vierdayanti et al., 2013); however, Equations (5.4) and (5.5) are already good enough as a first-order approximation to test the consistency of a slim disk model for ULX-1. From Equation (5.5), we find that a slim disk peak temperature $kT_{\rm in} \approx 0.7$ keV requires a black hole mass $M \gtrsim 100 M_\odot$ (confirmed also by the numerical results of Vierdayanti et al., 2008); but such a black hole would be far below Eddington at the observed luminosity $L \approx 2 \times 10^{39}$ erg s^{-1}, contrary to our initial slim disk assumption. Therefore, the slim disk model cannot be self-consistently applied to the spectrum of ULX-1.

Table 5.8: As in Table 5.6, for a *TBabs* × *TBabs* × (*mekal* + *mekal* + *diskpbb*) model. Goodness-of-fit $\chi^2_\nu = 1.00$ (238.3/239).

Component	Parameter	Epoch 13812	13813	13814
TBabs	$n_{\rm H,0}$ (10^{22}cm^{-2})		[0.02]	
TBabs	$n_{\rm H,int}$ (10^{22}cm^{-2})	$0.05^{+0.02}_{-0.05}$	$0.06^{+0.03}_{-0.04}$	$0.04^{+0.04}_{-0.04}$
mekal	kT_1 (keV)		$0.18^{+0.04}_{-0.03}$	
	N_1		$8.1^{+7.0}_{-4.5}\times10^{-6}$	
mekal	kT_2 (keV)		$0.84^{+0.10}_{-0.08}$	
	N_2		$6.7^{+1.1}_{-1.0}\times10^{-6}$	
diskpbb	$kT_{\rm in}$ (keV)	$0.69^{+0.11}_{-0.09}$	$0.63^{+0.08}_{-0.07}$	$0.72^{+0.12}_{-0.09}$
	p	< 0.60	< 0.57	< 0.58
	K[a]	$3.5^{+7.6}_{-1.7}\times10^{-3}$	$7.7^{+8.8}_{-3.2}\times10^{-2}$	$3.8^{+5.8}_{-1.7}\times10^{-3}$
	$f_{0.3-8.0}$ (10^{-14} erg cm^{-2} s^{-1})	$7.00^{+0.36}_{-0.38}$	$8.16^{+0.40}_{-0.42}$	$9.00^{+0.48}_{-0.50}$
	$L_{0.3-8.0}$ (10^{39} erg s^{-1})	$1.8^{+0.4}_{-0.4}$	$2.4^{+0.4}_{-0.4}$	$1.5^{+0.3}_{-0.3}$
	$L_{\rm bol}$ (10^{39} erg s^{-1})	$2.8^{+0.6}_{-0.6}$	$3.2^{+0.7}_{-0.7}$	$2.8^{+0.6}_{-0.6}$

[a]Disk normalisation in units of $(r_{\rm in}/{\rm km})^2 \cos\theta\,(d/10\,{\rm kpc})^{-2}$.

Based on those physical arguments, we conclude that the best fits in all three epochs are obtained with a Comptonisation model, with the addition of multi-temperature optically-thin thermal plasma emission. From the fit statistics alone, we cannot rule out a broadened disk model, with a heavy stellar-mass black hole at sub-Eddington accretion rates; however, the observed presence of strong soft X-ray residuals points to an ultraluminous regime. We list the best-fitting parameters of two equivalent Comptonisation models in Tables 5.6, 5.7; for comparison, we also list the best-fitting parameters of the broadened-disk model (Table 5.8).

5.3.4.2 Continuum and line luminosity of ULX-1

The unabsorbed X-ray luminosity $L_{\rm X}$ is related to the absorption-corrected flux $f_{\rm X}$ by the relation $L_{\rm X} = 2\pi d^2 f_{\rm X}/\cos\theta$, where d is the distance to the source and θ is the viewing angle, when the emission is from a (sub-Eddington) standard disk surface, and $L_{\rm X} = 4\pi d^2 f_{\rm X}$ for a spherical or point-like emitter. We do not have direct information on the geometry of the emitting region in ULX-1; however, analytical models and numerical simulations of near-Eddington and super-Eddington sources predict mild geometrical beaming, that is, most of the X-ray flux is emitted along the direction perpendicular to the disk plane (Kawashima et al., 2012; Jiang et al., 2014; Sądowski and Narayan, 2016), and the emission should appear fainter and down-scattered in a disk wind when a source is observed at high inclination (as in our case, given the presence of eclipses). Therefore, we choose to use the simplest angle-dependent expression for the luminosity $L_{\rm X} = 2\pi d^2 f_{\rm X}/\cos\theta$.

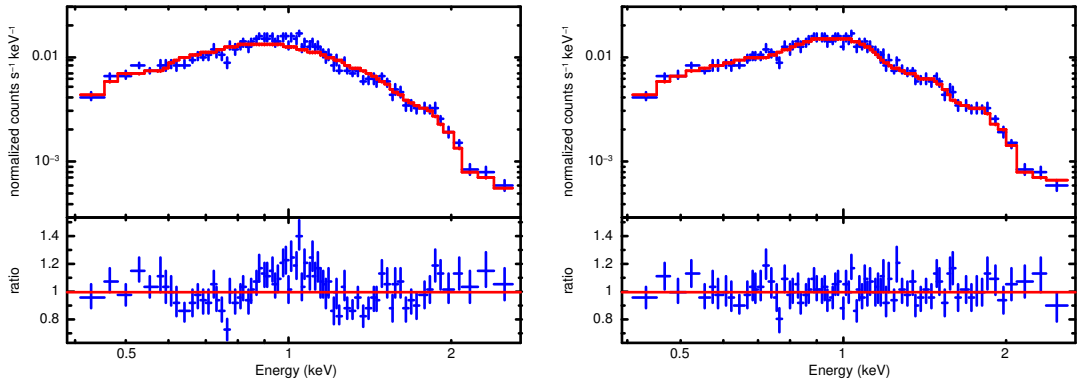

Figure 5.15: Left panel: datapoints, best-fitting continuum model and spectral residuals for the combined spectrum of all ten *Chandra*/ACIS-S observations of ULX-1, selecting only non-eclipse time intervals. The model fitted to the combined spectrum is $TBabs \times TBabs \times (diskbb + comptt)$. Significant residuals are seen at photon energies $\sim$1 keV. The datapoints have been binned to a signal-to-noise ratio ≥ 9. Right panel: the same spectrum and residuals after the addition of three thermal plasma emission components (*mekal* model) at $kT_1 \approx 0.13$ keV, $kT_2 \approx 0.73$ keV and $kT_3 \approx 1.74$ keV, which account well for the residuals.

We also identify for simplicity (and in the absence of conflicting evidence) the viewing angle θ to the plane of the inner disk with the inclination angle of the binary system, which we have constrained to be high from the presence of eclipses; that is, we neglect the possibility of a warped, precessing disk. Instead, we estimate the unabsorbed X-ray luminosity of the thermal plasma components as $L_{\rm X} = 4\pi d^2 f_{\rm X}$, because we assume that the distribution of hot plasma is quasi-spherical above and beyond the disk plane, and its emission is approximately isotropic. With those caveats in mind, we estimate an emitted 0.3–8.0 keV luminosity of the two-temperature thermal plasma component $L_{\rm X,mekal} \approx 1.3 \times 10^{38}$ erg s^{-1} (Tables 5.6, 5.7, 5.8), essentially all below 2 keV. Assuming $\theta \approx 80^\circ$, we then estimate the total (i.e., thermal plasma plus continuum) 0.3–8.0 keV luminosity as $L_{\rm X} \approx (1.5\text{–}2.0) \times 10^{39}$ erg s^{-1}, during the three longest *Chandra* observations, regardless of whether the continuum is fitted with a Comptonisation model or with a slim disk.

To increase the signal-to-noise ratio of the thermal plasma emission component, we extracted and combined (using CIAO's *specextract* tool) the spectra and responses of all ten *Chandra* observations (Table 5.1), for a grand total of $\approx$700 ks out of eclipse. We fitted the resulting spectrum with the same smooth continuum models (Comptonisation and slim-disk models) used for the three long spectra: regardless of the choice of continuum, strong systematic residuals appear at energies around 1 keV. As a representative case, we show the residuals corresponding to a *comptt* fit (Figure 5.15, left panel); for this continuum-only model, $\chi^2_\nu = 1.54(217.0/141)$. When two *mekal* components are added to the continuum

Table 5.9: Best-fitting parameters for the combined spectrum of ULX-1 from all 10 *Chandra* observations, modelled with *TBabs* × *TBabs* × (*mekal* + *mekal* + *mekal* + *diskbb* + *comptt*). The first *TBabs* component (in square brackets) is fixed to the line-of-sight value for all epochs, while the intrinsic absorption is left free. Errors indicate the 90 per cent confidence interval for each parameter of interest. Fluxes are the observed values; luminosities are corrected for absorption and assume an inclination angle $\theta = 80°$. Goodness-of-fit $\chi^2_\nu = 1.03(139.5/135)$.

Component	Parameter	Value
TBabs	$n_{\rm H,0}$ (10^{22}cm^{-2})	[0.02]
TBabs	$n_{\rm H,int}$ (10^{22}cm^{-2})	$0.001^{+0.007}_{-0.001}$
mekal	kT_1 (keV)	$0.13^{+0.01}_{-0.01}$
	N_1[a]	$5.0^{+1.7}_{-1.6}\times10^{-6}$
mekal	kT_2 (keV)	$0.73^{+0.05}_{-0.05}$
	N_2[a]	$3.2^{+0.5}_{-0.5}\times10^{-6}$
mekal	kT_3 (keV)	$1.74^{+0.16}_{-0.12}$
	N_3[a]	$1.10^{+0.18}_{-0.18}\times10^{-5}$
diskbb	$kT_{\rm in}$ (keV)	$0.17^{+0.02}_{-0.01}$
	K[b]	$0.72^{+0.25}_{-0.25}$
comptt	kT_0 (keV)[c]	$0.17^{+0.02}_{-0.01}$
	$kT_{\rm e}$ (keV)	$0.64^{+0.27}_{-0.18}$
	τ	$9.7^{+0.3}_{-0.3}$
	$N_{\rm c}$	$7.8^{+0.7}_{-0.7}\times10^{-5}$
	$f_{0.3-8.0}$ (10^{-14} erg cm^{-2} s^{-1})	$7.75^{+0.22}_{-0.22}$
	$L_{0.3-8.0}$ (10^{39} erg s^{-1})	$1.4^{+0.3}_{-0.3}$
	$L_{\rm bol}$ (10^{39} erg s^{-1})	$2.2^{+0.6}_{-0.6}$

[a]The *mekal* normalisations (N_1, N_2 and N_3) are in units of $10^{-14}/(4\pi d^2)\int n_e\, n_{\rm H}\, {\rm d}V$.

[b]The *diskbb* normalisation is in units of $(r_{\rm in}/{\rm km})^2 \cos\theta\, (d/10\,{\rm kpc})^{-2}$, where $r_{\rm in}$ is the apparent inner-disk radius.

[c]The seed photon temperature for the Comptonising medium, kT_0, is locked to peak colour temperature of the disk, $kT_{\rm in}$.

(as we did for the spectra of ObsIDs 13812, 13813 and 13814), the goodness-of-fit improves to $\chi^2_\nu = 1.10(150.7/137)$. We tried introducing a third *mekal* component, and obtained a further improvement to the fit (significant to the 99.5% level), down to $\chi^2_\nu = 1.03(139.5/135)$. We show the 3-*mekal* model fit and its residuals in Figure 5.15 (right panel), and list the best-fitting parameters in Table 5.9. The best-fitting *mekal* temperatures are $kT_1 \approx 0.13$ keV, $kT_2 \approx 0.7$ keV, and $kT_3 \approx 1.7$ keV. (Instead, adding a third *mekal* component to the best-fitting model for ObsIDs 13812, 13813 and 13814 does not significantly improve that fit.) We estimate an unabsorbed 0.3–8.0 keV luminosity of the three-temperature thermal plasma component $L_{\rm X,mekal} \approx 2.4 \times 10^{38}$ erg s^{-1}. This is moderately higher than the value we estimated for a two-temperature model, because now part of the emission at energies $\gtrsim$2 keV is also attributed to optically-thin thermal plasma. The total (continuum plus thermal plasma) unabsorbed luminosity in the 0.3–8.0 keV band is $L_{\rm X} \approx 1.5 \times 10^{39}$ erg s^{-1}, consistent with the luminosity estimated in ObsIDs 13812, 13813 and 13814. Alternatively, we replaced the three *mekal* components with a *cemekl*, which is a multi-temperature thermal plasma model with a power-law distribution of temperatures. The best-fitting *cemekl* + *diskbb* + *comptt* model has $\chi^2_\nu = 1.11(154.1/139)$, maximum temperature $kT_{\rm max} \approx 2.2$ keV, thermal plasma luminosity $L_{\rm X,cemekl} \approx 1.4 \times 10^{38}$ erg s^{-1}, and total luminosity $L_{\rm X} \approx 2 \times 10^{39}$ erg s^{-1}.

As noted earlier, the role of the disk component in this class of models is to provide the seed photons for the Comptonisation component, as well as a soft excess due to the fraction of disk photons that reach us directly. A best-fitting seed temperature $kT_{\rm in} \approx 0.17$ keV and inner-disk size $r_{\rm in}(\cos\theta)^{1/2} \approx 700$ km are consistent with the characteristic temperatures and sizes of the soft thermal components seen in other ULXs (e.g., Miller et al. 2004; Stobbart et al. 2006; Kajava and Poutanen 2009). The direct luminosity contribution of the disk in the 0.3–8 keV band is $\approx (4 \pm 1) \times 10^{38}$ erg s^{-1}.

Finally, we inspected the spectral emission in eclipse. We extracted a combined spectrum of the eclipse intervals in ObsIDs 1622, 13813 and 13814. Although we only have ≈60 counts, the energy distribution of the counts is similar (Figure 5.16) to the thermal plasma emission component out of eclipse, rather than to the continuum emission. After rebinning the eclipse spectrum to 1 count per bin, we applied the Cash statistics (Cash, 1979) to fit the normalisation of the same two *mekal* components previously found in the out-of-eclipse spectra of ObsIDs 13812, 13813 and 13814 (temperatures fixed at $kT_1 \approx 0.2$ keV and $T_2 \approx 0.9$ keV). We find a C-stat value of 49.5 over 54 degrees of freedom for the best-fitting model. The emitted luminosity is $\approx 2.4 \times 10^{37}$ erg s^{-1}, consistent with our previous simpler estimate based on count rates (Section 5.3.2). We then

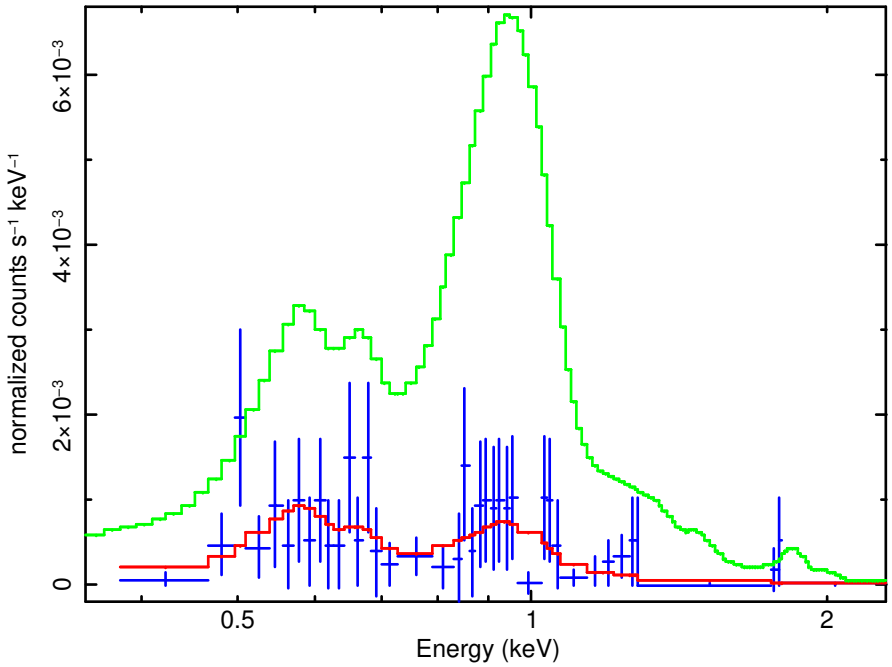

Figure 5.16: Combined *Chandra*/ACIS-S spectrum of ULX-1 during the three eclipses in ObsIDs 1622, 13813 and 13814. The datapoints have been grouped to 1 count per bin. The green curve illustrates the contribution from the best-fitting *mekal* components (at $T_1 \approx 0.18$ keV and $T_2 \approx 0.86$ keV) during the non-eclipse intervals of the three longest *Chandra* observations (Table 5.6). The red curve is the contribution from two *mekal* components at the same fixed temperatures but with free normalisations, fitted to the eclipse data with the Cash statistics. This plot supports our suggestion that the residual emission during eclipses is due to thermal plasma.

let the temperatures free, but did not obtain any significant improvement to the quality of the fit (C-stat value of 49.2 over 52 degrees of freedom). Nor do we improve the fit by adding a third *mekal* component.

5.3.4.3 Spectral models and luminosity of ULX-2

As we did for ULX-1, we started by fitting the spectra of ULX-2 during *Chandra* ObsIDs 13812, 13813 and 13814 with a simple power-law model (Table 5.5). The fit is good ($\chi^2_\nu \approx 0.99$), but there are residuals consistent with a high-energy downturn. The best-fitting power-law index is $\Gamma = 2.1 \pm 0.1$; however, this value may be an over-estimate if the high-energy steepening is not properly accounted for. Hence, we re-fitted the spectrum with a cutoff power-law (*TBabs* × *TBabs* × *cutoffpl)*, and found that the fit is significantly improved: $\chi^2_\nu \approx 0.93$, with an F-test significance $\approx 99.99\%$ with respect to the unbroken power-law. The power-law index below the cutoff is $\Gamma = 1.1 \pm 0.2$ and the characteristic energy of the cutoff is 3.0 ± 0.6 keV. This is evidence that the spectrum of ULX-2 is significantly curved. Therefore, as we did for ULX-1, we tried a series of models

suitable to curved spectra: disk models and a Comptonisation model.

Among disk models, we find that a broadened disk is a significantly better fit (F-test significance >99.99%) than a standard disk; a *TBabs* × *TBabs* × *diskpbb* model provides $\chi^2_\nu \approx 0.93$ (Table 5.5). The peak disk temperature $kT_{\rm in} \approx$ 1.4–2.0 keV and $p \approx 0.6$, perfectly in line with the expected values for a mildly super-Eddington slim-disk model around a stellar-mass black hole. The best-fit parameters can be found in Table 5.10; the model is illustrated in Figure 5.17. The *diskpbb* normalisation, K, translates into a characteristic inner disk radius

$$R_{\rm in} \approx 3.18 K^{1/2}\, d_{\rm 10kpc}\, (\cos\theta)^{-1/2} \ \ {\rm km}, \tag{5.6}$$

using the conversion factors suitable for slim-disk models (Vierdayanti et al., 2008); $d_{\rm 10kpc}$ is the distance in units of 10 kpc. A feature of super-critical slim disks is that $R_{\rm in}$ is located slightly inside the innermost stable circular orbit (Watarai and Mineshige, 2003; Vierdayanti et al., 2008). When this correction is taken into account, the mass $M_\bullet$ of a non-rotating black hole can be estimated as $M_\bullet \approx 1.2 \times R_{\rm in}c^2/(6G) \approx 1.2 R_{\rm in}/(8.9\,{\rm km}) M_\odot$. Characteristic radii $R_{\rm in}(\cos\theta)^{1/2}$ ≈29–56 km are consistent with all the three long *Chandra* observations considered here (Table 5.10). For $\theta \approx 80°$, this corresponds to characteristic masses $M_\bullet \approx$ 9–18$M_\odot$, consistent with the observed mass distribution of Galactic black holes (Kreidberg et al., 2012). For a range of viewing angles $70° \lesssim \theta \lesssim 85°$, the corresponding black hole mass range becomes $M_\bullet \approx$ 7–25$M_\odot$. The emitted luminosity in the 0.3–8.0 keV band is $\approx 2\times10^{39}$ erg s^{-1} (assuming again a viewing angle $\theta = 80°$) and the bolometric disk luminosity is $\approx 3\times10^{39}$ erg s^{-1} ≈1–3$L_{\rm Edd}$ for the range of black hole masses estimated earlier. In this model, ULX-2 would be classified as a broadened-disk ULX in the scheme of Sutton et al. (2013b).

Although we favour the slim disk model because of its self-consistency, we cannot rule out the possibility that ULX-2 is fitted by a Comptonisation model (Table 5.11): for example, *TBabs* × *TBabs* × *(diskbb + comptt)* yields $\chi^2_\nu \approx$ 0.93, statistically equivalent to the slim disk model (Table 5.5), with electron temperatures $kT_e \approx$ 1–1.5 keV and optical depth $\tau \approx$ 9–13 (slightly hotter and more optically thick than the best-fitting *comptt* models in ULX-1). Similar values of χ^2_ν and kT_e are also obtained from other Comptonisation models such as *diskir*.

Regardless of the model, the unfolded $E\,F_E$ spectrum peaks at ≈5 keV, similar to the sources classified as hard ultraluminous by Sutton et al. (2013b). The original definition of the hard ultraluminous regime requires also the presence of a soft excess. In our spectra, it is difficult to constrain the significance of a direct soft emission component (in addition to the Comptonised component or

Table 5.10: Best-fitting parameters for the spectrum of ULX-2 in ObsIDs 13812, 13813 and 13814, modelled with *TBabs* × *TBabs* × *diskpbb*. The first *TBabs* component (in square brackets) is fixed to the line-of-sight value for all epochs, while the intrinsic absorption is left free but locked across all epochs. Errors indicate the 90 per cent confidence interval for each parameter of interest. Unabsorbed luminosities assume an inclination angle $\theta = 80°$. Goodness-of-fit $\chi^2_\nu = 0.93(238.9/258)$.

Component	Parameter	Epoch		
		13812	13813	13814
TBabs	$n_{\rm H,0}$ (10^{22}cm^{-2})		[0.02]	
TBabs	$n_{\rm H,int}$ (10^{22}cm^{-2})		$0.09^{+0.04}_{-0.04}$	
diskpbb	$kT_{\rm in}$ (keV)	$1.5^{+0.4}_{-0.2}$	$1.7^{+0.8}_{-0.4}$	$1.8^{+0.7}_{-0.4}$
	p	$0.58^{+0.07}_{-0.04}$	$0.56^{+0.06}_{-0.04}$	$0.54^{+0.04}_{-0.03}$
	K[a]	$4.5^{+7.9}_{-3.2}\times10^{-4}$	$2.1^{+5.6}_{-1.7}\times10^{-4}$	$1.5^{+3.3}_{-1.1}\times10^{-4}$
	$f_{0.3-8.0}$ (10^{-14} erg cm^{-2} s^{-1})	$8.18^{+0.49}_{-0.50}$	$8.23^{+0.60}_{-0.59}$	$8.67^{+0.50}_{-0.53}$
	$L_{0.3-8.0}$ (10^{39} erg s^{-1})	$2.2^{+0.4}_{-0.4}$	$2.3^{+0.4}_{-0.4}$	$2.5^{+0.4}_{-0.4}$
	$L_{\rm bol}$ (10^{39} erg s^{-1})	$2.7^{+0.4}_{-0.4}$	$3.0^{+0.5}_{-0.5}$	$3.9^{+0.6}_{-0.6}$

[a]Disk normalisation in units of $(r_{\rm in}/{\rm km})^2 \cos\theta\,(d/10\,{\rm kpc})^{-2}$.

Table 5.11: As in Table 5.10, for a *TBabs* × *TBabs* × (*diskbb* + *comptt*) model. Goodness-of-fit $\chi^2_\nu = 0.93(234.1/252)$.

Component	Parameter	Epoch		
		13812	13813	13814
TBabs	$n_{\rm H,0}$ (10^{22}cm^{-2})		[0.02]	
TBabs	$n_{\rm H,int}$ (10^{22}cm^{-2})		< 0.15	
diskbb	$kT_{\rm in}$ (keV)	$0.16^{+0.76}_{-0.06}$	$0.26^{+0.66}_{-0.11}$	$0.23^{+0.60}_{-0.15}$
	K[a]	< 0.25	< 0.12	< 0.40
comptt	kT_0 (keV)[b]	$0.16^{+0.76}_{-0.06}$	$0.26^{+0.66}_{-0.11}$	$0.23^{+0.60}_{-0.15}$
	$kT_{\rm e}$ (keV)	$1.0^{+0.2}_{-0.1}$	$1.5^{+*}_{-0.4}$	$1.1^{+1.0}_{-0.3}$
	τ	$13.3^{+2.6}_{-2.7}$	$9.2^{+3.3}_{-7.4}$	$11.7^{+*}_{-3.9}$
	$K_{\rm c}$	$4.5^{+0.8}_{-0.9}\times10^{-5}$	$2.5^{+1.3}_{-2.2}\times10^{-5}$	$3.4^{+2.0}_{-1.7}\times10^{-5}$
	$f_{0.3-8.0}$ (10^{-14} erg cm^{-2} s^{-1})	$8.12^{+0.47}_{-0.48}$	$8.28^{+0.62}_{-0.63}$	$8.65^{+0.53}_{-0.52}$
	$L_{0.3-8.0}$ (10^{39} erg s^{-1})	$1.9^{+0.3}_{-0.3}$	$1.9^{+0.3}_{-0.3}$	$2.1^{+0.3}_{-0.3}$
	$L_{\rm bol}$ (10^{39} erg s^{-1})	$1.9^{+0.3}_{-0.3}$	$2.1^{+0.4}_{-0.4}$	$2.3^{+0.4}_{-0.4}$

[a]The *diskbb* normalisation is in units of $(r_{\rm in}/{\rm km})^2 \cos\theta\,(d/10\,{\rm kpc})^{-2}$, where $r_{\rm in}$ is the apparent inner-disk radius.

[b]The seed photon temperature kT_0 is locked to the peak temperature of the disk, $kT_{\rm in}$.

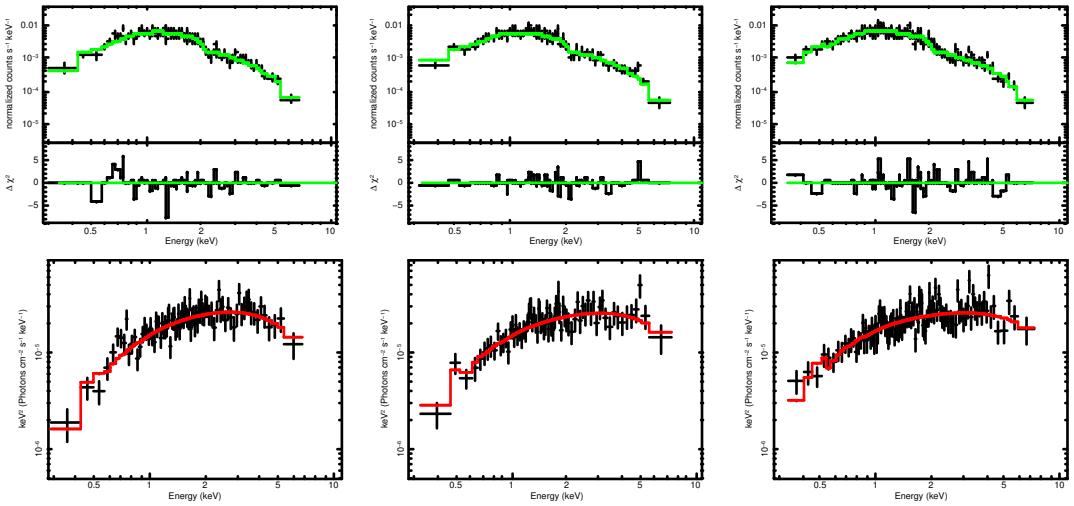

Figure 5.17: Upper panels: *Chandra*/ACIS-S spectra of ULX-2 in ObsIDs 13812, 13813 and 13814, with model fits and χ^2 residuals. The model is *TBabs* × *TBabs* × *diskpbb*; see Table 5.11 for the best-fitting parameters. Lower panels: unfolded spectra from the same epochs. The red curve represents the *diskpbb* component. This plot confirms that the spectrum of ULX-2 is harder than that of ULX-1, and does not have significant contributions from thermal plasma.

the cutoff power-law) because of the low sensitivity of ACIS-S below 0.5 keV. When we fit the spectrum with a *diskbb* + *comptt* model, we find that no more than ∼50% of the flux in the 0.3–1.0 keV band is in the direct *diskbb* component (90% upper limit), but the *diskbb* normalisation is also consistent with 0 within the 90% confidence limit. Regardless of classification semantics, it is clear that ULX-2 has a hard spectrum in the *Chandra* band, with a high-energy curvature.

No significant residuals are found at ≈0.8–1 keV in the individual spectra from ObsIDs 13812, 13813 and 13814; however, in at least one observation (ObsID 13812), the spectrum shows two emission features with >90% significance at $E \approx 1.3$ keV and $E \approx 1.8$ keV. Similar lines are typically found in thermal plasma emission. They are usually interpreted as emission from a blend of Mg XI lines at 1.33–1.35 keV, and from a Si XIII line at 1.84 keV (with the likely additional contribution of slightly weaker Mg XII lines at 1.75 keV and 1.84 keV). To investigate these and possible other emission features, we extracted a combined *Chandra* spectrum of ULX-2 from all ten observations, as we did for ULX-1. We fitted the combined spectrum with a *diskpbb* model, and obtain an excellent fit, $\chi^2_\nu = 0.86$ (Table 5.12). The significance of the two candidate emission features seen in ObsID 13812 fades to <90% in the combined spectrum (Figure 5.18). Adding thermal plasma components to the combined spectrum does not produce any significant improvement. The characteristic disk temperature $kT_{\rm in} \approx 1.6$ keV, radial temperature index $p \approx 0.57$ and inner-disk radius $R_{\rm in}(\cos\theta)^{1/2} \approx 40$ km (Table 5.12) are consistent with those expected for a super-critical disk, and

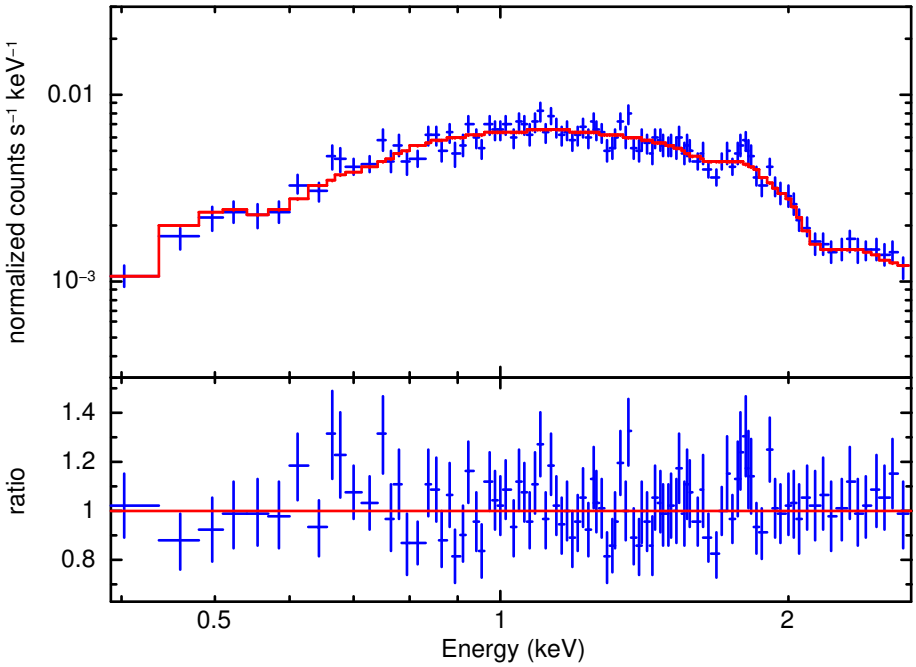

Figure 5.18: Datapoints, best-fitting continuum model and spectral residuals for the combined spectrum of all ten *Chandra*/ACIS-S observations of ULX-2, selecting only non-eclipse time intervals. The model fitted to the combined spectrum is *TBabs*×*TBabs*×*diskpbb*. The datapoints have been binned to a signal-to-noise ratio ≥ 7. The combined spectrum of ULX-2 does not show any significant systematic residuals around 1 keV (unlike the spectrum of ULX-1).

with the values obtained from the individual fits to ObsIDs 13812, 13813 and 13814. The corresponding range of black hole masses is $M_\bullet \approx 8$–$20 M_\odot$, for a non-rotating black hole and a viewing angle $\theta = 80°$.

Finally, we examined the spectrum of ULX-2 in eclipse (Figure 5.19). It appears different from what is seen in ULX-1: there is no evidence of a bimodal distribution of counts and it is not possible (from the few counts available) to determine whether the eclipse emission has the same origin as the out-of-eclipse continuum (e.g., a small fraction of the direct emission scattered into our line-of-sight by an extended corona), or comes from thermal plasma at higher temperatures or from bremsstrahlung emission.

5.4 Discussion

5.4.1 Two eclipsing ULXs in one field: too unlikely?

Luminous stellar-mass black hole X-ray binaries or ULXs with X-ray eclipses are very rare sources. SS 433 in the Milky Way shows eclipses of its X-ray emission caused by the donor star on a 13.1-d binary period (e.g., Stewart et al., 1987; Fabrika, 2004; Brinkmann et al., 2005; Kubota et al., 2010; Cherepashchuk et al.,

Table 5.12: Best-fitting parameters for the combined *Chandra* spectrum of ULX-2, modelled with *TBabs* × *TBabs* × *diskpbb*. The first *TBabs* component (in square brackets) is fixed to the line-of-sight value, while the intrinsic absorption is left free. Errors indicate the 90 per cent confidence interval for each parameter of interest. Unabsorbed luminosities assume an inclination angle $\theta = 80°$. Goodness-of-fit $\chi^2_\nu = 0.87(190.4/219)$.

Component	Parameter	Value
TBabs	$n_{\rm H,0}$ (10^{22}cm^{-2})	[0.02]
TBabs	$n_{\rm H,int}$ (10^{22}cm^{-2})	$0.08^{+0.03}_{-0.03}$
diskpbb	$kT_{\rm in}$ (keV)	$1.5^{+0.2}_{-0.2}$
	p	$0.58^{+0.04}_{-0.03}$
	K[a]	$3.9^{+3.9}_{-2.1}\times10^{-4}$
	$f_{0.3-8.0}$ (10^{-14} erg cm^{-2} s^{-1})	$8.12^{+0.22}_{-0.23}$
	$L_{0.3-8.0}$ (10^{39} erg s^{-1})	$2.2^{+0.4}_{-0.4}$
	$L_{\rm bol}$ (10^{39} erg s^{-1})	$2.9^{+0.5}_{-0.5}$

[a]Disk normalisation in units of $(r_{\rm in}/{\rm km})^2 \cos\theta\,(d/10\,{\rm kpc})^{-2}$.

2013; Marshall et al., 2013). Unlike M 51 ULX-1 and ULX-2, SS 433 does not appear as luminous as a ULX because the direct X-ray emission from the inner disk/corona region is already occulted from us. Its donor star periodically eclipses the thermal bremsstrahlung radiation ($L_{\rm X} \sim 10^{36}$ erg s^{-1}) from the base of the jet. The first unambiguous eclipsing behaviour in a candidate black hole X-ray binary outside the Milky Way was found in IC 10 X-1, located in a Local Group dwarf galaxy, with a Wolf-Rayet donor star, a binary period of 1.45 days, and an X-ray luminosity $L_{\rm X} \approx 10^{38}$ erg s^{-1} (Prestwich et al., 2007; Laycock et al., 2015a; Steiner et al., 2016). For IC 10 X-1, it is still disputed whether the accreting compact object is a black hole or a neutron star (Laycock et al., 2015b). Outside the Local Group, NGC 300 X-1 ($L_{\rm X} \approx 5 \times 10^{38}$ erg s^{-1}; binary period ≈33 hr) shows X-ray dips, consistent with occultation from geometrically thick structures in the outer disk, or absorption in the wind of the donor star, but not with true eclipses (Binder et al., 2015). A strong candidate for a true eclipse is the sharp dip in the *Swift*/X-Ray Telescope flux recorded once from the ULX P13 in NGC 7793, at an orbital phase consistent with the inferior conjunction of its supergiant donor star (Motch et al., 2014); however, there is no further confirmation of that single monitoring datapoint at subsequent epochs. Thus, we argue that the two M 51 ULXs discussed in this chapter are the first unambiguous eclipsing sources observed in or near the Eddington regime.

It is rare enough to find two such bright sources projected close to each other

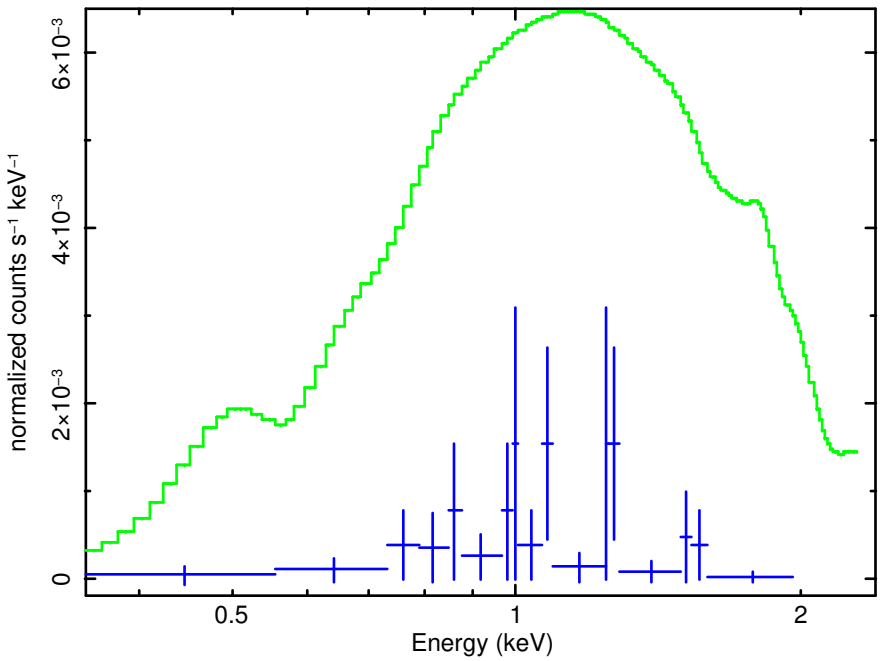

Figure 5.19: *Chandra*/ACIS-S spectrum of ULX-2 during the eclipse in ObsID 13813. The green curve illustrates the contribution from the best-fitting *diskpbb* component during the combined non-eclipse observations. The datapoints have been grouped to 1 count per bin.

in what is not a particularly active starburst region: it is obviously even stranger that both of them show eclipses. Therefore, we tried to assess the statistical significance of this finding. Firstly, we assume that any distance between ULX-1 and ULX-2 not in the plane of M 51 is negligible and thus only consider the ≈ 350 pc separation. We want to discover the chances of finding two randomly distributed, luminous X-ray binaries in the same galaxy within 350 pc of each other, both having inclination angles >80°. Assuming for example 10 ULXs with $L_{\rm X} \gtrsim 10^{39}$ erg s^{-1} in the same spiral galaxy within a radius of 8 kpc (an overestimate of the real number of ULXs detected in local-universe galaxies), we used a Monte-Carlo simulation, placing ULXs at random and recording the number of occurrences in which two ULXs were found within a radius of 350 pc; for 10 million trials, we find $P_1 \approx 6.6\%$. The probability of finding two nearby ULXs then has to be multiplied by the probability $(P_2)^2$ that they both show eclipses. Assuming no preferential orientation angle, the likelihood of finding a ULX with a viewing angle, for example, $\theta > \theta_{\rm min} = 70°$ is $P_2 = \cos 70°$. However, if the orientation is too close to 90°, the direct X-ray emission is likely blocked by the outer disk and the source would not appear as a ULX. The thickness of the disk in ULXs is unknown (likely a few degrees), and the minimum angle $\theta_{\rm min}$ that produces eclipses is model-dependent, as a function of the ratio between stellar radius R_* and binary separation a, namely $\cos\theta_{\rm min} \approx R_*/a$. For plausible distributions of

such quantities, $P_2 \lesssim 0.3$ (Pooley and Rappaport, 2005). The final probability becomes $P_1(P_2)^2 \lesssim$ a few 10^{-3}: we only expect this to happen once every few hundred major galaxies.

5.4.2 Spectral properties: broadened disks, Comptonisation and thermal plasma

Luminosity (or more precisely, mass accretion rate) and viewing angle are thought to be the main parameters that determine the observational appearance of ULXs in the X-ray band (e.g., Chapter 4 and Sutton et al., 2013b; Middleton et al., 2015a); disentangling and quantifying their roles is still an unsolved problem. M 51 ULX-1 and ULX-2 have approximately the same luminosity and inclination angle (as they both show eclipses); however, their spectral appearance is substantially different. ULX-1 has soft colours in the *Chandra* band and is well modelled by a soft thermal component (blackbody or disk-blackbody) plus Comptonisation; ULX-2 has hard colours and is well modelled by a slim disk with $kT_{\rm in} \approx 1.5$–2.0 keV (hotter than a standard disk). Also, ULX-1 has significant line residuals around 1 keV (consistent with thermal plasma emission), which are not seen in ULX-2. Thus, we propose that there are other physical parameters that determine the spectral appearance of a ULX in addition to Eddington ratio and viewing angle. We also discovered that ULX-1 has strong radio and optical evidence of a jet (as we will discuss in the following chapter) while ULX-2 does not; understanding the relation between outflow structure and spectral appearance remains a key unsolved problem.

The different role played by an optically-thick thermal component in the modelling of ULX-1 and ULX-2 exemplifies the confusion sometimes found in the literature about the properties of ULX disks. In ULX-1, the "disk" emission is much cooler ($kT \sim 0.1$–0.2 keV) and comes from a large area, with characteristic size ≈2000–3000 km (as inferred from the normalisation of the *diskir* component in Table 5.7 and/or the normalisation of the *diskbb* component in Table 5.9). This is much further out than the innermost stable circular orbit around a black hole; it is probably located at, or just outside, the spherisation radius, where massive radiation-driven outflows are predicted to be launched. This thermal component represents what is sometimes referred to as the "soft excess" in ULXs (e.g., Miller et al., 2003; Roberts et al., 2005; Stobbart et al., 2006; Gladstone et al., 2009). In M 51 ULX-1 and in many other similar ULXs, it contributes $\lesssim 10\%$ of the continuum flux in the *Chandra* band. Despite being often modelled with a *diskbb* component for practical purposes, it is by no means clear whether or not it originates from the disk; it could come instead from the more optically

thick parts of the outflow (as discussed in Chapter 4 and Middleton et al. 2015a). On the other hand, the "disk" in ULX-2 is the dominant continuum emission component. It is probably emitted by a non-standard, geometrically thicker disk with advection, photon trapping and outflows (slim disk model), extending all the way down to the innermost stable circular orbit and possibly even a little further inside it (Vierdayanti et al., 2008). This state is the natural progression from the high/soft state of stellar-mass black holes ($L \lesssim 0.3 L_{\rm Edd}$; Remillard and McClintock, 2006), to the "apparently standard" regime (Kubota and Makishima, 2004) and the super-Eddington regime. It is also sometimes referred to as the "broadened disk" ultraluminous regime (Sutton et al., 2013b).

A temperature $kT_e \approx 0.8$ keV for the Comptonising region in ULX-1 is certainly unusually low for a ULX, but not unique. The ULX NGC 55 X-1 has a similar Comptonisaton temperature, similar seed photon temperature $kT_0 \approx 0.2$ keV, similar optical depth $\tau \approx 10$ and similar luminosity $L_{\rm X} \approx 2 \times 10^{39}$ erg s^{-1} (Gladstone et al., 2009). It is a classic example of a ULX in the soft ultraluminous regime (Sutton et al., 2013b). NGC 55 X-1 is also viewed at high inclination, as proved by X-ray dips attributed to clumps of obscuring material in the outer disk (Stobbart et al., 2004). As for M 51 ULX-1, NGC 55 X-1 gets softer during the dips: this is consistent with the obscuration of the harder emission from the inner disk region, while a more extended source of soft X-ray photons remains partially unocculted (Stobbart et al., 2004).

It is important to underline the detection of the thermal plasma emission in ULX-1 out of eclipse, with a luminosity $L_{\rm X,mekal} \approx 2 \times 10^{38}$ erg s^{-1} and an emission measure $\sim n_e^2 V \approx 10^{61}$ cm^{-3} (as fitted to the spectra of ObsIDs 13812, 13813 and 13814). The detection of residual soft emission in eclipse, with a luminosity $L_{\rm X} \approx 2 \times 10^{37}$ erg s^{-1}, is consistent with a fraction of the emitting hot gas (perhaps the outer part of the same outflow responsible for the Comptonised component) extending on a scale similar to, or larger than, the size of the companion star; namely, a radius $\gtrsim$ a few $\times 10^{12}$ cm (as we shall discuss in Section 5.4.3). Conversely, the fact that $\approx$90% of the thermal plasma emission seen out of eclipse also disappears in eclipse is evidence that the emission comes directly from a region of comparable size to the binary system, and not for example from the hot spots of a compact jet on a scale of a few pc (which would still be unresolved by *Chandra* but unaffected by eclipses). An extended hot halo is a characteristic feature of the best-studied eclipsing X-ray binary, the low-mass Galactic system EXO 0748−676 (Bonnet-Bidaud et al., 2001). Soft X-ray residuals consistent with thermal plasma emission (and/or absorption) have been reported in several other (non-eclipsing) ULXs such as NGC 5408 X-1 (Middleton et al., 2014, 2015b; Sutton et al., 2015; Pinto et al., 2017b), NGC 6946 X-1 (Middleton et al., 2014),

Ho II X-1 (Miyaji et al., 2001; Dewangan et al., 2004), NGC 4395 X-1 (Stobbart et al., 2006), NGC 4559 X-1 (Roberts et al., 2004), NGC 7424 ULX2 (Soria et al., 2006b), NGC 1313 X-1 (Bachetti et al., 2013; Pinto et al., 2017b) and Ho IX X-1 (Walton et al., 2014); the last two of those ULXs are hard ultraluminous sources, while all the others are classified as soft ultraluminous.

5.4.3 Constraints on the donor star of ULX-1

Wind accretion is not an effective mechanism to produce X-ray luminosities $\gtrsim 10^{39}$ erg s^{-1}; at such luminosities, stellar-mass black holes require feeding via Roche-lobe overflow, or at the very least, via a focused wind from a donor star that is almost filling its Roche lobe. For the following discussion we will assume that the donor star in ULX-1 (and in ULX-2, although not discussed here for a lack of constraints) is at least close to filling its Roche lobe. Therefore, we will express the radius of the donor star R_* as a function of binary separation a as,

$$R_*/a \approx \frac{0.49q^{2/3}}{0.6q^{2/3} + \ln(1+q^{1/3})}, \tag{5.7}$$

valid to better than 1% for any q (Eggleton, 1983). We have already shown (Figure 5.10) that there are only selected pairs of values for the binary period P and the eclipse duration $\tau_{\rm ecl}$ consistent with the empirical data. Each value of $\phi \equiv \pi\tau_{\rm ecl}/P$ corresponds to one particular solution (Equations 4 and 5 in Chanan et al., 1976) for the pair of (θ, q) where θ is, as usual, the viewing angle, and $q \equiv M_*/M_\bullet$ is the ratio of donor star mass over compact object mass. Analytic solutions of $q(\phi)$ can be obtained (Pooley and Rappaport, 2005) in the limiting case of $\theta = 90°$:

$$\begin{aligned} \phi &= \arcsin(R_*/a), \\ &\approx \arcsin\left[\frac{0.49q^{2/3}}{0.6q^{2/3} + \ln(1+q^{1/3})}\right]. \end{aligned} \tag{5.8}$$

As an example, in Figure 5.10 we labelled 4 representative values of $q(\theta = 90°)$ corresponding to 4 permitted values of ϕ (marked as A,B,C,D). For a fixed value of ϕ, q increases going to lower (less edge-on) values of θ (Table 1 in Chanan et al., 1976). For example, for $\phi = \pi\tau_{\rm ecl}/P = 0.17$, $q(\theta = 80°) \approx 1.3q(\theta = 90°)$, and $q(\theta = 70°) \approx 2.8q(\theta = 90°)$; for $\pi\tau_{\rm ecl}/P = 0.08$, $q(\theta = 80°) \approx 2.0q(\theta = 90°)$, and $q(\theta = 70°) \approx 7.4q(\theta = 90°)$. Regardless of the uncertainty in the true value of θ for ULX-1, the robust result is that permitted periods of ≈6 days always correspond to $q(\theta) \geq q(90°) \gtrsim 4$ (with a more likely range $q \sim 5$–10), while permitted periods of ≈12–13 days correspond to $q(\theta) \geq q(90°) \approx 0.25$–1.2. In the

young stellar environment in which ULX-1 is located, with a likely OB donor star, the higher range of mass ratios (longer eclipse fraction) is indicative of a neutron star accretor, or a low-mass stellar black hole seen almost edge-on; instead, the lower range of mass ratios (shorter eclipse fraction) is consistent with a larger range of black hole masses, or with a neutron star seen at intermediate angles $\theta \sim 60°$–$70°$.

If q is known or well constrained, we can then derive a period-density relation for the donor star, and constrain its mass and evolutionary stage. In the limiting case of $q \lesssim 0.5$, such a relation reduces to $\bar{\rho} \approx 110 P_{\rm hr}^{-2}$ g cm^{-3}; however, in the more general case (Eggleton, 1983),

$$\bar{\rho} \approx \frac{10.89}{P_{\rm hr}^2} \left(\frac{q}{1+q} \right) \left[\frac{0.49 q^{2/3}}{0.6 q^{2/3} + \ln(1+q^{1/3})} \right]^{-3} \text{g cm}^{-3}. \quad (5.9)$$

For example, for $q = 1$, $\bar{\rho} \approx 99 P_{\rm hr}^{-2}$ g cm^{-3}; for $q = 5$, $\bar{\rho} \approx 65 P_{\rm hr}^{-2}$ g cm^{-3}.

We chose two representative values of q consistent with the 6-day range of period solutions ($q = 4$ and $q = 10$), and two values of q consistent with periods in the 12-day range ($q = 0.5$ and $q = 1$). For those four values of q, we calculated the average density of the Roche-lobe-filling donor star (Table 5.13). Typical values are $\bar{\rho} \approx 3 \times 10^{-3}$ g cm^{-3} for the shorter period solution, and $\bar{\rho} \approx 10^{-3}$ g cm^{-3} for the longer one. Finally, we used the latest set of Padova isochrones [2] (Bressan et al., 2012; Chen et al., 2015) with metallicity $Z = 0.019$, to estimate what types of stars have such densities, for a series of stellar population ages. In practice, we know that both ULXs reside in a region of the M 51 disk with recent star formation (which we will show in Chapter 6). Therefore, we only focused on population ages $\leq$100 Myr as the most likely candidates for the ULX donor stars. We find (Figure 5.20) that both ranges of permitted periods correspond to blue supergiants ($B-V$ colour index ≈ -0.2–0 mag) with absolute brightness M_V spanning the range between $M_V \approx -3$ mag and $M_V \approx -6$ mag, depending on their age; stars corresponding to the longer period are approximately half a magnitude brighter than those associated with the shorter period. For the youngest ages ($\approx$5 Myr), the characteristic periods allowed for ULX-1 are consistent with donor stars of masses $\approx$29–31 $M_\odot$, and radii $\approx$24–35 $R_\odot$; for an age of $\approx$20 Myr, the predicted mass is $\approx$11 $M_\odot$, with radii $\approx$17–25 $R_\odot$; for an age of $\approx$50 Myr, the predicted mass is $\approx$7 $M_\odot$, with radii $\approx$14–20 $R_\odot$ (Table 5.13). In Chapter 6, we will discuss how the observed optical brightness of the ULX-1 counterpart and of the neighbouring stars overlaps with these predictions.

The mass $M_\bullet$ of the compact object is still unknown, but from the analysis

[2] Available at http://stev.oapd.inaf.it/cgi-bin/cmd

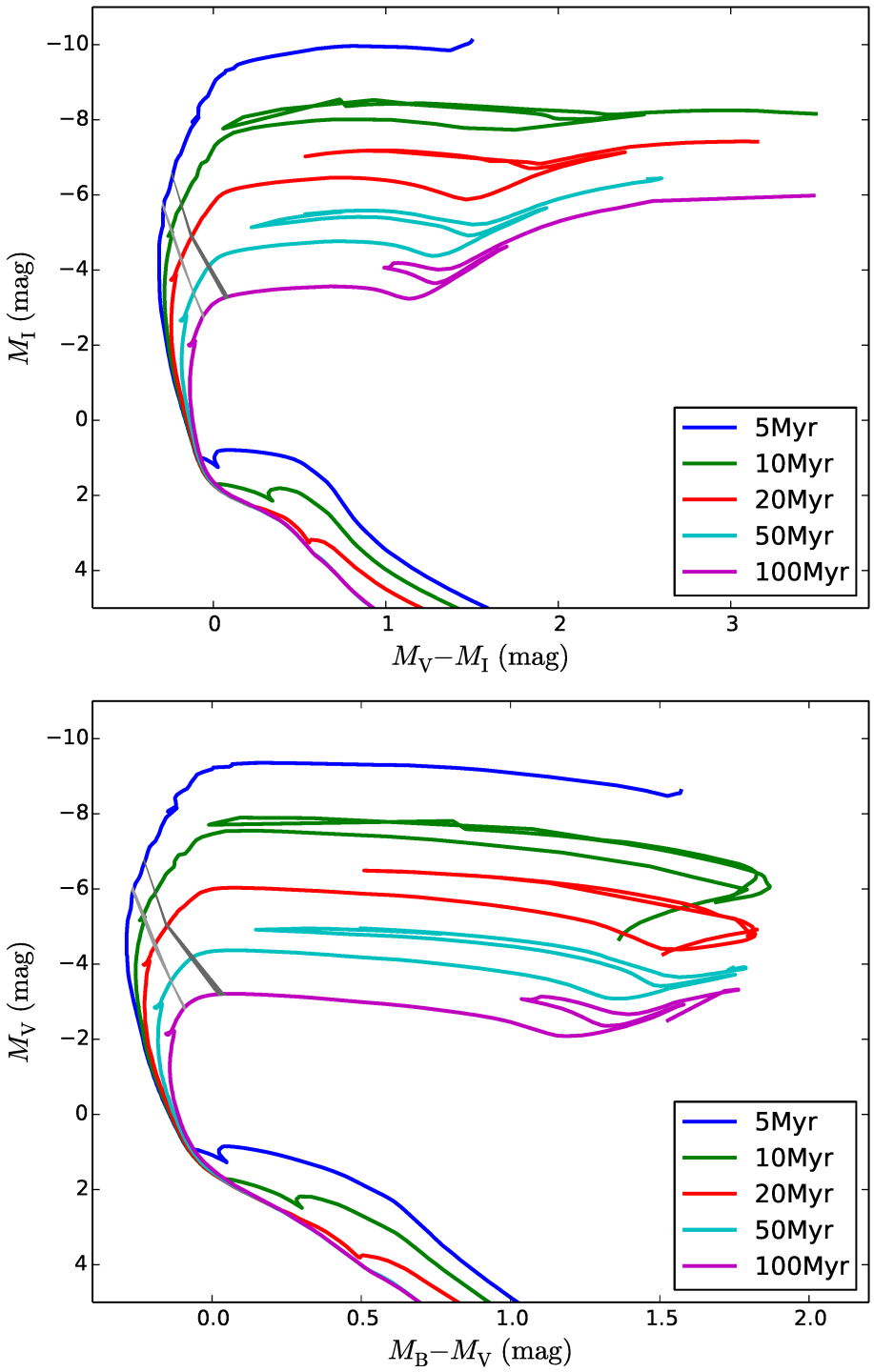

Figure 5.20: Top panel: theoretical stellar-population (I, $V-I$) isochrones, with the location of the potential donor stars of ULX-1 consistent with the permitted range of binary periods. The dark shaded grey band represents (young) stars with a mean density consistent with a period $12.2\,\mathrm{d} \leq P \leq 13.1\,\mathrm{d}$. The light shaded grey band represents stars with a mean density consistent with a period $6.1\,\mathrm{d} \leq P \leq 6.4\,\mathrm{d}$. Bottom panel: as in the the top panel, for the (V, $B-V$) isochrones.

Table 5.13: Main properties of Roche-lobe-filling donor stars for a representative sample of acceptable binary periods for ULX-1.

Age	M_*	R_*	M_V	$T_{\rm eff}$	$M_\bullet$	M_*	R_*	M_V	$T_{\rm eff}$	$M_\bullet$
(Myr)	$(M_\odot)$	$(R_\odot)$	(mag)	(K)	$(M_\odot)$	$(M_\odot)$	$(R_\odot)$	(mag)	(K)	$(M_\odot)$
	$P = 6.2$d, $q = 4.0$					$P = 6.3$d, $q = 10.0$				
5	29.7	23.8	−6.2	26,800	7.4	30.3	26.9	−6.4	25,600	3.0
10	17.3	19.8	−5.4	22,300	4.3	17.3	22.3	−5.6	21,000	1.7
15	13.1	18.1	−4.9	19,000	3.3	13.1	20.3	−5.1	18,000	1.3
20	11.0	17.1	−4.6	17,100	2.8	11.0	19.2	−4.8	16,200	1.1
30	8.8	15.8	−4.2	14,900	2.2	8.8	17.8	−4.3	14,100	0.9
40	7.7	15.1	−3.9	13,600	1.9	7.7	17.0	−4.1	12,800	0.8
50	6.9	14.6	−3.7	12,600	1.7	6.9	16.4	−3.8	11,900	0.7
70	5.9	13.9	−3.4	11,300	1.5	5.9	15.6	−3.5	10,700	0.6
100	5.1	13.2	−3.0	10,100	1.3	5.1	14.8	−3.1	9,400	0.5
	$P = 12.8$d, $q = 0.5$					$P = 13$d, $q = 1.0$				
5	30.8	33.2	−6.7	23,600	61.7	30.9	35.1	−6.8	23,000	30.9
10	17.3	27.4	−5.8	19,100	34.6	17.3	28.9	−5.9	18,600	17.3
15	13.1	25.0	−5.3	16,200	26.2	13.1	26.2	−5.4	15,800	13.1
20	11.0	23.6	−5.0	14,600	22.1	11.0	24.8	−5.1	14,200	11.0
30	8.8	21.9	−4.6	12,700	17.7	8.8	23.0	−4.6	12,400	8.8
40	7.7	20.9	−4.3	11,500	15.3	7.7	22.0	−4.3	11,200	7.7
50	6.9	20.1	−4.0	10,700	13.8	6.9	21.2	−4.1	10,400	6.9
70	5.9	19.1	−3.7	9,500	11.9	5.9	20.2	−3.7	9,300	5.9
100	5.1	18.2	−3.2	8,400	10.2	5.1	19.2	−3.2	8,200	5.1

outlined above we can see how observational constraints on q and M_* lead to constraints on the nature of the accretor. For example, for a period in the 6-day range, there are intermediate-age, evolved donor stars that have a mean density consistent with the period-density relation, but would imply (Table 5.13) a mass of the accreting object $\lesssim 2M_\odot$, consistent only with a neutron star accretor. On the other hand, an ≈6-day period is consistent with a stellar-mass black hole accretor only for a narrow range of massive, young (<10 Myr) donor stars. Conversely, mass ratios $\lesssim 1$ (corresponding to a period in the 12-day range) are consistent only with a black hole accretor. Independent observational constraints on the mass and age of the donor star in ULX-1 from the brightness of its optical counterpart will be presented and discussed in Chapter 6.

Mass transfer from a donor star more massive than the accretor shrinks the binary separation and therefore causes higher, sustained mass transfer rates; this

happens for $q > 5/6$ for the conservative mass transfer case, but we must account for possible additional shrinking of the system due to angular momentum losses in a wind (Frank et al., 2002). Blue supergiants have radiative envelopes; hence, mass transfer for $q \gtrsim 1$ should proceed on a thermal (Kelvin-Helmholtz) timescale of the envelope, $\sim 10^4$ yr. For $q \lesssim 5/6$ (permitted only for periods in the 12-day range), mass transfer would proceed instead on the nuclear timescale of the donor as it expands to the supergiant state. Therefore, determining the binary period of ULX-1 with future observations may reveal whether thermal-timescale or nuclear-timescale mass transfer is associated with strong ULX outflows.

Semi-detached, eclipsing systems such as ULX-1 and ULX-2 also offer the best chance to determine the accretor mass from optical spectroscopic observations. Let us assume, for example, that with future observations we will measure the binary period and strongly constrain the mass M_* and radius R_* of the donor star, and that we take spectra of the optical counterpart. If the donor star has absorption lines, phase-resolved optical spectroscopy might reveal its radial velocity curve, and hence the mass function $f(M_\bullet)$ of the compact object,

$$f(M_\bullet) = \frac{M_\bullet^3 \sin^3\theta}{(M_\bullet + M_*)^2} \approx \frac{M_\bullet^3}{(M_\bullet + M_*)^2}, \tag{5.10}$$

from which $M_\bullet$ can be determined. Even without phase-resolved spectroscopy (hard to schedule on an 8-m telescope), one can still constrain the accretor mass if double-peaked (disk) emission lines are detected in the optical spectrum (typically, Hα, Hβ and He II λ4686). Such lines are usually emitted from the outer rings of the accretion disk, and their full-width at half-maximum $V_{\rm fwhm}$ depends on the projected velocity of rotation of the gas at the outer disk radius $R_{\rm d}$:

$$V_{\rm fwhm}^2 \approx \frac{4GM_\bullet}{R_{\rm d}} \sin^2\theta \approx \frac{4GM_\bullet}{0.7R_{\rm RL}}, \tag{5.11}$$

where we have used the empirical and theoretical constraint (Whitehurst, 1988) that the accretion disks extends to an outer radius of ≈70% of the primary Roche lobe radius $R_{\rm RL}$. The Roche lobe radius is also a function of q; for example a useful approximation is

$$R_{\rm RL} \approx R_*(M_\bullet/M_*)^{0.45}, \tag{5.12}$$

(Frank et al., 2002). From Equations (5.11) and (5.12), $M_\bullet$ can be obtained without the need for phase-resolved spectroscopy.

5.5 Conclusions

Using archival *Chandra* and *XMM-Newton* observations, we found X-ray eclipses in two ULXs in the same region of M 51. Eclipsing systems among the ULX and luminous black hole X-ray binary populations are very rare: finding two of them not only in the same galaxy but a few arcsec (~ 350 pc in projection) from each other is a surprising result. Our serendipitous discovery in the archival data suggests that perhaps other eclipsing sources may have been missed, or misclassified as variable/transient in previous X-ray source catalogs. If persistent ULXs are stellar-mass black holes fed by Roche-lobe-filling B-type supergiants, with a mass ratio $q \sim 1$, systems seen at inclination angles $\gtrsim 75^\circ$ are expected to spend up to ≈15% of their time in eclipse, over characteristic binary periods ∼10 days. Neutron star accretors are expected to have even longer eclipse fractions when seen edge-on (≈20%), and to have eclipses for viewing angles as low as 55°. Thus, a statistical study of the observed eclipse fractions in ULXs is a possible way to determine whether the ULX population is dominated by black holes or neutron stars.

We analysed the presence and duration of the eclipses in ULX-1 and ULX-2 using a sequence of archival *Chandra* and *XMM-Newton* observations. For ULX-1, we argued that the most likely binary period is either ≈6.3 days, or ≈12.5–13 days. Assuming that the donor star fills its Roche lobe (a plausible assumption in ULXs, given the accretion rate needed to power them), we used the period-density relation to constrain the mass and evolutionary state of the donor star corresponding to those periods. For example, we showed that for a characteristic age ≈10 Myr, the donor-star mass is $\approx 17 M_\odot$, while for a characteristic age ≈20 Myr, $M_* \approx 11 M_\odot$.

We compared and discussed the X-ray spectral and timing properties of the two eclipsing ULXs. ULX-1 is softer, and has a spectrum well-fitted by Comptonisation models in a cool, dense medium. ULX-2 is harder, consistent with either a slim disk or Comptonisation in a hotter medium. Both sources are clearly seen at high inclination, given the presence of eclipses; however, neither of them is a ULS. This supports our earlier suggestion from Chapter 4 that ULSs require not only a high viewing angle, but also an accretion rate high enough to produce effectively optically thick outflows.

ULX-1 has strong spectral residuals around 0.8–1.0 keV: a spectral feature seen in other ULXs (usually those with a softer spectrum, thought to be viewed at higher inclination) but not well understood yet. Its most likely interpretation is a combination of thermal plasma emission and absorption lines from a dense outflow. In ULX-1, a residual thermal plasma emission (∼10% of the thermal

plasma emission out of eclipse) is still seen in eclipse, while the continuum component completely disappears. This suggests that the thermal plasma emission originates from a region slightly larger than the size of the eclipsing star (that is, from a characteristic size of a few 10^{12} cm), rather than from the inner disk (which would be completely eclipsed) or from pc-scale shock-ionised gas (which would not be eclipsed at all). Instead, ULX-2 does not show significant thermal plasma emission, although it does show residual emission in eclipse. In conclusion, ULX-1 and ULX-2 are important sources to help us disentangle the effects of inflow/outflow structure versus viewing angle, and we investigate them further with follow-up multiband studies, detailed in Chapter 6.

5.6 Summary

In this chapter, we presented the discovery of the first eclipsing ULXs. We used *Chandra* and *XMM-Newton* timing data to identify lightcurves with deep, step-function-like signatures which we interpret as occultations by the respective companion stars. Additionally, we also found that:

- Despite both ULXs having similar inclination angles and luminosities ($L_X \approx 2 \times 10^{39}\,\mathrm{erg\ s^{-1}}$), they have different X-ray properties (ULX-1 is a soft ULX while ULX-2 is a hard ULX).
- ULX-1 has a soft spectrum, best-fit with a Comptonised model with temperature $kT_e \approx 1$ keV. It also has thermal plasma emission, 10% of which remains visible during the eclipses, suggesting that the emission region is slightly larger than the companion star.
- ULX-2 has a hard spectrum, best-fit with a slim disk with $kT_{\rm in} \approx 1.5 - 1.8\,\mathrm{keV}$ and no significant thermal plasma emission.

Importantly, ULX-1 and ULX-2 represent two contrasting spectral classes: soft ultraluminous and broadened disk, respectively. It has been suggested (Sutton et al., 2013b) that harder ULXs are those sources seen at low inclination angles (down the polar funnel) while softer ULXs represent sources at high inclination angles (looking through the soft, Componising disk wind). However, our sources, both seen at high inclination angles, do not fit this interpretation, indicating that inclination angle alone cannot explain the different spectral properties of ULXs. Additionally, neither source is seen as a ULS, despite their high inclination angle and high accretion rate. This supports our argument that ULSs are a physically distinct class of sources, not just due to viewing angle. We explore these ideas further in Chapter 8.

Chapter 6

Multiband counterparts of two ULXs in M 51

This chapter is adapted from:

R. Urquhart, R. Soria, H. M. Johnston, M. W. Pakull, C. Motch, A. Schwope, J. C. A. Miller-Jones and G. E. Anderson. 2018. "Multiband counterparts of two eclipsing ultraluminous X-ray sources in M 51", *Monthly Notices of the Royal Astronomical Society*, Volume 475, Issue 3, p.3561-3576, DOI:10.1093/mnras/sty014

For this chapter, the new LBT spectroscopic observations were conducted by my co-author A. Schwope. The reduction and calibration of these data was performed by my co-author H. Johnston. Archival VLA+Effelsberg radio maps of M 51 were provided by G. Dumas. Detailed calculations on the ionising power of ULX-1 and ULX-2 were performed together with my co-author M. Pakull. I conducted all remaining work under the guidance of my supervisory panel.

After studying the accretion and outflow conditions (via their X-ray properties) in the inner regions of the two eclipsing ULXs, in this chapter, we look at the effect that ULXs have on their surroundings. This can be studied with optical (Figure 6.1) and radio observations of the large-scale structures associated with some ULXs. The high radiative and mechanical power outputs of ULXs can ionise their surrounding media via photo-ionisation and shock-ionisation, respectively.

In the previous chapters (Chapters 4 and 5), we suggest that, contrary to previous studies, the spectral classification of ULXs likely results from differences

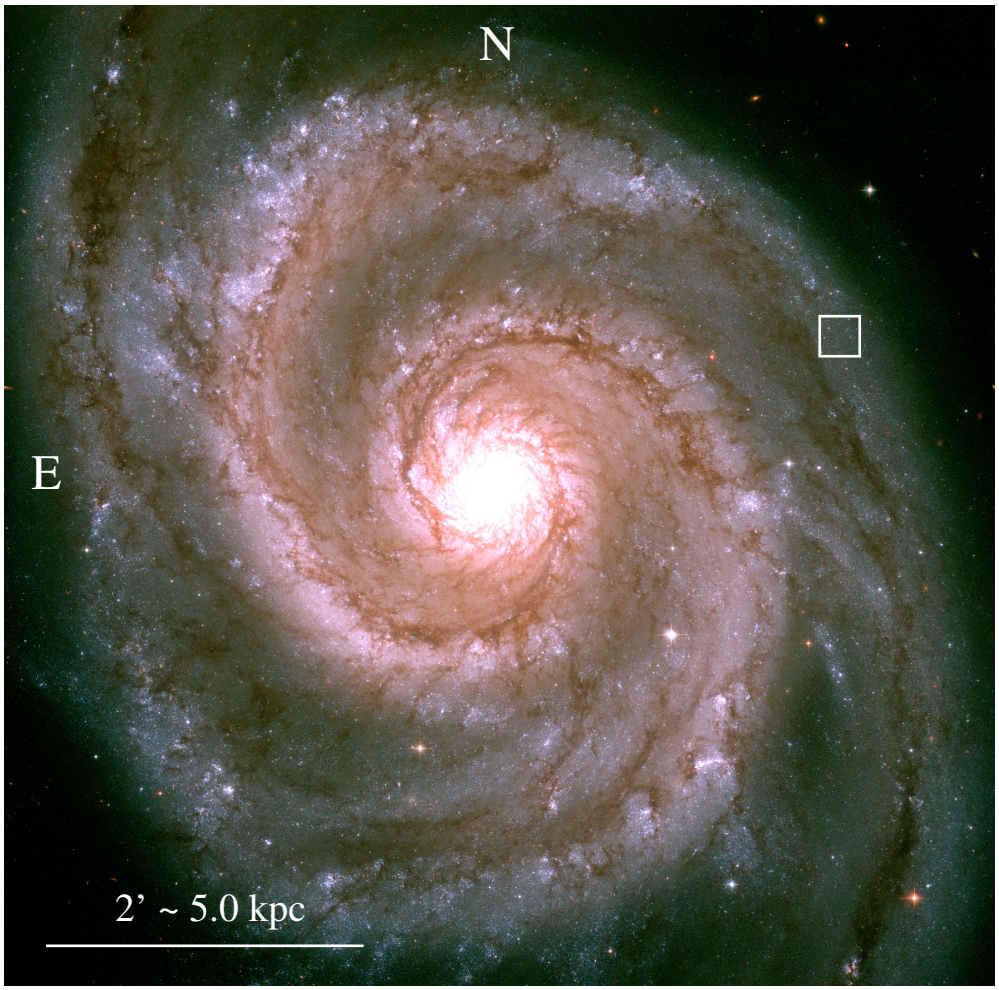

Figure 6.1: *HST*/ACS-WFC RGB colour image of M 51. Blue represents the F435W filter, green represents F555W and red represents F814W. The 15″×15″ white box contains ULX-1 and ULX-2 and shows the region in which we performed PSF photometry. This image is locked to the same coordinates and scale (including the white box) as the X-ray image Figure 5.1.

in, at least, the accretion rate and inclination angles. In this chapter, we study two ionised nebulae associated with the eclipsing ULXs we recently discovered, affording us the opportunity to investigate the outflow properties of these ULXs. In this chapter, we show that both ULXs are surrounded by ionised gas. ULX-1 is coincident with an elongated “jet-like” bubble, while ULX-2 is surrounded by a quasi-circular bubble. We will argue that in ULX-2 the nebula is consistent with an ordinary H II region photo-ionised by young stars, while in ULX-1, the gas is shock-ionised and the morphology suggests a jet origin. We will also show that the candidate jet source has a radio counterpart, while the other ULX does not.

Being highly energetic sources, ULXs have a significant impact on their surroundings. Their extreme X-ray luminosity photo-ionises the surrounding gas. Examples of ULX nebulae with a dominant X-ray photo-ionised component are

Holmberg II X-1 (Pakull and Mirioni, 2002) and NGC 5408 X-1 (Kaaret et al., 2003a; Soria et al., 2006a). The ionising X-ray luminosities inferred from the optical line emission of these nebulae match (within a factor of a few) the apparent X-ray luminosities of the compact objects, suggesting that at least those ULXs are not strongly beamed and their luminosities are intrinsically high (e.g., Pakull and Mirioni, 2002; Kaaret and Corbel, 2009). In addition to high photon luminosity, there is theoretical and observational evidence of powerful outflows (winds or jets) in ULXs (Ohsuga et al., 2005; Ohsuga and Mineshige, 2011; Pinto et al., 2016), consistent with their nature of super-critical accretors. The kinetic power of the outflows produces shock-ionised nebulae (ULX bubbles), such as those around IC 342 X-1 (Cseh et al., 2012) or Holmberg IX X-1 (Miller, 1995; Grisé et al., 2006). Tell-tale signs of the presence of shock-ionised gas are the expansion velocity of the bubble ($\sim$100–300 km s^{-1}) and the high [S II]/Hα line ratio; in fact, some ULX bubbles were previously mistakenly identified as supernova or hypernova remnants. In most cases, photo-ionised and shock-ionised gas coexists in a ULX bubble; the origin of the ionising photons may be both the direct emission from the central object and the forward shock precursor.

In a small number of shock-ionised ULX bubbles there is also direct evidence of collimated jets instead of (or in addition to) wide-angle outflows. The evidence is the elongated morphology of the bubble with symmetrical hot spots or lobes/ears. In nearby galaxies, this is seen in NGC 7793-S26 (Pakull et al., 2010; Soria et al., 2010) and of M 83-MQ1 (Soria et al., 2014); in the Milky Way, SS 433 very likely belongs to the same class of jetted, super-critical sources, with its shock-ionised "ears" protruding out of the W 50 bubble (Farnes et al., 2017; Goodall et al., 2011; Brinkmann et al., 2007; Fabrika, 2004; Zealey et al., 1980). Curiously, in all three cases, the X-ray luminosity from the central source is less than the ULX threshold ($\approx 10^{39}$ erg s^{-1}), either because our direct view of the source is mostly obscured, or because the instantaneous accretion rate is currently low. It is their kinetic power ($P_{\rm jet} > 10^{39}$ erg s^{-1}), inferred from the expansion velocity of the shocked gas and from the optical/IR line emission of the bubble (Pakull et al., 2010), that puts those three sources in the class of super-critical accreting stellar-mass objects. Another well-known ULX bubble, MF16 in NGC 6946 (Roberts and Colbert, 2003; van Dyk et al., 1994), has an elongated morphology consistent with the propagation of a symmetrical jet into the interstellar medium (ISM); in that case, the direct X-ray luminosity of the central source does exceed the ULX threshold, but may still be only a small part of the bolometric luminosity, mostly reprocessed in the UV band (Kaaret et al., 2010).

Evidence of powerful jets has also been found in a couple of other ULXs that do not have shock-ionised hot spots/lobes: Holmberg II X-1 (Cseh et al., 2014,

2015a) and M 81 ULS-1 (Liu et al., 2015). In Holmberg II X-1, the jet is revealed by a flaring radio core and radio-bright "knots" of synchrotron emission either side of the core. In M 81 ULS-1, the jet is revealed by the red and blue Doppler shifts of its Balmer emission lines, corresponding to $v \approx 0.17$c. The presence of a collimated jet in the M 81 ULS suggests that jets can co-exist with thick winds, which are likely to be the hallmark of the ULS subclass (Chapter 4, Soria and Kong 2016; Poutanen et al. 2007). No evidence of jets has been found so far in other ULSs.

Bright radio emission with 5-GHz luminosity $\nu f_\nu \gtrsim 10^{34}$ erg s^{-1} is another indication of the presence of a jet. The reason is that some of the bulk kinetic energy of the jet is used to accelerate relativistic electrons at the reverse shock; compression of the magnetic field lines in the shocked ISM leads to electron cooling via synchrotron radiation (Begelman et al., 1984). In addition to the flaring radio jet detected in Holmberg II X-1, the four prototypical sources with elongated bubbles mentioned above (NGC 7793-S26, M 83-MQ1, NGC 6946-MF16, and SS 433) all have strong optically-thin synchrotron emission. By analogy, the equally strong, optically-thin radio nebula (diameter ≈ 40 pc; Lang et al. 2007) around NGC 5408 X-1 is interpreted as evidence of a jet. However, not every optically-bright, shock-ionised ULX bubble has a radio counterpart (NGC 1313 X-2 is a classical example of a radio-quiet ULX bubble), and not every ULX with a bright radio counterpart is surrounded by an optically-bright shock-ionised bubble (as we said for Holmberg II X-1). For a given kinetic power in the jet, the composition of the jet (leptonic or baryonic), the collimation angle, the black hole spin, the gas density and magnetic field strength in the ISM, and the age of the bubble may affect the fraction of kinetic power that goes into synchrotron cooling.

In this chapter, we use an updated distance measurement to M 51 ($d = 8.58 \pm 0.10$ Mpc; McQuinn et al. 2016).

6.1 Observations and Data Reduction

6.1.1 Archival *HST* images

Publicly available *HST* data for M 51 were downloaded from the Hubble Legacy Archive[1]. The observations were part of the *HST* Mosaic of M 51 (proposal ID 10452) taken on 2005 January 12 with the Advanced Camera for Surveys (ACS), Wide Field Channel (WFC). This dataset includes three broadband filters (F435W, F555W, F814W) and the narrowband filter F658N, which covers

[1] http://hla.stsci.edu/hlaview.html

Hα and the two adjacent [N II] lines (central wavelength of 6584Å and effective width of 75Å). The total exposure time for the F814W and F555W bands was 8160 s, while for F435W it was 16320 s and for F658N 15640 s. The archival data were processed "on-the-fly" using the standard ACS pipeline (CALACS: Hack and Greenfield 2000), correcting for flat-fielding, bias and dark current. We then built a normalised, weighted average of the images in the F814W and F555W bands, and subtracted it from the F658N image, in order to remove the continuum stellar contribution from the narrow-band filter. Henceforth, when we refer to the F658N image, we mean the continuum-subtracted image unless stated otherwise.

We performed aperture and PSF photometry on the F435W, F555W and F814W filters, using the DAOPHOT package (Stetson, 1987) embedded within the Image Reduction and Analysis Facility (IRAF) software Version 2.16 (Tody, 1993). The *daofind* task was used to identify point-like sources within a 50″×50″ region centred on the mid-point between ULX-1 and ULX-2 (a concentric region approximately four times larger than the white box in Figure 6.1). Aperture photometry was then performed on these stars using *phot*. Due to the crowded nature of the field (Figure 6.2), a circular source aperture with a radius of 3 pixels (0.″15) was used; the encircled energy fraction within that radius, for a point-like source, is ≈80%. For the PSF photometry, several bright, isolated sources were manually selected and inspected (with the tasks *pstselect* and *psf*); each candidate PSF star was manually inspected and those that appeared slightly extended were rejected. The average PSF created from those stars was then used as input to the photometry task *allstar*. PSF photometry was conducted on all stars within a 15″×15″ box centred on the mid-point of ULX-1 and ULX-2 (white box overplotted in Figure 6.1 and displayed in its entirety in Figure 6.2). In addition to the photometry of point-like sources, we measured the total background-subtracted count rates of the emission nebulae around the two ULXs. Finally, count rates of stellar and nebular sources were converted to physical magnitudes and fluxes in the various bands, using the zeropoint tables for ACS-WFC available on the STScI web site[2].

6.1.2 New Large Binocular Telescope spectra

Optical spectroscopic data together with the corresponding calibration exposures (dark and bias frames, flat fields, arcs) were taken with the LBT's Multi-Object Double Spectrograph (MODS; Pogge et al., 2010). The targets were observed from 2016-05-10 UTC 06:31:53.064 (MJD 57518.272142) for a total of

[2]http://www.stsci.edu/hst/acs/analysis/zeropoints/old_page/localZeropoints

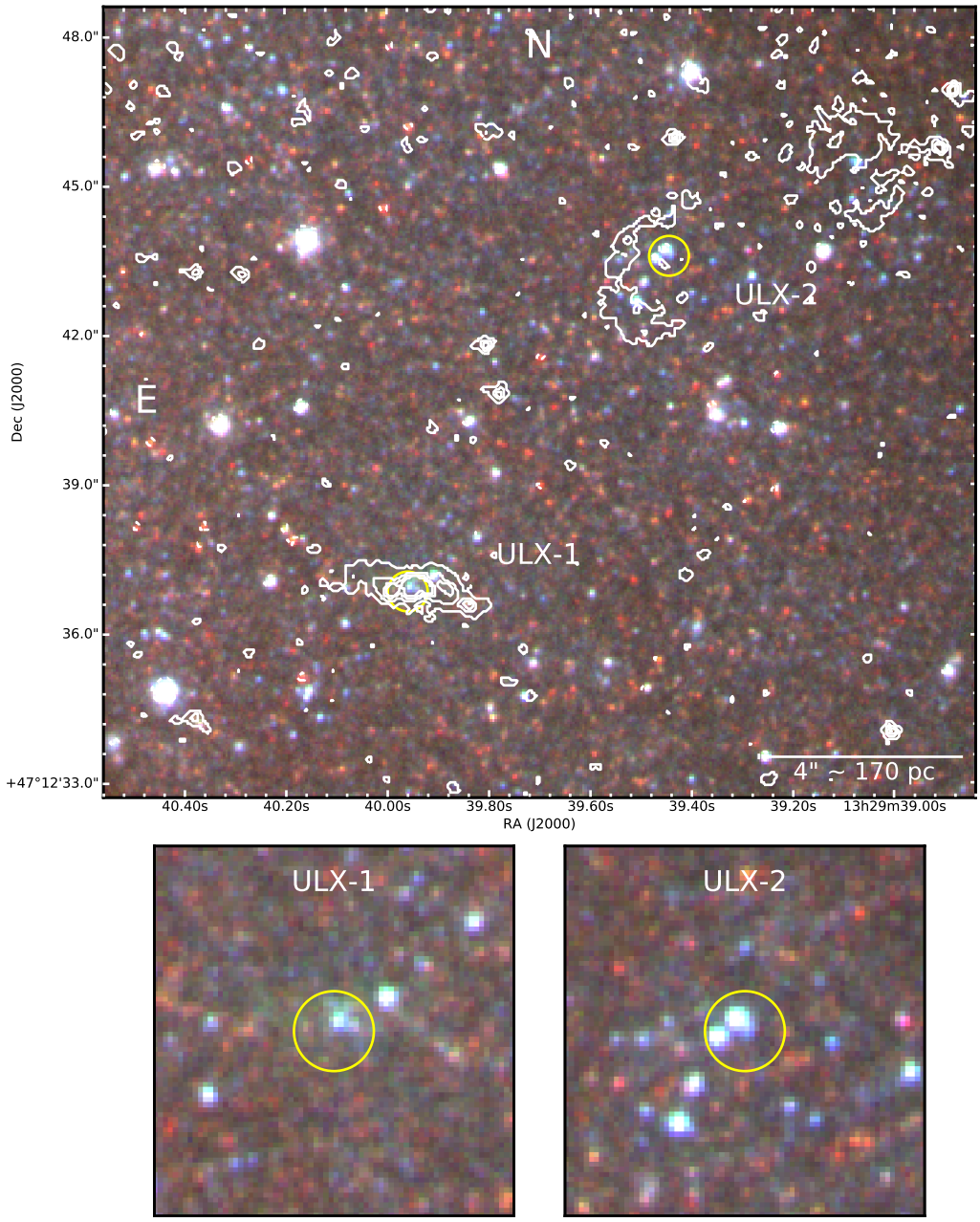

Figure 6.2: Top panel: zoomed-in *HST*/ACS image of the white box displayed in Figure 6.1. Blue represents the F435W band, green = F555W and red = F814W. Yellow circles represent the *Chandra* positions of ULX-1 and ULX-2 with 0.″4 errors. White contours represent optical line emission in the continuum-subtracted F658N band. Line emission can be seen near both ULXs; in ULX-1 there is an elongated jet-like structure while ULX-2 is inside a more spherical nebula. Contours levels are arbitrary and are simply used to indicate the morphology of the ionised gas nebulae. Bottom left panel: zoomed-in view of the ULX-1 field. Bottom right panel: zoomed-in view of the ULX-2 field.

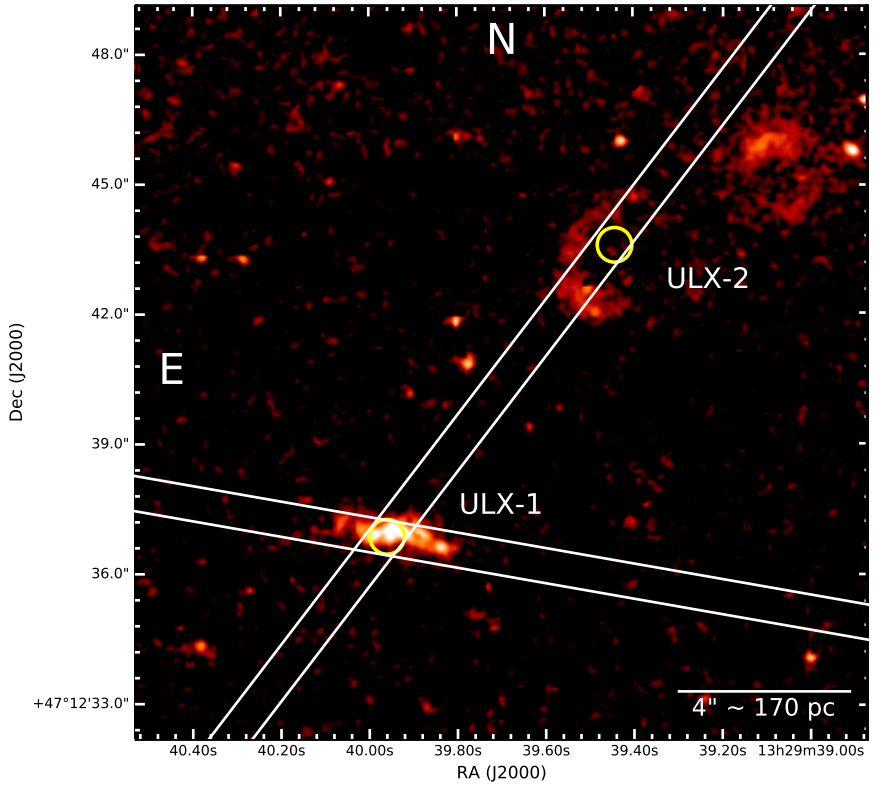

Figure 6.3: LBT slit positions, overplotted on the continuum-subtracted F658N image. In the first observation, the slit was aligned along the jet-like structure near ULX-1, including also the candidate optical counterpart of the ULX. This corresponded to an instrument celestial position angle of 80° East of North. The second slit was positioned so as to observe the candidate optical counterparts of both ULX-1 and ULX-2, along with some of the diffuse emission around the two X-ray sources. This corresponded to a position angle of 322.5°. The yellow circles represent the *Chandra* positions of ULX-1 and ULX-2 with 0″.4 uncertainty.

3×900=2700 seconds, on each of the two MODS, and for each of two slit positions. We used a 0″.8-wide, segmented long slit with gratings G400L and G670L for the blue and red beam channels, respectively. The blue G400L grating has a resolution of 1850 at 4000Å and a nominal dispersion of 0.5Å per pixel, while the red G670L has a resolution of 2300 at 7600Å and nominal dispersion of 0.8Å per pixel. In the first observing configuration (OB1), the slit was oriented along the jet-like structure of ULX-1 (position angle PA = 80°, measured from North to East); in the second configuration (OB2), the slit was oriented to contain both the (candidate) point-like optical counterparts of ULX-1 and ULX-2 (Figure 6.3), at PA = 322.5°.

The raw data were bias-subtracted and flat-fielded with the reduction package modsCCDRed[3] Version 2.0.1, provided by the Ohio State University. Spectral trimming and wavelength calibration were done with the Munich Image Data

[3]http://www.astronomy.ohio-state.edu/MODS/Software/modsCCDRed/

Analysis System (MIDAS; Warmels 1992). We then used standard IRAF tasks for further analysis. We extracted one-dimensional background-subtracted spectra with the IRAF task *apall*. We flux-calibrated the red and blue spectra using the response files provided by the MODS instrumentation team. Finally, we analysed the spectra using the IRAF task *splot*; in particular, for each emission line, we measured equivalent width (EW), full width at half maximum (FWHM), and central wavelength (by fitting a Gaussian profile).

One of the main parameters we were interested in was the total Hα flux from the elongated nebula around ULX-1. The LBT slit was placed and oriented in order to cover as much of that region as possible (Figure 6.3) but some of the flux (about 20 percent) falls out of the slit. However, we can measure the total emission of that nebula from the *HST* F658N image, which includes the flux from Hα plus [N II] λ6548 and [N II] λ6583. We combined the information on the Hα/[N II] line ratio obtained from the LBT spectra, with the measurement of the total Hα + [N II] flux from the *HST* image. This gave us an absolute measurement of the total Hα luminosity of the nebula, regardless of what fraction of it falls on the LBT slit. After calibrating the Hα flux, we could then obtain the fluxes of all other emission lines in the LBT spectra, using their ratios to Hα. We applied a similar procedure to determine the total Hα flux (and by extension, the fluxes in the other lines) of the nebula around ULX-2, which could only be partly covered by the 0.″8 LBT slit (Figure 6.3). Finally, we de-reddened the spectra assuming line-of-sight extinction $A_{\rm v} = 0.095$ mag corresponding to $E(B-V) = 0.031$ mag (Schlafly and Finkbeiner, 2011). We list the extinction-corrected emission line fluxes for both nebulae later in this chapter.

An additional, important caveat to keep into account is that MODS does not have an Atmospheric Dispersion Corrector, so the spectral data suffer from slit losses due to atmospheric dispersion, when the slit is not fixed at or near the parallactic angle. Normalising the Hα line flux to the value inferred from the *HST* image allows us to sidestep this problem, at least for the red spectra. We used the Ohio State University's online calculator[4] to estimate the effect that differential atmospheric refraction may have on our MODS spectra. The observations with the slit in the OB1 configuration were taken at an hour angle $\approx 0^h.9$–$1^h.2$; the differential refraction between Hα and Hβ is $\lesssim$0.″2. For the OB2 configuration, the spectra were taken at hour angles $\approx 2^h.2$–$2^h.5$, corresponding to differential refractions $\approx$0.″3 between Hα and Hβ and $\approx$0.″4 between Hα and Hγ. This shift is already of the same size as the typical scale of structural inhomogeneities in the two nebulae; therefore, slightly brighter clumps in the two nebulae may be on the slit at Hα but fall outside the slit at bluer wavelengths.

[4] http://www.astronomy.ohio-state.edu/MODS/ObsTools/obstools.html#DAR

6.1.3 Archival VLA data

Radio maps of M 51 were provided by G. Dumas (private communication); see Dumas et al. (2011) for a detailed discussion of the instrumental setup. In summary, observations were taken from 1998 to 2005 using the Very Large Array (VLA) at 1.4 GHz (20 cm) in the A, B, C and D configurations, at 4.9 GHz (6 cm) in the B, C and D configurations, and at 8.4 GHz (3.6 cm) in the C and D configurations. A total integration time of $\sim$ 170 hr over all three frequencies was achieved. The 8.4 and 4.9 GHz observations had been combined with data from the Effelsberg 100-m telescope Dumas et al. (2011), to detect extended emission regions that are resolved out in the VLA maps. The synthesised beam sizes for the 8.4 GHz, 4.9 GHz and 1.4 GHz images are $2\farcs4$, $2\farcs0$ and $1\farcs5$ respectively. Radio flux densities were determined using the Astronomical Imaging Processing System (AIPS; Greisen 2003). We fitted elliptical Gaussian profiles in the image plane, using the task `jmfit` to determine the integrated flux of the detected sources; we also calculated peak fluxes and root-mean-square noise in the field around the ULXs. We placed 3-σ upper limits on non-detections.

6.1.4 Astrometric alignment

In order to identify any optical and/or radio candidate counterparts of ULX-1 and ULX-2, we first needed to verify and, if necessary, improve the astrometric alignment between the *Chandra*, *HST*, and VLA images. For our first iteration, we took the default *Chandra* astrometry of the re-processed and stacked archival data from Chapter 5. The *Chandra*/ACIS-S astrometry is known to be accurate within $\approx 0\farcs5$ for 68% of the observations, and within $\approx 0\farcs7$ for 90% of the observations[5]. The *HST* astrometry was aligned onto the 2MASS catalogue (Skrutskie et al., 2006), which provides an accuracy within $0\farcs3$. The VLA astrometry was assumed absolutely correct by default. With this first set of astrometric solutions, we looked for coincidences between the X-ray, optical, and radio sources (not including the ULXs that were the subject of our study), within $\approx 0\farcs5$.

The positions of the X-ray sources were determined with the CIAO task `wavdetect`; the optical centroids of point-like sources with profile fitting in the DS9 package (Joye and Mandel, 2003); the radio positions with the AIPS package `jmfit`. We found seven coincidences between X-ray and optical point-like sources, four coincident optical and radio sources, and four X-ray/radio coincidences. From a comparison of the optical/X-ray and optical/radio coincidences, we noticed that the *HST* astrometry was systematically offset by $\approx 0\farcs1$ in both RA and Dec; therefore, we corrected the *HST* astrometry by that amount. The revised *HST*

[5] http://cxc.harvard.edu/cal/ASPECT/celmon/

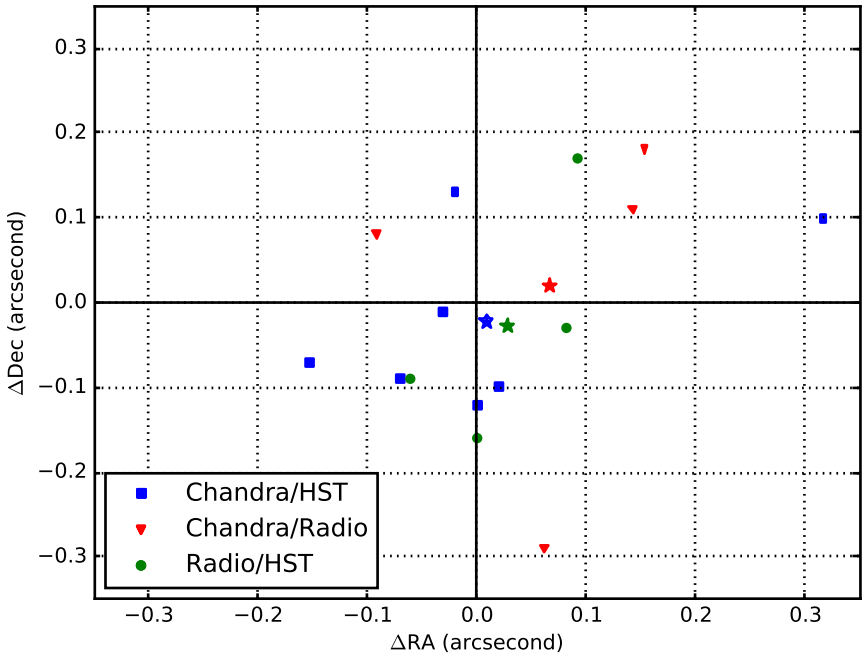

Figure 6.4: Relative positions of coincident, point-like *Chandra*, *HST* and VLA/Effelsberg sources. *Chandra* and *HST* coincidences are plotted as blue squares; *Chandra* and radio coincidences as red triangles; *HST* and radio coincidences as green circles. Stars represent the average offset between each pair of bands; systematic offsets are $<0\farcs1$ between any pair of bands. The residual discrepancies ($<0\farcs4$) are due to random scatter, mostly because of poor centroid determination of X-ray sources located far from the ACIS aimpoint.

astrometry is still within the $0\farcs3$ uncertainty of the 2MASS catalog. The X-ray positions (based on only 4 coincidences) were already within $0\farcs1$ of the radio positions and also within $0\farcs02$ of the improved *HST* positions. The resulting relative astrometry can be seen in Figure 6.4, with the average offsets between the three bands marked by stars. We did not find it necessary to make any further systematic corrections to any band. The residual discrepancies between the bands are simply random scatter of the individual sources. This is mostly due to the fact that the point spread function of point-like sources a few arcmin away from the *Chandra*/ACIS aimpoint becomes very extended and elongated, which increases the uncertainty in their central positions. In summary, we adopt the following X-ray positions for our ULXs: RA (J2000) = $13^{\rm h}29^{\rm m}39\fs960$, Dec. (J2000) = $+47\degr12\arcmin36\farcs86$ for ULX-1; RA (J2000) = $13^{\rm h}29^{\rm m}39\fs444$, Dec. (J2000) = $+47\degr12\arcmin43\farcs60$ for ULX-2. For both positions, we estimate a 3σ error radius of $0\farcs4$ arcsec, due to their off-axis positions and elongated PSF shape.

Table 6.1: De-reddened brightness of the candidate optical counterparts. Brightness values have been corrected for a line-of-sight Galactic reddening $E(B-V) = 0.031$ mag, corresponding to an extinction $A_{\rm F435W} = 0.13$ mag, $A_{\rm F555W} = 0.10$ mag and $A_{\rm F814W} = 0.06$ mag. All three optical sources are consistent with bright giants (luminosity class II) or supergiants (class Ib), of approximate spectral type B5–B6 for the ULX-1 star, and B3–B4 for the ULX-2 stars.

Source ID	F435W (mag)	F555W (mag)	F814W (mag)
ULX-1	24.62 ± 0.03	24.64 ± 0.05	24.87 ± 0.07
ULX-2 (north)	23.14 ± 0.03	23.33 ± 0.03	23.59 ± 0.03
ULX-2 (south)	23.60 ± 0.04	23.77 ± 0.02	23.87 ± 0.04

6.2 Results

6.2.1 Point-like optical counterparts

For ULX-1, only one bright optical candidate lies within the *Chandra* error circle (Figure 6.2, bottom left). This candidate is embedded in the brightest part of the elongated Hα nebula (Figure 6.3). For ULX-2, there are two potential optical counterparts within the *Chandra* error circle (Figure 6.2, bottom right), separated by $\approx 0\farcs25$, with comparable brightnesses and colours. The relatively low precision of the *Chandra* position makes it impossible to rule out either candidate at this stage. The Vegamag brightnesses of the three sources in the *HST* bands (de-reddened for a line-of-sight extinction corresponding to $A_V = 0.095$ mag) are summarised in Table 6.1. At a distance modulus of 29.67 mag, the absolute magnitudes and colours of all three sources are consistent with those of blue supergiants; if two of those three sources are the true counterparts of ULX-1 and ULX-2, they are likely to contain also a contribution from disk emission.

To constrain the ages of the three sources and of the surrounding stellar population, we used colour-magnitude diagrams in the three *HST* broadband filters (Figure 6.5); we plotted all stars with reliable brightness values within the $15'' \times 15''$ field shown in Figure 6.2. The black arrow in each plot indicates the effect of a hypothetical additional intrinsic extinction $A_V = 1$ mag. We compared the data with a set of theoretical isochrones [6] (Bressan et al., 2012; Chen et al., 2015) for a metallicity $Z = 0.015$ (Figure 6.5, top panels) and $Z = 0.040$ (Figure 6.5, bottom panels). The choice of those two alternative metal abundances reflects the two discrepant classes of values generally quoted in the literature for the disk of M 51; see, e.g., Croxall et al. (2015) and Bresolin et al. (2004) for the argument in favour of slightly sub-solar metallicities, and Moustakas et al. (2010) and Zaritsky et al. (1994) in favour of super-solar values. We will return to this

[6] Available at http://stev.oapd.inaf.it/cgi-bin/cmd

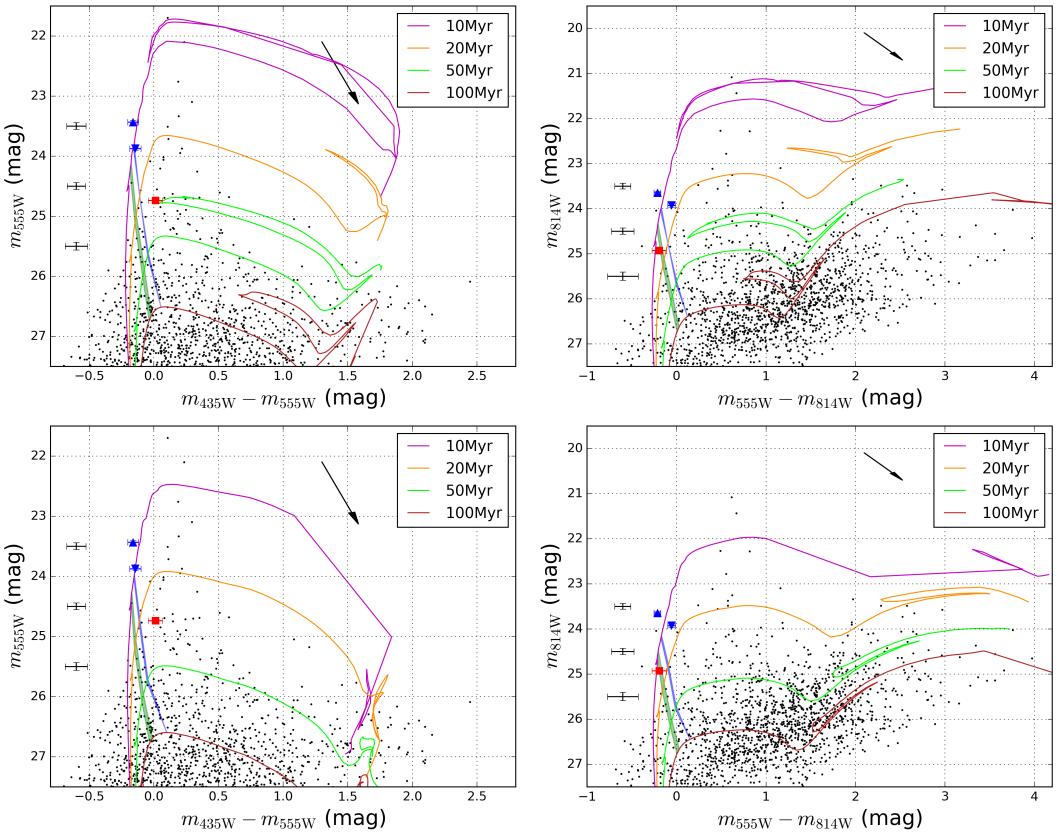

Figure 6.5: Top left panel: colour-magnitude diagram in the (F435W − F555W) versus F555W bands. The red square represents the candidate optical counterpart of ULX-1. The blue triangle represents the northern candidate counterpart for ULX-2 while the upside-down blue triangle represents the southern candidate counterpart. Black datapoints show the surrounding stars, with the black error bars on the left indicating their average uncertainties for each F555W magnitude interval. The black arrow shows the effect of one magnitude of extinction in F555W. Overlaid are Padova stellar isochrones for metallicity $Z = 0.015$. The isochrones have been corrected for a line-of-sight extinction $A_V = 0.095$ mag. The green and blue shaded zones represent the expected brightness and colour of Roche-lobe-filling stars with stellar densities consistent with a binary period of 6 or 12 days respectively, as seen in the X-ray light-curve of ULX-1 (see Section 6.2.1). Top right panel: as in the top left panel, but for F555W − F814W versus F814W. Bottom left panel: as in the top left panel, but with Padova stellar isochrones corresponding to a metallicity $Z = 0.040$. Bottom right panel: as for the top right panel, but for $Z = 0.040$.

metallicity discrepancy in Section 6.2.2.2.

Comparing the colour-magnitude plots, we notice that the inferred ages of the optical companion of ULX-1 are not consistent: ≈30 Myr in the (F435W − F555W) versus F555W diagram, and ≈10–20 Myr in the (F555W − F814W) versus F814W diagram, regardless of metal abundance. The two ages cannot be made consistent with the addition of intrinsic extinction; the star is ≈0.15 mag brighter in the F555W band than predicted by stellar isochrones. The reason for this small discrepancy is unclear. We note that the source is embedded in the most luminous part of the optical nebula, with its strong [O III] λ4959,5007 emission lines falling into the F555W band, which makes the subtraction of the local background emission more challenging and may be responsible for the small excess in that band. Alternatively, some of the optical emission from that point-like source is coming from the accretion disk or the outflow around the ULX, so that its colours are slightly different from a pure stellar spectrum. Distinguishing between the optical emission from donor star and accretion flow is a notoriously difficult task in ULXs (Heida et al., 2014; Gladstone et al., 2013; Soria et al., 2012; Grisé et al., 2012; Tao et al., 2012b, 2011); we will return to this issue later in this section.

Keeping those caveats in mind, we conclude that the optical counterpart for ULX-1 has a most likely age of ∼20 Myr, if dominated by a single donor star. We also plot stellar density bands (blue and green shaded regions in Figure 6.5). These shaded regions indicate regions of the parameter space where stars have a stellar density consistent with a Roche-lobe-overflow binary of period 6 or 12 days respectively. These two alternative values of the period come from the recurrent eclipses discussed in Chapter 5; the 6-day period is a solution suitable for mass ratios $4 \lesssim q \lesssim 10$, while the 12-day period is the solution corresponding to mass ratios $0.5 \lesssim q \lesssim 1$, where $q \equiv M_2/M_1$. Those two characteristic periods are then converted to stellar densities via the period-density-q relation (Eggleton, 1983). The current optical data (taking into account also the possible contamination from disk and nebular emission) are not sufficient to test whether the candidate star sits in either band. Thus we cannot yet use this method to rule out either of the proposed orbital periods of ULX-1, and constrain its mass ratio. However, we illustrate this method as a proof of concept, and to highlight the fact that the candidate optical star is at least approximately consistent with the kind of Roche-lobe-filling donor star required for ULX-1.

For ULX-2, both candidate optical counterparts have ages consistent with ≈10 Myr, and mass $M \approx 18 M_\odot$. Stars at this evolutionary stage have a characteristic radius $\sim 30\ R_\odot$ and a characteristic density $\rho \sim 3 \times 10^{-4}$ g cm^{-3}. This would imply a characteristic binary period of 24 days for $q \approx 1$ (i.e., for the case of a

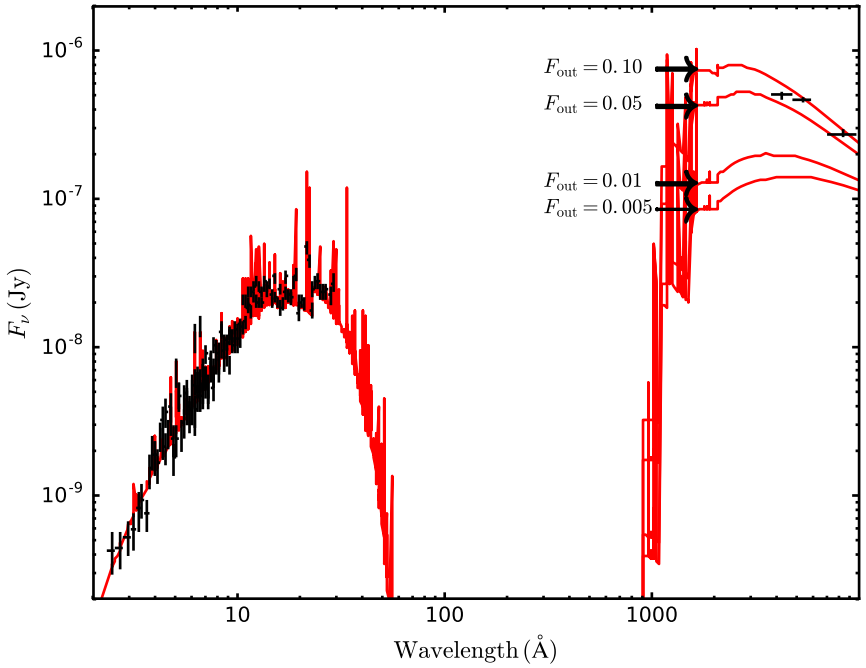

Figure 6.6: Stacked *Chandra*/ACIS-S spectrum and *HST* datapoints (black) for ULX-1, fitted with a *diskir* plus thermal plasma models (red curves). A sequence of four models has been plotted, differing only for their optical reprocessing fraction $f_{\rm out}$. A very high reprocessing fraction (almost 10%) is formally required in this model to reproduce the high optical/X-ray flux ratio. Such a high value strongly suggests that we are seeing a significant contribution to the optical continuum flux from the donor star, although we cannot separate the disk and star components with the data at hand.

canonical black hole primary), or a period of 10 days for $q \approx 17$ (i.e., for the case of a canonical neutron star primary). As we discussed in Chapter 5, the period of ULX-2 could not be determined from its X-ray light-curve and thus we have no observational constraint to test this prediction yet.

We have assumed so far that the candidate counterparts of both ULXs are dominated by the donor star. We can check this condition, at least for the case of ULX-1, by comparing the optical and X-ray fluxes. From Chapter 5, we know that the X-ray spectrum of ULX-1 is well fitted by an irradiated disk model. In Figure 6.6, we plot the combined X-ray spectrum and optical data points, together with a sequence of *diskir* models with varying levels of reprocessing ($f_{\rm out} = 0.1$, 0.05, 0.01 and 0.005). If we want to explain the optical flux as the intercepted and reprocessed component of the X-ray flux, we need a reprocessing fraction $f_{\rm out} \approx 0.075$. This is an order of magnitude higher than predicted (Dubus et al., 1999; King et al., 1997; de Jong et al., 1996; Vrtilek et al., 1990) or observed (Russell et al., 2014; Gierliński et al., 2009; Hynes et al., 2002) in Galactic X-ray binaries with sub-Eddington standard disks. However, much less is known about the reprocessing fraction in ULXs. For a transient ULX in M 83, Soria

et al. (2012) estimated a reprocessing fraction of $f \approx 5 \times 10^{-3}$; for other ULXs, reprocessing fractions of a few 10^{-2} were inferred (Sutton et al., 2014). Even a more geometrically thick disk (associated with super-critical accretion) cannot directly intercept such a high fraction of the X-ray emission; however, if the ULX has a broad disk outflow and polar funnel geometry, some of the X-ray photons emitted along the funnel may be scattered by the wind and irradiate the outer disk (Sutton et al., 2014; Narayan et al., 2017). Indeed, we argued previously that ULX-1 may have a strong wind, because of its soft X-ray spectral residuals, which in other ULXs are associated with outflows (Middleton et al., 2015b; Pinto et al., 2016). Nonetheless, we also know that ULX-1 must have a fairly large donor star, because of its eclipses, and we have already shown that the inferred size of the star is roughly consistent with the observed optical flux. We can use a similar argument for ULX-2. In that case, we previously found that the best-fitting XSPEC model to the X-ray spectrum is a *diskpbb* model (slim disk) rather than *diskir*, so we cannot directly constrain the reprocessing fraction from the model parameters. However, forcing a fit of the same spectrum with *diskir* we obtain a reprocessing fraction ≈ 0.2; this is because the observed X-ray flux is approximately the same as from ULX-1, while the optical flux is three times brighter. That makes it even more difficult to explain the optical emission as dominated by an irradiated disk rather than by a supergiant donor star.

6.2.2 Ionised nebulae

The *HST*/ACS image in the continuum-subtracted F658N filter clearly shows the presence of line emission around both ULXs (Figures 6.2 and 6.3). The nebula around ULX-1 is elongated, with a length of $\approx 2\farcs5$ $\approx$100 pc and a width of $\approx 0\farcs7$ $\approx$30 pc. The nebula around ULX-2 is more circular, with an outer radius of $\approx 1\farcs6$ $\approx$65 pc. There is also another region of line emission $\approx$200 pc to the northwest of ULX-2, of similar size and brightness, but without any bright X-ray source inside. In the absence of other evidence, we assume that this nebula is unrelated to ULX-2, rather than (for example) being part of a double-lobed structure powered by the ULX.

We defined source and background regions suitable for the two nebulae, and extracted their net count rates. We obtain rates of 21.52 ± 0.10 ct s^{-1} and 12.79 ± 0.25 ct s^{-1} for the ULX-1 and ULX-2 nebulae, respectively, in the F658N band. We then used the *HST*/ACS Zeropoint tables available online[7] (see also Bohlin 2016) to convert count rates to fluxes. A count rate of 1 ct s^{-1} corresponds to a flux of $\approx 1.95 \times 10^{-18}$ erg cm^{-2} s^{-1} Å^{-1} in that band. The effective width of

[7] https://acszeropoints.stsci.edu/

Table 6.2: Extinction-corrected emission line fluxes for the nebulae around ULX-1 and ULX-2, inferred from our LBT spectra integrated by the *HST* images. Fluxes were corrected for a line-of-sight extinction $A_V = 0.095$ mag. All fluxes were re-normalised so that the Hα + [N II] fluxes match the corresponding line fluxes measured from the *HST* image. Fluxes are displayed in terms of their relative strength to the Hβ line.

Line	$100 \times (f_\lambda / f_{\mathrm{H}\beta})$	
	ULX-1	ULX-2
3426 [Ne V]	16 ± 1	
3728 [O II] (λ3726 + λ3729)	605 ± 28	88 ± 6
3726 [O II][a]	243 ± 11	
3729 [O II][a]	353 ± 16	
3869 [Ne III]	92 ± 5	
3889 Hζ + He I	17 ± 2	
3967 [Ne III] + Hϵ λ3970	47 ± 2	
4069 [S II][b]	22 ± 5	
4104 Hδ	24 ± 2	
4340 Hγ	46 ± 3	30 ± 2
4363 [O III]	23 ± 2	
4686 He II	22 ± 1	
4861 Hβ	100 ± 4	100 ± 4
4959 [O III]	207 ± 10	30 ± 3
5007 [O III]	604 ± 28	96 ± 5
5200 [N I] (λ5198 + λ5202)	15 ± 1	
6300 [O I]	66 ± 3	
6364 [O I]	24 ± 2	
6548 [N II]	127 ± 6	48 ± 2
6563 Hα	299 ± 14	307 ± 15
6583 [N II]	377 ± 19	95 ± 5
6716 [S II]	132 ± 6	51 ± 3
6731 [S II]	111 ± 5	35 ± 3
7136 [Ar III]	21 ± 1	
7320 [O II]	51 ± 4	
9069 [S III]	20 ± 1	
9532 [S III]	40 ± 3	
10049 H I Paα	3.0 ± 0.2	
12818 H I Paβ	2.2 ± 0.3	
*Hβ flux (10^{-16} erg cm^{-2} s^{-1})	4.21 ± 0.18	4.47 ± 0.17

[a] Deblended with IRAF line-fitting tools
[b] Slightly contaminated by [S II] λ4076

the filter is 75 Å. Thus, the integrated line fluxes from the two nebulae are (3.39 ± 0.02) × 10^{-15} erg cm^{-2} s^{-1} and (2.01 ± 0.04) × 10^{-15} erg cm^{-2} s^{-1}, respectively, where we have also applied a de-reddening correction for line-of-sight extinction. At a distance of 8.6 Mpc, this corresponds to line luminosities of ≈3.0 ×10^{37} erg s^{-1} and ≈1.8 ×10^{37} erg s^{-1}, respectively, in the F658N filter. The filter bandpass covers [N II] λ6548, Hα λ6563, and [N II] λ6583. (Note that those three lines are redshifted by Δλ ≈ 9 Å with respect to their rest-frame wavelengths, because of the systemic velocity of M 51. This ensures that the flux from the [N II] λ6548 line is entirely included in the F658N bandpass, given the moderate line widths that we will discuss later in this section.) Of course the *HST* image alone cannot tell us how the line flux is split between Hα and the [N II] lines. For this, we need to examine the LBT spectra.

The LBT spectra across the ULX-1 and ULX-2 nebulae are displayed in Figures 6.7 and 6.8 respectively. The emission lines significantly detected in the two spectra, and their flux ratios to Hβ, are listed in Table 6.2. Those values are the total emission from the whole of each nebula. We recall that we obtain the total flux of each line by rescaling the Hα + [N II] emission from the LBT slit to the total nebular emission measured from the *HST* image in the F658N filter, and then rescaling the LBT fluxes of every other line according to their ratios to Hα. We also recall that ULX-1 was observed both in the OB1 (slit along the bubble) and OB2 (slit across the bubble) configurations. To a first approximation, the two spectra are identical; in this chapter, we use the spectra for the OB1 slit, because they provide a better approximation to the average emission of the whole nebula. A more comprehensive comparison of the two spectra and of the internal structure of the ULX-1 nebula is left to further work. Here we focus instead on the most significant differences between the two nebulae.

6.2.2.1 ULX-1 nebula

We see strong [N II] and [S II] lines relative to Hα (Figure 6.7), with a flux ratio ([N II] λ6548 + [N II] λ6583)/Hα ≈ 1.7 and ([S II] λ6716 + [S II] λ6731)/Hα ≈ 0.81. Such high ratios (even after accounting for a possible super-solar abundance in the disk of M 51) are traditionally good indicators of shock-ionised material (Mathewson and Clarke, 1973; Blair and Long, 1997; Gordon et al., 1998). Based on those ratios alone, the bubble could be classified as a typical supernova remnant; however, its very elongated morphology and the presence of a ULX in the middle make it more likely that the gas is shocked by a jet from kinetic power of the compact object, as is the case in other ULX bubbles. The ULX-1 bubble also shows He II λ4686 emission, and strong [O III] λ5007 emission relative to Hβ (Figure 6.7). Both features are consistent with shock-ionised gas and/or X-ray

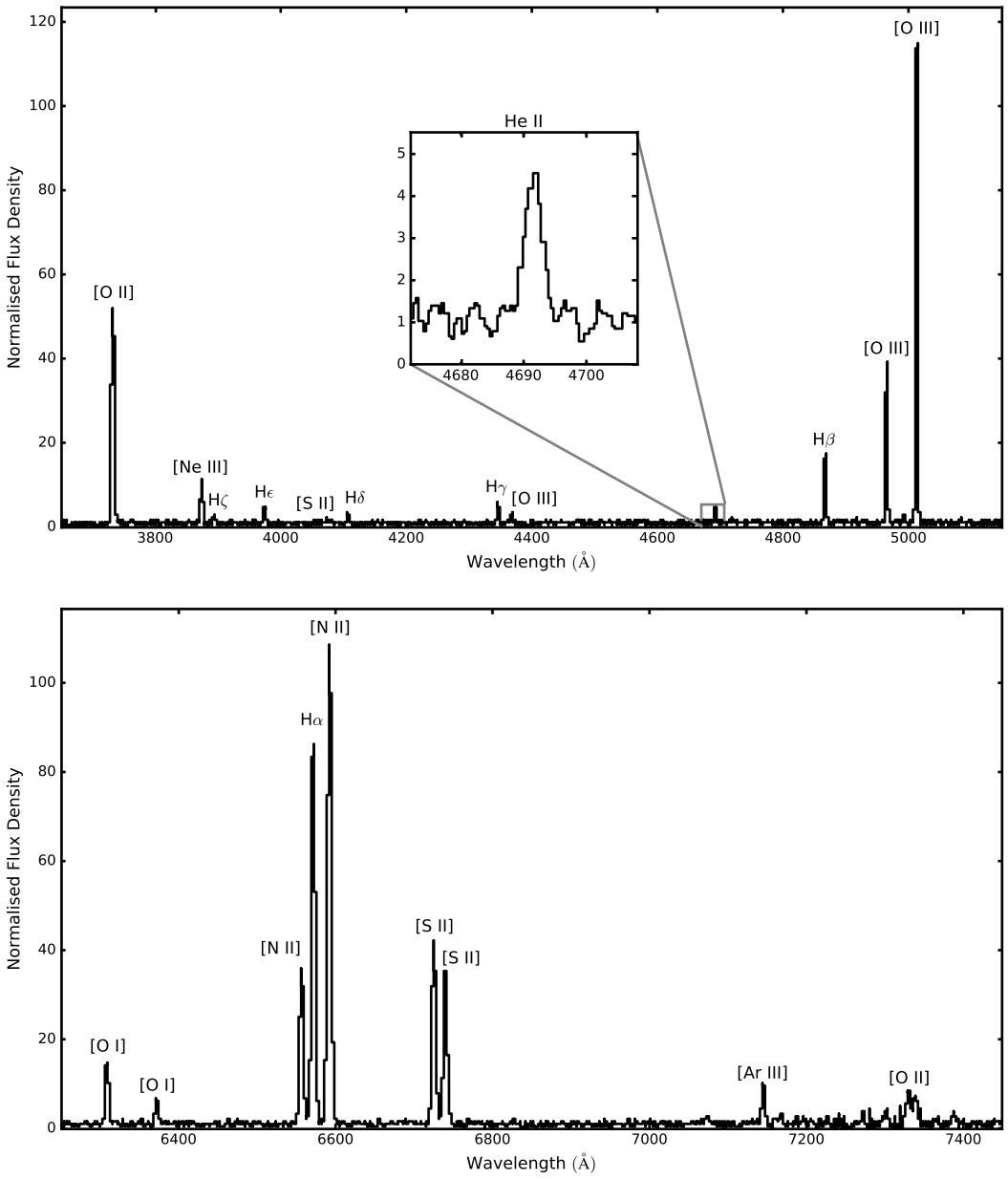

Figure 6.7: Top panel: LBT MODS1 plus MODS2 spectrum (blue arm) of the nebula around ULX-1, normalised to the continuum. The spectrum comes from the OB1 slit configuration (PA = 80°), that is along the long axis of the jet-like nebula. Inset: zoomed-in view of the He II λ4686 emission line. Bottom panel: as in top panel, but for the red side of the spectrum. (Note the different flux density scales of the two panels.) The spectra are consistent with emission from shock-ionised material.

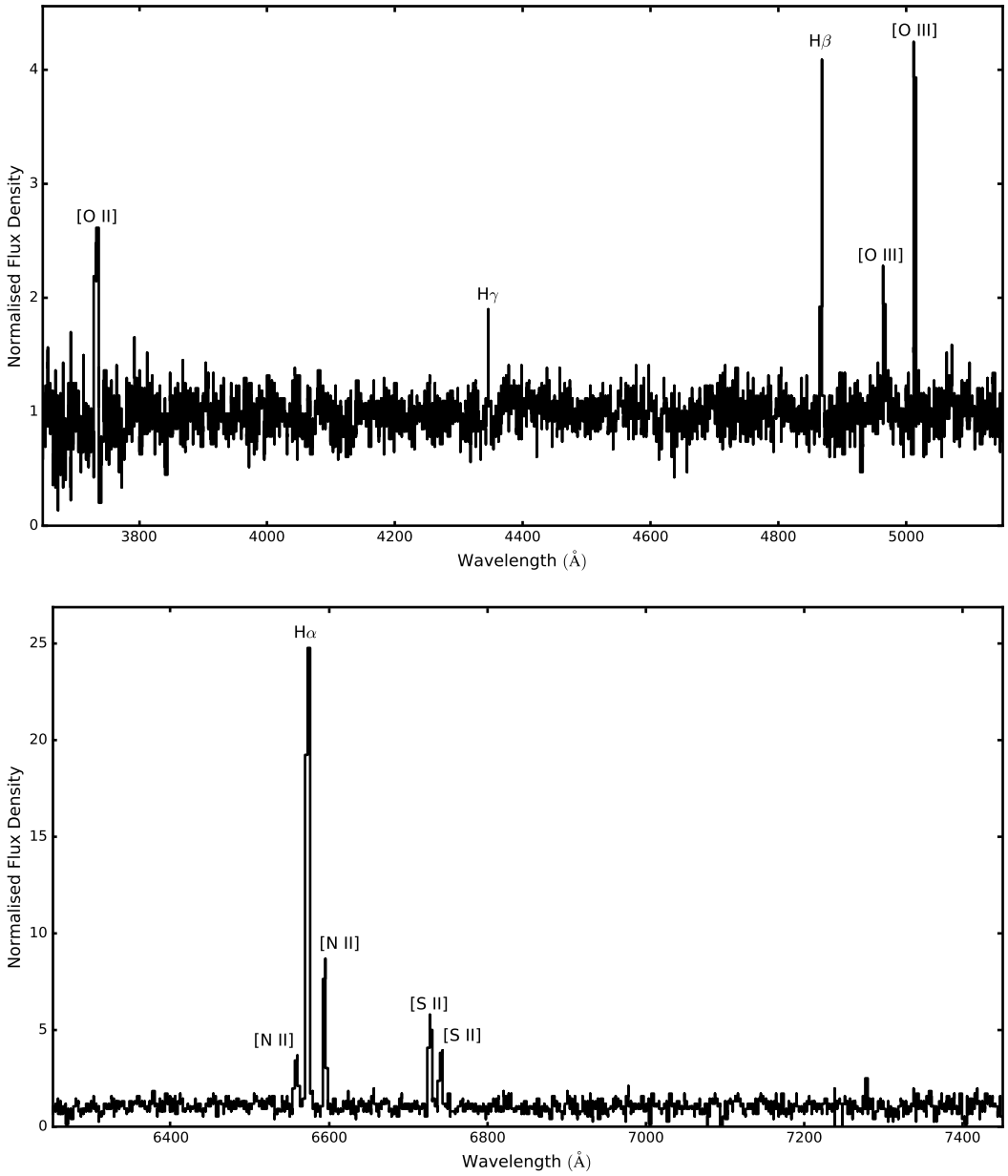

Figure 6.8: Top panel: LBT MODS1 plus MODS2 spectrum (blue arm) of the nebula around ULX-2, normalised to the continuum. The spectrum comes from the OB2 slit configuration (PA = 322°.5); the stellar continuum includes both candidate optical counterparts of ULX-2. Bottom panel: as in the top panel, but for red side of the spectrum. (Note the different flux density scales of the two panels.) The spectra are consistent with emission from photo-ionised material.

photo-ionised gas, but are not consistent with stellar photo-ionisation.

In order to estimate the electron temperature and density of the gas, we used standard diagnostic line ratios (Osterbrock, 1989), coded in the task `temden` in IRAF (Shaw and Dufour, 1994). For the [O III] line (sensitive to electron temperature), we measure an intensity ratio $I(\lambda4959 + \lambda5007)/I(\lambda4363) \approx 35$, which corresponds to T_e[O III]$= 25,000 \pm 2000$ K. From the [O II] line intensity ratio $I(\lambda3726 + \lambda3729)/I(\lambda7320 + \lambda7330) \approx 35$, we measure instead T_e[O II]$=$ $18,000 \pm 1000$ K. Those temperatures are a factor of two higher than expected for typical H II regions, and suggest that there is a significant component of shock-ionised gas. For the [S II] line (sensitive to electron density), we find an intensity ratio [S II] $I(\lambda6716)/I(\lambda6731) \approx 1.20$. Around the previously estimated values of T_e, this ratio corresponds to $n_e = 280 \pm 60$ cm^{-3}. This is to be interpreted as the density of the compressed gas behind the shock, much higher than the density of the undisturbed ISM, typically $\sim$1 cm^{-3} in the spiral arms of a galaxy.

From the dereddened Hβ flux, at the distance of M 51, we calculate an emitted luminosity $L_{\mathrm{H}\beta} \approx 3.7 \times 10^{36}$ erg s^{-1}. Knowing the characteristic temperature and density of the emitting gas, and using the Hβ volume emissivity for Case B recombination (Osterbrock, 1989), we infer an emitting volume $V_e \approx 8 \times 10^{56}$ cm^3. This is much lower than the volume inferred from the appearance of the nebula in the *HST* image, that is (roughly) an elongated bubble with a size of $\approx$30 $\times$ 100 pc corresponding to a volume of $\approx 10^{60}$ cm^3. Such a discrepancy is expected for a shock-ionised bubble, because the line-emitting gas occupies only a very thin layer behind the shock. For the inferred density and volume of the shocked layer, the mass of currently line-emitting gas is $\sim$200 $M_\odot$. The total gas mass originally present in the 10^{60} cm^3 region that has now been swept up in the bubble must have been $\sim$1000 $M_\odot$ for ISM densities $\sim$1 cm^{-3}. The cooling timescale of gas with $T_e \approx 20,000$ K and $n_e \approx 300$ cm^{-3} is only $\sim 10^4$ yr, while typical ages of shock-ionised ULX bubbles are $\sim$ a few 10^5 yr; thus, it is likely that much of the swept-up gas has already cooled.

We then investigated whether the lines are broad or narrow. From the bright night-sky lines [O I] λ5577 and Hg I λ4358, we find an instrumental full width at half maximum FWHM$_{\mathrm{ins,b}} = 2.95$ Å for the blue spectrum. In the red spectrum, strong unblended interstellar lines are seen at $\lambda = 6329$ Å, $\lambda = 6498$ Å, $\lambda = 6863$ Å: from the average width of those lines, we measure FWHM$_{\mathrm{ins,r}} = 4.76$ Å. The intrinsic line width FWHM$_{\mathrm{int}}$ is obtained from the observed width FWHM$_{\mathrm{obs}}$, following the relation FWHM$_{\mathrm{int}} = (\mathrm{FWHM}^2_{\mathrm{obs}} - \mathrm{FWHM}^2_{\mathrm{ins}})^{1/2}$. Gaussian fits to the H$\beta$ and Hα line profiles give observed FWHM$_{\mathrm{obs}}$ of $\approx$3.7 and 4.0 Å, respectively, corresponding to intrinsic widths of 140 ± 20 km s^{-1} and 110 ± 20 km s^{-1}. Other low-ionisation lines have similar intrinsic widths: 115 ± 20 km s^{-1} for

[O I] λ6300, 115 ± 20 km s^{-1} for [N II] $\lambda\lambda$6548,6583, and 130 ± 20 km s^{-1} for [S II] $\lambda\lambda$6716,6731. Thus, all low-ionisation lines are significantly resolved, and are indicative of a shock velocity $v_s \approx \mathrm{FWHM_{int}} \approx$ 110–130 km s^{-1}. Further evidence of line broadening is obtained from the intrinsic half-width at zero-intensity (HWZI) for the Balmer lines; we measure HWZI(Hα) $\approx$ 280 km s^{-1}, and HWZI(Hβ) $\approx$ 250 km s^{-1}. On the other hand, somewhat unexpectedly, high-ionisation lines are slightly narrower than low-ionisation ones. Both [O III] λ4959 and [O III] λ5007 have intrinsic FWHMs $= 90 \pm 5$ km s^{-1} and HWZI $\approx$ 200 km s^{-1}. He II λ4686 is even narrower, with an intrinsic FWHM $= 60 \pm 20$ km s^{-1} and HWZI $\approx$ 180 km s^{-1}.

Finally, we examined the more characteristic line ratios. A detailed modelling of the spectrum is beyond the scope of this chapter; however, here we highlight the presence and strength of the high ionisation lines [Ne V] λ3426, with $I(\lambda3426)/I(\mathrm{H}\beta) = 0.16 \pm 0.01$, and He II λ 4686, with $I(\lambda4686)/I(\mathrm{H}\beta) = 0.22 \pm 0.01$. Neither of those lines can be produced at such intensity by a relatively slow ($\approx$120 km s^{-1}) shock plus precursor. The combined presence of [Ne V] λ3426 and He II λ 4686 is the most intriguing feature of some ultracompact dwarf galaxies (Izotov et al., 2012); the origin of the lines in those galaxies was unclear, but the most likely candidates were suggested to be fast radiative shocks or an AGN contribution. In M 51 ULX-1, we have the rare opportunity to identify a source of such line emission. Moreover, the emission from [Ne III] λ3869, [O III] λ4959,5007, and [N II] λ6548,6583 is remarkably strong, with $I(\lambda3869)/I(\mathrm{H}\beta) = 0.92 \pm 0.05$, $I(\lambda4959)/I(\mathrm{H}\beta) = 2.1 \pm 0.1$ and $I(\lambda6548)/I(\mathrm{H}\beta) = 1.27 \pm 0.05$. If entirely due to shock-ionisation, those line ratios are approximately consistent only with shock velocities $\sim$500–600 km s^{-1}. Based on the shock plus precursor models of (Allen et al., 2008), this range of velocities is only weakly dependent on the unperturbed ISM density, metal abundance and magnetic field. However, we do not see any high ionisation lines with high-velocity wings in the LBT spectra (Figure 6.9).

6.2.2.2 ULX-2 nebula

The spectrum of the nebula around ULX-2 (Table 6.1 and Figure 6.8) is clearly different from that of the ULX-1 nebula. From an analysis of the line width, we find that all lines are consistent with the instrumental widths (see Section 6.2.2.1). That is evidence that the gas is photo-ionised rather than shock-ionised. The [N II] and [S II] lines are much weaker, relative to Hα, with flux ratios ([N II] λ6548 + [N II] λ6583)/H$\alpha \approx 0.47$ and ([S II] λ6716 + [S II] λ6731)/H$\alpha \approx 0.28$. This is again consistent with a photo-ionised H II region.

Again we tried using standard diagnostic line ratios for temperature and density. Unfortunately, the [O III] λ4363 line is too faint to provide meaningful

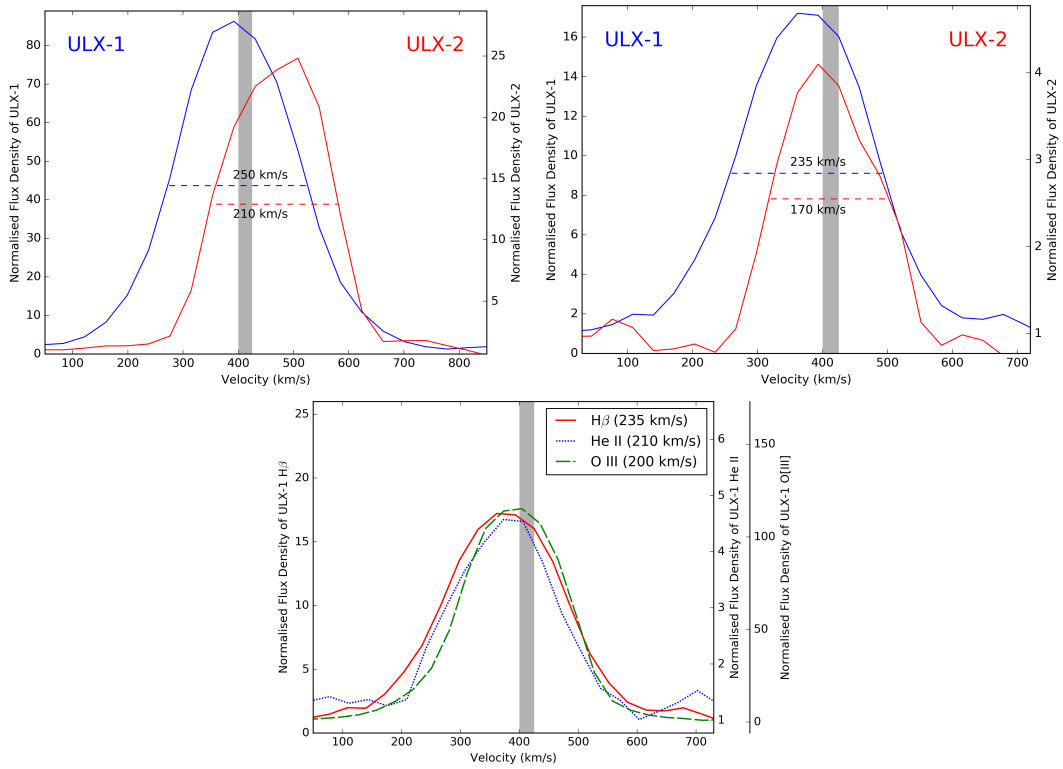

Figure 6.9: Top left panel: Hα line profile for the nebulae around ULX-1 (blue) and around ULX-2 (red). The shaded band indicates the systemic velocity expected in the M 51 spiral arm at the location of ULX-1 and ULX-2 (≈400–425 km s^{-1}, from Vlahakis et al. (2013) and Shetty et al. (2007)). The FWHM of the two lines is also overplotted; both the FWHM and the FWZI are higher in the ULX-1 nebula. Top right panel: same as the left panel, but for the Hβ line; again, the line from the ULX-1 nebula is broader. Bottom panel: comparison between the line profiles of He II λ4686, [O III] λ5007, and Hβ (plotted with the same peak intensity for convenience) for the ULX-1 nebula: the relative small FWHM and lack of broad wings in the higher-ionisation lines is inconsistent with the high shock velocity that would be required to produce such lines entirely from shocks, and suggests a significant contribution to those line from X-ray photo-ionisation.

temperature constraints. Instead, for the [S II] line doublet, we find an intensity ratio [S II] $I(\lambda6716)/I(\lambda6731) \approx 1.45 \pm 0.05$. For temperatures $\sim 10^4$ K, this ratio corresponds to the low-density limit, $n_e < 10$ cm^{-3}, consistent with the standard ISM density of $\sim$1 cm^{-3}. Given the close proximity and similar environment of ULX-1 and ULX-2, it is plausible to assume that was also the unperturbed ISM density around ULX-1, before the gas was compressed by the shock front.

With log ([N II] λ6583/Hα) ≈ -0.51, log ([S II] λ6716 + λ6731/Hα) ≈ -0.55, and log ([O III] λ5007/Hα) ≈ -0.02, the nebula sits along the sequence of H II regions photo-ionised by stellar emission (Kewley and Dopita, 2002; Veilleux and Osterbrock, 1987; Baldwin et al., 1981). The lack of high-ionisation lines such as He II λ4686 and [Ne V] λ3426 (detected in the ULX-1 nebula, Section 6.2.2.1) is

further evidence that most of the ionising photons come from the stellar population rather than the ULX. Non-detection of [O I] λ6300 suggests the lack of a partial ionisation zone, which we would expect to find if the nebula were ionised by soft X-ray photons from ULX-2.

Using nitrogen and oxygen lines as metallicity indicators, we run into the well-known discrepancy (Kennicutt et al., 2003; Bresolin et al., 2004) between the "direct" metallicity calibration based on oxygen temperatures, and the "indirect" calibration based on photo-ionisation models. The direct T_e-based measurements require detection of faint auroral lines (e.g., [O III] λ4363 (Kennicutt et al., 2003), while photo-ionisation models constrain the metal abundance from the intensity of stronger lines, for example the ratio between [N II] λ6584 and [O II] $\lambda\lambda$3726,3729 (Kewley and Dopita, 2002). It was noted (Bresolin et al., 2004) that indirect photo-ionisation abundances of H II regions in nearby spiral galaxies are systematically higher than T_e-measured abundances by a factor of 2–3. For our present study, we cannot directly measure T_e abundances for the ULX-2 nebula; we have to rely on stronger lines (Table 6.2) and use either the direct or the indirect calibration between those line ratios and the metal abundance. Applying the T_e-based calibration, from our measured values of log ([N II] λ6583/Hα) and of log [([O III] λ5007/Hβ)/([N II] λ6583/Hα)] we find log (O/H) $+12 \approx 8.6 \pm 0.1$, that is about 20% below solar (using the definition of solar abundance from Allende Prieto et al., 2001). This is the same as the metal abundance directly measured for several other H II regions in the same spiral arm of M 51, at similar radial distances from the galactic nucleus (Croxall et al., 2015; Bresolin et al., 2004). On the other hand, based on the indirect calibration of Kewley and Dopita (2002), Kobulnicky and Kewley (2004), and Pilyugin and Thuan (2005), the same line ratios correspond to log (O/H) $+12 \approx 9.1 \pm 0.1$, that is $Z \approx 2.5 Z_{\odot}$. A similar discrepancy also occurs if we use the so-called R_{23} metallicity indicator, that is the intensity ratio between ([O II] $\lambda\lambda$ 3726,3729 + [O III] $\lambda\lambda$4959,5007) over Hβ (Pagel et al., 1979; Edmunds and Pagel, 1984; Kewley and Dopita, 2002; Kewley and Ellison, 2008). The traditional calibration of this ratio based on photo-ionisation models gives log (O/H) $+12 \approx 9.1$, 3 times higher than the value derived from the direct measurements of Kennicutt et al. (2003) and Bresolin et al. (2004) (see in particular Figure 7 in the latter paper). Previous work in the literature supporting a super-solar metallicity for the M 51 disk (Moustakas et al., 2010; Zaritsky et al., 1994) was also calibrated on photo-ionisation models. Resolving the systematic discrepancy between the two metallicity calibrations will be important for population synthesis models of ULXs, because the ratio between neutron stars and black holes produced from stellar collapses increases strongly at super-solar metallicities (Heger et al., 2003).

6.2.3 Radio counterpart of ULX-1

The VLA+Effelsberg data show a faint radio source near ULX-1, detected both at 1.4 GHz and at 4.9 GHz, however not detected at 8.4 GHz. In the 1.4 and 4.9 GHz radio images the source is marginally resolved, elongated in the east-west direction (Figure 6.10), that is the same long axis of the optical nebula. The position of the peak intensity in the radio source is slightly offset, by $\approx 1''$, to the east of the *Chandra* position and of the central region of the ULX bubble in the *HST* image. Such an offset is significantly larger than the astrometric uncertainty (Section 6.1.4) of the X-ray and optical images. Thus, we speculate that the peak radio emission comes from a hot spot where the eastern jet interacts with the ISM, rather than being associated with the core. From the primary-beam corrected data, we determined peak fluxes $f_{1.4\,\mathrm{GHz}} = (44.8 \pm 9.2)\,\mu\mathrm{Jy\,beam^{-1}}$, $f_{4.9\,\mathrm{GHz}} = (29.8 \pm 7.3)\,\mu\mathrm{Jy\,beam^{-1}}$, and an 8.4-GHz upper-limit of $f_{8.4\,\mathrm{GHz}} < 54\,\mu\mathrm{Jy\,beam^{-1}}$. The root-mean-square noise is $\sigma_{1.4\,\mathrm{GHz}} = 9.2\,\mu\mathrm{Jy\,beam^{-1}}$, $\sigma_{4.9\,\mathrm{GHz}} = 7.3\,\mu\mathrm{Jy\,beam^{-1}}$, and $\sigma_{8.4\,\mathrm{GHz}} = 18\,\mu\mathrm{Jy\,beam^{-1}}$. The integrated fluxes are $f_{1.4\,\mathrm{GHz}} = (110 \pm 23)\,\mu\mathrm{Jy}$ and $f_{4.9\,\mathrm{GHz}} = (52.7 \pm 12.4)\,\mu\mathrm{Jy}$. At the distance of M 51, this corresponds to a 4.9-GHz luminosity[8] $L_{4.9\,\mathrm{GHz}} = (2.3 \pm 0.5) \times 10^{34}$ erg s^{-1}. From the integrated fluxes, we determine a spectral index[9] $\alpha = -0.6 \pm 0.3$, consistent with the optically-thin synchrotron emission expected from hot spots. Radio emission may also come from free-free emission associated with the ionised bubble: however, based on the Balmer emission, we only expect a free-free flux density of ≈ 1.5 μJy at 4.9 GHz (Appendix A of Caplan and Deharveng 1986), entirely negligible.

We do not detect any radio emission associated with ULX-2 or its surrounding nebula. We can only place 3σ upper limits on the peak flux densities: $f_{1.4\,\mathrm{GHz}} < 28\,\mu\mathrm{Jy\,beam^{-1}}$, $f_{4.9\,\mathrm{GHz}} < 22\,\mu\mathrm{Jy\,beam^{-1}}$, and $f_{8.4\,\mathrm{GHz}} < 54\,\mu\mathrm{Jy\,beam^{-1}}$. This corresponds to an upper limit to the 4.9-GHz luminosity $L_{4.9\,\mathrm{GHz}} < 10^{34}$ erg s^{-1}. The expected free-free emission from the H II region around ULX-2 is ≈ 2 μJy at 4.9 GHz (Caplan and Deharveng, 1986), well below the detection limit.

6.3 Discussion

Although the X-ray luminosities of ULX-1 and ULX-2 are only moderately above 10^{39} erg s^{-1}, the two sources have interesting properties that can help us understand the behaviour of super-critical accretion. Here we have shown that both ULXs are associated with ionised gas nebulae, with different optical spectral properties. We have also shown that ULX-1 (but not ULX-2) has a radio counterpart (usually taken as a signature of jet activity). We shall now discuss

[8] The luminosity is defined as $L_\nu = 4\pi d^2 \nu f_\nu$.
[9] Defined as $f_\nu \propto \nu^\alpha$

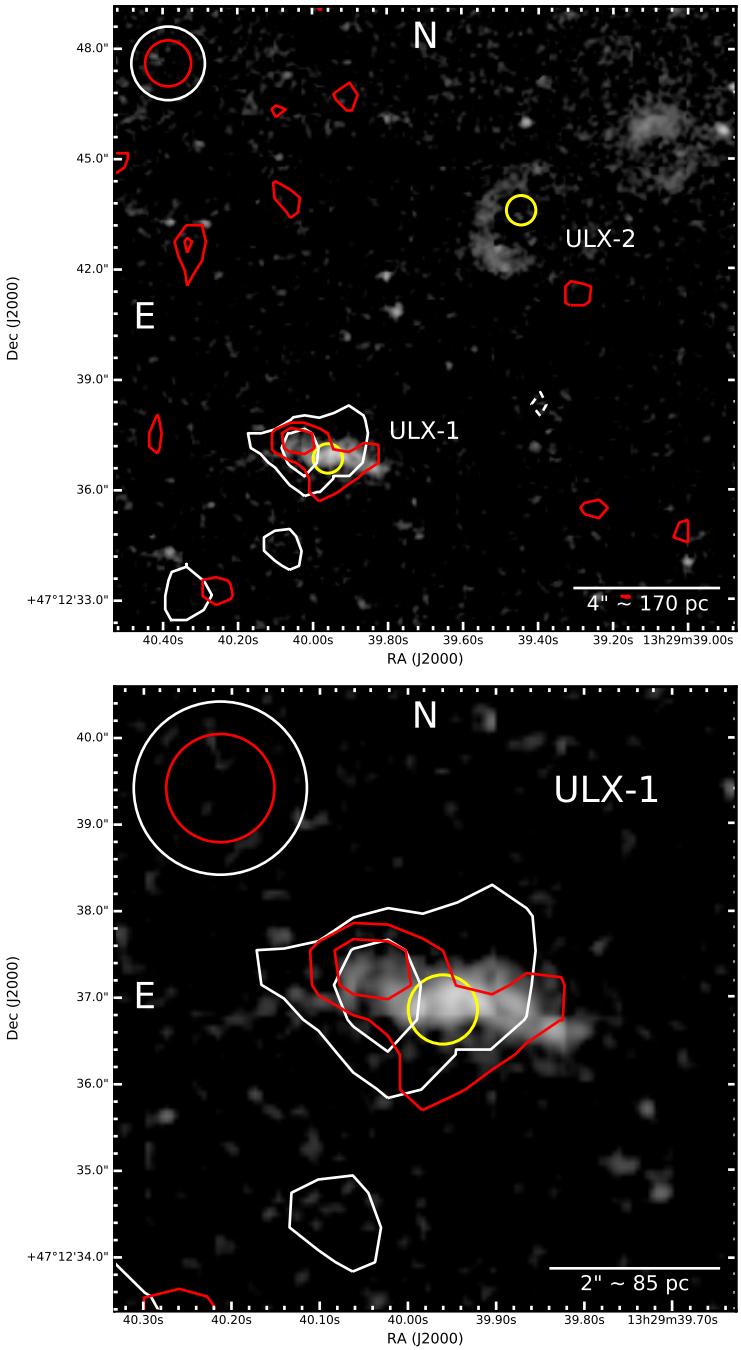

Figure 6.10: Top panel: *HST*/ACS continuum-subtracted F658N image of the ULX field, with VLA radio contours overplotted. White and red contours represent the 4.9-GHz and 1.4-GHz flux densities, respectively. Both sets of contours have levels of $-2\sqrt{2}\sigma$, $2\sqrt{2}\sigma$ and 4σ, where σ is the respective noise level ($\sigma_{4.9} = 7.3$ μJy beam^{-1}, $\sigma_{1.4} = 9.2$ μJy beam^{-1}). Beams for both frequencies are indicated in the top left corner of the image. The yellow circles represent the *Chandra* positions of ULX-1 and ULX-2 with $0\farcs4$ uncertainty. Bottom panel: zoomed-in view of the ULX-1 bubble.

the physical interpretation of the sources, putting together the various clues from these multiband observations.

6.3.1 Energetics of the two nebulae

As we have shown in Section 6.2.2, the most obvious difference between the two nebulae is that one is dominated by shock ionisation (with possible additional contribution from X-ray photo-ionisation), the other by near-UV photo-ionisation. We shall discuss here how much kinetic and radiative energy is required to produce the luminosity observed from the two nebulae, and whether the two ULXs are the origin of such power.

6.3.1.1 Mechanical power of ULX-1

From standard bubble theory (Weaver et al., 1977), the mechanical power $P_{\rm jet}$ inflating the bubble is equal to $\approx$77/27 of the total radiative luminosity $L_{\rm rad}$. The luminosity in the Hβ line ($L_{\rm H\beta}$) is between $\approx 4 \times 10^{-3}$ and $\approx 7 \times 10^{-3}$ times the total radiative luminosity, for all shock velocities $100 \lesssim v_{\rm s} \lesssim 500$ km s^{-1} (from the set of pre-run shock-ionisation Mappings III models for equipartition magnetic field and either solar or twice-solar abundance; Allen et al., 2008). Thus, $P_{\rm jet} \approx$ (400–650) $\times L_{\rm H\beta}$. Knowing that $L_{\rm H\beta} \approx 3.7 \times 10^{36}$ erg s^{-1}, we infer a mechanical power $P_{\rm jet} \approx (1.5\text{–}2.5) \times 10^{39}$ erg s^{-1}. This value is comparable to the X-ray luminosity of ULX-1, taking into account the uncertainty in the viewing angle and therefore the geometric projection factor for the disk emission. It is also similar to the jet power inferred for SS 433 (Panferov, 2017; Fabrika, 2004). There is no direct conversion between jet power and luminosity of the radio counterpart because the latter also depends on other factors such as the ISM density and magnetic field, and the fraction of kinetic power carried by protons and ions; however, it is interesting to note that the 5-GHz luminosity $L_{4.9\,\rm GHz} \approx 2.3 \times 10^{34}$ erg s^{-1} is within a factor of two of the radio luminosity of other jetted ULXs such as Holmberg II X-1 (Cseh et al., 2014, 2015a) and NGC 5408 X-1 (Cseh et al., 2012; Lang et al., 2007; Soria et al., 2006a). Thus, the radio luminosity of the M 51 ULX-1 nebula seems to correspond to "average" jetted ULX properties: it is a factor of 5 more radio luminous than SS 433, but an order of magnitude fainter than the most exceptional radio bubbles in the local universe, namely NGC 7793 S26 (Pakull et al., 2010; Soria et al., 2010) and IC 342 X-1 (Cseh et al., 2012), which are also a few times larger. The radio spectral index $\alpha = -0.6 \pm 0.3$ confirms that the radio counterpart is dominated by optically-thin synchrotron emission, as expected for jet lobes.

An alternative method to estimate the jet power (Weaver et al., 1977) is to

assume that the moderate shock velocity ≈100–150 km s^{-1} inferred from the FWHM of the Balmer lines also corresponds to the advance speed of the jet-powered forward shock into the ISM. In that scenario, the characteristic age of the bubble is ≈3 $\times 10^5 v_{100}^{-1}$ yr and the jet power $P_{\rm jet} \approx 1.0 \times 10^{39} v_{100}^3 n_e$ erg s^{-1}, where $v_{100} \equiv v_{\rm s}/(100$ km s$^{-1})$ and n_e is the ISM number density. This is consistent with the other jet power estimate.

There is clearly a strong discrepancy between the moderately low FWHM of all the lines (∼100 km s^{-1}) and the high shock velocity (∼500 km s^{-1}) that would be needed to produce the higher ionisation lines with the observed ratios; such high shock velocities are also inconsistent with the observed HWZIs and the moderate gas temperature inferred from the [S II] lines. Even if we account for the fact that about half of the high-ionisation line emission occurs in the precursor region (low turbulent velocity), the discrepancy remains difficult to explain. One possibility is that there is a contribution from X-ray photo-ionisation, from ULX-1. The source appears almost edge-on to us, but if, as expected, its polar funnel is aligned with the major axis of the bubble (i.e., along the jet), there is stronger direct X-ray irradiation and lower intrinsic absorption along that direction. The fact that high-ionisation lines are slightly narrower than low-ionisation lines supports the idea that the former are partly enhanced by X-ray photo-ionisation. Another possibility is that the shocked gas does have a faster expansion velocity (comparable with the shock velocity) along the direction of the jet (which is located approximately in the plane of the sky for us) and a slower expansion in the other two directions perpendicular to the jet axis; in that case, the line width observed by us only reflects the lateral expansion speed. Soft thermal X-ray emission is a possible test for the presence of fast shocks: a shock velocity ≈500 km s^{-1} corresponds to a shock temperature ≈0.3 keV. We showed in the previous chapter that soft thermal emission was indeed detected in the X-ray spectrum of ULX-1; unfortunately, the location of the source away from the aimpoint in the *Chandra* observations, and the low spatial resolution of *XMM-Newton*, do not enable us to determine whether the thermal-plasma component comes only from the central point-like source or from the larger bubble. In the former case, the X-ray line emission would be directly linked to the disk outflow around the ULX; in the latter case, it would be from the jet/ISM interaction. New *Chandra* observations with the source at the aimpoint may answer this question.

6.3.1.2 Radiative power of ULX-2

The optical spectrum of the nebula around ULX-2 is consistent with a typical H II region; this would mean that it is only a coincidence that a ULX is apparently located inside the nebula, without contributing to its ionisation. To determine

whether this is the case, we start by measuring its extinction-corrected Hβ luminosity: $L_{\mathrm{H}\beta} \approx 4.0 \times 10^{36}$ erg s^{-1}. At $T_e \approx 10,000$ K, the emission of one Hβ photon requires ≈8.5 ionising photons above 12.6 eV (Osterbrock, 1989), and below ≈0.2 keV (above which energy the ionisation cross section becomes too low). Therefore, the observed nebular luminosity implies an ionising photon flux $Q(\mathrm{H}^0) \approx 8 \times 10^{48}$ photons s^{-1}. From the best-fitting parameters in the solar-metallicity stellar tracks, we estimate that the two blue stars in the error circle of ULX-2 have effective temperatures of ≈20,000 K and ≈17,000 K, and radii of ≈25 $R_\odot$ and ≈36 $R_\odot$, respectively. Approximating the spectra of the two stars as blackbodies, we expect a combined ionising flux of ≈1.4 $\times 10^{48}$ photons s^{-1} above 12.6 eV. Adding a few other blue stars inside the outer boundary of the nebula still leaves us a factor of 3 short of the required ionising flux. However, using only the bright blue supergiants for this type of photon accounting can be misleading. For example, the addition of a single main-sequence mid-type O star (O6V or O7V), with a temperature ≈35,000–37,000 K, would suffice to provide the remaining ionising flux (Simón-Díaz and Stasińska, 2008). Such O-type dwarfs have an absolute brightness $M_V \approx -4.5$ mag, negligible compared with the characteristic absolute brightness $M_V \approx -6$ mag of the B4–B6 supergiants around ULX-2. Thus, if one of the four supergiants visible around ULX-2 (Figure 6.2, bottom right) is in a binary system with a mid-type O star, the supergiants will determine the optical colours and V-band luminosity, but the O star will provide most of the ionising UV flux. Another way to tackle the problem is to use STARBURST99 (Leitherer et al., 1999, 2014) simulations: we find that for a single population age of 7 Myr, a stellar mass of ≈$10^4 M_\odot$ would be required to provide the necessary ionising flux. Adding a dust reddening correction for the M 51 halo (as discussed in Sections 6.1.2 and 6.2.1) would increase the intrinsic ionising luminosity of the stars by ≈50%, making it easier to meet the energy requirements for the H II region.

Estimating whether there may also be a direct photo-ionising contribution from ULX-2 is not trivial. The X-ray source is seen at a high inclination angle θ, which implies that an isotropic conversion of observed high-energy flux into emitted luminosity may underestimate the disk emission; a conversion factor ≈$2\pi\, d^2 / \cos\theta$ is more appropriate than a factor of $4\pi\, d^2$. Taking this into account, we can always find a sufficiently high viewing angle (in particular, $\theta \gtrsim 80°$) to increase the true emitted disk luminosity of the source. To boost the number of UV photons, we must also assume that the X-ray source is surrounded by a large disk that intercepts and reprocesses more than 1% of the X-ray flux. Thus, an ionising flux $Q(\mathrm{H}^0) \approx 8 \times 10^{48}$ photons s^{-1} is consistent with the X-ray and optical luminosity of ULX-2. However, the problem of this irradiated-disk

scenario is that it also produces copious amount of photons at energies > 54 eV, which leads to the emission of He II λ4686 via recombination of He^{++} into He^{+}. No He II λ4686 emission is detected in the LBT spectra of this nebula, with an upper limit on its flux of $\approx 10^{-16}$ erg cm^{-2} s^{-1}, corresponding to an emitted photon flux $\lesssim 2 \times 10^{47}$ λ4686 photons s^{-1}. At $T_e \sim 10,000$ K, it takes $\approx$4.2 primary ionising photons >54 eV to produce one λ4686 photon (Pakull and Angebault, 1986; Osterbrock, 1989): thus, the flux of $E > 54$ eV photons seen by the nebular gas must be $\lesssim 8 \times 10^{47}$ photons s^{-1} $\approx 0.1 Q(H^0)$. Typical models of irradiated disks (e.g., *diskir* in XSPEC) luminous enough to produce the required number of photons >13.6 eV will also predict too many photons >54 eV (typically, the latter are predicted to be $\approx$1/4 of the former, rather than $\lesssim$1/10, as required by the observed spectrum). Given this evidence, we conclude that the ionised nebula projected around ULX-2 is a typical H II region and the ULX, whether located inside the nebula or not, is not its major ionising source.

6.3.2 Radio brighter and radio fainter ULX bubbles

ULX bubbles are a crucial tool to estimate the emitted power (radiative and kinetic luminosity) of the compact object, averaged over the characteristic cooling timescale of the gas. Moreover, they enable us to identify compact objects with likely super-critical accretion that currently appear X-ray faint, either because they are in a low state, or because they are collimated away from us, or because the direct X-ray emission along our line of sight is blocked by optically thick material. As more ULX bubbles get discovered or recognised, we are starting to see that there is no simple correlation between the X-ray luminosity of the central source and the radio or Balmer line luminosity of the bubble. The differences between M 51 ULX-1 and ULX-2 illustrated in this chapter are a clear example. This is also the case when we compare the M 51 ULX-1 bubble with ULX bubbles in other galaxies. For example, the collisionally ionised ULX bubble around Holmberg IX X-1 (Grisé et al., 2011; Abolmasov and Moiseev, 2008; Pakull and Grisé, 2008; Pakull and Mirioni, 2002) has an Hα luminosity $\approx 10^{38}$ erg s^{-1} (Abolmasov and Moiseev, 2008; Miller, 1995; Miller and Hodge, 1994), an order of magnitude higher than that of the M 51 ULX-1 bubble, consistent with a mechanical power of $\approx 10^{40}$ erg s^{-1}; the central ULX powering the Holmberg IX bubble has an X-ray luminosity $L_X \approx 2 \times 10^{40}$ erg s^{-1} (Walton et al. 2017 and references therein), again an order of magnitude higher than M 51 ULX-1. However, the Holmberg IX ULX bubble has a 1.4-GHz luminosity of $\approx 2 \times 10^{34}$ erg s^{-1} (our estimate based on the radio maps of Krause et al. 1989), similar to the radio luminosity of M 51 ULX-1. Conversely, there are ULXs with more

luminous radio nebulae (such as Holmberg II X-1 and NGC 5408 X-1; see Section 6.3.1.1 for references) and proof of powerful jets, but with relatively weak or no collisionally ionised gas detectable from optical lines. The different ratio of synchrotron radio luminosity to mechanical power (or radio luminosity to total accretion power) in different ULXs may be due to various factors: i) a different initial kinetic energy distribution between a collimated, relativistic jet and a slower, more massive disk wind; ii) different composition of the jet (leptonic or baryonic); iii) different amount of entrainment of ISM matter along the jet path (related to different ISM densities). We will explore a general classification of ULX bubbles in terms of their multiband luminosity ratios briefly in Chapter 8.

For the ULXs that do show radio evidence of extended jets, typical 5-GHz luminosities span an order of magnitude between $\approx 2\times10^{34}$ erg s^{-1} in M 51 ULX-1 to $\approx 2\times10^{35}$ erg s^{-1} in NGC 7793-S26 (Soria et al., 2010) and IC 342 X-1 (Cseh et al., 2012); the characteristic age of the ULX bubbles is $\sim$ a few 10^5 yr. This luminosity range corresponds to a range of observed fluxes $f_{5\rm GHz} \approx (30–300)\, d_{10}^{-2}\,\mu$Jy, where d_{10} is the source distance in units of 10 Mpc. The synchrotron radio flux observed from microquasar lobes during the active expansion phase, that is when the jet is still inflating them, was modelled by Heinz (2002) as $f_{5\rm GHz} \sim 10\, n_e^{0.45}\, P_{\rm jet,39}^{1.3}\, \left[2\varphi^{3/4}/(1+\varphi)\right]\, t_5^{0.4}\, d_{10}^{-2}$ mJy, where φ is the ratio between the magnetic pressure and the gas pressure at the base of the jet, $P_{\rm jet,39}$ is the jet power in units of 10^{39} erg s^{-1}, t_5 is the age of the jet active phase in units of 10^5 yr, and n_e is the number density in the ISM. While the Heinz (2002) scaling relation works well for the radio nebula around the neutron star microquasar Cir X-1, it overestimates the synchrotron radio luminosity of the bubble around the black hole microquasar Cyg X-1 by at least two orders of magnitude Gallo et al. (2005); it also over-estimates the synchrotron radio luminosity of ULX bubbles (given the input mechanical power inferred from line-emission studies) by a similar amount. For Cyg X-1, this may be the result of a significant fraction of the jet energy being stored in baryons that do not radiate (Gallo et al., 2005; Heinz, 2006). A similar explanation may apply to jet-driven ULX bubbles (Soria et al., 2010).

6.4 Conclusions

We presented the discovery and multiband study of two ionised nebulae spatially associated with the two eclipsing ULXs in M 51, using new and archival data from *Chandra*, the LBT, the *HST*, and the VLA. The nebula around ULX-1 has a very elongated morphology, indicative of a jet-driven bubble. We showed that the optical emission lines are collisionally ionised, and that there is a spatially

resolved radio counterpart. Such findings are consistent with a jet interpretation. We know from X-ray photometry that ULX-1 is seen almost edge on; therefore the jet is likely propagating in the plane of the sky, which explains the lack of systemic velocity shifts observed between the eastern and western ends of the optical bubble. The mechanical power of the jet estimated from the Hβ luminosity, $P_{\rm jet} \approx 2 \times 10^{39}$ erg s^{-1}, agrees with the power estimated from the FWHM of the lines (proportional to the shock velocity) and the characteristic age of the source ($t \sim 10^5$ yr). However, high-ionisation lines (specifically, [Ne V] λ3426, He II λ4686, and a few [O III] lines) are too strong for the shock velocity $v_{\rm s} \sim$ 100–150 km s^{-1} inferred from the width of the low-ionisation lines. Either there is also a shock component with $v_s \sim 500$ km s^{-1}, or the high-ionisation lines are boosted by X-ray photo-ionisation. We favour the latter scenario because the high-ionisation lines are slightly narrower than the Balmer lines.

Conversely, the nebula around ULX-2 has a quasi-circular appearance and its line ratios and widths are consistent with a normal H II region, that is with stellar photo-ionisation from one or two O-type dwarfs and a few blue supergiants. There is no radio counterpart and no other evidence of jet emission. The reason why some ULXs produce jets while others (with comparable X-ray luminosities) do not, both in the case of the two M 51 sources and in the ULX class as a whole, remains unknown. The lack of high-ionisation lines indicative of X-ray photo-ionisation suggests that ULX-2 does not have a strong direct contribution to the ionisation of the nebula. It is likely that the nebula is a chance alignment and is not powered by the ULX.

The X-ray and multiband flux from the two compact objects and surrounding nebulae is at the low end of the ULX class distribution; however, the peculiar property of both sources is that they show X-ray eclipses, from which one can in principle strongly constrain the binary parameters, the masses of the two compact objects, and the geometry of accretion and emission. Therefore, they are particularly suitable targets for follow-up multiband studies.

The metallicity of the parent stellar population can have a direct effect on the type of ULXs and on their observational appearance. For example at super-solar metallicities, the ratio of neutron stars over black holes is strongly increased, which may be relevant to the ongoing debate over the relative proportion of neutron star and black hole accretors in the ULX population. Neutron stars with a Roche-lobe-filling massive donor star are also more likely to be eclipsing systems than black holes with the same type of donor star, which may explain why two eclipsing ULXs (Chapter 5) and another eclipsing X-ray binary with a luminosity just below the ULX threshold (Wang et al., 2018) were all found in this galaxy. Our LBT spectra of the ionised gas around ULX-2 are in agreement with the line

ratios observed in previous optical studies of H II regions in the disk of M 51 (as discussed in Section 6.2.2.2); however, the conversion between such line ratios and a metallicity scale remains a subject of debate, with alternative models suggesting either $Z \approx 0.015$ (slightly sub-solar) or $Z \approx 0.04$ (2.5 times super-solar). Future, more accurate, determinations of the metallicity in nearby spiral galaxies will provide an important input parameter to test population synthesis models of ULXs.

6.5 Summary

In this chapter we presented the optical and radio counterparts to the eclipsing ULXs discovered in M 51, ULX-1 and ULX-2. This multiwavelength effort was designed to better understand the mechanical power output of each ULX. The key results are:

- We discovered an elongated, 100×30 pc optical emission-line nebula coincident with ULX-1. The optical spectra suggests the gas is shock-ionised, consistent with the effects of a jet with mechanical power of $P_{\rm jet} \sim 2 \times 10^{39}$ erg s^{-1}, which is equivalent to the radiative power.

- Steep-spectrum radio emission is also found coincident with ULX-1, further evidence of a relativistic jet.

- Conversely, the circularly-shaped ionised optical nebula coincident with ULX-2 is photo-ionised and has no radio counterpart. This nebula is ionised by UV photons, rather than X-ray photons from the ULX. We argue that it is a chance alignment with the ULX, ionised by stellar emission instead.

As we showed in Chapter 5, both ULXs have similar X-ray luminosities ($L_{\rm X} \approx$ a few 10^{39} erg s^{-1}), must be viewed at high inclination (being eclipsing sources), and are likely to be located in ISM regions with similar properties (as they are only $\sim$ 400 pc apart along the same spiral arm); however, they have different X-ray spectral characteristics. Interestingly, we now know that both ULXs are coincident with extended optical nebulae, although only ULX-1 shows evidence of recent jet activity. What is driving these contrasting observational properties is unclear. We discuss potential implications in Chapter 8.

Chapter 7

Discovery of a new microquasar in NGC 300

This chapter is adapted from:

R. Urquhart, R. Soria, M. W. Pakull, J. C. A. Miller-Jones, G. E. Anderson, R. M. Plotkin, C. Motch, T.J. Maccarone, A.F. McLeod and S. Scaringi. "A newly discovered double-double candidate microquasar in NGC 300", *accepted for publication in the Monthly Notices of the Royal Astronomical Society*, DOI:10.1093/mnras/sty2771

For this chapter, my supervisor R. Soria and myself performed data reduction and analysis on the VLT data. I conducted all remaining work under the guidance of my supervisory panel.

Work done in the previous chapters on ULXs, and specifically on M 51 ULX-1, showed how the mechanical power of the jets or winds in super-Eddington systems can also exceed 10^{39} erg s^{-1}. This is a very high power, that, for example, is only reached by one known galactic source, SS 433. While our previous chapters have focused on very luminous systems, in this chapter we examine a candidate super-Eddington source that does not have an outstanding radiative output but is remarkable for its mechanical power output.

Using similar techniques to those presented in Chapter 6, we explore the multiwavelength properties of the candidate super-Eddington microquasar NGC 300 S 10. We present X-ray observations that show multiple discrete thermal knots linearly aligned over a length of ≈150 pc which we interpret as a jet interacting with the ISM. We also detected a similar scale and aligned radio nebula along with a coincident optical bubble. Unlike the previously discussed jetted source,

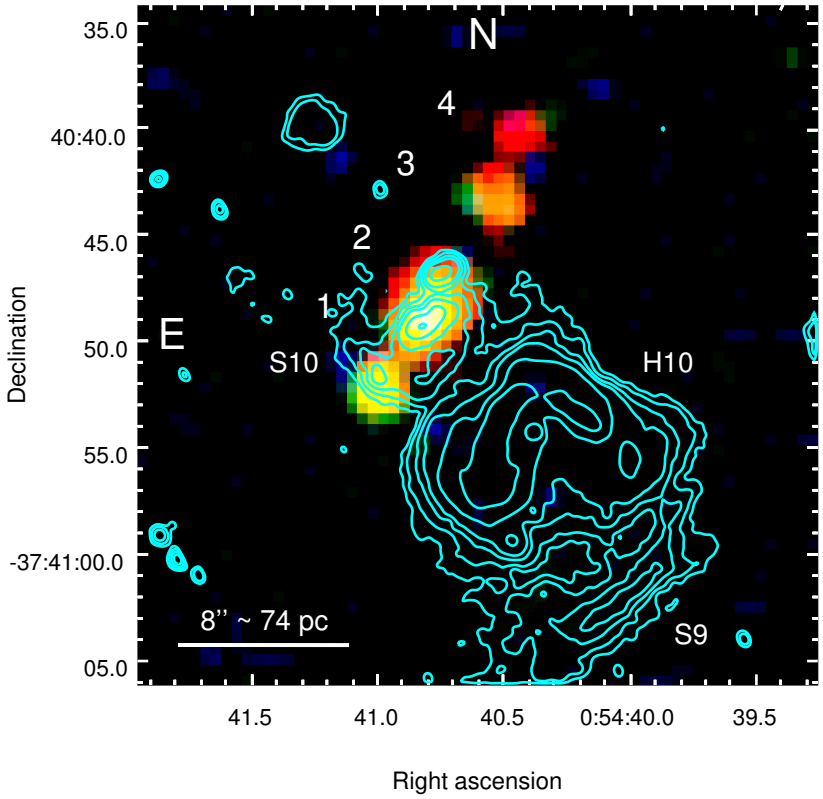

Figure 7.1: Stacked *Chandra* ACIS-I image of NGC 300 S 10, showing 4 aligned sources; we refer to those sources as "knots" 1–4, throughout this chapter, as labelled in this image. Red represents 0.3–1.0 keV, green 1–2 keV, and blue 2–7 keV. Cyan contours show the smoothed VLT continuum-subtracted Hα intensity map; contour levels are arbitrary and for visualisation purposes. The complex structure of the Hα emission can be divided into the shock-ionised S 10 region (associated with the X-ray knots), a photo-ionised H II region (H 10 in Blair and Long 1997) to the south-west of S 10, and another (smaller) shock-ionised region (the S 9 SNR in Blair and Long 1997) at the southernmost end, without an X-ray counterpart. The alignment of X-ray knots and shock-ionised optical line emission in S 10 is strongly suggestive of a jet.

M 51 ULX-1, the radiative luminosity from the compact object is below the Eddington limit for a stellar-mass black hole or neutron star. However, we argue that the morphology, size and luminosity of the extended X-ray, optical and radio structure suggest that NGC 300 S 10 belongs to the same class of powerful ($P_{\rm jet} > 10^{39}$ erg s^{-1}) microquasars as SS 433, Ho II X-1 and NGC 7793-S 26.

Motivated by the re-identification of S 26, which was originally misclassified as an SNR (Blair and Long, 1997) before being recognised as a microquasar, we set out to look for other powerful microquasars in SNR catalogues. SNRs and jet sources have similar physical properties: they both show evidence of shocked gas and optical line emission, along with coincident X-ray and radio features. In order to distinguish between the two classes of object, the morphology and

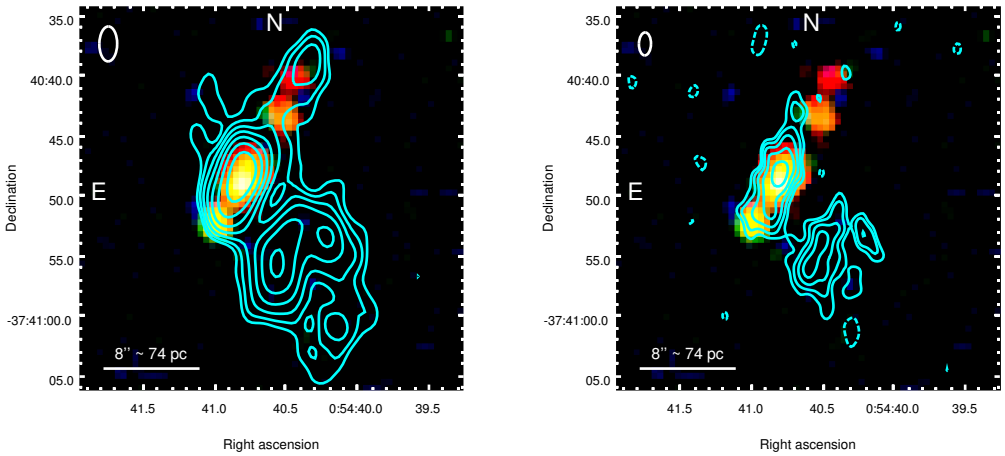

Figure 7.2: Left panel: Stacked *Chandra* ACIS-I image of NGC 300 S 10. Red represents 0.3–1.0 keV, green 1–2 keV, and blue 2–7 keV. Cyan contours show the ATCA 5.5 GHz map; contour levels are $2\sigma \times \sqrt{2}^n$, where $\sigma = 2.72\,\mu\mathrm{Jy\,beam^{-1}}$. The beam size is $2\farcs91 \times 1\farcs47$. Similarly to the H$\alpha$ emission (Figure 7.1), the radio emission consists of a component associated and aligned with the X-ray knots in the S 10 region, plus a component associated with the H 10 H II region (Blair and Long, 1997) and another component corresponding to the S 9 SNR (Blair and Long, 1997). Right panel: Same as top panel, but the contours are now from the ATCA 9 GHz map; contour levels are $2\sigma \times \sqrt{2}^n$, where $\sigma = 2.78\,\mu\mathrm{Jy\,beam^{-1}}$. The beam size is $1\farcs91 \times 1\farcs01$. The radio emission at S 10 is spatially resolved both along the direction of the jet, and in the transverse direction, both at 5.5 and at 9 GHz.

multiband properties must be carefully investigated.

In our search, we noticed an intriguing source previously identified as a bright optical SNR by D'Odorico et al. (1980) (listed as source number 2 in their Table 3; see also the finding chart in their Figure 3). It is located in the nearby, late-type spiral NGC 300, at a distance of 1.88 ± 0.05 Mpc (Gieren et al., 2005). The same optical source was observed and studied in more detail by Blair and Long (1997), who list it as NGC 300 S 10 = DDB2. In both studies, the SNR identification is based on the high ratio between [S II]$\lambda\lambda$6716,6732 and Hα line emission; line ratios [S II]:H$\alpha \gtrsim 0.4$ are indicative of shock-ionised gas (Mathewson and Clarke, 1973; D'Odorico et al., 1978). What is striking about S 10 is that we found four X-ray sources spatially resolved by *Chandra*, aligned in the plane of the sky and associated with the shock-ionised Hα emission (Figure 7.1). This is very unusual for an SNR; instead, we interpret the X-ray appearance as an unambiguous signature of a jet. Henceforth, we refer to those four X-ray sources as knots 1 through 4 (Figure 7.1). Spurred by this discovery, we then observed the field in the radio band with the ATCA. We found a bright, elongated radio nebula, overlapping with the X-ray jet (Figure 7.2). This is further evidence for the presence of collimated, relativistic ejections.

Table 7.1: Observations used for this work. The exposure time for the radio observations refers to the total time on source.

Telescope	Obs ID/Filter/ν	Obs Date	Exposure
Chandra/ACIS-I	12238	2010-09-24	63.00 ks
	16028	2014-05-16	64.24 ks
	16029	2014-11-17	61.27 ks
	Total		188.51 ks
HST/ACS	F814W	2006-11-09	1542 s
	F606W	2006-11-09	1515 s
	F475W	2006-11-09	1488 s
VLT/FORS2	Hα	2010-07-10	180 s*
	Hα/4500	2010-07-10	180 s*
ATCA	5.5/9 GHz	2015-10-21	4.53 hr
	5.5/9.0 GHz	2015-10-22	10.75 hr
	5.5/9.0 GHz	2015-10-23	10.32 hr
	5.5/9.0 GHz	2016-08-25	9.95 hr
	5.5/9.0 GHz	2016-08-26	9.86 hr
	Total		45.41 hr

* Stack of two 90-s exposures

7.1 Data Analysis

7.1.1 X-ray observations

NGC 300 has been observed by *Chandra* a total of five times. However, in one of those observations (ID 9883) the candidate microquasar target of our study does not fall on any of the chips. A second short observation (ID 7072), taken with the imaging High Resolution Camera (HRC-I), does not have the sensitivity required to detect the source. Thus, we only used three of the five observations for our X-ray data analysis (Table 7.1): ACIS-I observations 12238, 16028 and 16029. We downloaded the data from the public archive, and reprocessed them using standard tasks from the CIAO Version 4.9 software package (Fruscione et al. 2006). We filtered out high particle background intervals. For our imaging analysis, we used HEASARC's DS9 visualisation package. After we identified a number of discrete X-ray sources associated with the target of our study (as discussed in Section 7.2.1), we used the CIAO task *specextract* to extract the background-subtracted spectrum for each source, in each observation. For the two southernmost sources (knots 1 and 2), we extracted the source counts from circular regions of radius 3″; for the other two sources (knbts 3 and 4), we used elliptical regions of axes $3'' \times 2''$ (position angle = 330°), to avoid contamination from the brighter, neighbouring sources. A local background region was selected, approximately 3 times larger

than the source regions. Spectral fitting was performed using XSPEC version 12.9.1 (Arnaud, 1996). Because of the low number of counts for each source, to test the goodness of our fits we used XSPEC's implementation of W statistics.

7.1.2 Radio observations

NGC 300 S 10 was observed with the ATCA over three consecutive nights, starting on 2015 October 21. A total integration time on source of 25.6 hours was achieved. We then re-observed NGC 300 one year later, this time for two consecutive nights, 2016 August 25–26. For the 2015 observations, S 10 was the target and hence at the phase centre, while the follow-up observations were offset to observe another source in the same field, with the phase centre at RA = $00^h55^m02\overset{s}{.}5$, Dec = $-37°40'10\overset{''}{.}5$, approximately $4\overset{'}{.}5$ from S 10. For both observation sets, two 2048 MHz bands were observed simultaneously, centred at 5.5 GHz and 9.0 GHz, using the Compact Array Broadband Backend (CABB; Wilson et al., 2011). The telescope was in its extended 6A configuration during all of the observations, resulting in a maximum baseline of 5938.8 m. B1934−638 was used as both a bandpass and flux calibrator. We used B0104−408 as the phase calibrator. The bandpass/flux calibrator was observed at the start of the observation for 10 minutes while the phase calibrator was observed for 1 minute every 15 minute block.

We used the MIRIAD package (Sault et al., 1995) for gain and phase calibration. The data were then imaged with the CASA (McMullin et al., 2007) software package, with the CLEAN algorithm. All three nights (two nights for the 2016 observing run) of observations were stacked at each frequency and we imaged the data with Briggs weighting at a robust value of one in order to downweight the sidelobes from nearby sources. Finally, we combined the two observing runs to create a single mosaic image for each frequency. The cleaned, primary beam corrected images for both frequencies are shown in Figure 7.3. The 5.5 GHz image has a Gaussian restoring beam of $2\overset{''}{.}91 \times 1\overset{''}{.}47$ (position angle $-0\overset{°}{.}6$ East of North) and an rms noise level of 2.72 μJy beam^{-1} at the location of S 10. The 9 GHz image has a Gaussian restoring beam of $1\overset{''}{.}91 \times 1\overset{''}{.}01$ (position angle $-1\overset{°}{.}2$ East of North) and a local rms noise level of 2.78 μJy beam^{-1}.

In order to construct a spectral index map (Figure 7.3, right), we first convolved the 9 GHz image with the beam of the 5.5 GHz image. The 5.5 GHz image was then re-gridded to match the 9 GHz image, with the CASA task IMREGRID. We then created a two-point spectral index map (Figure 7.3, top right), along with a corresponding error map (Figure 7.3, bottom right). Both data sets were masked to their respective 3σ thresholds prior to use.

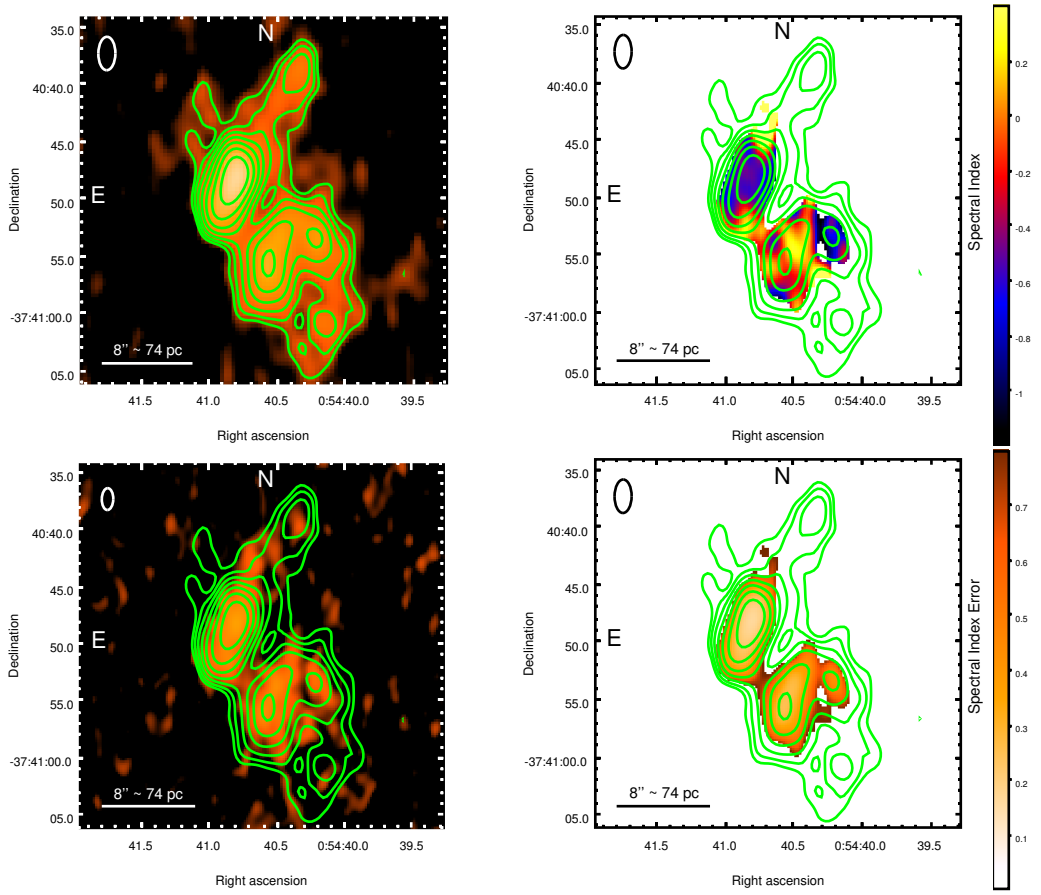

Figure 7.3: Top left panel: ATCA 5.5 GHz image. Contours levels are $2\sigma \times \sqrt{2}^n$, where $\sigma = 2.72\,\mu$Jy beam^{-1}. Bottom left panel: ATCA 9 GHz image with 5.5 GHz contours for reference. In both images, the radio nebula is aligned with the X-ray knots, which suggests that both are the result of a jet. Top right panel: Spectral index map made from the ATCA 5.5 and 9 GHz images. The 9 GHz image was convolved with the 5.5 GHz beam. We mask values below 3σ in their respective 5.5 and 9 GHz images. Bottom right panel: Error values for our spectral index map. We find that the central source has a steep spectral index ($\alpha = -0.4 \pm 0.2$), consistent with optically-thin synchrotron emission. To the southwest we see the HII region, H 10 (Blair and Long, 1997), which, as expected, has a flatter spectral index ($\alpha \sim -0.1 - 0.3 \pm 0.3$) than S 10.

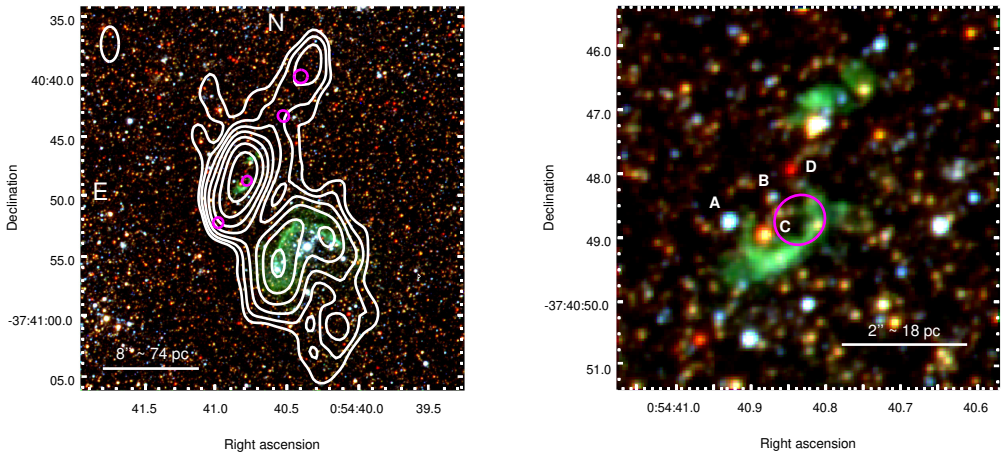

Figure 7.4: Left panel: *HST*/ACS-WFC RGB colour image of S 10. Red represents the F814W band, green is the F606W band and blue is the F475W band. Overlaid are the ATCA 5.5 GHz contours in white and, in magenta, the 95% confidence *Chandra* error circles (Section 7.1.4) for the peak-emission location of each knot. There is nebular emission (likely Hα plus [N II], which are covered by the F606W bandpass) coincident with X-ray knot 2 and the peak radio emission. The star-forming region and photo-ionised nebula H 10 (Blair and Long, 1997) is to the south-west. Right panel: Zoomed-in image of the inner part of the S 10 complex around the extended X-ray knot 2, more clearly showing the two separate nebulae (in green). The magenta circle represents the 95% confidence *Chandra* central position of the brightest knot (Section 7.2.3.2). Letters indicate potential optical counterparts for the accreting compact object. The distinct morphology of the line-emitting nebula around the peak X-ray and radio emission could be a result of anisotropic ejecta from a progenitor SN or it could be gas shock-ionised by the jet and the counterjet.

7.1.3 Optical observations

7.1.3.1 *HST* imaging

We downloaded publicly available *HST* data for NGC 300 from the Hubble Legacy Archive[1]. The observations (proposal ID 10915) were taken on 2006 November 9 with the WFC of the ACS. We used the broadband filters F475W, F606W and F814W, with exposure times 1488 s, 1515 s and 1542 s respectively. We created a three-colour image using the F475W, F606W and F814W bands (Figure 7.4).

We performed aperture photometry on potential optical counterparts to the X-ray knots. Source count rates for each filter were extracted from 0.15 arcsec (3 pixels) circular regions. We selected nearby backgrounds at least three times larger than the source regions. We used the encircled energy fractions of Sirianni et al. (2005) to determine the aperture correction and calculate the source count rates at infinite apertures. Finally, we converted count rates to physical

[1]http://hla.stsci.edu/hlaview.html

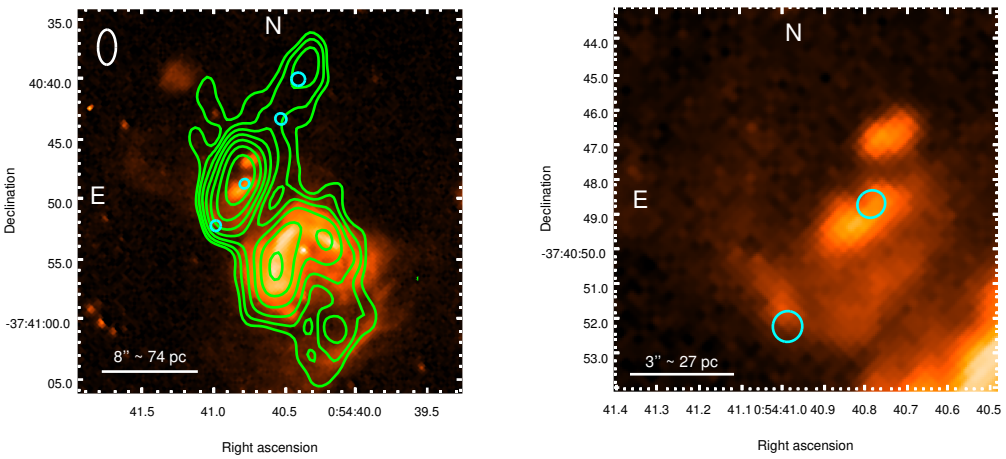

Figure 7.5: Left panel: smoothed VLT/FORS2 continuum-subtracted Hα image of S 10 with the *Chandra* 95% error circles for the four X-ray knots in cyan and 5.5 GHz ATCA contours overlaid in green. As already noted in the *HST* image (Figure 7.4), the two regions with the strongest Hα emission are located on either side of X-ray knot 2. However, the VLT image also shows a larger Hα nebula, extending south as far as X-ray knot 1. Right panel: Zoomed-in view of the core region, from the continuum-subtracted VLT/FORS2 image. The cyan circles mark the position of X-ray knots 1 and 2.

magnitudes using the zeropoint tables for ACS-WFC[2].

7.1.3.2 VLT imaging

Finally, from the ESO Science Archive Facility[3], we downloaded publicly available VLT data to better study the narrow-band Hα emission. NGC 300 S 10 was observed on 2010 July 10 with two consecutive FORS2 90 s exposures (with the first exposure starting at Universal Time 09:54:45) with the "H_Alpha+83" interference filter[4]. The filter has a central wavelength of 6563 Å and a FWHM of 61 Å; thus, it also includes the [N II]$\lambda\lambda$6548,6583 lines. The collimator was in standard resolution. The seeing was $\approx 0\farcs6$ and the airmass $\sec z = 1.03$. This was followed by two consecutive 90 s exposures with the "H_Alpha/4500+61" interference filter, centred at 6665 Å, for continuum subtraction.

We stacked the two 90 s Hα exposures and the corresponding continuum exposures using the IRAF software Version 2.16 (Tody, 1993) package *imcombine*. We aligned the stacked Hα and continuum images with the IRAF package *ccmap*, relying on $\approx$ 30 common bright sources. Finally, we subtracted the continuum using the IRAF package *imarith*. The resulting image is displayed in Figure 7.5. We used the continuum-subtracted image for flux measurements (Section 7.2.3).

[2]http://www.stsci.edu/hst/acs/analysis/zeropoints
[3]http://archive.eso.org/cms.html
[4]http://www.eso.org/sci/facilities/paranal/instruments/fors/inst/Filters.html

Table 7.2: Central position of each X-ray knot; knot 2 is spatially resolved, while knots 1, 3 and 4 are unresolved.

	RA (J2000)	Dec (J2000)
Knot 1	$00^h54^m40\overset{s}{.}99$ ($\pm0\overset{''}{.}44$)	$-37°40'52\overset{''}{.}2$ ($\pm0\overset{''}{.}42$)
Knot 2	$00^h54^m40\overset{s}{.}79$ ($\pm0\overset{''}{.}41$)	$-37°40'48\overset{''}{.}7$ ($\pm0\overset{''}{.}38$)
Knot 3	$00^h54^m40\overset{s}{.}53$ ($\pm0\overset{''}{.}48$)	$-37°40'43\overset{''}{.}3$ ($\pm0\overset{''}{.}45$)
Knot 4	$00^h54^m40\overset{s}{.}41$ ($\pm0\overset{''}{.}57$)	$-37°40'40\overset{''}{.}0$ ($\pm0\overset{''}{.}55$)

7.1.4 Astrometric alignment

The default *Chandra*/ACIS-I astrometry is known to be accurate within $\approx0\overset{''}{.}75$ for 90% of the observations[5]. To improve on this value, we aligned the stacked *Chandra* image to the DR1 *Gaia* astrometric frames (Lindegren et al., 2016; Gaia Collaboration et al., 2016a,b) which has a mean uncertainty $\sigma \approx 0.3$ mas. Because of the low number of X-ray sources, we were only able to find five common, bright point sources suitable for frame alignment. After alignment, we find position error residuals of $\approx0\overset{''}{.}1$–$0\overset{''}{.}2$. We determined the central position of each X-ray source using the CIAO task *wavdetect* on the stacked *Chandra*/ACIS-I image. To estimate their respective confidence error circles, we calculated the 95% statistical uncertainty for the central position of each source using Eq. (5) from Hong et al. (2005); we then combined (in quadrature) those statistical uncertainties and the *Chandra*/*Gaia* alignment residuals. We also aligned our *HST* images in the F475W, F606W and F814W bands and our VLT Hα/4500 and Hα bands onto the *Gaia* astrometric frame, using > 100 common, bright, non-saturated sources. This provides a positional accuracy within $0\overset{''}{.}009$ for the *HST* images and $0\overset{''}{.}03$ for the VLT images. We assume that the radio and *Gaia* astrometric frames are consistent with each other, within the relative uncertainties.

7.2 Results

7.2.1 X-ray results

7.2.1.1 X-ray knots

The *Chandra* data reveal the presence of four X-ray sources that appear linearly aligned with a total projected length of $\approx 17'' \approx 150$ pc (Figure 7.2). No other X-ray sources are detected within a circle of radius $\approx 1'$. Additionally, we only expect $\approx 4 \times 10^{-3}$ extragalactic sources (Lehmer et al., 2012) with $0.5 - 2.0$ keV fluxes greater than $f_{0.5-2.0\,\mathrm{keV}} = 1.9 \times 10^{-15}$ erg cm^{-2} s^{-1} (the flux of the dimmest

[5] http://cxc.harvard.edu/cal/ASPECT/celmon/

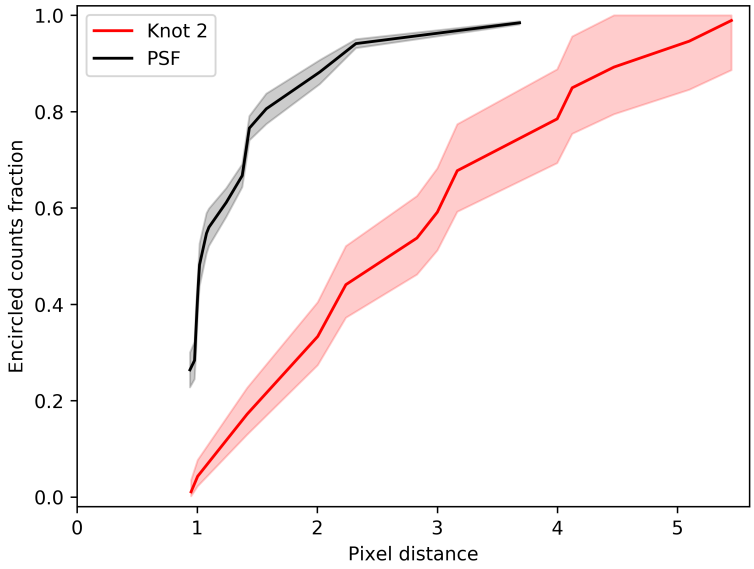

Figure 7.6: Enclosed ACIS-I count fraction as a function of distance from the centre of a source. The black points represent the PSF of *Chandra*/ACIS-I, from a 1000-iteration Monte Carlo simulation, at the location of S 10, for ObsID 16028. The red points represent the measured extent of knot 2 from the same observation. Shaded regions indicate 1σ errors. At the distance of 1.88 Mpc, 1 ACIS-I pixel corresponds to ≈4.5 pc. The comparison shows that the source is significantly extended.

source, knot 4) within a region equivalent to the projected area of the radio bubble (i.e., $19'' \times 6'' \approx 8.80 \times 10^{-6}$ deg^2); therefore a physical connection between those aligned sources is highly likely. We shall refer to those four visually distinct X-ray sources as knots 1 to 4 (starting from the southernmost one). The central positions of those four knots are listed in Table 7.2.

Of those four sources, knot 2 appears, at first sight, spatially extended (Figure 7.2) and larger than the other three. We quantified this visual impression with the MARX[6] simulation software. Using the task *simulate_psf*, we simulated 1000 PSFs at the location of S 10 on the ACIS-I chip during ObsID 16028. For this ensemble of simulated PSFs, the average encircled energy fraction as a function of radius was determined with the CIAO task *ecf_calc*. We compared this value to the observed encircled energy fraction of knot 2 during ObsID 16028. The results are displayed in Figure 7.6. The shape of the PSF does not match that observed for knot 2, indicating that knot 2 is indeed extended. It is consistent with two point-like sources separated by ≈1.″2 and oriented roughly along the same direction defined by the other knots.

There are insufficient counts to do meaningful spectral analyses on the individual X-ray knots for individual epochs. However, we can investigate source

[6]http://cxc.harvard.edu/ciao/threads/marx/

variability and evolution of the hardness ratios from the three epochs spaced over ≈4 years. For the hardness ratios, we define the soft band as 0.3–1.2 keV (following the combined ultra-soft and soft bands in the Chandra Source Catalogue; Evans et al. 2010), and 1.2–7.0 keV for the hard band. Since the ACIS-I detector has lost sensitivity over the years, especially in the soft band, we must correct the count rates measured in ObsID 12338 (Cycle 11) to make them comparable with the count rates measured in Cycle 15 (ObsIDs 16028 and 16029). We did that using the online tool PIMMS[7] version 4.8e. For knot 1, we assumed a thermal plasma model with temperature $kT \approx 0.8$ keV, while for knots 2, 3 and 4 we assumed a temperature of $kT \approx 0.4$ keV. These assumptions are based on our spectral fitting after we combined the spectra from all three *Chandra* epochs, as described later in this section.[8] The cycle-corrected hard and soft count rates are displayed in Table 7.3. We find no significant variability for any of the knots, in either band, over all three epochs. The corresponding hardness ratios are displayed in Table 7.4. While knots 2, 3 and 4 all have similar spectral hardnesses, knot 1 appears harder. As with the count rates, no significant hardness ratio variability is detected across all four knots and all three epochs.

In order to conduct spectral modelling of the knots, we stacked the three *Chandra* epochs. Each of the knots has insufficient counts for χ^2 statistics and so W statistics were used. We first attempted to fit each of the knots with a simple absorbed power-law model (*TBabs* × *po*). However all power-law fits yielded unphysically high absorption and photon indices. For example, fitting knot 2 with an absorbed power-law model yields a best-fit photon index $\Gamma \approx 10$ and column density $n_{\rm H} = 10^{22}\,{\rm cm}^{-2}$, for a W statistic of 87.7 and 72 degrees of freedom. Instead, we find (Table 7.5) that all four knots are well described by thermal plasma models, such as *mekal* (Mewe et al., 1986, 1985). No additional intrinsic absorption is required, and thus we use a single *TBabs* component fixed to the line-of-sight column density towards NGC 300 ($n_{\rm H} = 3 \times 10^{20}\,{\rm cm}^{-2}$; Dickey and Lockman 1990; Kalberla et al. 2005). As expected from the hardness ratios (Table 7.4), knot 1 appears hotter than the rest. The unabsorbed X-ray luminosities of the knots ranges from ≈1 $\times 10^{36}$ erg s^{-1} for the dimmest knot (knot 4) to ≈7 $\times 10^{36}$ erg s^{-1} for the brightest (knot 2). For the spectrum of the combined emission of all knots, we find a best-fitting thermal plasma temperature $T \approx 0.6$ keV and an unabsorbed bolometric luminosity $L \approx 1.1 \times 10^{37}$ erg s^{-1}. The model for this best-fitting thermal plasma is shown in Figure 7.7 with the fit parameters

[7] http://cxc.harvard.edu/toolkit/pimms.jsp

[8] The cycle-to-cycle corrections to the ACIS-I count rates are relatively small and do not substantially depend on the choice of model; the results listed in Table 7.3 are essentially unchanged (differences $\lesssim 10\%$) if we assume the same plasma temperature for all knots, or if we use a steep power-law spectral model.

Table 7.3: *Chandra*/ACIS-I count rates for the hard (1.2–7.0 keV) and soft (0.3–1.2 keV) bands. *Chandra* Obs 12238 (Cycle 11) has been scaled to match the *Chandra* sensitivity of the other observations (Cycle 15). Count rates are in units of 10^{-4} count s^{-1}.

Obs ID	Knot 1		Knot 2		Knot 3		Knot 4		Combined	
	Hard	Soft	Hard	Soft	Hard	Soft	Hard	Soft	Hard	Soft
12238	1.8 ± 0.6	2.3 ± 0.6	2.7 ± 0.7	9.5 ± 1.1	≤ 0.4	2.4 ± 0.5	0.4 ± 0.3	0.7 ± 0.3	5.0 ± 1.0	15.6 ± 1.4
16028	2.4 ± 0.6	1.9 ± 0.5	2.5 ± 0.7	10.9 ± 1.3	0.5 ± 0.4	2.3 ± 0.6	≤ 0.6	1.4 ± 0.5	6.0 ± 1.0	17.0 ± 1.6
16029	1.5 ± 0.5	3.9 ± 0.8	1.9 ± 0.6	7.0 ± 1.1	0.7 ± 0.4	1.3 ± 0.5	0.4 ± 0.1	0.3 ± 0.2	4.6 ± 0.9	12.9 ± 1.5
Total	2.1 ± 0.3	3.0 ± 0.4	2.4 ± 0.4	10.2 ± 0.7	0.5 ± 0.2	2.4 ± 0.4	0.3 ± 0.2	0.9 ± 0.2	5.2 ± 0.6	16.7 ± 0.9

Table 7.4: Hardness ratios corresponding to the count rates listed in Table 7.3. The hardness ratios are defined as (1.2–7.0 keV)/(0.3–1.2 keV).

Obs ID	Knot 1	Knot 2	Knot 3	Knot 4	Combined
12238	0.78 ± 0.33	0.28 ± 0.08	≤ 0.17	0.57 ± 0.49	0.32 ± 0.07
16028	1.27 ± 0.50	0.23 ± 0.07	0.22 ± 0.16	≤ 0.41	0.35 ± 0.07
16029	0.38 ± 0.16	0.27 ± 0.09	0.50 ± 0.33	1.1 ± 0.8	0.36 ± 0.08
Total	0.70 ± 0.15	0.23 ± 0.04	0.19 ± 0.08	0.28 ± 0.18	0.31 ± 0.04

Table 7.5: Best-fitting parameters for the spectra of the individual knots and for the combined spectrum, from the merged *Chandra*/ACIS-I observations 12238, 16028 and 16029, fitted with *TBabs* × *mekal*. We fixed the absorbing column density $n_{\rm H}$ to the Galactic line-of-sight value; adding intrinsic local absorption does not produce statistically significant improvements. Errors are 90% confidence limits for one interesting parameter. We report the observed fluxes and de-absorbed luminosities.

Model	Parameter	Knot 1	Knot 2	Knot 3	Knot 4	Combined
	Net Counts (0.3–7.0 keV)	99	234	58	26	432
TBabs	$n_{\rm H}\left(10^{22}\,{\rm cm}^{-2}\right)$	[0.03]	[0.03]	[0.03]	[0.03]	[0.03]
mekal	k_eT (keV)	$0.80^{+0.15}_{-0.14}$	$0.53^{+0.07}_{-0.10}$	$0.37^{+0.15}_{-0.08}$	$0.28^{+0.31}_{-0.07}$	$0.57^{+0.05}_{-0.06}$
	K $\left(10^{-6}\right)$	$2.1^{+0.4}_{-0.3}$	$5.8^{+1.3}_{-0.8}$	$1.8^{+0.9}_{-0.6}$	$1.2^{+1.3}_{-0.7}$	$9.2^{+1.0}_{-0.9}$
	$f_{0.3-8.0}$ $\left(10^{-15}{\rm erg\ cm^{-2}\ s^{-1}}\right)$	$4.7^{+0.8}_{-0.8}$	$14.4^{+1.9}_{-1.9}$	$3.8^{+1.1}_{-1.1}$	$2.1^{+1.3}_{-1.3}$	$22.9^{+2.2}_{-2.2}$
	$L_{0.3-8.0}$ $\left(10^{36}\,{\rm erg\ s^{-1}}\right)$	$2.2^{+0.4}_{-0.4}$	$6.9^{+0.9}_{-0.9}$	$1.9^{+0.6}_{-0.6}$	$1.1^{+0.7}_{-0.7}$	$11.0^{+1.0}_{-1.1}$
	W statistic/d.o.f.	79.3/55	64.2/73	37.6/37	14.1/15	115.8/108

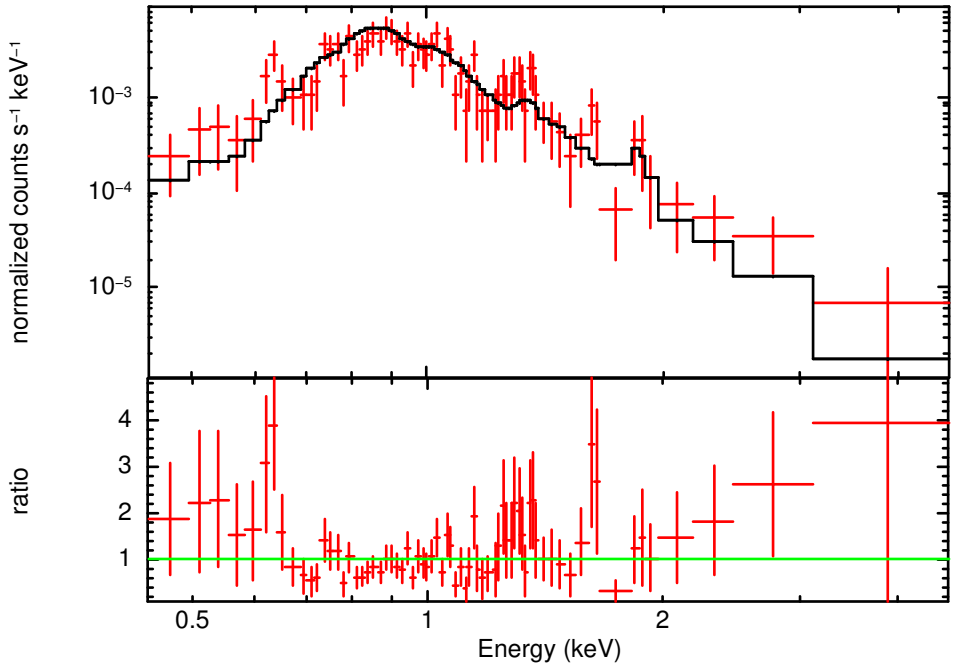

Figure 7.7: *Chandra*/ACIS-I stacked spectrum of the combined knots emission from observations 12238, 16028 and 16029, fitted with a thermal plasma model; the best-fitting plasma temperature is $kT = 0.6 \pm 0.1$ keV. See Table 7.5 for the fit parameters.

displayed in Table 7.5. While the spectrum is well fitted by thermal plasma alone, we also try a thermal plasma plus power-law model. We fix the power-law photon index to $\Gamma = 1.7$, typical of X-ray binaries with X-ray luminosities similar to the core of S 10 (see Sections 7.2.1.2 and 7.3.4 for more details). However, we find no statistically significant improvement to the fit, with a maximum power-law contribution of $L < 2 \times 10^{36}$ erg s^{-1} at the 90% confidence level. Thus, by Occam's razor, our preferred model is the simple best-fitting thermal plasma model.

The normalisation constant for the *mekal* component (at zero redshift) is defined as $K = 10^{-14} \int (n_e\, n_{\rm H}\, dV)/(4\pi d^2) \approx 10^{-14}\, n_e^2\, V/(4\pi d^2)$, where V is the volume of the emitting region, n_e is the electron density, $n_{\rm H}$ is the nuclear density and d is the distance. We approximate the X-ray structure as five spherical sources (two of them corresponding to knot 2) with radii similar to or smaller than the *Chandra* resolution, $\approx 0\farcs4 \approx 1.1 \times 10^{19}$ cm; this corresponds to a total volume $V \lesssim 3 \times 10^{58}$ cm^3 for the emitting plasma region. Thus, for the best-fitting normalisation $K \approx 9 \times 10^{-6}$ in our spectral model (Table 7.5), we estimate a lower limit to the density of the hot plasma component, $n_e \gtrsim 4$ cm^{-3}.

7.2.1.2 X-ray core

If, as we suggest, S 10 is a powerful microquasar within NGC 300, then we expect to find a hard X-ray source at its core, a signature of accretion. However, we do

not observe this; all the knots are best-fitted with soft thermal plasma models, with the majority of emission being < 2 keV. We do find a marginal detection of 6^{+8}_{-5} net counts[9] in the 2–7 keV band, near the central position of the brightest knot (knot 2). However, this is also consistent with the ≈5.8 net counts expected from a thermal plasma at a temperature of 0.53 keV, fitted to the spectrum of knot 2. From that, we estimate a 90% upper limit of ≈6 $\times 10^{-5}$ net ct s^{-1} from a point-like power-law core (in addition to the soft thermal emission). For an assumed photon index $\Gamma = 1.7$, this corresponds to a luminosity $L_{0.3-7\,\mathrm{keV}} \approx 10^{36}$ erg s^{-1}. No other knots have significant 2–7 keV emission, and thus, regardless of where the central source is, we can take this value as the upper limit of the current accretion luminosity of the central engine.

In the absence of a well-resolved, point-like hard source, we can use indirect arguments to constrain the possible location of the candidate microquasar core. Spatially resolved X-ray jets comprising a series of bright knots are seen in some AGN: most famously, in M 87 (Wilson and Yang, 2002; Marshall et al., 2002b) and NGC 5128 (Hardcastle et al., 2003; Kraft et al., 2002). In those cases, the active nucleus is generally located at one end of the string of X-ray knots, because the jet coming towards us is brighter than the (usually undetected) counter-jet. In the NGC 300 candidate microquasar, this would correspond to knot 1 (which is also the one with the hardest X-ray colours and hottest *mekal* fit temperatures). However, the lobe-like morphology of the inner knot of Hα emission (pointing towards the south-east: Figure 7.4), and the shape of the larger Hα bubble (Figure 7.5) suggest that knot 1 is unlikely to be the origin of the jet, and that the core is most likely associated with knot 2 (the most luminous part of the system in X-rays, radio and Hα). We have already shown that knot 2 is extended (Figure 7.6), and suggest that it likely consists of two sources separated by ≈1.″2 and also aligned in the general direction of the other knots. Thus, we suggest that knot 2 consists of a pair of ejecta or hot spots from the approaching and receding jet and that the core resides somewhere between the two.

7.2.2 Radio results

From the ATCA images, we discovered a bright, resolved and elongated radio structure aligned along the axis of the X-ray knots (Figure 7.2). The majority of the radio emission comes from a region coincident with the first and second X-ray knots, with the radio peak coincident with X-ray knot 2. In the 5.5 GHz image, we also detect a region of enhanced radio emission, which we refer to as a 'radio

[9] Within the 1.″5 aperture, we expect ≈0.6 background counts, which makes the X-ray emission in the hard band significant at the $\geq$ 99% level, according to Poisson statistics in the presence of a background (Kraft et al., 1991).

Table 7.6: Integrated ATCA 5.5 and 9 GHz fluxes. For fluxes values obtained via the CASA task IMFIT we provide spectral indices. The steep spectral index of the core suggests that the emission is coming from optically-thin synchrotron emission, as expected from other radio bubbles.

Object	5GHz flux μJy	9GHz flux μJy	α
Total	520 ± 15	380 ± 20	
Core	429 ± 30	352 ± 29	-0.4 ± 0.2
Knot	75 ± 7	$39 \pm 17^*$	-1.3 ± 0.9
H II Region	511 ± 15	302 ± 24	

* Flux integrated over region defined by radio node in the 5.5 GHz image

node', north-west of the bright, central radio component, near X-ray knot 4; the same radio node is a marginal detection at 9 GHz. From the 5.5 GHz image, we measure a total size of the elongated radio bubble as $19'' \times 6'' \approx 170 \times 55$ pc (for a distance of 1.88 Mpc). This emitting region is clearly resolved both along and across the jet direction, because the beam size is only $\approx 26 \times 13$ pc (Section 7.1.2).

We find total integrated flux densities of $f_{5.5\,\mathrm{GHz}} = 520 \pm 15\,\mu$Jy and $f_{9\,\mathrm{GHz}} = 380 \pm 20\,\mu$Jy for the 5.5 and 9 GHz bands, respectively. This equates to a 5.5 GHz radio luminosity of $L_{5.5\,\mathrm{GHz}} \approx 1.2 \times 10^{34}$ erg s^{-1}. We fitted a 2-dimensional Gaussian profile to the central, and brightest, region of S 10 using the CASA task IMFIT, to estimate the flux coming from the core. We find peak intensities of $87.8 \pm 2.7\,\mu$Jy beam^{-1} and $35.0 \pm 2.8\,\mu$Jy beam^{-1} at 5.5 and 9 GHz respectively, and integrated flux densities of $429 \pm 30\,\mu$Jy and $371 \pm 29\,\mu$Jy. We also used a 2-dimensional Gaussian profile fit in the 5.5 GHz map to measure the integrated flux of the radio node to the northwest of the core; we find a flux of $79.5 \pm 5.3\,\mu$Jy. The knot is only marginally detected in the 9 GHz image, with an integrated flux of $17.9 \pm 4.4\,\mu$Jy. Our measured radio fluxes are summarised in Table 7.6.

The spectral index α (defined as $f_\nu \propto \nu^\alpha$) ranges from about -0.7 to about -0.4 (with typical errors of $\approx \pm 0.2$) near the central region (where the radio emission is strongest), at the location of X-ray knot 2 (Figure 7.3). This is consistent with optically-thin synchrotron emission. There are also hints of a flattening of the spectral index towards the edges (near X-ray knots 1 and 3). We also measured the spectral index of the radio node at the north-west end of the bubble, finding $\alpha = -1.3 \pm 0.9$ there[10]. It is unclear whether this radio node

[10] The node is only marginally detected at 9 GHz. To determine its spectral index, we used the region defined by the 5.5 GHz IMFIT output and integrated the flux over this same area for the 9 GHz image.

is associated with the X-ray knot 4, as the peak radio emission (in the 5.5 GHz band) of the radio node appears to be slightly offset to the northwest of the X-ray knot (Figure 7.2, top panel).

We also detect radio emission from the nearby, unassociated HII region H 10 (Blair and Long, 1997), southwest of S 10 (Figure 7.3). The spectral index in this region is much flatter than in the candidate microquasar bubble (Figure 7.3), as expected for the spectral index of an HII region. At 5.5 GHz, the peak flux density of the HII region is $52.6 \pm 2.7\,\mu$Jy beam^{-1} and the integrated flux density is $511 \pm 15\,\mu$Jy. At 9 GHz, the peak flux density is $30.1 \pm 2.8\,\mu$Jy beam^{-1} and the integrated flux is $302 \pm 24\,\mu$Jy. A few arcsec further to the southwest, another region with steep spectral index corresponds to the supernova remnant catalogued as S 9 in Blair and Long (1997). A study of H 10 and S 9 is beyond the scope of this work.

7.2.3 Optical results

7.2.3.1 Diffuse emission

Blair and Long (1997) used CCD imaging and spectroscopic data taken in 1987 with the 2.5-m du Pont telescope to measure Hα and [S II] fluxes of optical SNR candidates in NGC 300. Their source S 10 = DDB2 corresponds to the X-ray and radio structures discussed in this chapter. S 10 is listed in the catalogue of Blair and Long (1997) with a line ratio [S II]:(Hα plus [N II]) ≈ 0.67, indicative of shock-ionised gas, and with an Hα flux $F_{\mathrm{H}\alpha} \approx 8.3 \times 10^{-15}$ erg cm^{-2} s^{-1} (Blair and Long, 1997, from the average surface brightness and size in their Table 3A). This value has already been corrected for spectral contamination from [N II]$\lambda\lambda$6548,6583, which Blair and Long (1997) assumed to be 25% of the Hα emission, based on an average value over their sample of SNR candidates in NGC 300. In fact, individual long-slit spectra of S 10 also from Blair and Long (1997) show a slightly larger [N II] contribution of $\sim$35%, implying an Hα flux $F_{\mathrm{H}\alpha} \approx 7.7 \times 10^{-15}$ erg s^{-1}. The diameter of this line-emitting region was reported by Blair and Long (1997) as only $\approx$14 pc[11]. This is much smaller than the size of the Hα structure we see for example in the VLT images (Figure 7.5). We suspect that the S 10 measurements of Blair and Long (1997) refers only to the brightest core of the nebula, near X-ray knot 2, not to the larger structure around it. Thus, we expect the total Hα flux from the whole region to be a few times larger.

In 2006, follow-up spectroscopic observations of NGC 300 by Millar et al. (2011), with the 2.3-m Advanced Technology Telescope at Siding Spring Observatory, indicated a slightly lower [SII]:Hα ratio of 0.35 ± 0.15 for S 10, although

[11] Rescaled to our adopted distance of 1.88 Mpc; Blair and Long (1997) used 2.1 Mpc.

the source was still classified as an SNR based on its multiband properties. More importantly, Millar et al. (2011) found that the S 10 emission region is significantly larger (diameter of ≈56 pc) than originally reported, and an order of magnitude more luminous ($F_{\mathrm{H}\alpha} = (10.5 \pm 1.4) \times 10^{-14}$ erg cm^{-2} s^{-1}). This flux value was based on the extrapolation to the whole nebula of the integrated line flux measured from a long-slit observation; such extrapolations are fraught with uncertainties. Moreover, at the average seeing of Siding Spring Observatory, S 10 is inevitably contaminated by emission from the nearby H 10 HII region, which may explain the lower value of [SII]:Hα measured by Millar et al. (2011). Size and flux discrepancies for several other NGC 300 sources between Blair and Long (1997) and Millar et al. (2011) are also discussed in the latter paper.

To improve on those previous two studies and resolve their discrepancies, we investigated the diffuse optical emission at S 10 using archival *HST*/ACS images in the F475W, F606W and F814W filters. This is possible because the broadband filter F606W also includes the wavelengths around Hα; therefore, we expect regions of strong Hα emission to show up in green, in a true-colour image from those three bands. There are indeed two bright regions of Hα emission (Figure 7.4, bottom panel), separated by a distance of ≈20 pc, on either side of the central location of X-ray knot 2. The southern Hα source has a lobe-like structure, which suggests that the gas has been shocked by some kind of fast ejection: either a microquasar jet or collimated ejecta during a supernova (SN) explosion. The lobe-like source has a diameter of ≈0.″8, corresponding to ≈15 pc; it is aligned along the same direction defined by the string of X-ray knots and by the elongated radio source. This is most likely the source identified and measured by Blair and Long (1997, their Figure 3).

To investigate the presence of fainter, much more extended Hα emission, and to measure its flux, we used the continuum-subtracted VLT image. Although at lower spatial resolution, we clearly recover (Figure 7.5) the two innermost Hα emission regions already seen in the broadband *HST* image. Additionally, we see an extended bubble, stretching between and around X-ray knots 1 and 2 (characteristic size of ≈60 pc), with a brighter spot almost coincident with X-ray knot 1 (Figure 7.5). The emission region is bounded on its southern side by a slightly brighter rim. We speculate that this Hα-emitting bubble has been inflated by a source of kinetic power probably located near X-ray knot 2: the same source of kinetic power responsible for the radio and X-ray emission.

To measure the flux of the extended Hα region, we defined suitable source and background regions in the continuum-subtracted VLT image (Figure 7.5), with the imaging and photometry tool DS9. We then used the VLT FORS2

Exposure Time Calculator in Imaging Mode[12] to convert from the measured net count rate to a physical line emission flux. We assumed a contribution of [N II]$\lambda\lambda$6548,6583 equal to $(30 \pm 5)\%$ of the Hα flux. This choice is based on the line ratios measured directly for S 10 by Blair and Long (1997) and Millar et al. (2011), and takes also into account the small fraction of [N II] flux that falls outside the VLT filter passband. We obtain a flux $F_{\mathrm{H}\alpha} = (4.1 \pm 0.5) \times 10^{-14}$ erg cm^{-2} s^{-1}. The error is the quadrature sum of the uncertainty on the [N II]$\lambda\lambda$6548,6583 contribution and a rough estimate of the range of values we obtained for slightly different choices of the outer boundary of the S 10 bubble. We also verified this flux estimate by estimating the ratio (a factor of 5) between the Hα counts in the whole bubble and in the bright core, for which Blair and Long (1997) had reported a flux of $\approx 8 \times 10^{-15}$ erg cm^{-2} s^{-1}. Finally, we confirmed the consistency of our estimate by comparing our measured VLT count rates for S 10 and for isolated SNR candidates that have a more reliable flux measurement in Blair and Long (1997); we obtained the same estimate of an S 10 Hα flux between ≈ 4–5×10^{-14} erg cm^{-2} s^{-1}. At the distance of 1.88 Mpc, this corresponds to a luminosity $L_{H\alpha} = (1.7 \pm 0.2) \times 10^{37}$ erg s^{-1} and (for a standard Balmer decrement from Case B recombination) $L_{H\beta} = (6 \pm 1) \times 10^{36}$ erg s^{-1}.

7.2.3.2 Stellar counterparts

We selected a few potential optical counterparts in the *HST* images (Figure 7.4) located close to knot 2, as this is the most likely location of the true nuclear source (as discussed in Section 7.2.1.2 and from the Hα morphology discussed in 7.2.3.1); we measured their optical brightnesses and colours with IRAF. We interpreted their physical properties by comparing those values with the Padova theoretical stellar isochrones[13] (Bressan et al., 2012; Chen et al., 2015) for a metallicity $Z = 0.015$ (Table 7.7). Specifically, we estimated the age, mass, radius and temperature on the nearest isochrone to each star. In doing so, we assumed that any emission we see is due to a single star and not to an accretion disc around the compact object or to multiple stars. Source A is the bluest and brightest stellar source in the field, a B-type giant; however, it appears unlikely to be the true optical counterpart of the central engine, as it resides outside of a lobe-shaped Hα nebula (Figure 7.4), and therefore, offset from the likely direction of the jet that inflated that structure[14]. Star C is also outstanding in brightness and colour from the rest of the stellar population in the field: it is consistent with an intermediate-

[12] https://www.eso.org/observing/etc/

[13] Available at http://stev.oapd.inaf.it/cgi-bin/cmd

[14] If we attribute the offset from the jet axis to proper motion of the star after the main jet activity phase, we require a projected velocity of $\approx$100 km s^{-1} for $\approx 10^5$ yr.

Table 7.7: *HST* magnitudes and physical parameters of three potential optical counterparts of the true nuclear source of S 10. The optical counterparts (along with the lettering) corresponds to those outlined in Figure 7.4. Observed magnitudes are converted to physical properties using the theoretical isochrones for a metallicity $Z = 0.015$. The stellar radii are calculated using the surface gravity and total mass. Colours for Star 4 are dominated by intrinsic reddening and thus comparison to theoretical isochrones are meaningless.

#	F814W	F606W	F475W	Age	Mass	Radius	Temperature	Luminosity
	mag	mag	mag	Myr	$M_\odot$	$R_\odot$	K	erg s^{-1}
A	-3.67 ± 0.02	-3.86 ± 0.02	-3.88 ± 0.02	~ 50	7	110	12,300	2×10^{37}
B	-2.77 ± 0.07	-2.10 ± 0.05	-1.86 ± 0.06	~ 200	4	120	6,600	2×10^{36}
C	-4.91 ± 0.01	-2.30 ± 0.06	-0.66 ± 0.05	~ 500	3	1,600	3,400	2×10^{37}
D	-3.30 ± 0.04	≥ -0.7	≥ -0.1	N/A	N/A	N/A	N/A	N/A

age AGB star (near the top of the AGB branch), and it lies along the direction of the jet. Perhaps the most intriguing candidate optical counterpart is star D. It is also located along the direction of the jet, approximately half way between the two peaks of Hα emission (Figure 7.4). It is detected as a moderately bright source only in the F814W image (Vegamag $m_{814} \approx 23.1$ mag). Its extremely red colour ($m_{606} - m_{814} > 2.6$ mag; $m_{475} - m_{814} > 3.2$ mag) suggest a high intrinsic reddening, higher than for any other neighbouring star; this could be due for example to circumstellar dust. For example, among the possible alternative interpretations, we cannot rule out that star D is a hypergiant or Wolf-Rayet star with intrinsic absolute brightness $M_V < -7$ mag, but a strong extinction $A_V \gtrsim 7$ mag. We shall mention later (Section 7.3.2) that a massive donor star surrounded by shells of ejected material is consistent with one of the scenarios discussed for the feeding of this candidate microquasar. Further investigations on the nature of star D is beyond the scope of this work. A discussion on the relative contributions of accretion disk and donor star to the optical emission is also left to further work.

We also searched for unusually bright, point-like optical sources at the location of the other X-ray knots, but did not find any unusual candidate. Most of the other stars visible in the *HST* image of the field (Figure 7.4) are red giants from an intermediate-age population (age of $\sim$ a few 10^8 yr), with a few B-type main sequence stars from a younger population.

As in our ATCA data, the HII region the the southwest, H 10 (Blair and Long, 1997), is clearly visible. The *HST* images show that there is strong F606W emission coincident with a population of bright, blue stars (Figure 7.4).

7.3 Discussion

We have identified a chain of four thermal X-ray sources aligned with each other and with an elongated 170-pc-long radio structure. The X-ray and optical sources are associated with an optical nebula originally identified as an SNR, but which is also reminiscent of jet-powered ULX bubbles. Here, we argue that the most likely explanation for the multiband structure is that S 10 is a powerful microquasar, although we also consider alternative explanations. The X-ray spectra for the knots are dominated by optically-thin thermal plasma emission, likely a result of jet/ISM interactions. The radio emission has a steep spectral index, consistent with optically-thin synchrotron emission; this is consistent with a relativistic electron population energized by a microquasar jet. Finally, the associated optical line-emission regions are shock-ionised, consistent with a forward shock propagating into the ISM, caused by the impact of a microquasar jet or fast SN ejecta. This is displayed in Figure 7.8, where the *Chandra*, ATCA and VLT images have been aligned and rotated to demonstrate the connections between structures observed in each band. In this section, we collate and examine in more detail the observational properties of S 10 that have led to our microquasar interpretation. Finally, we attempt to determine the jet power of S 10.

7.3.1 Emission processes in the knots

An important finding of our *Chandra* analysis is that the X-ray emission is from thermal plasma. This is likely the result of jet-driven shocks propagating into the ISM. The density inferred for the X-ray emitting hot plasma (Section 7.2.1) is consistent with typical pre-shock ISM densities ~ 1 cm^{-3}. It is hard to compare the knotty structure of the NGC 300 candidate microquasar (Figure 7.8) with the fine details of X-ray jet knots seen in nearby AGN such as M 87 and NGC 5128, because of the much higher spatial resolution (relative to jet length) and signal-to-noise ratio for the latter class of jets. Instead, the *Chandra* images of the S 10 jet are reminiscent of the X-ray appearance of jets in higher-redshift radio galaxies and quasars (e.g., Massaro et al., 2011, 2015; McKeough et al., 2016). However, appearances can be deceptive. The X-ray emission from AGN and quasar jets (including the emission from their hot spots) is almost always non-thermal (Harris and Krawczynski, 2006): either synchrotron radiation from relativistic electrons (with Lorentz factors $\gamma \gtrsim 10^7$), or inverse Compton scattering of cosmic microwave background photons off slightly less energetic electrons ($\gamma \sim 10^3$). The only few exceptions, where X-ray hot spots have been attributed to thermal emission, are sources in which the AGN jet is colliding with a dense, cold cloud; e.g., the jets in the radio galaxies PKS 2152−699 (Ly

et al., 2005), 4C+29.30 (Siemiginowska et al., 2012), and 3C 277.3 (Worrall et al., 2016). Instead, in both of the known off-nuclear microquasars (NGC 7793 S 26 and NGC 300 S 10) with evidence of X-ray jets, the hot spots are dominated by thermal emission at temperatures ∼0.5 keV. In both sources, the total X-ray emission from shocked gas is $\sim 2 \times 10^{37}$ erg s^{-1}. Another iconic microquasar, the Galactic source SS 433, also has a hot spot consistent with thermal emission, along the eastern jet (Brinkmann et al., 2007) (instead, the termination shock further downstream is non-thermal). We do not have enough sources to determine whether the higher contribution of thermal emission in microquasar hot spots is due to a comparatively higher ISM density, or to a different composition and Lorentz factor in the jet.

Another key observational property of S 10 is the elongated radio structure aligned with the chain of X-ray knots. How the radio and X-ray emission are linked is unclear: they arise from differing emission mechanisms (synchrotron and thermal-plasma respectively) but share similar morphologies. In the 5.5 GHz ATCA image, we detect a radio node beyond (further downstream along the jet) the outer X-ray knot (Figure 7.2). Soria et al. (2010) find that the X-ray hotspots of S 26 slightly (≈ 20 pc) trail the radio lobes, further evidence that they arise from different physical processes. We cannot determine whether the outer X-ray knot and the radio node of S 10 are related (Figure 7.8): the true X-ray counterpart to the radio node (if there is one) may have already faded.

7.3.2 Origin of the discrete knot structure

The presence of multiple thermal X-ray knots rather than only two termination hot spots is the main difference between NGC 300 S 10 (Figure 7.8) and NGC 7793 S 26 (Soria et al., 2010). In this section, we outline possible scenarios that can give rise to a string of bright knots along the jet.

(i) Discrete relativistic ejecta:
Numerous compact accreting sources produce large-scale moving jets in the form of discrete ejecta. Ejection of relativistic plasma knots that emit via synchrotron processes have been observed at radio and X-ray wavelengths in the sub-Eddington LMXBs H1743-322 (Corbel et al., 2005), XTE J1550-564 (Corbel et al., 2002; Kaaret et al., 2003b) and XTE J1752-223 (Ratti et al., 2012). On the super-Eddington side, the ULX Ho II X-1 shows evidence of multiple discrete radio ejecta (Cseh et al., 2014). While each of the Ho II X-1 knots are not detected in X-rays, the S 10 jet could be made up of similar discrete ejecta where each southeast-northwest knot pair is due to a flare or outburst. In this scenario, the

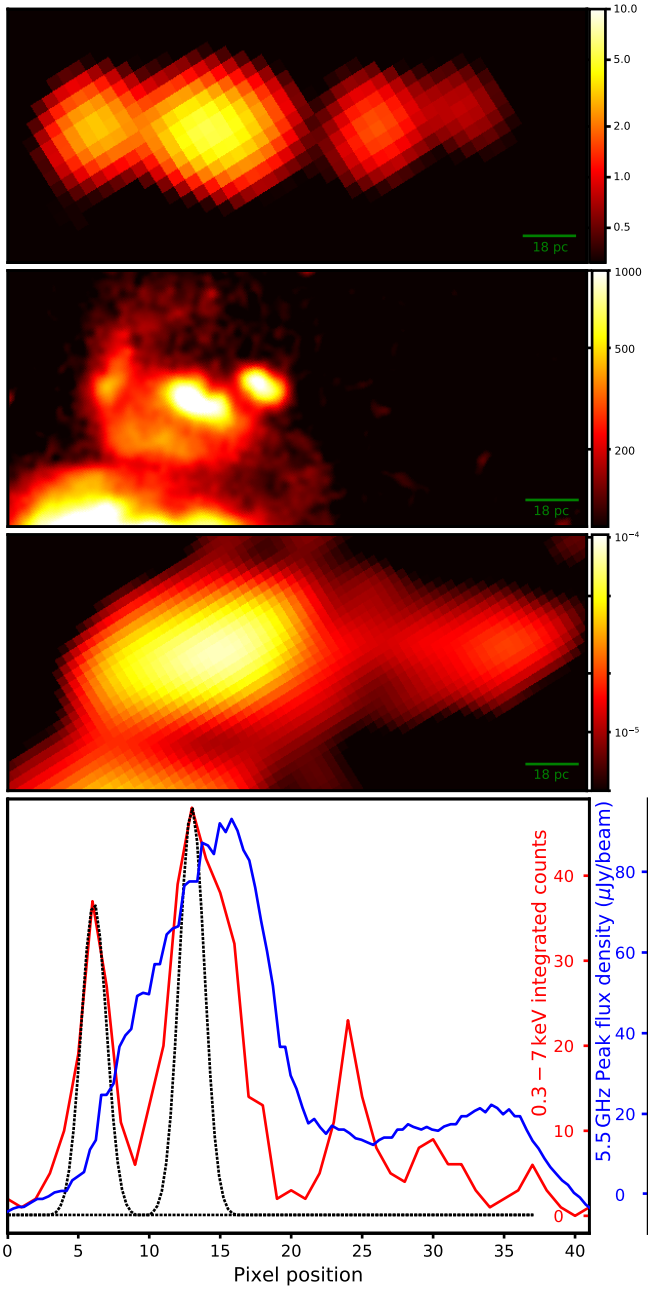

Figure 7.8: From top to bottom: S 10 jet in X-rays ($0.3-7$ keV; scalebar in units of counts), Hα line (scalebar in units of ADU for the VLT/FORS2 CCD), and 5.5 GHz band (scalebar in units of Jy beam^{-1}), rotated to a horizontal position; and corresponding brightness distribution along the jet in X-rays (red curve) and radio (blue curve), on the same spatial scale. For the bottom panel, we measured the X-ray brightness by integrating the pixel counts in 1-pixel-wide strips perpendicular to the jet axis; we measured the radio intensity from the peak value along the jet. The dotted black line represents a symmetric Gaussian approximation of the *Chandra* PSF of a point-like source at the location of S 10, determined from our PSF modelling (Section 7.2.1). At the distance of 1.88 Mpc, 1 ACIS-I pixel corresponds to ≈4.5 pc. The comparison shows that the second X-ray knot is extended and likely composed of (at least) two distinct sources, displaced by ≈1.″2 along the direction of the jet. For comparison, we show that the first knot instead matches the *Chandra* PSF.

most recent ejecta would be the two unresolved blobs that constitute knot 2; the previous outburst would have produced knots 1 and 3; knot 4 would be the oldest ejection event whose southeastern counterpart has since faded (Figure 7.8). However, we rule out this scenario as the X-ray knots would have to be radiating via synchrotron emission, not thermally as we see for S 10.

(ii) Internal shocks:
The multiple-knot morphology may be a result of internal shocks within the jet (Rees and Meszaros, 1994; Malzac, 2014). Faster-moving ejecta catch up to slower-moving, previously ejected material further downstream, the collision causing shocks and accelerating particles. This would make S 10 analogous to the AGN jets we see in M87 (Rees, 1978; Sparks et al., 1996) and 3C 264 (Meyer et al., 2015). As with the previous scenario, internal shocks would produce synchrotron emission in the X-ray band and thus we can rule out this interpretation.

(iii) Multiple layers of ISM:
If instead we are looking at a more steady, continuous jet, with a persistent flow, then the additional knots could be explained by the jet punching through different layers of the ISM. The jet may be passing through shells of denser ISM, shocking the gas as it penetrates each layer. The resulting shocked gas would produce thermal X-ray emission. These over-densities in the ISM may simply be a result of random fluctuations in the ISM, or could be shells of material ejected by the massive progenitor either via stellar winds, or in giant eruptions, or during the SN explosion that produced the compact object. Nebulae around even the most powerful Luminous Blue Variable (LBV) stars are $\lesssim$ a few pc in size (Weis, 2011), an order of magnitude smaller than the size of the jet in S 10. However, the presence of numerous OB stars and likely SNRs in the nearby H II region H 10 leaves open the possibility that stellar activity created supershells and filaments in the ISM on scales of $\sim$100 pc.

(iv) Multiple outbursts:
The accretion rate and/or the kinetic power carried by the jet may not be steady; the system may undergo state transitions. This could also be the reason for the current low X-ray luminosity of the core (further discussed in Section 7.3.5). If this is the case, then we do not expect a continuous jet, but rather phases of enhanced activity. Recurrent outbursts may be creating pairs of hotspots in a Sedov-Taylor phase that keep expanding and cooling as they propagate out from the central object. In between outbursts, the channel drilled by the jet during the previous phase of activity would be refilled by the ISM. The innermost X-ray

hotspots, that is the two marginally resolved sources that form *Chandra* knot 2, would be those created during the most recent epoch of jet activity. The uneven number of knots may be due to an over density to the east of S 10 resulting in a pile-up of multiple knots. In AGN, a similar scenario of intermittent activity has been proposed to explain the so called "double-double radio galaxies", characterised by multiple pairs of hot spots (often aligned along the same direction) sharing the same core (Brocksopp et al., 2011; Saikia and Jamrozy, 2009; Kaiser et al., 2000; Schoenmakers et al., 2000). In this scenario, NGC 300 S 10 would be the first unambiguous example of a double-double microquasar.

The fading and/or appearance of new knots would undoubtedly result in X-ray variability. Two or three major episodes of enhanced activity over a timescale of a few 10^5 yr correspond to a recurrence timescale too long to be explained by thermal-viscous accretion disk instabilities, for a stellar-mass compact object. It is instead consistent, for example, with the timescale of thermal pulsations in an AGB donor star (e.g., Marigo et al., 2013), or of giant eruptions in LBV stars and other types of SN impostors (e.g., Tartaglia et al., 2015; Berger et al., 2009; Smith and Owocki, 2006). In particular, if the massive star is in a binary system with a neutron star or a black hole, giant eruptions are expected to produce phases of highly super-Eddington mass transfer onto the compact object, and may trigger powerful episodes of jet activity. This scenario was used to explain the behaviour of a transient neutron star ULX (coincidentally also located in NGC 300) associated with the SN impostor 2010da (e.g., Carpano et al., 2018; Binder et al., 2016; Villar et al., 2016). One of the hallmarks of such a scenario is that the erupting donor star would be surrounded by thick circumstellar dust, and would appear highly reddened (e.g., Lau et al., 2016; Berger et al., 2009). We mentioned earlier (Section 7.2.3.2) that one of the candidate optical counterparts, star D, is indeed highly reddened. We leave a detailed investigation of this possibility to further work.

(v) Sheath-spine jet:
A stratified jet has previously been used to explain the emission from gamma-ray bursts (GRBs) (Mészáros and Rees, 2001; Ramirez-Ruiz et al., 2002; Vlahakis et al., 2003). Known as a 'spine-sheath' jet model, a fast moving core (spine) is surrounded by a slower moving outflow (sheath) (see Figure 1 in Ito et al., 2013). This is thought to result from the GRB jet punching through the progenitor envelope, entraining the material to create the sheath (Mészáros and Rees, 2001; Ramirez-Ruiz et al., 2002), or from a decoupled neutron sheath and proton jet core (Vlahakis et al., 2003). For S 10, we do not expect direct emission from the jet, but instead suggest that a similar stratified jet may be causing multiple

hotspots via external shocks. As the jet propagates out, the slower moving outer layer (or layers) shock the ISM, creating the inner knots, while the faster moving core punches through, decelerating further downstream, creating the outer knots.

We cannot discriminate between interpretations iii–v based on our current observations. Differentiating between a persistent or transient jet is important because it will help us identify the power of S 10. In the following section we attempt to estimate the time averaged jet power. However, if the jet does switch on and off, then our jet power will be a lower limit; because we do not know the duty cycle of S 10, we cannot determine the instantaneous power of the jet.

7.3.3 Jet power

While S 10 has a unique morphology among Galactic and extragalactic stellar-mass objects, we relate it most closely to super-Eddington microquasars and ULXs such as SS 433, S 26 and Ho II X-1. These sources all demonstrate the presence of powerful jets either through radio/X-ray knots, shocked emission from jet/ISM interactions and/or extended radio nebulae. S 10 has a 5.5 GHz radio luminosity $L_{5.5\,\mathrm{GHz}} \approx 1 \times 10^{34}\,\mathrm{erg\ s^{-1}}$, which is a factor of two greater than the radio luminosity seen in the SS 433/W 50 complex (Downes et al., 1986; Dubner et al., 1998). On the other hand, it is an order of magnitude less radio luminous than the microquasars NGC 7793 S 26 (Soria et al., 2010) and M 83 MQ1 (Soria et al., 2014). The physical size of the radio nebula of S 10 ($\approx 170 \times 55\,\mathrm{pc}$) is also comparable to the bubbles of S 26 ($\sim 300 \times 150\,\mathrm{pc}$; Soria et al. 2010), Ho II X-1 ($\sim 81 \times 40\,\mathrm{pc}$; Cseh et al. 2012) and SS 433 ($\sim 100 \times 50\,\mathrm{pc}$; Dubner et al. 1998). Thus, in this section, we primarily compare S 10 to these super-Eddington sources and their jet-inflated radio nebulae.

Assuming equipartion between the magnetic field and energy in relativistic particles, we can determine the minimum energy conditions for synchrotron radiation. The minimum energy W_{min} can be expressed as

$$W_{\mathrm{min}} \approx 3.0 \times 10^{13} \eta^{4/7} V^{3/7} \nu^{2/7} L_{\nu}^{4/7}\,\mathrm{erg}, \tag{7.1}$$

(Longair, 2011) where $\eta - 1$ is the ratio of energy in baryons to that in relativistic electrons, V is the bubble volume in $\mathrm{m^3}$, ν is the observing frequency in Hz and L_{ν} is the luminosity density in $\mathrm{W\,Hz^{-1}}$. The elongated structure of S 10 has dimensions of $\approx 170 \times 55\,\mathrm{pc}$. If we assume a cylindrical shape, this equates to a total volume of $\approx 10^{55}\,\mathrm{m^3}$. Using this, and our 5.5 GHz luminosity density of $L_{\nu} = 2.2 \times 10^{17}\,\mathrm{W\,Hz^{-1}}$, we calculate a synchrotron minimum-energy condition $W_{\mathrm{min}} = 5.5 \times 10^{49} \eta^{4/7}\,\mathrm{erg}$ corresponding to a minimum magnetic field strength of $B_{\mathrm{min}} =$

7 μG. This is comparable to the minimum energies required to power the extended radio nebulae in other super-Eddington microquasars, such as NGC 5408 X-1 ($\sim 10^{49}$ erg: Lang et al. 2007; or $\sim 10^{50}$ erg: Soria et al. 2006a, depending on different assumptions for the electron energy distribution), IC 342 X-1 ($\approx 9.2 \times 10^{50}$erg: Cseh et al. 2012), and Ho II X-1 ($\approx 2.6 \times 10^{49}$erg: Cseh et al. 2012).[15] However, we note that there are several unknowns associated with our analysis. Firstly, without the viewing angle, we can only estimate the volume of the radio bubble based on its shape projected on the sky. The filling factor of the magnetic field throughout the bubble is also unknown. Additionally, the uncertainty on the minimum and maximum energy of the electron population, and therefore on the spectral index above and below the ATCA observing bands, also contribute to the uncertainty of the minimum-energy estimate.

We can estimate the jet power using the method outlined by Pakull et al. (2010). For a shock-ionised gas bubble, we know from standard theory (Weaver et al., 1977) that the total radiative luminosity $L_{\rm rad}$ is $\approx$27/77 of the mechanical power that is inflating the bubble. The total radiative luminosity of the cooling plasma can be determined from the luminosity in suitable diagnostic lines; for example, the Hβ line emission (derived from Equations 2.2 and 2.4 of Dopita and Sutherland 1995, or from the shock-ionization code MAPPINGS V: Allen et al. 2008) is a good proxy for the total luminosity, because its relative contribution does not depend too strongly on the shock velocity, or the metallicity of the shocked gas, or the density of the undisturbed ISM. For a plausible range of shock velocities $\approx$150–300 km s^{-1}, the total Hβ luminosity of shocked gas plus precursor is $\approx$(2–3)$\times 10^{-3}$ times the input mechanical power. For an Hβ luminosity $L_{H\beta} \approx (6 \pm 1) \times 10^{36}$ erg s^{-1}, this corresponds to a long-term-average jet power $P_{\rm kin} \approx$ (2–3) $\times 10^{39}$ erg s^{-1}, an order of magnitude lower than the values estimated for S 26 but the same order of magnitude as the jet power suggested for SS 433 (Brinkmann and Kawai, 2000; Marshall et al., 2002a; Krivosheyev et al., 2009) and for M 51 ULX-1 (Chapter 6). In a follow-up paper currently in preparation, we will refine and improve this estimate of jet power based on diagnostic line emission, using recently obtained data from the Multi Unit Spectroscopic Explorer (MUSE), an integral field spectrograph mounted on the VLT.

Other techniques have sometimes been used to estimate the kinetic power in radio/optical microquasar bubbles (Pakull et al., 2010). If the shock velocity is known (inferred from optical spectroscopic studies of the emission line profiles), together with the ISM density and the bubble size, one can derive the characteristic dynamical age of the shocked bubble as well as the jet power (Weaver et al., 1977). A spectroscopic study of the optical emission lines in S 10 is also left to our

[15] Assumes $\eta = 1$.

follow-up paper based on MUSE data. A much less reliable technique is based on the radio luminosity. Various scalings between the jet power and the optically thin synchrotron luminosity of hot spots, lobes and cavities have been proposed, for samples of radio galaxies (e.g., Willott et al., 1999; Cavagnolo et al., 2010; Godfrey and Shabala, 2013). The model assumptions underpinning these scaling relations are similar to those associated with the minimum energy synchrotron conditions discussed earlier, leading to a similar degree of uncertainty. However, Godfrey and Shabala (2016) have shown that the scaling relations commonly used in the literature are strongly biased by the mutual dependence on distance for both the jet power and the radio luminosity. Thus, we do not rely on those correlations for our study.

7.3.4 Synchrotron or thermal plasma emission?

From the synchrotron minimum energy conditions, we can estimate the cooling timescale for X-ray synchrotron emission. At an energy of 1 keV, the cooling timescale would be $3,000 \left(\frac{B_{\rm min}}{7\,\mu{\rm G}}\right)^{-3/2}$ yr (Tudose et al., 2006). This approximation is valid if the system is in equipartition; a stronger magnetic field will reduce the cooling timescale. Adiabatic expansion of the knots would also lead to faster cooling.

Based on the 5.5 GHz luminosity and average spectral index ($\alpha = -0.64$) for the radio bubble, the expected $0.3 - 8.0$ keV X-ray synchrotron luminosity is $\approx 3 \times 10^{37}$ erg s^{-1}. We have already tested (Section 7.2.1.1) that a power-law component with a photon index $\Gamma = 1.7$ does not provide a statistically significant contribution to the combined knot spectrum, and the 90% upper limit to its luminosity is $< 2 \times 10^{36}$ erg s^{-1}. For completeness, given the spectral index found in the radio analysis (Section 7.2.2) and that we now suspect the micro-quasar candidate core resides within X-ray knot 2 (Section 7.2.1.2), we perform the test with an X-ray power-law component of photon index $\Gamma = 1.64$ on the individual spectrum of knot 2. As expected, the result is essentially identical to the case for the combined spectra and for $\Gamma = 1.7$, that is there is no statistically significant need for such a component, and the 90% upper limit to its contribution is $< 8 \times 10^{35}$ erg s^{-1}. This is lower than the luminosity expected from the extrapolation of the radio synchrotron power law. The reason why we do not see synchrotron X-ray emission may be that particles were never accelerated up to energies where they could emit X-rays via this process; or there may be a break in the spectrum between radio and X-ray frequencies because of ageing. We also note that the radio and X-ray observations were not simultaneous. Alternatively, the S 10 core may be producing X-ray synchrotron emission that is strongly ab-

sorbed to the point where it is not detected. While the thermal X-ray emission does not show any evidence of strong absorption, it is likely a result of extended jet/ISM interactions, whereas the X-ray synchrotron emission must emanate from a region much closer to the compact object and could be obscured by an additional strong source of absorption; $n_{\rm H} > 4 \times 10^{23}$ atoms cm^{-2}. This scenario seems somewhat contrived and thus we prefer the simpler interpretation wherein the synchrotron power-law has a break below the soft X-ray band, in line with other microquasars (Russell et al., 2013), and both the radio synchrotron and the X-ray thermal emission come from similar regions of jet/ISM interactions.

While we do not detect any X-ray synchrotron emission, we do see thermal X-ray emission (Bremsstrahlung and line transitions), likely from shock-heated gas along and in front of the jet. The cooling timescale is approximately the ratio of total heat content over heat loss rate

$$t_{\rm cool} = \frac{3(n_{\rm e} + n)k_{\rm B}T}{2n^2\Lambda}, \tag{7.2}$$

(Dopita and Sutherland, 2003) where n is the atomic density of the hot gas, $k_{\rm B}$ is the Boltzmann constant, T is the plasma temperature and Λ is the cooling function. From our X-ray spectral fits, we know that $T \approx 0.6\,{\rm keV} \approx 7 \times 10^6\,{\rm K}$. At that temperature, $\Lambda \approx 4 \times 10^{-23}$ erg cm^3 s^{-1} for solar-metallicity plasma in collisional equilibrium, including both free-free and line emission (Sutherland and Dopita, 1993). From the thermal X-ray luminosity and the approximate volume estimated for the emitting gas, we also determined a lower limit on the density, $n \approx n_e \gtrsim 4\,{\rm cm}^{-3}$ (Section 7.2.1.1). Putting those constraints together, we obtain an upper limit on the (thermal) cooling timescale of $t_{\rm cool} \lesssim 570,000\,{\rm yr}$. We speculate that X-ray-emitting gas is replenished by bursts of increased accretion/ejection activity leading to the production of new discrete knots on a recurrence timescale shorter than the cooling timescale.

7.3.5 Faintness of the X-ray core

Three possibly super-Eddington microquasars have been found so far with large-scale X-ray evidence of collimated jets: NGC 300 S 10, NGC 7793 S 26 and SS 433 in the Milky Way. Curiously, all three have apparently faint cores: $L_{\rm X,core} \lesssim 10^{36}$ erg s^{-1} (Section 7.2.1.2), $L_{\rm X,core} \approx 6 \times 10^{36}\,{\rm erg\ s}^{-1}$ (Soria et al., 2010) and $\sim 10^{36}\,{\rm erg\ s}^{-1}$ (Kotani et al., 1996; Fabrika and Medvedev, 2011) for the three sources, respectively. In the case of SS 433, the reason is the occultation of the direct X-ray emission by the thick super-critical disk, seen at high inclination (Fabrika, 2004). For S 26 and S 10, we do not have any estimate of the viewing angle. No firm conclusions can be reached based on such a small sample of

objects. It is possible that there is a selection bias at play: large-scale jets appear longer and easier to discover when they are in the plane of the sky; as a result, the accretion disk around the compact object would preferentially appear edge-on. The situation would be analogous to that of "accretion disk corona" sources, a type of Galactic low-mass X-ray binary seen at high inclination, in which the direct X-ray emission from the disk surface is mostly occulted from us, and we can only see harder radiation scattered by a vertically extended corona (e.g., White and Holt, 1982; McClintock et al., 1982; Hellier and Mason, 1989). Alternatively, the compact object may be faint because its super-critical accretion phase has a short duration compared with the cooling timescale of the hot spots and bubble, or it is a transient source with a low duty cycle. Contrary to this scenario, it was noted (Pakull and Grisé, 2008) that the majority of large shock-ionised ULX bubbles (without direct evidence of a collimated jet) do contain a luminous X-ray core; if the typical duty cycle of super-Eddington accretors was low, or if the duration of the super-Eddington phase was much shorter than the cooling timescale of the ULX bubbles, we would see a large number of bubbles without a central source, which is not the case [16].

We can take the low-duty-cycle argument to an extreme, and suggest that all the kinetic power in the collimated jet was injected at an instantaneous burst event, for example a SN associated with a GRB. After that event, the collimated ejecta would continue to expand passively, now dominated by entrained material from the ISM. This scenario leads us back to the original interpretation of S 10 as an SNR. Magneto-hydrodynamical simulations of jet/ISM interactions in GRBs suggest that the jet loses collimation at a distance of $\sim$1 pc from the origin (De Colle et al., 2012). This makes it difficult to explain the much larger length of the S 10 structure. To test this scenario further, we searched for evidence of current accretion activity at the (candidate) location of the central object, as explained in the next section.

7.3.6 Search for X-ray and radio variability

Spurred by the possibility that the central engine of S 10 is a transient or variable accretor, currently in a low state, we searched for hints of previous variability in the core emission. S 10 has been observed on several occasions with the *ROSAT* and the *XMM Newton* X-ray telescopes: in both cases, the source was not resolved, because of their poorer spatial resolution (see, e.g., Figures 8e and 8f in Payne et al. 2004). For the *ROSAT* observations, we used the count rates listed in the Second Position-Sensitive Proportional Counter (PSPC) Catalog (Rosat,

[16] A similar argument also rules out beaming factors larger than a few for the X-ray emission of ULXs (Pakull and Grisé, 2008).

Table 7.8: Integrated radio flux of the core region at various epochs.

Telescope	Year	Frequency (GHz)	Flux density (mJy)	νL_ν (10^{33} erg s^{-1})
ATCA	2000-02-28	1.374	0.56 ± 0.03	3.3
ATCA	2000-02-28	2.496	0.38 ± 0.06	4.0
ATCA*	2015/16	5.5	0.429 ± 0.030	10.0
ATCA*	2015/16	9.0	0.352 ± 0.029	13.4

* ATCA observations from this study (October 2015 and August 2016) are stacked as per Section 7.1.2.

2000) and in the Source Catalog of Pointed Observations with the HRI (ROSAT Scientific Team, 2000). For the *XMM-Newton* observations, we used the observed fluxes from the 3XMM-Data Release 6 Catalog (Rosen, 2016). We then used the online tool PIMMS[17] version 4.8e to convert the count rates or fluxes of the various observations to unabsorbed 0.3–8 keV fluxes and then to luminosities, assuming a 0.6 keV thermal plasma model and a column density of $n_{\rm H} = 3 \times 10^{20}$ cm^3, as per our spectral modelling (Section 7.2.1, Table 7.5).

For the *ROSAT*/PSPC observations between 1991 November and 1992 January, we estimate a luminosity $L_{0.3-8\,\rm keV} = (1.3 \pm 0.3) \times 10^{37}$ erg s^{-1}; for the PSPC observations between 1992 May–June, $L_{0.3-8\,\rm keV} = (1.1 \pm 0.2) \times 10^{37}$ erg s^{-1}. For the *ROSAT*/HRI observation in 1995 May, we obtain a luminosity $L_{0.3-8\,\rm keV} = (1.5 \pm 0.4) \times 10^{37}$ erg s^{-1}. Finally, *XMM-Newton* observed NGC 300 between 2000 December and 2001 January; the absorbed 0.2–12 keV flux of $(3.44 \pm 0.13) \times 10^{-14}$ erg cm^{-2} s^{-1} converts to an emitted 0.3–8 keV luminosity $L_{0.3-8\,\rm keV} = (1.6 \pm 0.2) \times 10^{37}$ erg s^{-1}. Considering the model uncertainties and the differences between the PSFs and energy bands of the various detectors, we cannot claim any significant X-ray variability compared with our modelled *Chandra* luminosity $L_{0.3-8\,\rm keV} = (1.1 \pm 0.1) \times 10^{37}$ erg s^{-1} (average of the 2010 and 2014 observations). Any possible variability of the core was swamped by the higher and constant thermal emission from the various knots.

We then checked whether S 10 has varied in radio brightness over the last decades. NGC 300 was observed with the VLA at 4.885 GHz in May 1993 and at 1.465 GHz in June 1998 (Pannuti et al., 2000). It was also observed with the ATCA in February 2000 at 1.374 GHz and 2.496 GHz (Payne et al., 2004). We compared these data with our recent 2016–2017 ATCA observations. One major difficulty in this comparison is that the archival data have larger beam sizes: $6'' \times 6''$ for the old ATCA observations, $4''.70 \times 3''.76$ for the 1.465 GHz VLA observations, and $8''.63 \times 4''.22$ for the 4.885 GHz VLA observations (Table 2 in Payne

[17] http://cxc.harvard.edu/toolkit/pimms.jsp

et al. 2004). This makes it difficult to distinguish between the radio flux from the S 10 jet and that from the neighbouring H 10 HII region. The second major problem is that the archival observations were much less sensitive. The rms noise level was $\sigma \approx 37\mu$Jy beam^{-1} and $\sigma \approx 66\mu$Jy beam^{-1} for the VLA data at 4.885 GHz and at 1.465 GHz, respectively; for the archival ATCA data it was $\sigma \approx 58\mu$Jy beam^{-1} and $\sigma \approx 62\mu$Jy beam^{-1} at 1.374 GHz and 2.496 GHz, respectively. As a comparison, the rms noise was $\sigma \approx 2.7\mu$Jy beam^{-1} in the 2015–2017 ATCA data (Section 7.1.2). As a result, the emission from the core region (around the X-ray knot 2) is the only part of the radio jet that is significantly detected in the archival data (see for example Figure 8d of Payne et al. 2004). Keeping in mind all these caveats, and extrapolating the 2015–2016 flux measurements to lower frequencies using a spectral index $\alpha = -0.40 \pm 0.22$ for the core region, we find that the new ATCA flux measurements are consistent with the 2000 ATCA flux values within $\approx 2\sigma$. Instead, when compared with the VLA flux densities measured by Pannuti et al. (2000) and Payne et al. (2004), S 10 appears to have brightened by a factor of 2 in the ATCA observations; however, our re-analysis of the VLA data shows that the true uncertainties in the S 10 core flux are much larger than the formal error reported by Pannuti et al. (2000) and Payne et al. (2004), because of the mismatch in beam size and sensitivity mentioned above. To combat this, and properly compare the S 10 core fluxes, we re-analysed both the 4.8 GHz VLA data and our 5.5 GHz ATCA data. These observations were chosen to minimise uncertainties introduced by the spectral shape of S 10. Additionally, we applied the same *uv*-cut to both data sets and used the same restoring beam. We find peak fluxes of $f_{4.8\,\mathrm{GHz}} = 340 \pm 60\,\mu$Jy beam^{-1}and $f_{5.5\,\mathrm{GHz}} = 210 \pm 8\,\mu$Jy beam^{-1}. We find tentative evidence ($\sim 2\sigma$) of a decrease in the flux of the radio core, though future observations are required to conclusively establish the presence of variability.

7.4 Conclusions

We have presented a new, coherent interpretation of a complex X-ray, optical and radio source in NGC 300, using new and archival *Chandra*, *HST*, VLT and ATCA data. The source was previously classified as an SNR; however, we argued that it is a candidate microquasar, likely powered by super-Eddington accretion onto a compact object. We showed that the X-ray emission is made of a string of discrete knots, a tell-tale sign of a jet interacting with the ambient medium. We also showed for the first time that the radio emission is an elongated bubble ($\approx$170 $\times$55 pc in size), oriented along the same direction as the string of X-ray knots. While the radio emission is consistent with optically-thin synchrotron (as

expected), the X-ray emission is from thermal plasma at temperatures ≈0.3–0.8 keV. This is unlike the knots and hot spots typically seen in AGN jets, but is analogous to the thermal hot spots previously identified in the super-Eddington microquasar NGC 7793 S 26. The integrated radio luminosity at 5.5 GHz is $\approx 10^{34}$ erg s^{-1}, while the total X-ray luminosity of the knots is $\approx 2 \times 10^{37}$ erg s^{-1}. To complete the picture, we argued that the optical line spectrum of the shock-ionised nebula is exactly what is expected for this kind of system, as seen also in S 26 and in other shock-ionised ULX bubbles. In particular, we showed a spatial association between locations of enhanced Hα emission and locations of X-ray and radio features.

Using the Hα line luminosity ($L_{H\alpha} \approx 1.7 \times 10^{37}$ erg s^{-1}) as a proxy, we estimated that the nebula was shocked by the injection of a long-term-average jet power $P_{\rm kin} \approx$ (2–3) $\times 10^{39}$ erg s^{-1}. Thus, this candidate microquasar is in the same energy class as SS 433 and Ho II X-1; it is an order of magnitude less energetic and a factor of 2 smaller in linear size than S 26.

We have discussed the most likely location of the core, but found no bright, point-like X-ray source there, above the thermal-plasma emission. The upper limit to the X-ray luminosity of the core is $\approx 10^{36}$ erg s^{-1}. The direct emission from the accreting compact object may be occulted from our view by a thick, edge-on disk, like in SS 433; or the core could be in a low state. Neither did we find evidence of a brighter core in earlier *XMM-Newton* and *ROSAT* observations, which stretch back to 1991. The reason for the multiple knot structure remains unclear. We can rule out internal shocks (analogous to the knots seen for example in the M 87 jet), because the X-ray emission is thermal (that is, from shocked ISM) rather than synchrotron. For the same reason, we consider very unlikely that the knots are ballistic ejections. We discussed alternative scenarios, in particular: multiple layers of enhanced ISM density; multiple outbursts or jet activity episodes; or a sheath-spine jet structure, with the faster spine propagating a longer distance than the slower sheath.

7.5 Summary

In this chapter, we presented the discovery of a new and intriguing candidate microquasar, NGC 300 S 10. We used a combination of *Chandra*, *HST*, VLT and ATCA observations to identify the true nature and energetics of the source. The key results are:

- We detect four discrete X-ray knot aligned in the plane of the sky, projected over a length of ≈150 pc. We suggest that all knots are due to shocks from

jet/ISM interactions, with the accreting compact object either currently in a dim state or occulted from our view.

- We also find a radio nebula $\approx 170\times$ 55 pc in size with its major axis aligned to the X-ray chain.
- The optical nebula is shock-ionised (based on its optical line ratios), which we conclude to also be a result of the jet.
- We estimate that the nebula was inflated by the injection of a long-term-average jet power $P_{\rm kin} \approx$ (2–3) $\times 10^{39}$ erg s^{-1}.

S 10 is a key object to understanding jets in the super-critical accretion regime. While the emission from the compact accreting source is well below the Eddington limit, super-critical accretion must be taking place (or took place previously) to power the mechanical output. We speculate on how S 10, and other powerful low-luminosity microquasars, relate to the broader class of ULXs in Chapter 8.

Chapter 8

Discussion and conclusions

Astronomers are moving towards a consensus that the majority of ULXs house super-critically accreting stellar-mass objects rather than mildly-accreting IMBHs. There is a wide range of observational properties associated with super-Eddington sources. In previous chapters, we considered a limited number of sources, each thought to be super-Eddington for different reasons. In this chapter we will investigate the links between these seemingly disparate sources in the hopes of unifying our understanding of ULXs as a single class.

We have explored a range of ULX observational characteristics from the spectral properties associated with the accretion flow to large scale structures associated with powerful outflows. Numerous spectral states have been associated with ULXs, all of which appear to be distinct from the spectral states of Galactic black hole X-ray binaries (Remillard and McClintock, 2006). Unlike Galactic black hole X-ray binaries, ULXs predominantly display ultraluminous two-component spectra; a soft thermal excess and a hard, non-thermal component with curvature at high energies. These two-component models are thought to be a result of super-Eddington accretion (Gladstone et al., 2009). The relative strengths of the two components drive the spectral classification among ULXs; 'hard ultraluminous' sources are dominated by the hard component while the soft component dominates in 'soft ultraluminous' sources (Sutton et al., 2013b). Single-component ULXs are observed, although they still appear distinct from sub-Eddington states. The 'broadened disk' state has a single, broad continuum fit, thought to be a result of a radiatively inefficient accretion flow consistent with the spectrum emitted by an advection-dominated slim disk. Finally, as discussed in Chapter 4, ULSs represent a subset of ULXs where almost no flux is emitted above 1 keV. Here, a soft blackbody component dominates, with a very minor power-law component observed in some sources. Recent studies indicate that these spectral classes are not static and that some ULXs have been observed changing class (Pinto et al., 2017a; Pintore et al., 2017). What drives these state transitions, and in fact, the

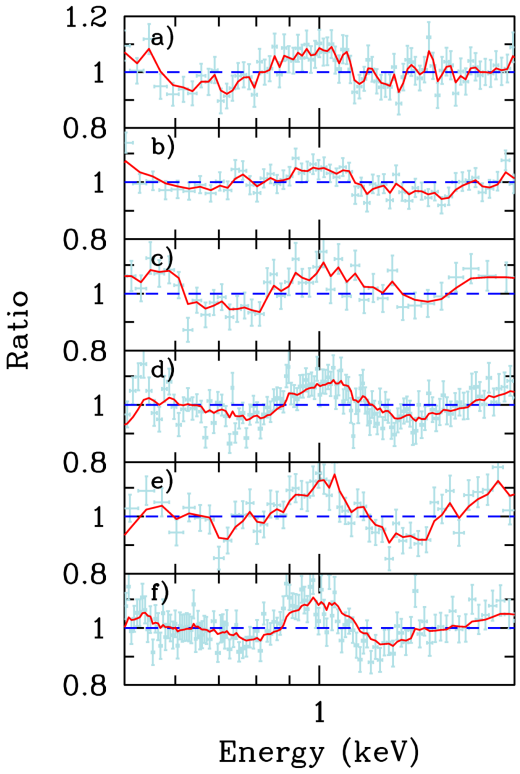

Figure 8.1: Plot of the data/model ratio for energies between 0.5−2 keV of several ULXs. The low-energy residuals are thought to be the result of a radiatively-driven wind. Image from Middleton et al. (2015b).

states themselves, is unclear at this point.

In addition to spectral changes, ULXs are also known to exhibit different outflow properties. Jets and winds have distinct observational signatures. On small scales, Middleton et al. (2014, 2015b) find soft energy spectral residuals which have been associated with broadened atomic emission and absorption features (Figure 8.1). The most likely explanation for these signatures is the presence of a powerful radiatively-driven wind, as expected from super-Eddington accretion. Follow-up studies by Pinto et al. (2016) were able to resolve more complex blueshifted ($\sim 0.2c$) absorption lines from highly ionised gas in an ultrafast wind. On larger scales, we witness ionised ULX bubbles. As discussed in Chapter 6, these optical nebulae can either be primarily shock-ionised (e.g. M 51 ULX-1) or photo-ionised (e.g., Ho II X-1; Pakull and Mirioni 2002). Additionally, both M 51 ULX-1 and Ho II X-1 also have associated extended radio emission. Finally, observational evidence of a collimated jet has been found in some ULXs, including M 51 ULX-1 (Chapter 6), NGC 300 S 10 (Chapter 7), M 81 ULS (Liu et al., 2015), Ho II X-1 (Cseh et al., 2014) and NGC 7793 S 26 (Pakull et al., 2010; Soria et al., 2010). As with the spectral classes, the physical characteristics that dictate the presence/absence of winds and jets in ULXs are currently unknown.

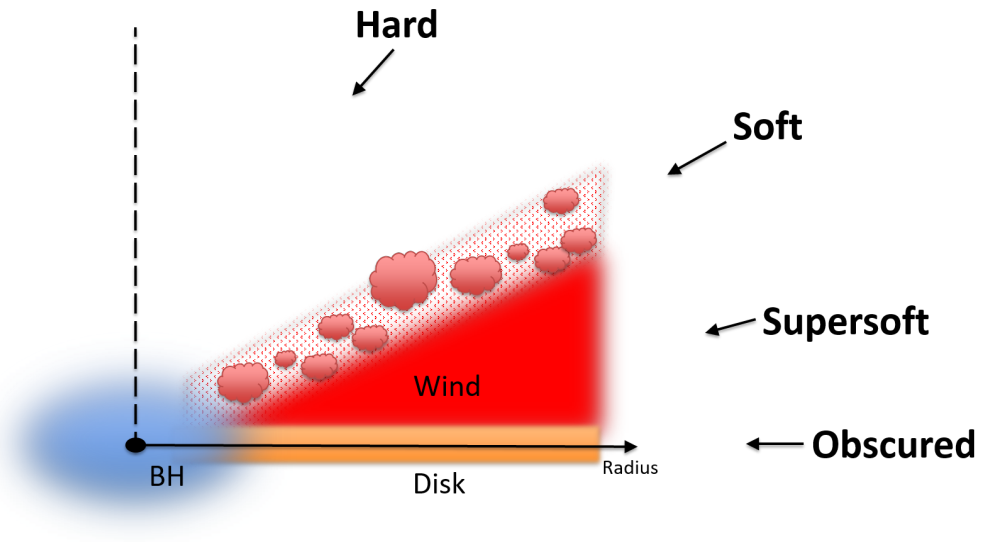

Figure 8.2: Cartoon of the current paradigm for ULX spectral classes. The optically thick wind (red) obscures and thermalises all photons emitted by the inner hot region (blue) when the ULX is observed at high inclination angles. Thus all hard sources are assumed to be seen close to face on, down the polar funnel, while softer sources are seen at intermediate-to-high inclination angles, where the wind blocks the hard emission.

8.1 Unification of ULX physical properties

A similar situation, in which a population of sources has a range of distinct observational properties, can be seen for AGN. The most popular theory to explain the different observable properties in AGN is the unification model, which is based on inclination angle (Urry and Padovani, 1995). This chapter explores the possibility that a similar unifying model could be applied to ULXs

The current ULX paradigm suggests that inclination dictates ULX spectral classes, as opposed to state transitions, as observed in Galactic X-ray binaries. The model is idealised in Figure 8.2. Magneto-hydrodynamic simulations of super-Eddington binaries (e.g., Narayan et al., 2017; Kitaki et al., 2017; Sądowski and Narayan, 2015; Jiang et al., 2014; Ohsuga and Mineshige, 2011; Ohsuga et al., 2005) find that strong optically-thick winds are generated by the disk, launched from radii $\sim \dot{m}R_{\rm in}$, leaving a lower-density polar funnel along the axis of rotation that may contain a fast jet. At low inclination angles (face-on), there is a direct line of sight to the hot central regions nearest to the compact object, resulting in harder observed spectra. At intermediate viewing angles, photons are down-scattered by the wind which results in the softer X-ray spectra dominated by a Comptonisation component. At high inclination angles, photons are completely thermalised by the wind and only the blackbody of the photosphere is detected, producing the ultrasoft spectra. Additionally, one could also explain the

ultra-powerful, low-luminosity sources like NGC 7793 S 26, SS 433 and NGC 300 S 10 through this classification; the thick accretion disks synonymous with the super-Eddington regime may completely occult direct X-ray emission from the innermost regions, for a larger range of viewing angles than in sub-Eddington sources, where the disk remains geometrically thin. Evidence for this can be seen in the enhanced variability observed in softer ULXs, introduced by the chaotic outflowing material of the wind (Middleton et al., 2011b).

8.1.1 The problem with inclination angle

While this inclination angle-dependent model seems to work well in describing ULX spectral properties, more and more shortcomings are being discovered. As discussed in Chapter 5, the distinction between the spectral properties in the two eclipsing ULXs in M 51 suggests that inclination cannot be the sole factor in determining spectral class. Neither source is a ULS, though both sources must be viewed at high inclination, because of the long eclipses. Clearly there are effects other than (or in addition to) inclination angle that determine the spectral properties of M 51 ULX-1 and ULX-2 and, by extension, the ULX population.

Another problem can be seen when observing sources that show spectral transitions. Pintore et al. (2017) studied a sample of bright ULXs and compared the two most different spectral classes for each source when fit with a simple continuum model (Figure 8.3). Some sources (e.g., NGC 1313 X-2 and NGC 5907 X-1) show a clear increase in luminosity as they transition into their harder spectral class. This is generally explained by the fact that harder sources are thought to be viewed at low inclination angles, where the line of sight looks down the polar funnel. The photons are preferentially able to escape through the polar funnel (King et al., 2001), increasing the luminosity. However, there are also sources that show the opposite; the softer spectra have higher luminosities. This can be seen in, for example, NGC 1313 X-1 and Ho IX X-1 (Figure 8.3) where the soft disk blackbody dominates or the power-law cut-off occurs at lower energies when the source is brighter. The same effect can be witnessed in the two ULXs in IC 342 (Kubota et al., 2001). This contradicts the idea that harder, low-inclination angle sources, where emission is able to escape without being downscattered by the dense wind, are brighter. Additionally, Sutton et al. (2013b) found no systematic trend in luminosity for the hardest sources. It is becoming clear that there must be more intrinsic effects that cannot be explained solely by inclination angle.

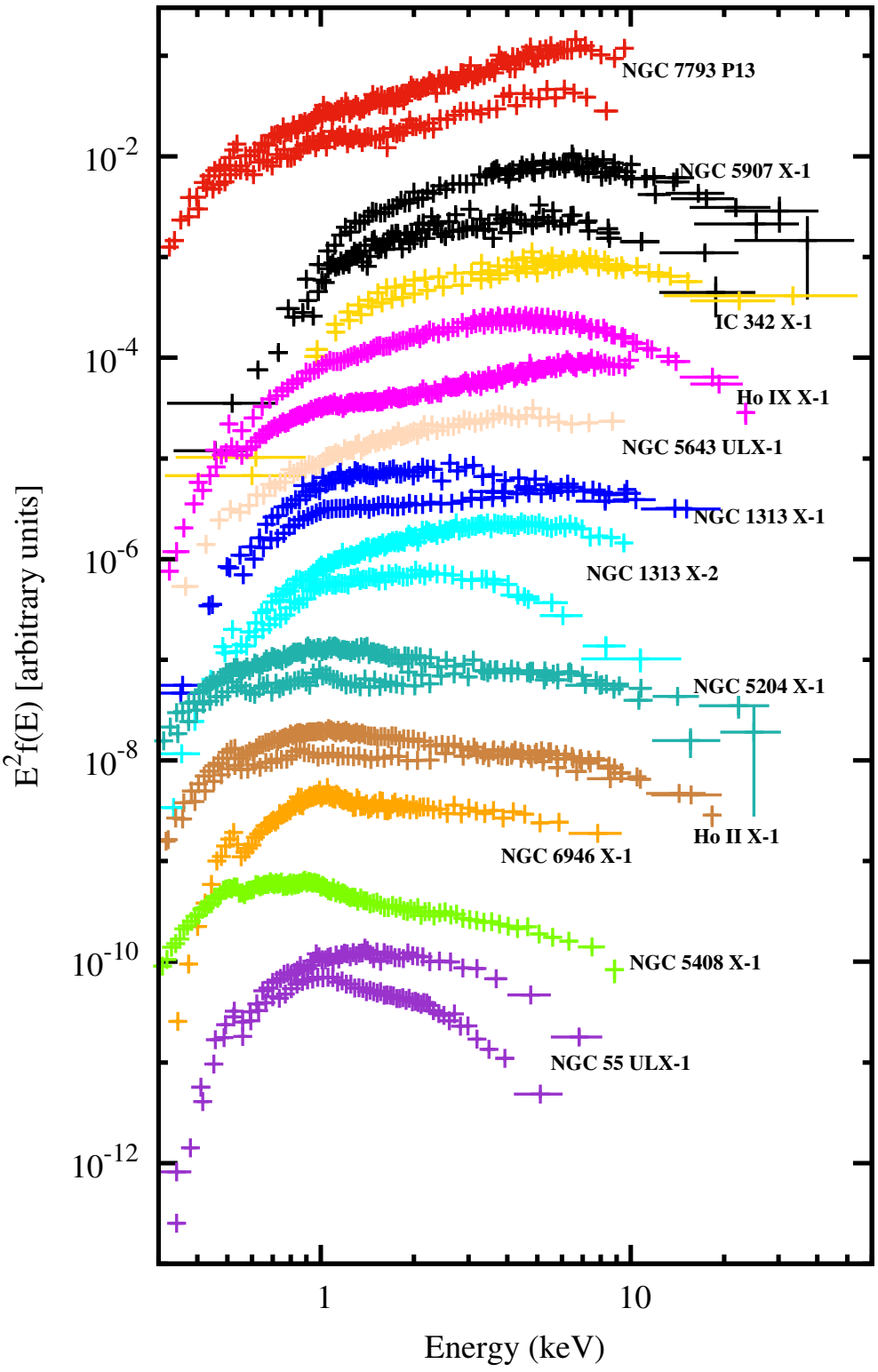

Figure 8.3: Sample of ULXs showing contrasting spectral classes for each individual source. Spectra are offset in the y-axis for display purposes. Image from Pintore et al. (2017).

8.1.2 Type of accretor

Perhaps one of the most important factors in determining spectral appearance is the type of compact object present; whether it is a black hole or neutron star. If it is a neutron star, then, additionally, whether it is highly magnetised or not will also be important. It is also unclear the effect the presence or absence of a surface and/or a strong magnetic field has on the observational properties of ULXs. For a highly-magnetised neutron star, the magnetic field interrupts the disk and then channels material along the field lines and onto the neutron star surface in a narrow 'accretion column' (Pringle and Rees, 1972). The inner disk is truncated at the magnetospheric radius $R_{\rm m}$, the point at which the magnetic pressure and the disk gas plus ram pressure of the inflow are balanced, where $R_{\rm m} \propto B^{4/7}\dot{m}^{-2/7}R_{\rm NS}^{5/7}M_{\rm NS}^{-3/7}$ (Takahashi and Ohsuga, 2017). If the magnetic field is sufficiently strong (typically $\gtrsim 10^{13}$ G), then the magnetospheric radius can extend beyond the radius at which outflows are launched, potentially preventing the thick disk winds and polar funnel from forming, allowing for an unobscured view of the inner part of the accretion flow (Mushtukov et al., 2015; Kawashima et al., 2016; Chashkina et al., 2017). This would result in a harder observed spectrum. The two-component spectra (soft excess plus hard power-law tail; Stobbart et al. 2006; Gladstone et al. 2009; Sutton et al. 2013b) seen in ULXs could be explained either by soft winds and a hot inner disk (Poutanen et al., 2007) in black hole ULXs or a hard accretion column and soft truncated disk (Shakura and Sunyaev, 1973) in neutron star ULXs (Koliopanos et al., 2017).

8.1.3 Mass accretion rate

Chapter 4 outlined a model in which inclination angle and accretion rate combine to dictate whether or not a source appears as a ULS. The optical depth of the disk wind increases with accretion rate, while at the same time the opening angle of the polar funnel will decrease. While this idea was restricted to ULSs in Chapter 4, it can be extended to all ULXs. For example, changes in $\dot{m}$ may help to explain the spectral differences observed in our two eclipsing ULXs. Sources at Eddington ($\dot{m} \sim 1$) will likely not have strong, optically-thick winds and thus hard photons from the inner disk will not be downscattered, regardless of viewing angle. This could explain both the absence of any significant thermal plasma emission in M 51 ULX-2 and its hard spectrum, even though the source is viewed close to edge on. This suggests ULX-2 could be accreting at close to Eddington, while ULX-1 is likely accreting at $1 \leq \dot{m} \lesssim 100$ (i.e., below the ULS accretion threshold but significantly higher than ULX-2). Both sources having the same luminosities ($L_X \approx 2 \times 10^{39}$ erg s^{-1}) indicates that ULX-2 may house a more massive compact

object, and thus has a lower relative accretion rate. Alternatively, it may be powered by a neutron star whose strong magnetic field is preventing the winds from being launched (Section 8.1.2).

8.1.4 Outflows and the large-scale structures of ULXs

So far, this chapter has explored how the physical characteristics of ULXs impact their spectral properties. However, there is one observable property yet to be touched on; the large-scale structures produced by jets and winds. These structures include ULX bubbles, hotspots and lobes.

There are many unanswered questions surrounding the mechanical output of ULXs. For example, it is still not known what leads to the production of collimated relativistic jets (though this is not a question exclusive to jets in ULXs). Jets from Galactic microquasars tend to be less powerful ($P_{\rm jet} \sim 10^{37}$ erg s^{-1}) than those from their ULX counterparts ($P_{\rm jet} > 10^{39}$ erg s^{-1}). While neutron stars in Galactic XRBs generally produce less powerful jet than black holes (Livio, 1999), a similar scenario may or may not be applicable for jets from super-Eddington neutron stars and black holes. Finally, it is still not clear if super-Eddington sources can simultaneously produce strong radiatively-driven winds and collimated relativistic jets. If the presence of winds quenches jet formation, then this would give insight into the geometry of the polar funnel and accretion flow.

While these questions remain unanswered, we are building up a sizeable sample of ULXs with jets, including the two jetted sources analysed in Chapters 6 and 7, with the hopes of tackling some of these problems. Importantly, direct observations of compact jets in ULXs are not possible, and thus we typically rely on the interactions with their environments, which manifest as ULX bubbles, to probe the characteristics of the outflow. We have compiled a comprehensive sample of bubbles around super-Eddington sources (Table 8.1), and attempt to use the contrasting observable properties to speculate on the nature of the outflows.

As in Table 8.1, the ULX bubble population can be divided into subclasses:

i) shock-ionised optical bubbles with radio emission;

ii) shock-ionised optical bubbles without radio emission;

iii) photo-ionised optical bubbles with radio emission; and

iv) photo-ionised optical bubbles without radio emission.

It is only predicted that the fourth subclass, photo-ionised bubbles with no radio emission present, exists as no examples of such bubbles are currently known. Importantly, ULX bubbles, predominately ionised by X-ray photons, are expected

Table 8.1: Comparison of ULX bubbles. Radio luminosities are calculated using flux densities at 5 GHz. X-ray luminosity is for $0.3 - 8.0$ keV. The table is divided into three sections by the dashed lines. The top section includes shock-ionised, radio-loud bubbles, the middle section includes shock-ionised, radio-quiet bubbles and the final section includes photo-ionised, radio-loud bubbles. There are currently no known photo-ionised, radio-quiet bubbles.

Name	$L_{\rm R}$	$L_{\rm X}$	$P_{\rm jet}$
	erg s^{-1}	erg s^{-1}	erg s^{-1}
M 51 ULX-1[a]	2.3×10^{34}	$(2 - 4) \times 10^{39}$	1.0×10^{39}
NGC 300 S 10[b]	1.2×10^{34}	$< 10^{36}$	3.0×10^{39}
S 26[c]	2.0×10^{35}	6×10^{36}	$\sim 10^{40}$
M 83 MQS1[d]	1.8×10^{35}	1.5×10^{38}	$\sim 10^{40}$
IC 342 X-1[e]	1.8×10^{35}	1.6×10^{40}	3.4×10^{39}
SS 433[f]	5.1×10^{33}	3×10^{35}	3.2×10^{38}
Ho IX X-1[g]	$\sim 3 \times 10^{34*}$	$(1 - 3) \times 10^{40}$	
NGC 1313 X-2[h]	$< 3.7 \times 10^{33}$	$(0.3 - 1.5) \times 10^{40}$	
NGC 5585 X-1[i]	2.0×10^{35}	3×10^{39}	
Ho II X-1[j]	4.6×10^{34}	$(0.5 - 2) \times 10^{40}$	
NGC 5408 X-1[k]	3.5×10^{34}	$(0.8 - 2) \times 10^{40}$	
NGC 6946 X-1[l]	1.2×10^{35}	$(0.3 - 1) \times 10^{40}$	

[a] Chapter 6
[b] Chapter 7
[c] Soria et al. (2010)
[d] Russell et al. (in prep); Soria et al. (2014)
[e] Rana et al. (2015); Marlowe et al. (2014); Yoshida et al. (2013); Cseh et al. (2012); Feng and Kaaret (2009)
[f] Downes et al. (1986); Marshall et al. (2002a)
[g] Krause et al. (1989); Wang et al. (2004); Walton et al. (2017)
[h] (R. Soria, priv. comm.); Wang et al. (2004); Mucciarelli et al. (2007)
[i] Soria et al. (in prep)
[j] Miller et al. (2005); Grisé et al. (2010)
[k] Walton et al. (2015); Feng and Kaaret (2009)
[l] van Dyk et al. (1994)
* Scaled to a 5 GHz flux density from 1.4 GHz. Assumed $\alpha = -0.7$.

to be observationally different from photo-ionised nebulae around massive stars, predominately ionised by UV photons (see e.g., M 51 ULX-2; Chapter 6). For now, this chapter focuses on the other three classifications and Table 8.1 is divided into these respective classes (horizontal dashed lines). It should be noted that even bubbles that are dominated by shock-ionised gas often also include a contribution from photo-ionisation, either from the photons directly emitted by the central source, or from the UV photons emitted behind the forward shock ("shock precursor"), particularly if the shock velocity is $\gtrsim 150\,\mathrm{kms}^{-1}$ (Dopita and Sutherland, 1995, 1996).

(i):*Shock-ionised optical bubbles with radio emission*

For some sources (e.g., M 51 ULX-1 and IC 342 X-1) the jet power is within an order of magnitude of the X-ray power of the central source. Numerous MHD simulations predict that the mechanical power is equal to (or greater than) the radiative power (Hashizume et al., 2015; Ohsuga and Mineshige, 2011). This mechanical energy comes from either the winds or the jet of the ULX. Whether or not both winds and jets can coexist is a topic of active research. In Galactic XRBs (in the sub-Eddington regime), winds are associated with the high/soft state while jets are seen in the low/hard state and thus have been suggested to be mutually exclusive (Ponti et al., 2012). The formation of the disk winds has been suggested to result in a suppression of any jet (Neilsen and Lee, 2009). However, a recent study by Homan et al. (2016) suggests that winds and jets could potentially coexist in LMXBs. Although not coincident, the authors found that the neutron star LMXB GX 13+1 produced radio emission and evidence for disk winds while in the same spectral state, suggesting that both winds and the jet could exist together. Homan et al. (2016) used similar arguments for the neutron star LMXBs GX 340+0, Cir X-1 and Sco X-1 and the black hole LMXBs V 404 Cyg and GRS 1915+105. A key point for all sources was their high luminosity during stages where both winds and jets were expected to exist ($0.3L_{\mathrm{Edd}}$ - L_{Edd}). Alternatively, Díaz Trigo et al. (2014) found that in the LMXB 4U 1630-47 winds were being launched in the hard state ($L < 0.03L_{\mathrm{Edd}}$), but were too ionised to be detected (see also Díaz Trigo and Boirin, 2016). Perhaps nearing (or crossing) the Eddington limit allows for the presence of both winds and jets simultaneously, an intriguing possibility for ULXs. AGN show a similar jet/wind connection with Tombesi et al. (2014) finding that, of a sample of radio-loud AGN, $50 \pm 20\%$ also produced ultra-fast outflows (UFOs). Thus there appears to be a range of both accretor mass and accretion rate that can produce coexisting winds and jets. ULXs fill an important parameter space for both mass and accretion rate.

(ii):*Shock-ionised optical bubbles without radio emission*

NGC 1313 X-2 has a bright, shock-ionised optical nebula, but no associated radio emission. The radio-faint source appears to have no jets so the shocked gas is likely a result of strong winds from the central ULX. The ratio between the radio synchrotron luminosity and optical line emission in a ULX bubble may depend on the kinetic energy carried by the wind or the jet. It may also be the result of a different cooling timescale between synchrotron cooling and optical thermal plasma cooling (Siwek et al., 2017). Much weaker Bremsstrahlung radio emission is likely being produced by the shocked gas, but is too faint to be detected. Future, deeper radio observations are required to confirm this. With only a single shock-ionised bubble with no radio emission, it is also possible that NGC 1313 X-2 is an outlier and not indicative of a population of sources.

(iii):*Photo-ionised optical bubbles with radio emission*

There are a number of ULX bubbles that have radio emission but do not show the signatures of shock-ionised gas (e.g., Holmberg II X-1 and NGC 5408 X-1). Importantly, photo-ionised ULX bubbles, primarily ionised by X-ray photons, are expected to differ from photo-ionised nebulae around massive stars, primarily ionised by UV photons. The lack of shocked gas may indicate that no jets or winds are being produced. This would suggest that, if the radio emission is associated with the ULX, then it comes from Bremsstrahlung emission from the hot gas. However, Ho II X-1 shows clear evidence of discrete jet ejecta (Cseh et al., 2014, 2015a). Additionally, Miller et al. (2005) found that only about 5% of the radio emission of Ho II X-1 could be attributed to a thermal Bremsstrahlung contribution. We also know that at least one source, NGC 5408 X-1 (and potentially NGC 6946 X-1), shows evidence of powerful, relativistic ($\sim 0.2c$) winds (Pinto et al., 2016). The reason behind the lack of any evidence of shock-ionised gas is unknown, and is an important question in classifying, and ultimately understanding, ULX bubbles. We may be looking at something intrinsic to the ULX, such as a weaker jet or slower wind, or something extrinsic, like a lower density ISM.

8.2 Conclusions

The purpose of this thesis was to investigate the radiative and mechanical outputs created by super-Eddington accretion. Super-Eddington accretion is an important process not just for ULXs, but also in galactic nuclei, in phenomena such as tidal disruption events (TDEs) or early-universe quasars. The most powerful lo-

cal AGN generally only reach a few times Eddington (Steinhardt and Elvis, 2010; Lusso et al., 2012; Dai et al., 2014) as they directly regulate the rate at which material is accreted from the surroundings. On the other hand, ULXs are fed by a companion star, which can produce extreme accretion rates ($\dot{m} > 100$) that AGN cannot reach. Additionally, whereas ULXs can be fed at super-Eddington rates for up to 10^6 yr, other occurrences of super-Eddington accretion are either limited to short epochs (in the case of TDEs) or difficult to study (in the case of quasars, being both highly obscured and distant). Thus ULXs offer some of the most favourable circumstances to study accretion at the highest rates.

We have presented the multiwavelength properties of a select number of super-Eddington sources. While we have analysed sources with a wide range of observational properties, including X-ray luminosity, spectral hardness, optical depth, presence of bubbles, lobes or hotspots, and jet power, each is an example of supercritical accretion. It was these contrasting observable properties that motivated our search for a unifying model. We propose that the combination of inclination angle, accretion rate, accretor type/magnetic field strength and the presence or absence of outflows can be used to explain the entire population of super-Eddington X-ray binaries; including standard ULXs, ULSs and low-luminosity, ultra-powerful microquasars.

Discerning the true nature of these sources is crucial for better understanding super-Eddington accretion across the Universe. ULX research has implications beyond compact binaries, whether it be determining the growth rate of SMBHs in the early Universe (Volonteri et al., 2015) or the contribution X-ray binaries had on heating the intergalactic medium during the epoch of reionisation (Mirabel et al., 2011).

8.3 Future Work

While we suggest that the variation in observable features of ULXs (e.g., X-ray spectral shape, X-ray/optical line emission, optical depth, etc.) can be explained by changes in the physical properties of a single population of ULXs (inclination angle, accretion rate, outflow structure, accretor type and magnetic field strength), more observational evidence is required to properly test this hypothesis. Here we review a number of tests that may provide more concrete evidence using ideal observations with current and next-generation telescopes.

Conducting an eclipsing ULX survey would help to find more edge-on ULXs, for which the inclination angle is well constrained. While our discovery of two eclipsing ULXs in M 51 was able to show that viewing angle cannot be the only cause behind ULX spectral shapes, comparing the X-ray spectral properties of

a population of high-inclination sources to the remaining ULX population will help in disentangling the effect that inclination angle has on ULX observable characteristics. Motivated by the discovery of the first two eclipsing ULXs, we are currently conducting a survey of bright ($\gtrsim 10^{38}$ erg s^{-1}) X-ray sources looking for evidence of eclipses by identifying step-function-like features in the lightcurves.

Additionally, identifying eclipses allows us to constrain the binary period, which can provide information about the nature of the companion star via the period-density relation. Furthermore, both the inclination angle and period are required to solve for the mass function. Then, if the radial velocity of the binary can be measured, the mass of the compact object can be determined, hence identifying the type of accretor. However, measuring the radial velocity in ULX companions has thus far proven difficult. While mass constraints on the compact object in NGC 7793 P 13 were placed by measuring the radial velocity of the B9Ia supergiant (Motch et al., 2014), the typical (less massive) optical counterparts of ULXs are too faint for us to detect significant lines in the optical spectra. Heida et al. (2016) took IR spectra of a number of red super-giants (RSGs) though no significant variations in the radial velocities were detected. This may be the result of RSGs only being companion stars in neutron star ULXs (Wiktorowicz et al., 2017) meaning that the companion star mass would dominate the total mass of the system. In the future, detection of IR Paschen lines with the James Webb Space Telescope will allow for better radial velocity measurements of typical ULX companions.

Numerous attempts are already in place to identify neutron star ULXs. For example, the EXTraS (Exploring the X-ray Transient and variable Sky; De Luca et al. 2016) project analysed the temporal information of hundreds of thousands of sources in publically-available *XMM-Newton*/EPIC observations. Two of the four known pulsating neutron stars were identified using this project (Israel et al., 2017b,a). For ULXs that do not show coherent pulsations, there are still methods available for identifying neutron star accretors. Recently, another neutron star ULX was discovered via cyclotron emission (Brightman et al., 2018). Additionally, as previously mentioned, RSG companions are predicted to be exclusive to neutron star ULXs (Wiktorowicz et al., 2017). Finally, it has been suggested by Pintore et al. (2017) that ULXs with the hardest X-ray colours represent those with neutron star accretors. Ultimately, to test if there is a systematic difference in the X-ray spectra and jet power of black hole and neutron star ULXs, a sample of confirmed black hole ULXs is needed, for which dynamical mass measurements are required.

If a large sample of neutron star ULXs can be identified, in both old and young stellar populations, an estimate of the effect magnetic field has on the spectral

properties of ULXs could be established. No comprehensive surveys of ULXs in old populations (globular clusters, elliptical galaxies) currently exist. These ULXs represent the high-luminosity tail of the LMXB population, while ULXs in young populations represent the high-luminosity tail of the HMXB population. Comparison between the populations is needed to test whether there are differences in ULX accretion flow and wind properties between ULXs fed by a high-mass or a low-mass donor (for the same apparent X-ray luminosity). Furthermore, it would enable us to test the idea that transient ULXs are fed by low-mass donors. Such a study could be conducted with eROSITA (extended ROentgen Survey with an Imaging Telescope Array) as it will provide an all sky survey of X-ray sources (including ULXs) down to a flux limit of 10^{-14} erg cm^{-2} s^{-1} in the soft band (0.5-2 keV) and 2×10^{-13} in the hard band (2-10 keV; Merloni et al., 2012). This larger sample will also help determine the high-luminosity cut-off and shape of the luminosity distribution above 10^{40} erg s^{-1} in the two populations.

The next generation of radio telescopes will improve our understanding of relativistic jets in ULXs. While telescopes like the Next Generation VLA (ngVLA) and the SKA will likely be unable to detect the compact core of a typical ULX[1], the improved sensitivities will allow for more detections of ULX radio bubbles (e.g., NGC 300 S 10; Chapter 7), hotspots and lobes (e.g., NGC 7793 S 26; Soria et al. 2010) and transient jet ejecta (e.g., Ho II X-1; Cseh et al. 2015a). This will enable us to explore potential differences in the populations of jetted and non-jetted ULXs.

Comparing the X-ray spectra of ULSs to those of standard ULXs offers a rare opportunity to identify how the presence/absence of strong outflows directly influences ULX X-ray spectral classification. Work studying the winds of ULXs is currently being conducted using high-resolution X-ray spectroscopy with *Chandra*/High Energy Transmission Grating Spectrometer (HETGS) and *XMM-Newton*/Reflection Grating Spectrometer (RGS) (e.g., Pinto et al. 2016). I am working as part of this group on projects pertaining to the ULXs NGC 1313 X-2 and NGC 55 X-1 (Pinto et al., 2017a). Sources like NGC 55 X-1, M 101 ULX-1 and NGC 247 ULX all demonstrate ULX-ULS transitions (Chapter 4; Pinto et al. 2017a) and thus are perfect for testing how the disk winds are related ULX spectral properties. Naturally, these sources are ideal targets for the next-generation of X-ray spectrometers, specifically ESO's *Athena* telescope (Ravera et al., 2014) and NASA's *Arcus* grating mission (Smith et al., 2017), with their higher spatial and spectral resolution (especially for soft X-rays) than current instruments.

So far we have not mentioned any efforts to constrain the mass accretion

[1]Compact core emission from XRB jets have radio flux densities of ~ 10 mJy at a distance of 10 kpc. Scaling this to 10 Mpc results in flux densities of ~ 10 nJy.

rate. Difficulties arise in estimating the accretion rate due to the nature of super-Eddington accretion. How much energy is advected in the accretion flow is difficult to quantify. Additionally, the strong winds remove considerable material and energy from the system, which is again difficult to accurately quantify. Mass accretion may remain a challenge to constrain, possibly until the effects of the remaining physical properties of ULXs can be pinned down.

This research project has highlighted the fact that ULX spectral properties are dependent on the physical characteristics of the accretion flow rather than being purely driven by changes in the viewing angle. While we suggest that the observable features of ULXs, including ULSs, can be explained by a unified model incorporating accretion rate, accretor type and outflow characteristics with inclination angle, further data from current and upcoming state-of-the-art instruments are required to fully test this hypothesis.

Bibliography

Abolmasov, P. and Moiseev, A. V. (2008). Kinematics of the Nebular Complex MH9/10/11 Associated with HoIX X-1. *Rev. Mex. Astron. Astrofis.*, 44:301–309.

Abramowicz, M. A., Chen, X., Kato, S., Lasota, J.-P., and Regev, O. (1995). Thermal equilibria of accretion disks. *ApJL*, 438:L37–L39.

Abramowicz, M. A., Czerny, B., Lasota, J. P., and Szuszkiewicz, E. (1988). Slim accretion disks. *ApJ*, 332:646–658.

Abramowicz, M. A. and Fragile, P. C. (2013). Foundations of Black Hole Accretion Disk Theory. *Living Reviews in Relativity*, 16:1.

Allen, M. G., Groves, B. A., Dopita, M. A., Sutherland, R. S., and Kewley, L. J. (2008). The MAPPINGS III Library of Fast Radiative Shock Models. *ApJS*, 178:20–55.

Allende Prieto, C., Lambert, D. L., and Asplund, M. (2001). The Forbidden Abundance of Oxygen in the Sun. *ApJL*, 556:L63–L66.

Armitage, P. J. and Livio, M. (1996). Accretion Disks in Interacting Binaries: Simulations of the Stream-Disk Impact. *ApJ*, 470:1024.

Arnaud, K., Smith, R., and Siemiginowska, A. (2011). *Handbook of X-ray Astronomy*.

Arnaud, K. A. (1996). XSPEC: The First Ten Years. In Jacoby, G. H. and Barnes, J., editors, *Astronomical Data Analysis Software and Systems V*, volume 101 of *Astronomical Society of the Pacific Conference Series*, page 17.

Bachetti, M., Harrison, F. A., Walton, D. J., Grefenstette, B. W., Chakrabarty, D., Fürst, F., Barret, D., Beloborodov, A., Boggs, S. E., Christensen, F. E., Craig, W. W., Fabian, A. C., Hailey, C. J., Hornschemeier, A., Kaspi, V., Kulkarni, S. R., Maccarone, T., Miller, J. M., Rana, V., Stern, D., Tendulkar, S. P., Tomsick, J., Webb, N. A., and Zhang, W. W. (2014). An ultraluminous X-ray source powered by an accreting neutron star. *Nature*, 514:202–204.

Bachetti, M., Rana, V., Walton, D. J., Barret, D., Harrison, F. A., Boggs, S. E., Christensen, F. E., Craig, W. W., Fabian, A. C., Fürst, F., Grefenstette, B. W., Hailey, C. J., Hornschemeier, A., Madsen, K. K., Miller, J. M., Ptak, A. F., Stern, D., Webb, N. A., and Zhang, W. W. (2013). The Ultraluminous X-Ray Sources NGC 1313 X-1 and X-2: A Broadband Study with NuSTAR and XMM-Newton. *ApJ*, 778:163.

Baldwin, J. A., Phillips, M. M., and Terlevich, R. (1981). Classification parameters for the emission-line spectra of extragalactic objects. *PASP*, 93:5–19.

Begelman, M. C., Blandford, R. D., and Rees, M. J. (1984). Theory of extragalactic radio sources. *Reviews of Modern Physics*, 56:255–351.

Belczynski, K., Bulik, T., Fryer, C. L., Ruiter, A., Valsecchi, F., Vink, J. S., and Hurley, J. R. (2010). On the Maximum Mass of Stellar Black Holes. *ApJ*, 714:1217–1226.

Belloni, T. M. (2010). States and Transitions in Black Hole Binaries. In Belloni, T., editor, *Lecture Notes in Physics, Berlin Springer Verlag*, volume 794 of *Lecture Notes in Physics, Berlin Springer Verlag*, page 53.

Berger, E., Soderberg, A. M., Chevalier, R. A., Fransson, C., Foley, R. J., Leonard, D. C., Debes, J. H., Diamond-Stanic, A. M., Dupree, A. K., Ivans, I. I., Simmerer, J., Thompson, I. B., and Tremonti, C. A. (2009). An Intermediate Luminosity Transient in NGC 300: The Eruption of a Dust-Enshrouded Massive Star. *ApJ*, 699:1850–1865.

Binder, B., Gross, J., Williams, B. F., and Simons, D. (2015). Energy-dependent orbital phases in NGC 300 X-1. *MNRAS*, 451:4471–4482.

Binder, B., Williams, B. F., Kong, A. K. H., Gaetz, T. J., Plucinsky, P. P., Skillman, E. D., and Dolphin, A. (2016). Recurring X-ray outbursts in the supernova impostor SN 2010da in NGC 300. *MNRAS*, 457:1636–1643.

Blackburn, J. K. (1995). FTOOLS: A FITS Data Processing and Analysis Software Package. In Shaw, R. A., Payne, H. E., and Hayes, J. J. E., editors, *Astronomical Data Analysis Software and Systems IV*, volume 77 of *Astronomical Society of the Pacific Conference Series*, page 367.

Blair, W. P. and Long, K. S. (1997). Identification of Supernova Remnants in the Sculptor Group Galaxies NGC 300 and NGC 7793. *ApJS*, 108:261–277.

Bohlin, R. C. (2016). Perfecting the Photometric Calibration of the ACS CCD Cameras. *AJ*, 152:60.

Bondi, H. (1952). On spherically symmetrical accretion. *MNRAS*, 112:195.

Bonnet-Bidaud, J. M., Haberl, F., Ferrando, P., Bennie, P. J., and Kendziorra, E. (2001). The eclipsing bursting X-ray binary EXO 0748-676 revisited by XMM-Newton. *A&A*, 365:L282–L287.

Bose, S. and Kumar, B. (2014). Distance Determination to Eight Galaxies Using Expanding Photosphere Method. *ApJ*, 782:98.

Bresolin, F., Garnett, D. R., and Kennicutt, Jr., R. C. (2004). Abundances of Metal-rich H II Regions in M51. *ApJ*, 615:228–241.

Bressan, A., Marigo, P., Girardi, L., Salasnich, B., Dal Cero, C., Rubele, S., and Nanni, A. (2012). PARSEC: stellar tracks and isochrones with the PAdova and TRieste Stellar Evolution Code. *MNRAS*, 427:127–145.

Brightman, M., Harrison, F. A., Fürst, F., Middleton, M. J., Walton, D. J., Stern, D., Fabian, A. C., Heida, M., Barret, D., and Bachetti, M. (2018). Magnetic field strength of a neutron-star-powered ultraluminous X-ray source. *Nature Astronomy*, 2:312–316.

Brinkmann, W. and Kawai, N. (2000). The jets of SS 433: second order effects. *A&A*, 363:640–646.

Brinkmann, W., Kotani, T., and Kawai, N. (2005). XMM-Newton observations of SS 433 I. EPIC spectral analysis. *A&A*, 431:575–586.

Brinkmann, W., Pratt, G. W., Rohr, S., Kawai, N., and Burwitz, V. (2007). XMM-Newton observations of the eastern jet of SS 433. *A&A*, 463:611–619.

Brocksopp, C., Kaiser, C. R., Schoenmakers, A. P., and de Bruyn, A. G. (2011). Double-double radio galaxies: further insights into the formation of the radio structures. *MNRAS*, 410:484–498.

Burke, B. F. and Graham-Smith, F. (1997). *An introduction to radio astronomy*.

Caplan, J. and Deharveng, L. (1986). Extinction and reddening of H II regions in the Large Magellanic Cloud. *A&A*, 155:297–313.

Carpano, S., Haberl, F., Maitra, C., and Vasilopoulos, G. (2018). Discovery of pulsations from NGC 300 ULX1 and its fast period evolution. *MNRAS*, 476:L45–L49.

Carpano, S., Pollock, A. M. T., King, A. R., Wilms, J., and Ehle, M. (2007). An ultraluminous supersoft source with a 4 hour modulation in NGC 4631. *A&A*, 471:L55–L58.

Carpano, S., Wilms, J., Schirmer, M., and Kendziorra, E. (2006). A new luminous supersoft X-ray source in NGC 300. *A&A*, 458:747–751.

Cash, W. (1979). Parameter estimation in astronomy through application of the likelihood ratio. *ApJ*, 228:939–947.

Cavagnolo, K. W., McNamara, B. R., Nulsen, P. E. J., Carilli, C. L., Jones, C., and Bîrzan, L. (2010). A Relationship Between AGN Jet Power and Radio Power. *ApJ*, 720:1066–1072.

Chanan, G. A., Middleditch, J., and Nelson, J. E. (1976). The Geometry of the Eclipse of a Pointlike Star by a Roche-Lobe Companion. *ApJ*, 208:512–517.

Chashkina, A., Abolmasov, P., and Poutanen, J. (2017). Super-Eddington accretion on to a magnetized neutron star. *MNRAS*, 470:2799–2813.

Chen, Y., Bressan, A., Girardi, L., Marigo, P., Kong, X., and Lanza, A. (2015). PARSEC evolutionary tracks of massive stars up to 350 M at metallicities $0.0001 \leq Z \leq 0.04$. *MNRAS*, 452:1068–1080.

Cherepashchuk, A. M., Sunyaev, R. A., Molkov, S. V., Antokhina, E. A., Postnov, K. A., and Bogomazov, A. I. (2013). INTEGRAL observations of SS433: system's parameters and nutation of supercritical accretion disc. *MNRAS*, 436:2004–2013.

Chiosi, E., Orio, M., Bernardini, F., Henze, M., and Jamialahmadi, N. (2014). Multiwavelength search for counterparts of supersoft X-ray sources in M31. *MNRAS*, 443:1821–1836.

Colbert, E. J. M. and Mushotzky, R. F. (1999). The Nature of Accreting Black Holes in Nearby Galaxy Nuclei. *ApJ*, 519:89–107.

Corbel, S., Fender, R. P., Tzioumis, A. K., Tomsick, J. A., Orosz, J. A., Miller, J. M., Wijnands, R., and Kaaret, P. (2002). Large-Scale, Decelerating, Relativistic X-ray Jets from the Microquasar XTE J1550-564. *Science*, 298:196–199.

Corbel, S., Kaaret, P., Fender, R. P., Tzioumis, A. K., Tomsick, J. A., and Orosz, J. A. (2005). Discovery of X-Ray Jets in the Microquasar H1743-322. *ApJ*, 632:504–513.

Cornwell, T. J. (2008). Multiscale CLEAN Deconvolution of Radio Synthesis Images. *IEEE Journal of Selected Topics in Signal Processing*, 2:793–801.

Croxall, K. V., Pogge, R. W., Berg, D. A., Skillman, E. D., and Moustakas, J. (2015). CHAOS II. Gas-phase Abundances in NGC 5194. *ApJ*, 808:42.

Cseh, D., Corbel, S., Kaaret, P., Lang, C., Grisé, F., Paragi, Z., Tzioumis, A., Tudose, V., and Feng, H. (2012). Black Hole Powered Nebulae and a Case Study of the Ultraluminous X-Ray Source IC 342 X-1. *ApJ*, 749:17.

Cseh, D., Kaaret, P., Corbel, S., Grisé, F., Lang, C., Körding, E., Falcke, H., Jonker, P. G., Miller-Jones, J. C. A., Farrell, S., Yang, Y. J., Paragi, Z., and Frey, S. (2014). Unveiling recurrent jets of the ULX Holmberg II X-1: evidence for a massive stellar-mass black hole? *MNRAS*, 439:L1–L5.

Cseh, D., Miller-Jones, J. C. A., Jonker, P. G., Grisé, F., Paragi, Z., Corbel, S., Falcke, H., Frey, S., Kaaret, P., and Körding, E. (2015a). The evolution of a jet ejection of the ultraluminous X-ray source Holmberg II X-1. *MNRAS*, 452:24–31.

Cseh, D., Webb, N. A., Godet, O., Barret, D., Corbel, S., Coriat, M., Falcke, H., Farrell, S. A., Körding, E., Lenc, E., and Wrobel, J. M. (2015b). On the radio properties of the intermediate-mass black hole candidate ESO 243-49 HLX-1. *MNRAS*, 446:3268–3276.

Curran, P. A. (2014). Monte Carlo error analyses of Spearman's rank test. *ArXiv e-prints*.

Dai, Y. S., Elvis, M., Bergeron, J., Fazio, G. G., Huang, J.-S., Wilkes, B. J., Willmer, C. N. A., Omont, A., and Papovich, C. (2014). Mid-infrared-selected Quasars. I. Virial Black Hole Mass and Eddington Ratios. *ApJ*, 791:113.

Davis, J. E. (2001). The Formal Underpinnings of the Response Functions Used in X-Ray Spectral Analysis. *ApJ*, 548:1010–1019.

De Colle, F., Ramirez-Ruiz, E., Granot, J., and Lopez-Camara, D. (2012). Simulations of Gamma-Ray Burst Jets in a Stratified External Medium: Dynamics, Afterglow Light Curves, Jet Breaks, and Radio Calorimetry. *ApJ*, 751:57.

de Jong, J. A., van Paradijs, J., and Augusteijn, T. (1996). Reprocessing of X rays in low-mass X-ray binaries. *A&A*, 314:484–490.

De Luca, A., Salvaterra, R., Tiengo, A., D'Agostino, D., Watson, M. G., Haberl, F., and Wilms, J. (2016). Science with the EXTraS Project: Exploring the X-Ray Transient and Variable Sky. *The Universe of Digital Sky Surveys*, 42:291.

Dewangan, G. C., Griffiths, R. E., Choudhury, M., Miyaji, T., and Schurch, N. J. (2005). XMM-Newton View of the Ultraluminous X-Ray Sources in M51. *ApJ*, 635:198–213.

Dewangan, G. C., Miyaji, T., Griffiths, R. E., and Lehmann, I. (2004). A Transition to a Low/Soft State in the Ultraluminous Compact X-Ray Source Holmberg II X-1. *ApJL*, 608:L57–L60.

Di Stefano, R. and Kong, A. K. H. (2003). Luminous Supersoft X-Ray Sources in External Galaxies. *ApJ*, 592:884–899.

Di Stefano, R. and Kong, A. K. H. (2004). The Discovery of Quasi-soft and Supersoft Sources in External Galaxies. *ApJ*, 609:710–727.

Díaz Trigo, M. and Boirin, L. (2016). Accretion disc atmospheres and winds in low-mass X-ray binaries. *Astronomische Nachrichten*, 337:368.

Díaz Trigo, M., Migliari, S., Miller-Jones, J. C. A., and Guainazzi, M. (2014). XMM-Newton observations reveal the disappearance of the wind in 4U 1630-47. *A&A*, 571:A76.

Díaz Trigo, M., Parmar, A. N., Boirin, L., Méndez, M., and Kaastra, J. S. (2006). Spectral changes during dipping in low-mass X-ray binaries due to highly-ionized absorbers. *A&A*, 445:179–195.

Dickey, J. M. and Lockman, F. J. (1990). H I in the Galaxy. *ARA&A*, 28:215–261.

D'Odorico, S., Benvenuti, P., and Sabbadin, F. (1978). Supernova remnants in M33. *A&A*, 63:63–68.

D'Odorico, S., Dopita, M. A., and Benvenuti, P. (1980). A catalogue of supernova remnant candidates in nearby galaxies. *A&AS*, 40:67–80.

Done, C., Davis, S. W., Jin, C., Blaes, O., and Ward, M. (2012). Intrinsic disc emission and the soft X-ray excess in active galactic nuclei. *MNRAS*, 420:1848–1860.

Dopita, M. A. and Sutherland, R. S. (1995). Spectral Signatures of Fast Shocks. II. Optical Diagnostic Diagrams. *ApJ*, 455:468.

Dopita, M. A. and Sutherland, R. S. (1996). Spectral Signatures of Fast Shocks. I. Low-Density Model Grid. *ApJS*, 102:161.

Dopita, M. A. and Sutherland, R. S. (2003). *Astrophysics of the diffuse universe*.

Downes, A. J. B., Pauls, T., and Salter, C. J. (1986). The supernova remnant W50 at 5 GHz. *MNRAS*, 218:393–407.

Dubner, G. M., Holdaway, M., Goss, W. M., and Mirabel, I. F. (1998). A High-Resolution Radio Study of the W50-SS 433 System and the Surrounding Medium. *AJ*, 116:1842–1855.

Dubus, G., Lasota, J.-P., Hameury, J.-M., and Charles, P. (1999). X-ray irradiation in low-mass binary systems. *MNRAS*, 303:139–147.

Dumas, G., Schinnerer, E., Tabatabaei, F. S., Beck, R., Velusamy, T., and Murphy, E. (2011). The Local Radio-IR Relation in M51. *AJ*, 141:41.

Edelson, R., Turner, T. J., Pounds, K., Vaughan, S., Markowitz, A., Marshall, H., Dobbie, P., and Warwick, R. (2002). X-Ray Spectral Variability and Rapid Variability of the Soft X-Ray Spectrum Seyfert 1 Galaxies Arakelian 564 and Ton S180. *ApJ*, 568:610–626.

Edmunds, M. G. and Pagel, B. E. J. (1984). On the composition of H II regions in southern galaxies. III - NGC 2997 and 7793. *MNRAS*, 211:507–519.

Eggleton, P. P. (1983). Towards consistency in simple prescriptions for stellar convection. *MNRAS*, 204:449–461.

Ehle, M., Pietsch, W., and Beck, R. (1995). ROSAT high-resolution X-ray observations of the galaxies M 51 and NGC 5195. *A&A*, 295:289–301.

Evans, I. N., Primini, F. A., Glotfelty, K. J., Anderson, C. S., Bonaventura, N. R., Chen, J. C., Davis, J. E., Doe, S. M., Evans, J. D., Fabbiano, G., Galle, E. C., Gibbs, II, D. G., Grier, J. D., Hain, R. M., Hall, D. M., Harbo, P. N., (Helen He, X., Houck, J. C., Karovska, M., Kashyap, V. L., Lauer, J., McCollough, M. L., McDowell, J. C., Miller, J. B., Mitschang, A. W., Morgan, D. L., Mossman, A. E., Nichols, J. S., Nowak, M. A., Plummer, D. A., Refsdal, B. L., Rots, A. H., Siemiginowska, A., Sundheim, B. A., Tibbetts, M. S., Van Stone, D. W., Winkelman, S. L., and Zografou, P. (2010). The Chandra Source Catalog. *ApJS*, 189:37–82.

Fabbiano, G., King, A. R., Zezas, A., Ponman, T. J., Rots, A., and Schweizer, F. (2003). A Variable Ultraluminous Supersoft X-Ray Source in "The Antennae": Stellar-Mass Black Hole or White Dwarf? *ApJ*, 591:843–849.

Fabian, A. C. (2012). Observational Evidence of Active Galactic Nuclei Feedback. *ARA&A*, 50:455–489.

Fabrika, S. (2004). The jets and supercritical accretion disk in SS433. *Astrophysics and Space Physics Reviews*, 12:1–152.

Fabrika, S. and Medvedev, A. (2011). X-ray radiation of the jets and the supercritical accretion disk in SS 433. In Romero, G. E., Sunyaev, R. A., and Belloni, T., editors, *Jets at All Scales*, volume 275 of *IAU Symposium*, pages 280–284.

Farnes, J. S., Gaensler, B. M., Purcell, C., Sun, X. H., Haverkorn, M., Lenc, E., O'Sullivan, S. P., and Akahori, T. (2017). Interacting large-scale magnetic fields and ionized gas in the W50/SS433 system. *MNRAS*, 467:4777–4801.

Farrell, S. A., Webb, N. A., Barret, D., Godet, O., and Rodrigues, J. M. (2009). An intermediate-mass black hole of over 500 solar masses in the galaxy ESO243-49. *Nature*, 460:73–75.

Fender, R. P., Belloni, T. M., and Gallo, E. (2004). Towards a unified model for black hole X-ray binary jets. *MNRAS*, 355:1105–1118.

Feng, H. and Kaaret, P. (2009). Spectral States and Evolution of Ultraluminous X-Ray Sources. *ApJ*, 696:1712–1726.

Feng, H. and Soria, R. (2011). Ultraluminous X-ray sources in the Chandra and XMM-Newton era. *NAR*, 55:166–183.

Fey, A. L., Gordon, D., Jacobs, C. S., Ma, C., Gaume, R. A., Arias, E. F., Bianco, G., Boboltz, D. A., Böckmann, S., Bolotin, S., Charlot, P., Collioud, A., Engelhardt, G., Gipson, J., Gontier, A.-M., Heinkelmann, R., Kurdubov, S., Lambert, S., Lytvyn, S., MacMillan, D. S., Malkin, Z., Nothnagel, A., Ojha, R., Skurikhina, E., Sokolova, J., Souchay, J., Sovers, O. J., Tesmer, V., Titov, O., Wang, G., and Zharov, V. (2015). The Second Realization of the International Celestial Reference Frame by Very Long Baseline Interferometry. *AJ*, 150:58.

Foschini, L., Di Cocco, G., Ho, L. C., Bassani, L., Cappi, M., Dadina, M., Gianotti, F., Malaguti, G., Panessa, F., Piconcelli, E., Stephen, J. B., and Trifoglio, M. (2002). XMM-Newton observations of ultraluminous X-ray sources in nearby galaxies. *A&A*, 392:817–825.

Frank, J., King, A., and Raine, D. J. (2002). *Accretion Power in Astrophysics: Third Edition*. Cambridge University Press.

Frank, J., King, A. R., and Lasota, J.-P. (1987). The light curves of low-mass X-ray binaries. *A&A*, 178:137–142.

Fruscione, A., McDowell, J. C., Allen, G. E., Brickhouse, N. S., Burke, D. J., Davis, J. E., Durham, N., Elvis, M., Galle, E. C., Harris, D. E., Huenemoerder,

D. P., Houck, J. C., Ishibashi, B., Karovska, M., Nicastro, F., Noble, M. S., Nowak, M. A., Primini, F. A., Siemiginowska, A., Smith, R. K., and Wise, M. (2006). CIAO: Chandra's data analysis system. In *Society of Photo-Optical Instrumentation Engineers (SPIE) Conference Series*, volume 6270 of *Society of Photo-Optical Instrumentation Engineers (SPIE) Conference Series*, page 1.

Fryer, C. L. and Kalogera, V. (2001). Theoretical Black Hole Mass Distributions. *ApJ*, 554:548–560.

Gaia Collaboration, Brown, A. G. A., Vallenari, A., Prusti, T., de Bruijne, J. H. J., Mignard, F., Drimmel, R., Babusiaux, C., Bailer-Jones, C. A. L., Bastian, U., and et al. (2016a). Gaia Data Release 1. Summary of the astrometric, photometric, and survey properties. *A&A*, 595:A2.

Gaia Collaboration, Prusti, T., de Bruijne, J. H. J., Brown, A. G. A., Vallenari, A., Babusiaux, C., Bailer-Jones, C. A. L., Bastian, U., Biermann, M., Evans, D. W., and et al. (2016b). The Gaia mission. *A&A*, 595:A1.

Gallo, E., Fender, R., Kaiser, C., Russell, D., Morganti, R., Oosterloo, T., and Heinz, S. (2005). A dark jet dominates the power output of the stellar black hole Cygnus X-1. *Nature*, 436:819–821.

Gehrels, N. (1986). Confidence limits for small numbers of events in astrophysical data. *ApJ*, 303:336–346.

Gerke, J. R., Kochanek, C. S., Prieto, J. L., Stanek, K. Z., and Macri, L. M. (2011). A Study of Cepheids in M81 with the Large Binocular Telescope (Efficiently Calibrated with Hubble Space Telescope). *ApJ*, 743:176.

Gieren, W., Pietrzyński, G., Soszyński, I., Bresolin, F., Kudritzki, R.-P., Minniti, D., and Storm, J. (2005). The Araucaria Project: Near-Infrared Photometry of Cepheid Variables in the Sculptor Galaxy NGC 300. *ApJ*, 628:695–703.

Gieren, W., Pietrzyński, G., Soszyński, I., Szewczyk, O., Bresolin, F., Kudritzki, R.-P., Urbaneja, M. A., Storm, J., Minniti, D., and García-Varela, A. (2009). The Araucaria Project: The Distance to the Sculptor Galaxy NGC 247 from Near-Infrared Photometry of Cepheid Variables. *ApJ*, 700:1141–1147.

Gierliński, M., Done, C., and Page, K. (2009). Reprocessing of X-rays in the outer accretion disc of the black hole binary XTE J1817-330. *MNRAS*, 392:1106–1114.

Gierliński, M. and Zdziarski, A. A. (2005). Patterns of energy-dependent variability from Comptonization. *MNRAS*, 363:1349–1360.

Gladstone, J. C., Copperwheat, C., Heinke, C. O., Roberts, T. P., Cartwright, T. F., Levan, A. J., and Goad, M. R. (2013). Optical Counterparts of the Nearest Ultraluminous X-Ray Sources. *ApJS*, 206:14.

Gladstone, J. C., Roberts, T. P., and Done, C. (2009). The ultraluminous state. *MNRAS*, 397:1836–1851.

Godfrey, L. E. H. and Shabala, S. S. (2013). AGN Jet Kinetic Power and the Energy Budget of Radio Galaxy Lobes. *ApJ*, 767:12.

Godfrey, L. E. H. and Shabala, S. S. (2016). Mutual distance dependence drives the observed jet-power-radio-luminosity scaling relations in radio galaxies. *MNRAS*, 456:1172–1184.

Goodall, P. T., Alouani-Bibi, F., and Blundell, K. M. (2011). When microquasar jets and supernova collide: hydrodynamically simulating the SS 433-W 50 interaction. *MNRAS*, 414:2838–2859.

Gordon, S. M., Kirshner, R. P., Long, K. S., Blair, W. P., Duric, N., and Smith, R. C. (1998). A New Optical Sample of Supernova Remnants in M33. *ApJS*, 117:89–133.

Greiner, J., editor (1996). *Supersoft X-Ray Sources*, volume 472 of *Lecture Notes in Physics, Berlin Springer Verlag*.

Greiner, J. and Di Stefano, R. (2002). X-ray off states and optical variability in CAL 83. *A&A*, 387:944–954.

Greisen, E. W. (2003). AIPS, the VLA, and the VLBA. *Information Handling in Astronomy - Historical Vistas*, 285:109.

Grimm, H.-J., Gilfanov, M., and Sunyaev, R. (2002). The Milky Way in X-rays for an outside observer. Log(N)-Log(S) and luminosity function of X-ray binaries from RXTE/ASM data. *A&A*, 391:923–944.

Grisé, F., Kaaret, P., Corbel, S., Cseh, D., and Feng, H. (2013). A long-term X-ray monitoring of the ultraluminous X-ray source NGC 5408 X-1 with Swift reveals the presence of dips but no orbital period. *MNRAS*, 433:1023–1038.

Grisé, F., Kaaret, P., Corbel, S., Feng, H., Cseh, D., and Tao, L. (2012). Optical Emission of the Ultraluminous X-Ray Source NGC 5408 X-1: Donor Star or Irradiated Accretion Disk? *ApJ*, 745:123.

Grisé, F., Kaaret, P., Feng, H., Kajava, J. J. E., and Farrell, S. A. (2010). X-ray Spectral State is not Correlated with Luminosity in Holmberg II X-1. *ApJL*, 724:L148–L152.

Grisé, F., Kaaret, P., Pakull, M. W., and Motch, C. (2011). Optical Properties of the Ultraluminous X-Ray Source Holmberg IX X-1 and Its Stellar Environment. *ApJ*, 734:23.

Grisé, F., Pakull, M. W., and Motch, C. (2006). The Ultraluminous X-ray Source in Holmberg IX and its Environment. In Meurs, E. J. A. and Fabbiano, G., editors, *Populations of High Energy Sources in Galaxies*, volume 230 of *IAU Symposium*, pages 302–303.

Hack, W. J. and Greenfield, P. (2000). Implementation of the Advanced Camera for Surveys Calibration Pipeline. In Manset, N., Veillet, C., and Crabtree, D., editors, *Astronomical Data Analysis Software and Systems IX*, volume 216 of *Astronomical Society of the Pacific Conference Series*, page 433.

Hardcastle, M. J., Worrall, D. M., Kraft, R. P., Forman, W. R., Jones, C., and Murray, S. S. (2003). Radio and X-Ray Observations of the Jet in Centaurus A. *ApJ*, 593:169–183.

Harris, D. E. and Krawczynski, H. (2006). X-Ray Emission from Extragalactic Jets. *ARA&A*, 44:463–506.

Hashizume, K., Ohsuga, K., Kawashima, T., and Tanaka, M. (2015). Radiation hydrodynamics simulations of wide-angle outflows from super-critical accretion disks around black holes. *PASJ*, 67:58.

Heger, A., Fryer, C. L., Woosley, S. E., Langer, N., and Hartmann, D. H. (2003). How Massive Single Stars End Their Life. *ApJ*, 591:288–300.

Heida, M., Jonker, P. G., Torres, M. A. P., Kool, E., Servillat, M., Roberts, T. P., Groot, P. J., Walton, D. J., Moon, D.-S., and Harrison, F. A. (2014). Near-infrared counterparts of ultraluminous X-ray sources. *MNRAS*, 442:1054–1067.

Heida, M., Jonker, P. G., Torres, M. A. P., Roberts, T. P., Walton, D. J., Moon, D.-S., Stern, D., and Harrison, F. A. (2016). Keck/MOSFIRE spectroscopy of five ULX counterparts. *MNRAS*, 459:771–778.

Heinz, S. (2002). Radio lobe dynamics and the environment of microquasars. *A&A*, 388:L40–L43.

Heinz, S. (2006). Composition, Collimation, Contamination: The Jet of Cygnus X-1. *ApJ*, 636:316–322.

Hellier, C. and Mason, K. O. (1989). EXOSAT observations of X1822-371 - Modelling of the accretion disc rim. *MNRAS*, 239:715–732.

Högbom, J. A. (1974). Aperture Synthesis with a Non-Regular Distribution of Interferometer Baselines. *A&AS*, 15:417.

Homan, J., Neilsen, J., Allen, J. L., Chakrabarty, D., Fender, R., Fridriksson, J. K., Remillard, R. A., and Schulz, N. (2016). Evidence for Simultaneous Jets and Disk Winds in Luminous Low-mass X-Ray Binaries. *ApJL*, 830:L5.

Homan, J., Wijnands, R., and van den Berg, M. (2003). XMM-Newton light curves of the low-mass X-ray binary EXO 0748-676: Dips, eclipses, and bursts. *A&A*, 412:799–812.

Hong, J., van den Berg, M., Schlegel, E. M., Grindlay, J. E., Koenig, X., Laycock, S., and Zhao, P. (2005). X-Ray Processing of ChaMPlane Fields: Methods and Initial Results for Selected Anti-Galactic Center Fields. *ApJ*, 635:907–919.

Howell, S. B. (2006). *Handbook of CCD Astronomy*.

Hoyle, F. and Lyttleton, R. A. (1941). On the accretion theory of stellar evolution. *MNRAS*, 101:227.

Hynes, R. I., Haswell, C. A., Chaty, S., Shrader, C. R., and Cui, W. (2002). The evolving accretion disc in the black hole X-ray transient XTE J1859+226. *MNRAS*, 331:169–179.

Israel, G. L., Belfiore, A., Stella, L., Esposito, P., Casella, P., De Luca, A., Marelli, M., Papitto, A., Perri, M., Puccetti, S., Castillo, G. A. R., Salvetti, D., Tiengo, A., Zampieri, L., D'Agostino, D., Greiner, J., Haberl, F., Novara, G., Salvaterra, R., Turolla, R., Watson, M., Wilms, J., and Wolter, A. (2017a). An accreting pulsar with extreme properties drives an ultraluminous x-ray source in NGC 5907. *Science*, 355:817–819.

Israel, G. L., Papitto, A., Esposito, P., Stella, L., Zampieri, L., Belfiore, A., Rodríguez Castillo, G. A., De Luca, A., Tiengo, A., Haberl, F., Greiner, J., Salvaterra, R., Sandrelli, S., and Lisini, G. (2017b). Discovery of a 0.42-s pulsar in the ultraluminous X-ray source NGC 7793 P13. *MNRAS*, 466:L48–L52.

Ito, H., Nagataki, S., Ono, M., Lee, S.-H., Mao, J., Yamada, S., Pe'er, A., Mizuta, A., and Harikae, S. (2013). Photospheric Emission from Stratified Jets. *ApJ*, 777:62.

Izotov, Y. I., Thuan, T. X., and Privon, G. (2012). The detection of [Ne V] emission in five blue compact dwarf galaxies. *MNRAS*, 427:1229–1237.

Jiang, Y.-F., Stone, J. M., and Davis, S. W. (2014). A Global Three-dimensional Radiation Magneto-hydrodynamic Simulation of Super-Eddington Accretion Disks. *ApJ*, 796:106.

Jin, J., Feng, H., Kaaret, P., and Zhang, S.-N. (2011). XMM-Newton Observations of NGC 247: X-Ray Population and a Supersoft Ultraluminous X-Ray Source. *ApJ*, 737:87.

Johnston, K. J. and de Vegt, C. (1999). Reference Frames in Astronomy. *ARA&A*, 37:97–125.

Joye, W. A. and Mandel, E. (2003). New Features of SAOImage DS9. In Payne, H. E., Jedrzejewski, R. I., and Hook, R. N., editors, *Astronomical Data Analysis Software and Systems XII*, volume 295 of *Astronomical Society of the Pacific Conference Series*, page 489.

Kaaret, P. and Corbel, S. (2009). A Photoionized Nebula Surrounding and Variable Optical Continuum Emission from the Ultraluminous X-Ray Source in NGC 5408. *ApJ*, 697:950–956.

Kaaret, P., Corbel, S., Prestwich, A. H., and Zezas, A. (2003a). Radio Emission from an Ultraluminous X-ray Source. *Science*, 299:365–368.

Kaaret, P., Corbel, S., Tomsick, J. A., Fender, R., Miller, J. M., Orosz, J. A., Tzioumis, A. K., and Wijnands, R. (2003b). X-Ray Emission from the Jets of XTE J1550-564. *ApJ*, 582:945–953.

Kaaret, P., Feng, H., and Roberts, T. P. (2017). Ultraluminous X-Ray Sources. *ARA&A*, 55:303–341.

Kaaret, P., Feng, H., Wong, D. S., and Tao, L. (2010). Direct Detection of an Ultraluminous Ultraviolet Source. *ApJL*, 714:L167–L170.

Kaaret, P., Prestwich, A. H., Zezas, A., Murray, S. S., Kim, D.-W., Kilgard, R. E., Schlegel, E. M., and Ward, M. J. (2001). Chandra High-Resolution Camera observations of the luminous X-ray source in the starburst galaxy M82. *MNRAS*, 321:L29–L32.

Kahabka, P. and van den Heuvel, E. P. J. (1997). Luminous Supersoft X-Ray Sources. *ARA&A*, 35:69–100.

Kaiser, C. R., Schoenmakers, A. P., and Röttgering, H. J. A. (2000). Radio galaxies with a 'double-double' morphology - II. The evolution of double-double radio galaxies and implications for the alignment effect in FRII sources. *MNRAS*, 315:381–394.

Kajava, J. J. E. and Poutanen, J. (2009). Spectral variability of ultraluminous X-ray sources. *MNRAS*, 398:1450–1460.

Kalberla, P. M. W., Burton, W. B., Hartmann, D., Arnal, E. M., Bajaja, E., Morras, R., and Pöppel, W. G. L. (2005). The Leiden/Argentine/Bonn (LAB) Survey of Galactic HI. Final data release of the combined LDS and IAR surveys with improved stray-radiation corrections. *A&A*, 440:775–782.

Kalemci, E., Dinçer, T., Tomsick, J. A., Buxton, M. M., Bailyn, C. D., and Chun, Y. Y. (2013). Complete Multiwavelength Evolution of Galactic Black Hole Transients during Outburst Decay. I. Conditions for "Compact" Jet Formation. *ApJ*, 779:95.

Kawashima, T., Mineshige, S., Ohsuga, K., and Ogawa, T. (2016). A radiation-hydrodynamics model of accretion columns for ultra-luminous X-ray pulsars. *PASJ*, 68:83.

Kawashima, T., Ohsuga, K., Mineshige, S., Yoshida, T., Heinzeller, D., and Matsumoto, R. (2012). Comptonized Photon Spectra of Supercritical Black Hole Accretion Flows with Application to Ultraluminous X-Ray Sources. *ApJ*, 752:18.

Kennicutt, Jr., R. C., Bresolin, F., and Garnett, D. R. (2003). The Composition Gradient in M101 Revisited. II. Electron Temperatures and Implications for the Nebular Abundance Scale. *ApJ*, 591:801–820.

Kewley, L. J. and Dopita, M. A. (2002). Using Strong Lines to Estimate Abundances in Extragalactic H II Regions and Starburst Galaxies. *ApJS*, 142:35–52.

Kewley, L. J. and Ellison, S. L. (2008). Metallicity Calibrations and the Mass-Metallicity Relation for Star-forming Galaxies. *ApJ*, 681:1183–1204.

King, A. L., Miller, J. M., Raymond, J., Reynolds, M. T., and Morningstar, W. (2015). High-resolution Chandra HETG Spectroscopy of V404 Cygni in Outburst. *ApJL*, 813:L37.

King, A. R. (2009). Masses, beaming and Eddington ratios in ultraluminous X-ray sources. *MNRAS*, 393:L41–L44.

King, A. R. (2010). Black hole outflows. *MNRAS*, 402:1516–1522.

King, A. R., Davies, M. B., Ward, M. J., Fabbiano, G., and Elvis, M. (2001). Ultraluminous X-Ray Sources in External Galaxies. *ApJL*, 552:L109–L112.

King, A. R., Kolb, U., and Szuszkiewicz, E. (1997). Why Low-Mass Black Hole Binaries Are Transient. *ApJ*, 488:89–93.

King, A. R. and Pounds, K. A. (2003). Black hole winds. *MNRAS*, 345:657–659.

Kippenhahn, R. and Weigert, A. (1990). *Stellar Structure and Evolution*.

Kitaki, T., Mineshige, S., Ohsuga, K., and Kawashima, T. (2017). Theoretical modeling of Comptonized X-ray spectra of super-Eddington accretion flow: Origin of hard excess in ultraluminous X-ray sources. *PASJ*, 69:92.

Kobulnicky, H. A. and Kewley, L. J. (2004). Metallicities of 0.3<z< t1.0 Galaxies in the GOODS-North Field. *ApJ*, 617:240–261.

Koliopanos, F., Vasilopoulos, G., Godet, O., Bachetti, M., Webb, N. A., and Barret, D. (2017). ULX spectra revisited: Accreting, highly magnetized neutron stars as the engines of ultraluminous X-ray sources. *A&A*, 608:A47.

Kong, A. K. H. and Di Stefano, R. (2003). A Luminous Recurrent Supersoft X-Ray Source in NGC 300. *ApJL*, 590:L13–L16.

Kong, A. K. H. and Di Stefano, R. (2005). An Unusual Spectral State of an Ultraluminous Very Soft X-Ray Source during Outburst. *ApJL*, 632:L107–L110.

Kong, A. K. H., Di Stefano, R., and Yuan, F. (2004). Evidence of an Intermediate-Mass Black Hole: Chandra and XMM-Newton Observations of the Ultraluminous Supersoft X-Ray Source in M101 during Its 2004 Outburst. *ApJL*, 617:L49–L52.

Kong, A. K. H., Garcia, M. R., Primini, F. A., Murray, S. S., Di Stefano, R., and McClintock, J. E. (2002). X-Ray Point Sources in the Central Region of M31 as Seen by Chandra. *ApJ*, 577:738–756.

Kotani, T., Kawai, N., Matsuoka, M., and Brinkmann, W. (1996). Iron-Line Diagnostics of the Jets of SS 433. *PASJ*, 48:619–629.

Kraft, R. P., Burrows, D. N., and Nousek, J. A. (1991). Determination of confidence limits for experiments with low numbers of counts. *ApJ*, 374:344–355.

Kraft, R. P., Forman, W. R., Jones, C., Murray, S. S., Hardcastle, M. J., and Worrall, D. M. (2002). Chandra Observations of the X-Ray Jet in Centaurus A. *ApJ*, 569:54–71.

Krause, M., Beck, R., and Hummel, E. (1989). The Magnetic Field Structures in Two Nearby Spiral Galaxies - Part Two - the Bisymmetric Spiral Magnetic Field in M81. *A&A*, 217:17.

Kreidberg, L., Bailyn, C. D., Farr, W. M., and Kalogera, V. (2012). Mass Measurements of Black Holes in X-Ray Transients: Is There a Mass Gap? *ApJ*, 757:36.

Krivosheyev, Y. M., Bisnovatyi-Kogan, G. S., Cherepashchuk, A. M., and Postnov, K. A. (2009). Monte Carlo simulations of the broad-band X-ray continuum of SS433. *MNRAS*, 394:1674–1684.

Kubota, A., Done, C., and Makishima, K. (2002). Another interpretation of the power-law-type spectrum of an ultraluminous compact X-ray source in IC 342. *MNRAS*, 337:L11–L15.

Kubota, A., Ebisawa, K., Makishima, K., and Nakazawa, K. (2005). On the Temperature Profile of Radiatively Efficient Geometrically Thin Disks in Black Hole Binaries with the ASCA GIS. *ApJ*, 631:1062–1071.

Kubota, A. and Makishima, K. (2004). The Three Spectral Regimes Found in the Stellar Black Hole XTE J1550-564 in Its High/Soft State. *ApJ*, 601:428–438.

Kubota, A., Mizuno, T., Makishima, K., Fukazawa, Y., Kotoku, J., Ohnishi, T., and Tashiro, M. (2001). Discovery of Spectral Transitions from Two Ultraluminous Compact X-Ray Sources in IC 342. *ApJL*, 547:L119–L122.

Kubota, A., Tanaka, Y., Makishima, K., Ueda, Y., Dotani, T., Inoue, H., and Yamaoka, K. (1998). Evidence for a Black Hole in the X-Ray Transient GRS 1009-45. *PASJ*, 50:667–673.

Kubota, K., Ueda, Y., Kawai, N., Kotani, T., Namiki, M., Kinugasa, K., Ozaki, S., Iijima, T., Fabrika, S., Yuasa, T., Yamada, S., and Makishima, K. (2010). Suzaku X-Ray and Optical Spectroscopic Observations of SS 433 in the 2006 April Multiwavelength Campaign. *PASJ*, 62:323–333.

Kuntz, K. D., Long, K. S., and Kilgard, R. E. (2016). A Deep Chandra ACIS Survey of M51. *ApJ*, 827:46.

Lang, C. C., Kaaret, P., Corbel, S., and Mercer, A. (2007). A Radio Nebula Surrounding the Ultraluminous X-Ray Source in NGC 5408. *ApJ*, 666:79–85.

Lau, R. M., Kasliwal, M. M., Bond, H. E., Smith, N., Fox, O. D., Carlon, R., Cody, A. M., Contreras, C., Dykhoff, D., Gehrz, R., Hsiao, E., Jencson, J.,

Khan, R., Masci, F., Monard, L. A. G., Monson, A. J., Morrell, N., Phillips, M., and Ressler, M. E. (2016). Rising from the Ashes: Mid-infrared Re-brightening of the Impostor SN 2010da in NGC 300. *ApJ*, 830:142.

Laycock, S. G. T., Cappallo, R. C., and Moro, M. J. (2015a). Chandra and XMM monitoring of the black hole X-ray binary IC 10 X-1. *MNRAS*, 446:1399–1410.

Laycock, S. G. T., Maccarone, T. J., and Christodoulou, D. M. (2015b). Revisiting the dynamical case for a massive black hole in IC10 X-1. *MNRAS*, 452:L31–L35.

Lehmer, B. D., Xue, Y. Q., Brandt, W. N., Alexander, D. M., Bauer, F. E., Brusa, M., Comastri, A., Gilli, R., Hornschemeier, A. E., Luo, B., Paolillo, M., Ptak, A., Shemmer, O., Schneider, D. P., Tozzi, P., and Vignali, C. (2012). The 4 Ms Chandra Deep Field-South Number Counts Apportioned by Source Class: Pervasive Active Galactic Nuclei and the Ascent of Normal Galaxies. *ApJ*, 752:46.

Leitherer, C., Ekström, S., Meynet, G., Schaerer, D., Agienko, K. B., and Levesque, E. M. (2014). The Effects of Stellar Rotation. II. A Comprehensive Set of Starburst99 Models. *ApJS*, 212:14.

Leitherer, C., Schaerer, D., Goldader, J. D., Delgado, R. M. G., Robert, C., Kune, D. F., de Mello, D. F., Devost, D., and Heckman, T. M. (1999). Starburst99: Synthesis Models for Galaxies with Active Star Formation. *ApJS*, 123:3–40.

Li, K. L., Kong, A. K. H., Charles, P. A., Lu, T.-N., Bartlett, E. S., Coe, M. J., McBride, V., Rajoelimanana, A., Udalski, A., Masetti, N., and Franzen, T. (2012). A Luminous Be+White Dwarf Supersoft Source in the Wing of the SMC: MAXI J0158-744. *ApJ*, 761:99.

Linares, M., Shahbaz, T., and Casares, J. (2018). Peering into the Dark Side: Magnesium Lines Establish a Massive Neutron Star in PSR J2215+5135. *ApJ*, 859:54.

Lindegren, L., Hernandez, J., Bombrun, A., Klioner, S., Bastian, U., Ramos-Lerate, M., de Torres, A., Steidelmuller, H., Stephenson, C., Hobbs, D., Lammers, U., Biermann, M., Geyer, R., Hilger, T., Michalik, D., Stampa, U., McMillan, P. J., Castaneda, J., Clotet, M., Comoretto, G., Davidson, M., Fabricius, C., Gracia, G., Hambly, N. C., Hutton, A., Mora, A., Portell, J., van Leeuwen, F., Abbas, U., Abreu, A., Altmann, M., Andrei, A., Anglada, E., Balaguer-Nunez, L., Barache, C., Becciani, U., Bertone, S., Bianchi, L., Bouquillon, S., Bourda, G., Brusemeister, T., Bucciarelli, B., Busonero, D.,

Buzzi, R., Cancelliere, R., Carlucci, T., Charlot, P., Cheek, N., Crosta, M., Crowley, C., de Bruijne, J., de Felice, F., Drimmel, R., Esquej, P., Fienga, A., Fraile, E., Gai, M., Garralda, N., Gonzalez-Vidal, J. J., Guerra, R., Hauser, M., Hofmann, W., Holl, B., Jordan, S., Lattanzi, M. G., Lenhardt, H., Liao, S., Licata, E., Lister, T., Loffler, W., Marchant, J., Martin-Fleitas, J.-M., Messineo, R., Mignard, F., Morbidelli, R., Poggio, E., Riva, A., Rowell, N., Salguero, E., Sarasso, M., Sciacca, E., Siddiqui, H., Smart, R. L., Spagna, A., Steele, I., Taris, F., Torra, J., van Elteren, A., van Reeven, W., and Vecchiato, A. (2018). Gaia Data Release 2: The astrometric solution. *ArXiv e-prints*.

Lindegren, L., Lammers, U., Bastian, U., Hernández, J., Klioner, S., Hobbs, D., Bombrun, A., Michalik, D., Ramos-Lerate, M., Butkevich, A., Comoretto, G., Joliet, E., Holl, B., Hutton, A., Parsons, P., Steidelmüller, H., Abbas, U., Altmann, M., Andrei, A., Anton, S., Bach, N., Barache, C., Becciani, U., Berthier, J., Bianchi, L., Biermann, M., Bouquillon, S., Bourda, G., Brüsemeister, T., Bucciarelli, B., Busonero, D., Carlucci, T., Castañeda, J., Charlot, P., Clotet, M., Crosta, M., Davidson, M., de Felice, F., Drimmel, R., Fabricius, C., Fienga, A., Figueras, F., Fraile, E., Gai, M., Garralda, N., Geyer, R., González-Vidal, J. J., Guerra, R., Hambly, N. C., Hauser, M., Jordan, S., Lattanzi, M. G., Lenhardt, H., Liao, S., Löffler, W., McMillan, P. J., Mignard, F., Mora, A., Morbidelli, R., Portell, J., Riva, A., Sarasso, M., Serraller, I., Siddiqui, H., Smart, R., Spagna, A., Stampa, U., Steele, I., Taris, F., Torra, J., van Reeven, W., Vecchiato, A., Zschocke, S., de Bruijne, J., Gracia, G., Raison, F., Lister, T., Marchant, J., Messineo, R., Soffel, M., Osorio, J., de Torres, A., and O'Mullane, W. (2016). Gaia Data Release 1. Astrometry: one billion positions, two million proper motions and parallaxes. *A&A*, 595:A4.

Lipunova, G. V. (1999). Supercritical disk accretion with mass loss. *Astronomy Letters*, 25:508–517.

Liu, J. (2009). Multi-Epoch Multi-Wavelength Study of an Ultraluminous X-ray Source in M101: The Nature of the Secondary. *ApJ*, 704:1628–1639.

Liu, J. (2011). Chandra ACIS Survey of X-ray Point Sources in 383 Nearby Galaxies. I. The Source Catalog. *ApJS*, 192:10.

Liu, J. and Di Stefano, R. (2008). An Ultraluminous Supersoft X-Ray Source in M81: An Intermediate-Mass Black Hole? *ApJL*, 674:L73–L76.

Liu, J.-F. (2008). No Periodicity Revealed for an "Eclipsing" Ultraluminous Supersoft X-Ray Source in M81. *ApJS*, 177:181–188.

Liu, J.-F., Bai, Y., Wang, S., Justham, S., Lu, Y.-J., Gu, W.-M., Liu, Q.-Z., di Stefano, R., Guo, J.-C., Cabrera-Lavers, A., Álvarez, P., Cao, Y., and Kulkarni, S. (2015). Relativistic baryonic jets from an ultraluminous supersoft X-ray source. *Nature*, 528:108–110.

Liu, J.-F., Bregman, J. N., Bai, Y., Justham, S., and Crowther, P. (2013). Puzzling accretion onto a black hole in the ultraluminous X-ray source M 101 ULX-1. *Nature*, 503:500–503.

Liu, Q. Z. and Mirabel, I. F. (2005). A catalogue of ultraluminous X-ray sources in external galaxies. *A&A*, 429:1125–1129.

Livio, M. (1999). Astrophysical jets: a phenomenological examination of acceleration and collimation. *Physics Reports*, 311:225–245.

Long, K. S., Helfand, D. J., and Grabelsky, D. A. (1981). A soft X-ray study of the Large Magellanic Cloud. *ApJ*, 248:925–944.

Long, K. S., Kuntz, K. D., Blair, W. P., Godfrey, L., Plucinsky, P. P., Soria, R., Stockdale, C., and Winkler, P. F. (2014). A Deep Chandra ACIS Survey of M83. *ApJS*, 212:21.

Longair, M. S. (2011). *High Energy Astrophysics*.

Lubow, S. H. (1989). On the dynamics of mass transfer over an accretion disk. *ApJ*, 340:1064–1069.

Lusso, E., Comastri, A., Simmons, B. D., Mignoli, M., Zamorani, G., Vignali, C., Brusa, M., Shankar, F., Lutz, D., Trump, J. R., Maiolino, R., Gilli, R., Bolzonella, M., Puccetti, S., Salvato, M., Impey, C. D., Civano, F., Elvis, M., Mainieri, V., Silverman, J. D., Koekemoer, A. M., Bongiorno, A., Merloni, A., Berta, S., Le Floc'h, E., Magnelli, B., Pozzi, F., and Riguccini, L. (2012). Bolometric luminosities and Eddington ratios of X-ray selected active galactic nuclei in the XMM-COSMOS survey. *MNRAS*, 425:623–640.

Ly, C., De Young, D. S., and Bechtold, J. (2005). The Discovery of Extended Thermal X-Ray Emission from PKS 2152-699: Evidence for a "Jet-Cloud" Interaction. *ApJ*, 618:609–617.

Maccarone, T. J. (2003). Do X-ray binary spectral state transition luminosities vary? *A&A*, 409:697–706.

Makishima, K., Maejima, Y., Mitsuda, K., Bradt, H. V., Remillard, R. A., Tuohy, I. R., Hoshi, R., and Nakagawa, M. (1986). Simultaneous X-ray and optical observations of GX 339-4 in an X-ray high state. *ApJ*, 308:635–643.

Malzac, J. (2014). The spectral energy distribution of compact jets powered by internal shocks. *MNRAS*, 443:299–317.

Maoz, D. (2007). *Astrophysics in a Nutshell*. Princeton University Press.

Margon, B. (1984). Observations of SS 433. *ARA&A*, 22:507–536.

Marigo, P., Bressan, A., Nanni, A., Girardi, L., and Pumo, M. L. (2013). Evolution of thermally pulsing asymptotic giant branch stars - I. The COLIBRI code. *MNRAS*, 434:488–526.

Markowitz, A., Edelson, R., and Vaughan, S. (2003). Long-Term X-Ray Spectral Variability in Seyfert 1 Galaxies. *ApJ*, 598:935–955.

Marlowe, H., Kaaret, P., Lang, C., Feng, H., Grisé, F., Miller, N., Cseh, D., Corbel, S., and Mushotzky, R. F. (2014). Spectral state transitions of the Ultraluminous X-ray Source IC 342 X-1. *MNRAS*, 444:642–650.

Marshall, H. L., Canizares, C. R., Hillwig, T., Mioduszewski, A., Rupen, M., Schulz, N. S., Nowak, M., and Heinz, S. (2013). Multiwavelength Observations of the SS 433 Jets. *ApJ*, 775:75.

Marshall, H. L., Canizares, C. R., and Schulz, N. S. (2002a). The High-Resolution X-Ray Spectrum of SS 433 Using the Chandra HETGS. *ApJ*, 564:941–952.

Marshall, H. L., Miller, B. P., Davis, D. S., Perlman, E. S., Wise, M., Canizares, C. R., and Harris, D. E. (2002b). A High-Resolution X-Ray Image of the Jet in M87. *ApJ*, 564:683–687.

Marston, A. P., Elmegreen, D., Elmegreen, B., Forman, W., Jones, C., and Flanagan, K. (1995). ROSAT observations of the luminous X-ray sources in M51. *ApJ*, 438:663–671.

Massaro, F., Harris, D. E., and Cheung, C. C. (2011). Large-scale Extragalactic Jets in the Chandra Era. I. Data Reduction and Analysis. *ApJS*, 197:24.

Massaro, F., Harris, D. E., Liuzzo, E., Orienti, M., Paladino, R., Paggi, A., Tremblay, G. R., Wilkes, B. J., Kuraszkiewicz, J., Baum, S. A., and O'Dea, C. P. (2015). The Chandra Survey of Extragalactic Sources in the 3CR Catalog: X-ray Emission from Nuclei, Jets, and Hotspots in the Chandra Archival Observations. *ApJS*, 220:5.

Mathewson, D. S. and Clarke, J. N. (1973). Supernova remnants in the Large Magellanic Cloud. *ApJ*, 180:725–738.

Matsumoto, H., Tsuru, T. G., Koyama, K., Awaki, H., Canizares, C. R., Kawai, N., Matsushita, S., and Kawabe, R. (2001). Discovery of a Luminous, Variable, Off-Center Source in the Nucleus of M82 with the Chandra High-Resolution Camera. *ApJL*, 547:L25–L28.

McClintock, J. E., London, R. A., Bond, H. E., and Grauer, A. D. (1982). The noncompact binary X-ray source 4U 2129+47. *ApJ*, 258:245–253.

McClintock, J. E. and Remillard, R. A. (2006). *Black hole binaries*, pages 157–213.

McGowan, K. E., Charles, P. A., Blustin, A. J., Livio, M., O'Donoghue, D., and Heathcote, B. (2005). XMM spectroscopy of the transient supersoft source RXJ0513.9 - 6951: probing the dynamic white dwarf photosphere. *MNRAS*, 364:462–474.

McKeough, K., Siemiginowska, A., Cheung, C. C., Stawarz, Ł., Kashyap, V. L., Stein, N., Stampoulis, V., van Dyk, D. A., Wardle, J. F. C., Lee, N. P., Harris, D. E., Schwartz, D. A., Donato, D., Maraschi, L., and Tavecchio, F. (2016). Detecting Relativistic X-Ray Jets in High-redshift Quasars. *ApJ*, 833:123.

McMullin, J. P., Waters, B., Schiebel, D., Young, W., and Golap, K. (2007). CASA Architecture and Applications. In Shaw, R. A., Hill, F., and Bell, D. J., editors, *Astronomical Data Analysis Software and Systems XVI*, volume 376 of *Astronomical Society of the Pacific Conference Series*, page 127.

McQuinn, K. B. W., Skillman, E. D., Dolphin, A. E., Berg, D., and Kennicutt, R. (2016). The Distance to M51. *ApJ*, 826:21.

Merloni, A., Predehl, P., Becker, W., Böhringer, H., Boller, T., Brunner, H., Brusa, M., Dennerl, K., Freyberg, M., Friedrich, P., Georgakakis, A., Haberl, F., Hasinger, G., Meidinger, N., Mohr, J., Nandra, K., Rau, A., Reiprich, T. H., Robrade, J., Salvato, M., Santangelo, A., Sasaki, M., Schwope, A., Wilms, J., and German eROSITA Consortium, t. (2012). eROSITA Science Book: Mapping the Structure of the Energetic Universe. *ArXiv e-prints*.

Mészáros, P. and Rees, M. J. (2001). Collapsar Jets, Bubbles, and Fe Lines. *ApJL*, 556:L37–L40.

Mewe, R., Gronenschild, E. H. B. M., and van den Oord, G. H. J. (1985). Calculated X-radiation from optically thin plasmas. V. *A&AS*, 62:197–254.

Mewe, R., Lemen, J. R., and van den Oord, G. H. J. (1986). Calculated X-radiation from optically thin plasmas. VI - Improved calculations for continuum

emission and approximation formulae for nonrelativistic average Gaunt factors. *A&AS*, 65:511–536.

Meyer, E. T., Georganopoulos, M., Sparks, W. B., Perlman, E., van der Marel, R. P., Anderson, J., Sohn, S. T., Biretta, J., Norman, C., and Chiaberge, M. (2015). A kiloparsec-scale internal shock collision in the jet of a nearby radio galaxy. *Nature*, 521:495–497.

Middleton, M. J., Heil, L., Pintore, F., Walton, D. J., and Roberts, T. P. (2015a). A spectral-timing model for ULXs in the supercritical regime. *MNRAS*, 447:3243–3263.

Middleton, M. J., Roberts, T. P., Done, C., and Jackson, F. E. (2011a). Challenging times: a re-analysis of NGC 5408 X-1. *MNRAS*, 411:644–652.

Middleton, M. J., Sutton, A. D., and Roberts, T. P. (2011b). X-ray spectral evolution in the ultraluminous X-ray source M33 X-8. *MNRAS*, 417:464–471.

Middleton, M. J., Walton, D. J., Fabian, A., Roberts, T. P., Heil, L., Pinto, C., Anderson, G., and Sutton, A. (2015b). Diagnosing the accretion flow in ultraluminous X-ray sources using soft X-ray atomic features. *MNRAS*, 454:3134–3142.

Middleton, M. J., Walton, D. J., Roberts, T. P., and Heil, L. (2014). Broad absorption features in wind-dominated ultraluminous X-ray sources? *MNRAS*, 438:L51–L55.

Millar, W. C., White, G. L., Filipović, M. D., Payne, J. L., Crawford, E. J., Pannuti, T. G., and Staggs, W. D. (2011). Optical spectra of supernova remnant candidates in the Sculptor Group galaxy NGC 300. *Ap&SS*, 332:221–239.

Miller, B. W. (1995). The Optical Counterpart to the Extremely Luminous X-Ray Source near Holmberg IX: A Possible Supershell in a Tidal Tail. *ApJL*, 446:L75.

Miller, B. W. and Hodge, P. (1994). H II regions in M81 group dwarf galaxies. *ApJ*, 427:656–675.

Miller, J. M., Bachetti, M., Barret, D., Harrison, F. A., Fabian, A. C., Webb, N. A., Walton, D. J., and Rana, V. (2014). Patchy Accretion Disks in Ultraluminous X-Ray Sources. *ApJL*, 785:L7.

Miller, J. M., Fabbiano, G., Miller, M. C., and Fabian, A. C. (2003). X-Ray Spectroscopic Evidence for Intermediate-Mass Black Holes: Cool Accretion Disks in Two Ultraluminous X-Ray Sources. *ApJL*, 585:L37–L40.

Miller, J. M., Fabian, A. C., and Miller, M. C. (2004). A Comparison of Intermediate-Mass Black Hole Candidate Ultraluminous X-Ray Sources and Stellar-Mass Black Holes. *ApJL*, 614:L117–L120.

Miller, J. M., Walton, D. J., King, A. L., Reynolds, M. T., Fabian, A. C., Miller, M. C., and Reis, R. C. (2013). Revisiting Putative Cool Accretion Disks in Ultraluminous X-Ray Sources. *ApJL*, 776:L36.

Miller, N. A., Mushotzky, R. F., and Neff, S. G. (2005). Radio Emission Associated with the Ultraluminous X-Ray Source in Holmberg II. *ApJL*, 623:L109–L112.

Mineo, S., Gilfanov, M., and Sunyaev, R. (2012). X-ray emission from star-forming galaxies - I. High-mass X-ray binaries. *MNRAS*, 419:2095–2115.

Mirabel, I. F., Dijkstra, M., Laurent, P., Loeb, A., and Pritchard, J. R. (2011). Stellar black holes at the dawn of the universe. *A&A*, 528:A149.

Mitsuda, K., Inoue, H., Koyama, K., Makishima, K., Matsuoka, M., Ogawara, Y., Suzuki, K., Tanaka, Y., Shibazaki, N., and Hirano, T. (1984). Energy spectra of low-mass binary X-ray sources observed from TENMA. *PASJ*, 36:741–759.

Miyaji, T., Lehmann, I., and Hasinger, G. (2001). Multiple Components of the Luminous Compact X-Ray Source at the Edge of Holmberg II Observed by ASCA and ROSAT. *AJ*, 121:3041–3047.

Miyamoto, S., Iga, S., Kitamoto, S., and Kamado, Y. (1993). Another canonical time variation of X-rays from black hole candidates in the very high flare state? *ApJL*, 403:L39–L42.

Miyamoto, S. and Kitamoto, S. (1991). A jet model for a very high state of GX 339 - 4. *ApJ*, 374:741–743.

Morii, M., Tomida, H., Kimura, M., Suwa, F., Negoro, H., Serino, M., Kennea, J. A., Page, K. L., Curran, P. A., Walter, F. M., Kuin, N. P. M., Pritchard, T., Nakahira, S., Hiroi, K., Usui, R., Kawai, N., Osborne, J. P., Mihara, T., Sugizaki, M., Gehrels, N., Kohama, M., Kotani, T., Matsuoka, M., Nakajima, M., Roming, P. W. A., Sakamoto, T., Sugimori, K., Tsuboi, Y., Tsunemi, H., Ueda, Y., Ueno, S., and Yoshida, A. (2013). Extraordinary Luminous Soft X-Ray Transient MAXI J0158-744 as an Ignition of a Nova on a Very Massive O-Ne White Dwarf. *ApJ*, 779:118.

Motch, C., Pakull, M. W., Soria, R., Grisé, F., and Pietrzyński, G. (2014). A mass of less than 15 solar masses for the black hole in an ultraluminous X-ray source. *Nature*, 514:198–201.

Moustakas, J., Kennicutt, Jr., R. C., Tremonti, C. A., Dale, D. A., Smith, J.-D. T., and Calzetti, D. (2010). Optical Spectroscopy and Nebular Oxygen Abundances of the Spitzer/SINGS Galaxies. *ApJS*, 190:233–266.

Mucciarelli, P., Zampieri, L., Treves, A., Turolla, R., and Falomo, R. (2007). X-Ray and Optical Variability of the Ultraluminous X-Ray Source NGC 1313 X-2. *ApJ*, 658:999–1005.

Mukai, K., Pence, W. D., Snowden, S. L., and Kuntz, K. D. (2003). Chandra Observation of Luminous and Ultraluminous X-Ray Binaries in M101. *ApJ*, 582:184–189.

Mukai, K., Still, M., Corbet, R. H. D., Kuntz, K. D., and Barnard, R. (2005). The X-Ray Properties of M101 ULX-1 = CXOKM101 J140332.74+542102. *ApJ*, 634:1085–1092.

Mushtukov, A. A., Suleimanov, V. F., Tsygankov, S. S., and Poutanen, J. (2015). On the maximum accretion luminosity of magnetized neutron stars: connecting X-ray pulsars and ultraluminous X-ray sources. *MNRAS*, 454:2539–2548.

Narayan, R., Sądowski, A., and Soria, R. (2017). Spectra of black hole accretion models of ultraluminous X-ray sources. *MNRAS*, 469:2997–3014.

Neilsen, J. and Lee, J. C. (2009). Accretion disk winds as the jet suppression mechanism in the microquasar GRS 1915+105. *Nature*, 458:481–484.

Ness, J.-U. (2010). Observational evidence for expansion in the SSS spectra of novae. *Astronomische Nachrichten*, 331:179–182.

Ness, J.-U., Osborne, J. P., Henze, M., Dobrotka, A., Drake, J. J., Ribeiro, V. A. R. M., Starrfield, S., Kuulkers, E., Behar, E., Hernanz, M., Schwarz, G., Page, K. L., Beardmore, A. P., and Bode, M. F. (2013). Obscuration effects in super-soft-source X-ray spectra. *A&A*, 559:A50.

Ohsuga, K. and Mineshige, S. (2011). Global Structure of Three Distinct Accretion Flows and Outflows around Black Holes from Two-dimensional Radiation-magnetohydrodynamic Simulations. *ApJ*, 736:2.

Ohsuga, K., Mori, M., Nakamoto, T., and Mineshige, S. (2005). Supercritical Accretion Flows around Black Holes: Two-dimensional, Radiation Pressure-dominated Disks with Photon Trapping. *ApJ*, 628:368–381.

Orio, M., Nelson, T., Bianchini, A., Di Mille, F., and Harbeck, D. (2010). A Census of the Supersoft X-ray Sources in M31. *ApJ*, 717:739–765.

Osterbrock, D. E. (1989). *Astrophysics of gaseous nebulae and active galactic nuclei*. University Science Books.

Paczynski, B. (1977). A model of accretion disks in close binaries. *ApJ*, 216:822–826.

Pagel, B. E. J., Edmunds, M. G., Blackwell, D. E., Chun, M. S., and Smith, G. (1979). On the composition of H II regions in southern galaxies. I - NGC 300 and 1365. *MNRAS*, 189:95–113.

Pakull, M. W. and Angebault, L. P. (1986). Detection of an X-ray-ionized nebula around the black hole candidate binary LMC X-1. *Nature*, 322:511–517.

Pakull, M. W. and Grisé, F. (2008). Ultraluminous X-ray Sources: Beambags and Optical Counterparts. In Bandyopadhyay, R. M., Wachter, S., Gelino, D., and Gelino, C. R., editors, *A Population Explosion: The Nature & Evolution of X-ray Binaries in Diverse Environments*, volume 1010 of *American Institute of Physics Conference Series*, pages 303–307.

Pakull, M. W., Grisé, F., and Motch, C. (2006). Ultraluminous X-ray Sources: Bubbles and Optical Counterparts. In Meurs, E. J. A. and Fabbiano, G., editors, *Populations of High Energy Sources in Galaxies*, volume 230 of *IAU Symposium*, pages 293–297.

Pakull, M. W. and Mirioni, L. (2002). Optical Counterparts of Ultraluminous X-Ray Sources. In *online proceedings of the symposium 'New Visions of the X-ray Universe in the XMM-Newton and Chandra Era'*, 26-30 November 2001, ESTEC, The Netherlands, (astro-ph/0202488).

Pakull, M. W. and Mirioni, L. (2003). Bubble Nebulae around Ultraluminous X-Ray Sources. In Arthur, J. and Henney, W. J., editors, *Revista Mexicana de Astronomia y Astrofisica Conference Series*, volume 15 of *Revista Mexicana de Astronomia y Astrofisica Conference Series*, pages 197–199.

Pakull, M. W., Motch, C., Bianchi, L., Thomas, H.-C., Guibert, J., Beaulieu, J. P., Grison, P., and Schaeidt, S. (1993). Optical/UV counterpart of the supersoft transient X-ray source RX J0513.9-6951 in the Large Magellanic Cloud. *A&A*, 278:L39–L42.

Pakull, M. W., Soria, R., and Motch, C. (2010). A 300-parsec-long jet-inflated bubble around a powerful microquasar in the galaxy NGC 7793. *Nature*, 466:209–212.

Palumbo, G. G. C., Fabbiano, G., Trinchieri, G., and Fransson, C. (1985). An X-ray study of M51 (NGC 5194) and its companion (NGC 5195). *ApJ*, 298:259–267.

Panferov, A. A. (2017). Jets of SS 433 on scales of dozens of parsecs. *A&A*, 599:A77.

Pannuti, T. G., Duric, N., Lacey, C. K., Goss, W. M., Hoopes, C. G., Walterbos, R. A. M., and Magnor, M. A. (2000). An X-Ray, Optical, and Radio Search for Supernova Remnants in the Nearby Sculptor Group Sd Galaxy NGC 300. *ApJ*, 544:780–804.

Payne, J. L., Filipović, M. D., Pannuti, T. G., Jones, P. A., Duric, N., White, G. L., and Carpano, S. (2004). Multi-frequency study of extragalactic supernova remnants and H II regions. Sculptor group Sd galaxy NGC 300. *A&A*, 425:443–456.

Pietsch, W., Freyberg, M., and Haberl, F. (2005). An XMM-Newton survey of M 31. *A&A*, 434:483–496.

Pilyugin, L. S. and Thuan, T. X. (2005). Oxygen Abundance Determination in H II Regions: The Strong Line Intensities-Abundance Calibration Revisited. *ApJ*, 631:231–243.

Pinto, C., Alston, W., Soria, R., Middleton, M. J., Walton, D. J., Sutton, A. D., Fabian, A. C., Earnshaw, H., Urquhart, R., Kara, E., and Roberts, T. P. (2017a). From ultraluminous X-ray sources to ultraluminous supersoft sources: NGC 55 ULX, the missing link. *MNRAS*, 468:2865–2883.

Pinto, C., Fabian, A., Middleton, M., and Walton, D. (2017b). Ultrafast outflows in ultraluminous X-ray sources. *Astronomische Nachrichten*, 338:234–240.

Pinto, C., Middleton, M. J., and Fabian, A. C. (2016). Resolved atomic lines reveal outflows in two ultraluminous X-ray sources. *Nature*, 533:64–67.

Pintore, F., Zampieri, L., Stella, L., Wolter, A., Mereghetti, S., and Israel, G. L. (2017). Pulsator-like Spectra from Ultraluminous X-Ray Sources and the Search for More Ultraluminous Pulsars. *ApJ*, 836:113.

Pintore, F., Zampieri, L., Sutton, A. D., Roberts, T. P., Middleton, M. J., and Gladstone, J. C. (2016). The ultraluminous X-ray source NGC 5643 ULX1: a large stellar mass black hole accreting at super-Eddington rates? *MNRAS*, 459:455–466.

Plucinsky, P. P., O'Dell, S. L., Tice, N. W., Swartz, D. A., Bautz, M. W., DePasquale, J. M., Edgar, R. J., Garmire, G. P., Giordano, R., Grant, C. E., Knollenberg, P., Kissel, S., LaMarr, B., Logan, R., Mach, M., Marshall, H. L., McKendrick, L., Prigozhin, G. Y., Schwartz, D., Schulz, N. S., Shropshire, D., Trinh, T., Vikhlinin, A. A., and Virani, S. N. (2004). An evaluation of a bake-out of the ACIS instrument on the Chandra X-Ray Observatory. In Hasinger, G. and Turner, M. J. L., editors, *UV and Gamma-Ray Space Telescope Systems*, volume 5488 of *Proc. SPIE*, pages 251–263.

Pogge, R. W., Atwood, B., Brewer, D. F., Byard, P. L., Derwent, M. A., Gonzalez, R., Martini, P., Mason, J. A., O'Brien, T. P., Osmer, P. S., Pappalardo, D. P., Steinbrecher, D. P., Teiga, E. J., and Zhelem, R. (2010). The multi-object double spectrographs for the Large Binocular Telescope. In *Ground-based and Airborne Instrumentation for Astronomy III*, volume 7735 of *Proc. SPIE*, page 77350A.

Ponti, G., Fender, R. P., Begelman, M. C., Dunn, R. J. H., Neilsen, J., and Coriat, M. (2012). Ubiquitous equatorial accretion disc winds in black hole soft states. *MNRAS*, 422:11–15.

Pooley, D. and Rappaport, S. (2005). X-Ray and Optical Eclipses in Ultraluminous X-Ray Sources as Possible Indicators of Black Hole Mass. *ApJL*, 634:L85–L88.

Pounds, K. A., King, A. R., Page, K. L., and O'Brien, P. T. (2003). Evidence of a high-velocity ionized outflow in a second narrow-line quasar PG 0844+349. *MNRAS*, 346:1025–1030.

Poutanen, J., Lipunova, G., Fabrika, S., Butkevich, A. G., and Abolmasov, P. (2007). Supercritically accreting stellar mass black holes as ultraluminous X-ray sources. *MNRAS*, 377:1187–1194.

Prestwich, A. H., Kilgard, R., Crowther, P. A., Carpano, S., Pollock, A. M. T., Zezas, A., Saar, S. H., Roberts, T. P., and Ward, M. J. (2007). The Orbital Period of the Wolf-Rayet Binary IC 10 X-1: Dynamic Evidence that the Compact Object Is a Black Hole. *ApJL*, 669:L21–L24.

Pringle, J. E. and Rees, M. J. (1972). Accretion Disc Models for Compact X-Ray Sources. *A&A*, 21:1.

Radburn-Smith, D. J., de Jong, R. S., Seth, A. C., Bailin, J., Bell, E. F., Brown, T. M., Bullock, J. S., Courteau, S., Dalcanton, J. J., Ferguson, H. C., Goudfrooij, P., Holfeltz, S., Holwerda, B. W., Purcell, C., Sick, J., Streich, D., Vlajic, M., and Zucker, D. B. (2011). The GHOSTS Survey. I. Hubble Space Telescope Advanced Camera for Surveys Data. *ApJS*, 195:18.

Rajoelimanana, A. F., Charles, P. A., Meintjes, P. J., Odendaal, A., and Udalski, A. (2013). Optical and X-ray properties of CAL 83 - I. Quasi-periodic optical and supersoft variability. *MNRAS*, 432:2886–2894.

Ramirez-Ruiz, E., Celotti, A., and Rees, M. J. (2002). Events in the life of a cocoon surrounding a light, collapsar jet. *MNRAS*, 337:1349–1356.

Rana, V., Harrison, F. A., Bachetti, M., Walton, D. J., Furst, F., Barret, D., Miller, J. M., Fabian, A. C., Boggs, S. E., Christensen, F. C., Craig, W. W., Grefenstette, B. W., Hailey, C. J., Madsen, K. K., Ptak, A. F., Stern, D., Webb, N. A., and Zhang, W. W. (2015). The Broadband XMM-Newton and NuSTAR X-Ray Spectra of Two Ultraluminous X-Ray Sources in the Galaxy IC 342. *ApJ*, 799:121.

Ratti, E. M., Jonker, P. G., Miller-Jones, J. C. A., Torres, M. A. P., Homan, J., Markoff, S., Tomsick, J. A., Kaaret, P., Wijnands, R., Gallo, E., Özel, F., Steeghs, D. T. H., and Fender, R. P. (2012). The black hole candidate XTE J1752-223 towards and in quiescence: optical and simultaneous X-ray-radio observations. *MNRAS*, 423:2656–2667.

Ravera, L., Barret, D., den Herder, J. W., Piro, L., Clédassou, R., Pointecouteau, E., Peille, P., Pajot, F., Arnaud, M., Pigot, C., Duband, L., Cara, C., den Hartog, R. H., Gottardi, L., Akamatsu, H., van der Kuur, J., van Weers, H. J., de Plaa, J., Macculi, C., Lotti, S., Torrioli, G., Gatti, F., Valenziano, L., Barbera, M., Barcons, X., Ceballos, M. T., Fàbrega, L., Mas-Hesse, J. M., Page, M. J., Guttridge, P. R., Willingale, R., Paltani, S., Genolet, L., Bozzo, E., Rauw, G., Renotte, E., Wilms, J., and Schmid, C. (2014). The X-ray Integral Field Unit (X-IFU) for Athena. In *Space Telescopes and Instrumentation 2014: Ultraviolet to Gamma Ray*, volume 9144 of *Proc. SPIE*, page 91442L.

Read, A. M. and Pietsch, W. (2001). X-ray emission from the Sculptor galaxy NGC 300. *A&A*, 373:473–484.

Read, A. M., Ponman, T. J., and Strickland, D. K. (1997). ROSAT PSPC observations of nearby spiral galaxies - I. The data. *MNRAS*, 286:626–668.

Rees, M. J. (1978). The M87 jet - Internal shocks in a plasma beam. *MNRAS*, 184:61P–65P.

Rees, M. J. and Meszaros, P. (1994). Unsteady outflow models for cosmological gamma-ray bursts. *ApJL*, 430:L93–L96.

Remillard, R. A. and McClintock, J. E. (2006). X-Ray Properties of Black-Hole Binaries. *ARA&A*, 44:49–92.

Risaliti, G., Elvis, M., Fabbiano, G., Baldi, A., and Zezas, A. (2005). Rapid Compton-thick/Compton-thin Transitions in the Seyfert 2 Galaxy NGC 1365. *ApJL*, 623:L93–L96.

Risaliti, G., Elvis, M., Fabbiano, G., Baldi, A., Zezas, A., and Salvati, M. (2007). Occultation Measurement of the Size of the X-Ray-emitting Region in the Active Galactic Nucleus of NGC 1365. *ApJL*, 659:L111–L114.

Rizzi, L., Bresolin, F., Kudritzki, R.-P., Gieren, W., and Pietrzyński, G. (2006). The Araucaria Project: The Distance to NGC 300 from the Red Giant Branch Tip Using HST ACS Imaging. *ApJ*, 638:766–771.

Roberts, T. P. (2007). X-ray observations of ultraluminous X-ray sources. *Ap&SS*, 311:203–212.

Roberts, T. P. and Colbert, E. J. M. (2003). Chandra reveals a black hole X-ray binary within the ultraluminous supernova remnant MF 16. *MNRAS*, 341:L49–L54.

Roberts, T. P., Gladstone, J. C., Hetf, L. M., Done, C., and Vaughan, S. A. (2010). The Ultraluminous State. *X-ray Astronomy 2009; Present Status, Multi-Wavelength Approach and Future Perspectives*, 1248:123–126.

Roberts, T. P., Warwick, R. S., Ward, M. J., and Goad, M. R. (2004). Chandra observations of five ultraluminous X-ray sources in nearby galaxies. *MNRAS*, 349:1193–1210.

Roberts, T. P., Warwick, R. S., Ward, M. J., Goad, M. R., and Jenkins, L. P. (2005). XMM-Newton EPIC observations of the ultraluminous X-ray source NGC 5204 X-1. *MNRAS*, 357:1363–1369.

Rosat, C. (2000). VizieR Online Data Catalog: Second ROSAT PSPC Catalog (ROSAT, 2000). *VizieR Online Data Catalog*, 9030.

ROSAT Scientific Team (2000). VizieR Online Data Catalog: ROSAT HRI Pointed Observations (1RXH) (ROSAT Team, 2000). *VizieR Online Data Catalog*, 9028.

Rosen, S. (2016). VizieR Online Data Catalog: Enhanced 3XMM catalogue (3XMMe) (Rosen+, 2016). *VizieR Online Data Catalog*, 9047.

Russell, D. M., Markoff, S., Casella, P., Cantrell, A. G., Chatterjee, R., Fender, R. P., Gallo, E., Gandhi, P., Homan, J., Maitra, D., Miller-Jones, J. C. A., O'Brien, K., and Shahbaz, T. (2013). Jet spectral breaks in black hole X-ray binaries. *MNRAS*, 429:815–832.

Russell, T. D., Soria, R., Miller-Jones, J. C. A., Curran, P. A., Markoff, S., Russell, D. M., and Sivakoff, G. R. (2014). The accretion-ejection coupling in the black hole candidate X-ray binary MAXI J1836-194. *MNRAS*, 439:1390–1402.

Rybicki, G. B. and Lightman, A. P. (1979). *Radiative processes in astrophysics*.

Saikia, D. J. and Jamrozy, M. (2009). Recurrent activity in Active Galactic Nuclei. *Bulletin of the Astronomical Society of India*, 37.

Sault, R. J., Teuben, P. J., and Wright, M. C. H. (1995). A Retrospective View of MIRIAD. In Shaw, R. A., Payne, H. E., and Hayes, J. J. E., editors, *Astronomical Data Analysis Software and Systems IV*, volume 77 of *Astronomical Society of the Pacific Conference Series*, page 433.

Sądowski, A. (2009). Slim Disks Around Kerr Black Holes Revisited. *ApJS*, 183:171–178.

Sądowski, A. and Narayan, R. (2015). Powerful radiative jets in supercritical accretion discs around non-spinning black holes. *MNRAS*, 453:3213–3221.

Sądowski, A. and Narayan, R. (2016). Three-dimensional simulations of supercritical black hole accretion discs - luminosities, photon trapping and variability. *MNRAS*, 456:3929–3947.

Schlafly, E. F. and Finkbeiner, D. P. (2011). Measuring Reddening with Sloan Digital Sky Survey Stellar Spectra and Recalibrating SFD. *ApJ*, 737:103.

Schoenmakers, A. P., de Bruyn, A. G., Röttgering, H. J. A., van der Laan, H., and Kaiser, C. R. (2000). Radio galaxies with a 'double-double morphology' - I. Analysis of the radio properties and evidence for interrupted activity in active galactic nuclei. *MNRAS*, 315:371–380.

Schweizer, F., Burns, C. R., Madore, B. F., Mager, V. A., Phillips, M. M., Freedman, W. L., Boldt, L., Contreras, C., Folatelli, G., González, S., Hamuy, M., Krzeminski, W., Morrell, N. I., Persson, S. E., Roth, M. R., and Stritzinger, M. D. (2008). a New Distance to the Antennae Galaxies (ngc 4038/39) Based on the Type ia Supernova 2007sr. *AJ*, 136:1482–1489.

Shakura, N. I. and Sunyaev, R. A. (1973). Black holes in binary systems. Observational appearance. *A&A*, 24:337–355.

Shappee, B. J. and Stanek, K. Z. (2011). A New Cepheid Distance to the Giant Spiral M101 Based on Image Subtraction of Hubble Space Telescope/Advanced Camera for Surveys Observations. *ApJ*, 733:124.

Shaw, R. A. and Dufour, R. J. (1994). The FIVEL Nebular Modelling Package in STSDAS. In Crabtree, D. R., Hanisch, R. J., and Barnes, J., editors, *Astronomical Data Analysis Software and Systems III*, volume 61 of *Astronomical Society of the Pacific Conference Series*, page 327.

Shen, R.-F., Barniol Duran, R., Nakar, E., and Piran, T. (2015). The nature of ULX source M101 X-1: optically thick outflow from a stellar mass black hole. *MNRAS*, 447:L60–L64.

Shetty, R., Vogel, S. N., Ostriker, E. C., and Teuben, P. J. (2007). Kinematics of Spiral-Arm Streaming in M51. *ApJ*, 665:1138–1158.

Siemiginowska, A., Stawarz, Ł., Cheung, C. C., Aldcroft, T. L., Bechtold, J., Burke, D. J., Evans, D., Holt, J., Jamrozy, M., and Migliori, G. (2012). Deep Chandra X-Ray Imaging of a nearby Radio Galaxy 4C+29.30: X-Ray/Radio Connection. *ApJ*, 750:124.

Silk, J. and Rees, M. J. (1998). Quasars and galaxy formation. *A&A*, 331:L1–L4.

Simón-Díaz, S. and Stasińska, G. (2008). The ionizing radiation from massive stars and its impact on HII regions: results from modern model atmospheres. *MNRAS*, 389:1009–1021.

Sirianni, M., Jee, M. J., Benítez, N., Blakeslee, J. P., Martel, A. R., Meurer, G., Clampin, M., De Marchi, G., Ford, H. C., Gilliland, R., Hartig, G. F., Illingworth, G. D., Mack, J., and McCann, W. J. (2005). The Photometric Performance and Calibration of the Hubble Space Telescope Advanced Camera for Surveys. *PASP*, 117:1049–1112.

Siwek, M., Sądowski, A., Narayan, R., Roberts, T. P., and Soria, R. (2017). Optical and X-ray luminosities of expanding nebulae around ultraluminous X-ray sources. *MNRAS*, 470:361–371.

Skrutskie, M. F., Cutri, R. M., Stiening, R., Weinberg, M. D., Schneider, S., Carpenter, J. M., Beichman, C., Capps, R., Chester, T., Elias, J., Huchra, J., Liebert, J., Lonsdale, C., Monet, D. G., Price, S., Seitzer, P., Jarrett, T., Kirkpatrick, J. D., Gizis, J. E., Howard, E., Evans, T., Fowler, J., Fullmer, L., Hurt, R., Light, R., Kopan, E. L., Marsh, K. A., McCallon, H. L., Tam, R., Van Dyk, S., and Wheelock, S. (2006). The Two Micron All Sky Survey (2MASS). *AJ*, 131:1163–1183.

Smith, N. and Owocki, S. P. (2006). On the Role of Continuum-driven Eruptions in the Evolution of Very Massive Stars and Population III Stars. *ApJL*, 645:L45–L48.

Smith, R. K., Abraham, M., Allured, R., Bautz, M., Bookbinder, J., Bregman, J., Brenneman, L., Brickhouse, N. S., Burrows, D., Burwitz, V., Cheimets, P. N., Costantini, E., Dawson, S., DeRoo, C., Falcone, A., Foster, A. R., Gallo, L., Grant, C. E., Günther, H. M., Heilmann, R. K., Hertz, E., Hine, B., Huenemoerder, D., Kaastra, J. S., Kreykenbohm, I., Madsen, K. K., McEntaffer, R., Miller, E., Miller, J., Morse, E., Mushotzky, R., Nandra, K., Nowak, M., Paerels, F., Petre, R., Poppenhaeger, K., Ptak, A., Reid, P., Sanders, J., Schattenburg, M., Schulz, N., Smale, A., Temi, P., Valencic, L., Walker, S., Willingale, R., Wilms, J., and Wolk, S. J. (2017). Arcus: exploring the formation and evolution of clusters, galaxies, and stars. In *Society of Photo-Optical Instrumentation Engineers (SPIE) Conference Series*, volume 10397 of *Society of Photo-Optical Instrumentation Engineers (SPIE) Conference Series*, page 103970Q.

Soria, R. (2007). Bridging the gap between stellar-mass black holes and ultraluminous X-ray sources. *Ap&SS*, 311:213–222.

Soria, R., Fender, R. P., Hannikainen, D. C., Read, A. M., and Stevens, I. R. (2006a). An ultraluminous X-ray microquasar in NGC5408? *MNRAS*, 368:1527–1539.

Soria, R. and Ghosh, K. K. (2009). Different Types of Ultraluminous X-Ray Sources in NGC 4631. *ApJ*, 696:287–297.

Soria, R. and Kong, A. (2016). Revisiting the ultraluminous supersoft source in M 101: an optically thick outflow model. *MNRAS*, 456:1837–1858.

Soria, R., Kuncic, Z., Broderick, J. W., and Ryder, S. D. (2006b). Multiband study of NGC7424 and its two newly discovered ultraluminous X-ray sources. *MNRAS*, 370:1666–1676.

Soria, R., Kuntz, K. D., Winkler, P. F., Blair, W. P., Long, K. S., Plucinsky, P. P., and Whitmore, B. C. (2012). The Birth of an Ultraluminous X-Ray Source in M83. *ApJ*, 750:152.

Soria, R., Long, K. S., Blair, W. P., Godfrey, L., Kuntz, K. D., Lenc, E., Stockdale, C., and Winkler, P. F. (2014). Super-Eddington Mechanical Power of an Accreting Black Hole in M83. *Science*, 343:1330–1333.

Soria, R., Pakull, M. W., Broderick, J. W., Corbel, S., and Motch, C. (2010). Radio lobes and X-ray hotspots in the microquasar S26. *MNRAS*, 409:541–551.

Southwell, K. A., Livio, M., Charles, P. A., O'Donoghue, D., and Sutherland, W. J. (1996). The Nature of the Supersoft X-Ray Source RX J0513-69. *ApJ*, 470:1065.

Sparks, W. B., Biretta, J. A., and Macchetto, F. (1996). The Jet of M87 at Tenth-Arcsecond Resolution: Optical, Ultraviolet, and Radio Observations. *ApJ*, 473:254.

Starrfield, S., Iliadis, C., Hix, W. R., Timmes, F. X., and Sparks, W. M. (2009). The Effects of the pep Nuclear Reaction and Other Improvements in the Nuclear Reaction Rate Library on Simulations of the Classical Nova Outburst. *ApJ*, 692:1532–1542.

Steiner, J. F., Walton, D. J., García, J. A., McClintock, J. E., Laycock, S. G. T., Middleton, M. J., Barnard, R., and Madsen, K. K. (2016). On the Spin of the Black Hole in IC 10 X-1. *ApJ*, 817:154.

Steinhardt, C. L. and Elvis, M. (2010). The quasar mass-luminosity plane - I. A sub-Eddington limit for quasars. *MNRAS*, 402:2637–2648.

Stetson, P. B. (1987). DAOPHOT - A computer program for crowded-field stellar photometry. *PASP*, 99:191–222.

Stewart, G. C., Watson, M. G., Matsuoka, M., Brinkmann, W., Jugaku, J., Takagishi, K., Omodaka, T., Kemp, J. C., Kenson, G. D., Kraus, D. J., Mazeh, T., and Leibowitz, E. M. (1987). Simultaneous observations of the X-ray and optical eclipse of SS433 and their implications. *MNRAS*, 228:293–303.

Stobbart, A.-M., Roberts, T. P., and Warwick, R. S. (2004). A dipping black hole X-ray binary candidate in NGC 55. *MNRAS*, 351:1063–1070.

Stobbart, A.-M., Roberts, T. P., and Wilms, J. (2006). XMM-Newton observations of the brightest ultraluminous X-ray sources. *MNRAS*, 368:397–413.

Strohmayer, T. E., Mushotzky, R. F., Winter, L., Soria, R., Uttley, P., and Cropper, M. (2007). Quasi-periodic Variability in NGC 5408 X-1. *ApJ*, 660:580–586.

Sutherland, R. S. and Dopita, M. A. (1993). Cooling functions for low-density astrophysical plasmas. *ApJS*, 88:253–327.

Sutton, A. D., Done, C., and Roberts, T. P. (2014). Irradiated, colour-temperature-corrected accretion discs in ultraluminous X-ray sources. *MNRAS*, 444:2415–2427.

Sutton, A. D., Roberts, T. P., Gladstone, J. C., Farrell, S. A., Reilly, E., Goad, M. R., and Gehrels, N. (2013a). A bright ultraluminous X-ray source in NGC 5907. *MNRAS*, 434:1702–1712.

Sutton, A. D., Roberts, T. P., and Middleton, M. J. (2013b). The ultraluminous state revisited: fractional variability and spectral shape as diagnostics of super-Eddington accretion. *MNRAS*, 435:1758–1775.

Sutton, A. D., Roberts, T. P., and Middleton, M. J. (2015). X-Ray Spectral Residuals in NGC 5408 X-1: Diffuse Emission from Star Formation, or the Signature of a Super-Eddington Wind? *ApJ*, 814:73.

Sutton, A. D., Swartz, D. A., Roberts, T. P., Middleton, M. J., Soria, R., and Done, C. (2016). Submitted. *ApJ, submitted*.

Swartz, D. A., Ghosh, K. K., Suleimanov, V., Tennant, A. F., and Wu, K. (2002). Chandra Discovery of Luminous Supersoft X-Ray Sources in M81. *ApJ*, 574:382–397.

Swartz, D. A., Ghosh, K. K., Tennant, A. F., and Wu, K. (2004). The Ultraluminous X-Ray Source Population from the Chandra Archive of Galaxies. *ApJS*, 154:519–539.

Swartz, D. A., Soria, R., and Tennant, A. F. (2008). Do Ultraluminous X-Ray Sources Exist in Dwarf Galaxies? *ApJ*, 684:282–286.

Swartz, D. A., Soria, R., Tennant, A. F., and Yukita, M. (2011). A Complete Sample of Ultraluminous X-ray Source Host Galaxies. *ApJ*, 741:49.

Takahashi, H. R. and Ohsuga, K. (2017). General Relativistic Radiation MHD Simulations of Supercritical Accretion onto a Magnetized Neutron Star: Modeling of Ultraluminous X-Ray Pulsars. *ApJL*, 845:L9.

Takeuchi, S., Ohsuga, K., and Mineshige, S. (2013). Clumpy Outflows from Supercritical Accretion Flow. *PASJ*, 65:88.

Takeuchi, S., Ohsuga, K., and Mineshige, S. (2014). Radiation hydrodynamic instability in a plane-parallel, super-Eddington atmosphere: A mechanism for clump formation. *PASJ*, 66:48.

Tao, L., Feng, H., Grisé, F., and Kaaret, P. (2011). Compact Optical Counterparts of Ultraluminous X-Ray Sources. *ApJ*, 737:81.

Tao, L., Feng, H., Kaaret, P., Grisé, F., and Jin, J. (2012a). Chandra and Hubble Space Telescope Observations of the Supersoft ULX in NGC 247: Candidate for Standard Disk Emission. *ApJ*, 758:85.

Tao, L., Kaaret, P., Feng, H., and Grisé, F. (2012b). The Nature of the UV/Optical Emission of the Ultraluminous X-Ray Source in Holmberg II. *ApJ*, 750:110.

Tartaglia, L., Pastorello, A., Taubenberger, S., Cappellaro, E., Maund, J. R., Benetti, S., Boles, T., Bufano, F., Duszanowicz, G., Elias-Rosa, N., Harutyunyan, A., Hermansson, L., Höflich, P., Maguire, K., Navasardyan, H., Smartt, S. J., Taddia, F., and Turatto, M. (2015). Interacting supernovae and supernova impostors. SN 2007sv: the major eruption of a massive star in UGC 5979. *MNRAS*, 447:117–131.

Taylor, G. B., Carilli, C. L., and Perley, R. A., editors (1999). *Synthesis Imaging in Radio Astronomy II*, volume 180 of *Astronomical Society of the Pacific Conference Series*.

Terashima, Y. and Wilson, A. S. (2004). The Luminous X-Ray Source Population in M51 Observed with Chandra. *ApJ*, 601:735–758.

Thompson, A. R., Moran, J. M., and Swenson, Jr., G. W. (2001). *Interferometry and Synthesis in Radio Astronomy, 2nd Edition*.

Titarchuk, L. (1994). Generalized Comptonization models and application to the recent high-energy observations. *ApJ*, 434:570–586.

Tody, D. (1993). IRAF in the Nineties. In Hanisch, R. J., Brissenden, R. J. V., and Barnes, J., editors, *Astronomical Data Analysis Software and Systems II*, volume 52 of *Astronomical Society of the Pacific Conference Series*, page 173.

Tombesi, F., Tazaki, F., Mushotzky, R. F., Ueda, Y., Cappi, M., Gofford, J., Reeves, J. N., and Guainazzi, M. (2014). Ultrafast outflows in radio-loud active galactic nuclei. *MNRAS*, 443:2154–2182.

Trinchieri, G. and Fabbiano, G. (1991). The discrete X-ray source population in M31. *ApJ*, 382:82–99.

Trudolyubov, S. P. and Priedhorsky, W. C. (2008). XMM-Newton Discovery of 217 s Pulsations in the Brightest Persistent Supersoft X-Ray Source in M31. *ApJ*, 676:1218–1225.

Tudose, V., Fender, R. P., Kaiser, C. R., Tzioumis, A. K., van der Klis, M., and Spencer, R. E. (2006). The large-scale jet-powered radio nebula of Circinus X-1. *MNRAS*, 372:417–424.

Urry, C. M. and Padovani, P. (1995). Unified Schemes for Radio-Loud Active Galactic Nuclei. *PASP*, 107:803.

van den Heuvel, E. P. J., Bhattacharya, D., Nomoto, K., and Rappaport, S. A. (1992). Accreting white dwarf models for CAL 83, CAL 87 and other ultrasoft X-ray sources in the LMC. *A&A*, 262:97–105.

van Dyk, S. D., Sramek, R. A., Weiler, K. W., Hyman, S. D., and Virden, R. E. (1994). The radio counterpart to the luminous X-ray supernova remnant in NGC 6946. *ApJL*, 425:L77–L79.

van Kerkwijk, M. H., Breton, R. P., and Kulkarni, S. R. (2011). Evidence for a Massive Neutron Star from a Radial-velocity Study of the Companion to the Black-widow Pulsar PSR B1957+20. *ApJ*, 728:95.

van Rossum, D. R. (2012). A Public Set of Synthetic Spectra from Expanding Atmospheres for X-Ray Novae. I. Solar Abundances. *ApJ*, 756:43.

Vaughan, S., Edelson, R., Warwick, R. S., and Uttley, P. (2003). On characterizing the variability properties of X-ray light curves from active galaxies. *MNRAS*, 345:1271–1284.

Veilleux, S. and Osterbrock, D. E. (1987). Spectral classification of emission-line galaxies. *ApJS*, 63:295–310.

Vierdayanti, K., Sadowski, A., Mineshige, S., and Bursa, M. (2013). Inner disc obscuration in GRS 1915+105 based on relativistic slim disc model. *MNRAS*, 436:71–81.

Vierdayanti, K., Watarai, K.-Y., and Mineshige, S. (2008). On Black Hole Mass Estimation from X-Ray Spectra of Ultraluminous X-Ray Sources. *PASJ*, 60:653–665.

Villar, V. A., Berger, E., Chornock, R., Margutti, R., Laskar, T., Brown, P. J., Blanchard, P. K., Czekala, I., Lunnan, R., and Reynolds, M. T. (2016). The Intermediate Luminosity Optical Transient SN 2010da: The Progenitor, Eruption, and Aftermath of a Peculiar Supergiant High-mass X-Ray Binary. *ApJ*, 830:11.

Vlahakis, C., van der Werf, P., Israel, F. P., and Tilanus, R. P. J. (2013). A CO J = 3-2 map of M51 with HARP-B: radial properties of the spiral structure. *MNRAS*, 433:1837–1861.

Vlahakis, N., Peng, F., and Königl, A. (2003). Neutron-rich Hydromagnetic Outflows in Gamma-Ray Burst Sources. *ApJL*, 594:L23–L26.

Vogler, A. and Pietsch, W. (1996). ROSAT observations of NGC 4631. *A&A*, 311:35–48.

Volonteri, M., Silk, J., and Dubus, G. (2015). The Case for Supercritical Accretion onto Massive Black Holes at High Redshift. *ApJ*, 804:148.

Vrtilek, S. D., Raymond, J. C., Garcia, M. R., Verbunt, F., Hasinger, G., and Kurster, M. (1990). Observations of Cygnus X-2 with IUE - Ultraviolet results from a multiwavelength campaign. *A&A*, 235:162–173.

Walton, D. J., Fürst, F., Harrison, F. A., Middleton, M. J., Fabian, A. C., Bachetti, M., Barret, D., Miller, J. M., Ptak, A., Rana, V., Stern, D., and Tao, L. (2017). The Broadband Spectral Variability of Holmberg IX X-1. *ApJ*, 839:105.

Walton, D. J., Harrison, F. A., Grefenstette, B. W., Miller, J. M., Bachetti, M., Barret, D., Boggs, S. E., Christensen, F. E., Craig, W. W., Fabian, A. C., Fuerst, F., Hailey, C. J., Madsen, K. K., Parker, M. L., Ptak, A., Rana, V., Stern, D., Webb, N., and Zhang, W. W. (2014). Broadband X-Ray Spectra of the Ultraluminous X-Ray Source Holmberg IX X-1 Observed with NuSTAR, XMM-Newton, and Suzaku. *ApJ*, 793:21.

Walton, D. J., Middleton, M. J., Rana, V., Miller, J. M., Harrison, F. A., Fabian, A. C., Bachetti, M., Barret, D., Boggs, S. E., Christensen, F. E., Craig, W. W., Fuerst, F., Grefenstette, B. W., Hailey, C. J., Madsen, K. K., Stern, D., and Zhang, W. (2015). NuSTAR, XMM-Newton, and Suzaku Observations of the Ultraluminous X-Ray Source Holmberg II X-1. *ApJ*, 806:65.

Walton, D. J., Roberts, T. P., Mateos, S., and Heard, V. (2011). 2XMM ultraluminous X-ray source candidates in nearby galaxies. *MNRAS*, 416:1844–1861.

Wang, Q. D., Yao, Y., Fukui, W., Zhang, S. N., and Williams, R. (2004). XMM-Newton Spectra of Intermediate-Mass Black Hole Candidates: Application of a Monte Carlo Simulated Model. *ApJ*, 609:113–121.

Wang, S., Soria, R., Urquhart, R., and Liu, J. (2018). Discovery of two eclipsing X-ray binaries in M 51. *MNRAS*, 477:3623–3645.

Warmels, R. H. (1992). The ESO–MIDAS System. In Worrall, D. M., Biemesderfer, C., and Barnes, J., editors, *Astronomical Data Analysis Software and Systems I*, volume 25 of *Astronomical Society of the Pacific Conference Series*, page 115.

Watarai, K.-y., Fukue, J., Takeuchi, M., and Mineshige, S. (2000). Galactic Black-Hole Candidates Shining at the Eddington Luminosity. *PASJ*, 52:133.

Watarai, K.-Y. and Mineshige, S. (2003). Where is a Marginally Stable Last Circular Orbit in Super-Critical Accretion Flow? *PASJ*, 55:959–965.

Watarai, K.-y., Mizuno, T., and Mineshige, S. (2001). Slim-Disk Model for Ultraluminous X-Ray Sources. *ApJL*, 549:L77–L80.

Weaver, R., McCray, R., Castor, J., Shapiro, P., and Moore, R. (1977). Interstellar bubbles. II - Structure and evolution. *ApJ*, 218:377–395.

Weis, K. (2011). Gone with the wind: Nebulae around LBVs. *Bulletin de la Societe Royale des Sciences de Liege*, 80:440–444.

White, N. E. and Holt, S. S. (1982). Accretion disk coronae. *ApJ*, 257:318–337.

White, N. E. and Swank, J. H. (1982). The discovery of 50 minute periodic absorption events from 4U 1915-05. *ApJL*, 253:L61–L66.

Whitehurst, R. (1988). Numerical simulations of accretion disks. I - Superhumps - A tidal phenomenon of accretion disks. *MNRAS*, 232:35–51.

Wiktorowicz, G., Sobolewska, M., Lasota, J.-P., and Belczynski, K. (2017). The Origin of the Ultraluminous X-Ray Sources. *ApJ*, 846:17.

Wiktorowicz, G., Sobolewska, M., Sądowski, A., and Belczynski, K. (2015). Nature of the Extreme Ultraluminous X-Ray Sources. *ApJ*, 810:20.

Willott, C. J., Rawlings, S., Blundell, K. M., and Lacy, M. (1999). The emission line-radio correlation for radio sources using the 7C Redshift Survey. *MNRAS*, 309:1017–1033.

Wilson, A. S. and Yang, Y. (2002). Chandra X-Ray Imaging and Spectroscopy of the M87 Jet and Nucleus. *ApJ*, 568:133–140.

Wilson, W. E., Ferris, R. H., Axtens, P., Brown, A., Davis, E., Hampson, G., Leach, M., Roberts, P., Saunders, S., Koribalski, B. S., Caswell, J. L., Lenc, E., Stevens, J., Voronkov, M. A., Wieringa, M. H., Brooks, K., Edwards, P. G., Ekers, R. D., Emonts, B., Hindson, L., Johnston, S., Maddison, S. T., Mahony, E. K., Malu, S. S., Massardi, M., Mao, M. Y., McConnell, D., Norris, R. P., Schnitzeler, D., Subrahmanyan, R., Urquhart, J. S., Thompson, M. A., and Wark, R. M. (2011). The Australia Telescope Compact Array Broad-band Backend: description and first results. *MNRAS*, 416:832–856.

Worrall, D. M., Birkinshaw, M., and Young, A. J. (2016). X-rays associated with the jet-cloud-interacting radio galaxy 3C 277.3 (Coma A): implications for energy deposition. *MNRAS*, 458:174–183.

Yoshida, T., Isobe, N., Mineshige, S., Kubota, A., Mizuno, T., and Saitou, K. (2013). Two Power-Law States of the Ultraluminous X-Ray Source IC 342 X-1. *PASJ*, 65:48.

Zaritsky, D., Kennicutt, Jr., R. C., and Huchra, J. P. (1994). H II regions and the abundance properties of spiral galaxies. *ApJ*, 420:87–109.

Zealey, W. J., Dopita, M. A., and Malin, D. F. (1980). The interaction between the relativistic jets of SS433 and the interstellar medium. *MNRAS*, 192:731–743.

Appendix A

Publications

Publications directly used in the thesis include:

- **R. Urquhart** and R. Soria. 2016. "Optically thick outflows in ultraluminous supersoft sources", *Monthly Notices of the Royal Astronomical Society*, 456(2), p. 1859-1880. DOI:10.1093/mnras/stv2293
- **R. Urquhart** and R. Soria. 2016. "Two eclipsing ultraluminous X-ray sources in M51", *The Astrophysical Journal*, 831(1), article id. 56, 23 pp. DOI:10.3847/0004-637X/831/1/56
- **R. Urquhart**, R. Soria, H. Johnston, M. Pakull, C. Motch, A. Schwope, J.C.A. Miller-Jones and G.E. Anderson. 2018. "Multiband counterparts of two eclipsing ultraluminous X-ray sources in M 51", *Monthly Notices of the Royal Astronomical Society*, 475(3), p. 3561-3576. DOI: 10.1093/mnras/sty014
- **R. Urquhart**, R. Soria, M. Pakull, J.C.A Miller-Jones, G.E Anderson, R.M. Plotkin, C. Motch, T.J. Maccarone, A.F McLeod and S. Scaringi, 2018. "A newly discovered double-double candidate microquasar in NGC 300", *accepted for publication in the Monthly Notices of the Royal Astronomical Society*, DOI: 10.1093/mnras/sty2771

Publications not directly used in the thesis include:

- C. Pinto, W. Alston, R. Soria, M.J. Middleton, D. J. Walton, A.D. Sutton, A.C. Fabian, H. Earnshaw, **R. Urquhart**, E. Kara and T.P. Roberts. 2017. "From ultraluminous X-ray sources to ultraluminous supersoft sources: NGC

55 ULX, the missing link", *Monthly Notices of the Royal Astronomical Society*, 468(3), pp. 2865-2883. DOI:10.1093/mnras/stx641

- S. J. Tingay, C. Tremblay, A. Walsh and **R. Urquhart**. 2016. "An opportunistic search for extraterrestrial intelligence (SETI) with the Murchison Widefield Array", *The Astrophysical Journal Letters*, 827(2), article id. L22, 5 pp. DOI:10.3847/0004-637X/831/1/56

- V.A. Moss, J.R. Allison, E.M. Sadler, **R. Urquhart**, R. Soria, J.R. Callingham, S.J. Curran, A. Musaeva, E.K. Mahony, M. Glowacki, S.A. Farrell, K.W. Bannister, A.P. Chippendale, P.G. Edwards, L. Harvey-Smith, I. Heywood, A.W. Hotan, B.T. Indermuehle, E. Lenc, J. Marvil, D. McConnell, J.E. Reynolds, M.A. Voronkov, R M. Wark and M.T. Whiting. 2017. "Connecting X-ray absorption and 21 cm neutral hydrogen absorption in obscured radio AGN", *Monthly Notices of the Royal Astronomical Society*, 471(3), p. 2952-2973. DOI: 10.1093/mnras/stx1679

- R. Soria, A. Musaeva, K. Wu, L. Zampieri, S. Federle, **R. Urquhart**, E. van der Helm and S. Farrell. 2017. "Outbursts of the intermediate-mass black hole HLX-1: a wind instability scenario", *Monthly Notices of the Royal Astronomical Society*, 469(1), p. 886-905. DOI: 10.1093/mnras/ stx888

- H. Rampadarth, R. Soria, **R. Urquhart**, M.K. Argo, M. Brightman, C.K. Lacey, E.M. Schlegel, R.J. Beswick, R. Baldi, T.W.B. Muxlow, I.M. McHardy, D.R.A. Wiliams and G. Dumas. 2018. "Jets, Arcs and Shocks: NGC 5195 at radio wavelengths", *Monthly Notices of the Royal Astronomical Society*, 476(3), p. 2876-2889. DOI: 10.1093/mnras/sty390

- S. Wang, R. Soria, **R. Urquhart** and J. Liu. 2018. "Discovery of two eclipsing sources in M 51", *Monthly Notices of the Royal Astronomical Society*, DOI: 10.1093/mnras/sty872

Appendix B

Contribution statements

The following section contains signed statements from each of the co-authors of one or more of the four publications used as part of this thesis. Each signed statement attests to the accuracy of the contribution declaration outlined at the start of each chapter adapted from a publication.

To Whom It May Concern,

I, Ryan Troy Urquhart, have outlined my contributions for the publications entitled

i. *Optically thick outflows in ultraluminous supersoft sources* (Urquhart and Soria. 2016a),
ii. *Two eclipsing ultraluminous X-ray sources in M51* (Urquhart and Soria. 2016b),
iii. *Multiband counterparts of two eclipsing ultraluminous X-ray sources in M51* (Urquhart et al. 2018), and,
iv. *A newly discovered double-double candidate microquasar in NGC300* (Urquhart et al. 2019)

at the start of each respective thesis chapter.

I, as a Co-Author of one or more of these publications, endorse that this level of contribution by the candidate indicated within the thesis chapter is appropriate.

Gemma Elizabeth Anderson

(Full Name of Co-Author) (Signature of Co-Author)

To Whom It May Concern,

I, Ryan Troy Urquhart, have outlined my contributions for the publications entitled

i. *Optically thick outflows in ultraluminous supersoft sources* (Urquhart and Soria. 2016a),
ii. *Two eclipsing ultraluminous X-ray sources in M51* (Urquhart and Soria. 2016b),
iii. *Multiband counterparts of two eclipsing ultraluminous X-ray sources in M51* (Urquhart et al. 2018), and,
iv. *A newly discovered double-double candidate microquasar in NGC300* (Urquhart et al. 2019)

at the start of each respective thesis chapter.

I, as a Co-Author of one or more of these publications, endorse that this level of contribution by the candidate indicated within the thesis chapter is appropriate.

Helen Johnston

(Full Name of Co-Author) (Signature of Co-Author)

To Whom It May Concern,

I, Ryan Troy Urquhart, have outlined my contributions for the publications entitled

i. *Optically thick outflows in ultraluminous supersoft sources* (Urquhart and Soria. 2016a),
ii. *Two eclipsing ultraluminous X-ray sources in M51* (Urquhart and Soria. 2016b),
iii. *Multiband counterparts of two eclipsing ultraluminous X-ray sources in M51* (Urquhart et al. 2018), and,
iv. *A newly discovered double-double candidate microquasar in NGC300* (Urquhart et al. 2019)

at the start of each respective thesis chapter.

I, as a Co-Author of one or more of these publications, endorse that this level of contribution by the candidate indicated within the thesis chapter is appropriate.

Thomas Maccarone

(Full Name of Co-Author) (Signature of Co-Author)

To Whom It May Concern,

I, Ryan Troy Urquhart, have outlined my contributions for the publications entitled

i. *Optically thick outflows in ultraluminous supersoft sources* (Urquhart and Soria. 2016a),
ii. *Two eclipsing ultraluminous X-ray sources in M51* (Urquhart and Soria. 2016b),
iii. *Multiband counterparts of two eclipsing ultraluminous X-ray sources in M51* (Urquhart et al. 2018), and,
iv. *A newly discovered double-double candidate microquasar in NGC300* (Urquhart et al. 2019)

at the start of each respective thesis chapter.

I, as a Co-Author of one or more of these publications, endorse that this level of contribution by the candidate indicated within the thesis chapter is appropriate.

Anna McLeod

(Full Name of Co-Author) (Signature of Co-Author)

To Whom It May Concern,

I, Ryan Troy Urquhart, have outlined my contributions for the publications entitled

i. *Optically thick outflows in ultraluminous supersoft sources* (Urquhart and Soria. 2016a),
ii. *Two eclipsing ultraluminous X-ray sources in M51* (Urquhart and Soria. 2016b),
iii. *Multiband counterparts of two eclipsing ultraluminous X-ray sources in M51* (Urquhart et al. 2018), and,
iv. *A newly discovered double-double candidate microquasar in NGC300* (Urquhart et al. 2019)

at the start of each respective thesis chapter.

I, as a Co-Author of one or more of these publications, endorse that this level of contribution by the candidate indicated within the thesis chapter is appropriate.

James C.A. Miller-Jones

(Full Name of Co-Author) (Signature of Co-Author)

To Whom It May Concern,

I, Ryan Troy Urquhart, have outlined my contributions for the publications entitled

i. *Optically thick outflows in ultraluminous supersoft sources* (Urquhart and Soria. 2016a),
ii. *Two eclipsing ultraluminous X-ray sources in M51* (Urquhart and Soria. 2016b),
iii. *Multiband counterparts of two eclipsing ultraluminous X-ray sources in M51* (Urquhart et al. 2018), and,
iv. *A newly discovered double-double candidate microquasar in NGC300* (Urquhart et al. 2019)

at the start of each respective thesis chapter.

I, as a Co-Author of one or more of these publications, endorse that this level of contribution by the candidate indicated within the thesis chapter is appropriate.

Christian Motch

(Full Name of Co-Author) (Signature of Co-Author)

To Whom It May Concern,

I, Ryan Troy Urquhart, have outlined my contributions for the publications entitled

i. *Optically thick outflows in ultraluminous supersoft sources* (Urquhart and Soria. 2016a),
ii. *Two eclipsing ultraluminous X-ray sources in M51* (Urquhart and Soria. 2016b),
iii. *Multiband counterparts of two eclipsing ultraluminous X-ray sources in M51* (Urquhart et al. 2018), and,
iv. *A newly discovered double-double candidate microquasar in NGC300* (Urquhart et al. 2019)

at the start of each respective thesis chapter.

I, as a Co-Author of one or more of these publications, endorse that this level of contribution by the candidate indicated within the thesis chapter is appropriate.

Manfred Pakull

(Full Name of Co-Author)

(Signature of Co-Author)

To Whom It May Concern,

I, Ryan Troy Urquhart, have outlined my contributions for the publications entitled

i. *Optically thick outflows in ultraluminous supersoft sources* (Urquhart and Soria. 2016a),
ii. *Two eclipsing ultraluminous X-ray sources in M51* (Urquhart and Soria. 2016b),
iii. *Multiband counterparts of two eclipsing ultraluminous X-ray sources in M51* (Urquhart et al. 2018), and,
iv. *A newly discovered double-double candidate microquasar in NGC300* (Urquhart et al. 2019)

at the start of each respective thesis chapter.

I, as a Co-Author of one or more of these publications, endorse that this level of contribution by the candidate indicated within the thesis chapter is appropriate.

Richard Plotkin

(Full Name of Co-Author) (Signature of Co-Author)

Richard M. Plotkin

To Whom It May Concern,

I, Ryan Troy Urquhart, have outlined my contributions for the publications entitled

i. *Optically thick outflows in ultraluminous supersoft sources* (Urquhart and Soria. 2016a),
ii. *Two eclipsing ultraluminous X-ray sources in M51* (Urquhart and Soria. 2016b),
iii. *Multiband counterparts of two eclipsing ultraluminous X-ray sources in M51* (Urquhart et al. 2018), and,
iv. *A newly discovered double-double candidate microquasar in NGC300* (Urquhart et al. 2019)

at the start of each respective thesis chapter.

I, as a Co-Author of one or more of these publications, endorse that this level of contribution by the candidate indicated within the thesis chapter is appropriate.

Simone Scaringi

(Full Name of Co-Author) (Signature of Co-Author)

To Whom It May Concern,

I, Ryan Troy Urquhart, have outlined my contributions for the publications entitled

i. *Optically thick outflows in ultraluminous supersoft sources* (Urquhart and Soria. 2016a),
ii. *Two eclipsing ultraluminous X-ray sources in M51* (Urquhart and Soria. 2016b),
iii. *Multiband counterparts of two eclipsing ultraluminous X-ray sources in M51* (Urquhart et al. 2018), and,
iv. *A newly discovered double-double candidate microquasar in NGC300* (Urquhart et al. 2019)

at the start of each respective thesis chapter.

I, as a Co-Author of one or more of these publications, endorse that this level of contribution by the candidate indicated within the thesis chapter is appropriate.

Axel Schwope

(Full Name of Co-Author) (Signature of Co-Author)

To Whom It May Concern,

I, Ryan Troy Urquhart, have outlined my contributions for the publications entitled

i. *Optically thick outflows in ultraluminous supersoft sources* (Urquhart and Soria. 2016a),
ii. *Two eclipsing ultraluminous X-ray sources in M51* (Urquhart and Soria. 2016b),
iii. *Multiband counterparts of two eclipsing ultraluminous X-ray sources in M51* (Urquhart et al. 2018), and,
iv. *A newly discovered double-double candidate microquasar in NGC300* (Urquhart et al. 2019)

at the start of each respective thesis chapter.

I, as a Co-Author of one or more of these publications, endorse that this level of contribution by the candidate indicated within the thesis chapter is appropriate.

Roberto Soria

(Full Name of Co-Author) (Signature of Co-Author)